Hybridization of block copolymer thin films with plasmonic nanoresonators for optical metamaterials design.

Alberto Alvarez Fernández

université de BORDEAUX

THÈSE PRÉSENTÉE

POUR OBTENIR LE GRADE DE

DOCTEUR DE

L'UNIVERSITÉ DE BORDEAUX

Ecole Doctorale des Sciences Chimiques

Spécialité : Polymères

Par Alberto ÁLVAREZ FERNÁNDEZ

Hybridization of block copolymer thin films with plasmonic nanoresonators for optical metamaterials design

Sous la direction de Virginie PONSINET et Guillaume FLEURY

Soutenue le 16 novembre 2018 devant un jury composé de

M. DAVIDSON Patrick, Directeur de Recherche, Université Paris-Sud	Rapporteur
Mme TRAN Yvette, Maitre de conférences, ESPCI, Paris	Rapportrice
Mme CAMELIO Sophie, Professeure, Université de Poitiers	Examinatrice
M. PORTALE Giuseppe, Maitre de conférences, Université de Groningen	Examinateur
Mme ZAKRI Cécile, Professeure, Université de Bordeaux	Présidente
M. HADZIIOANNOU Georges, Professeur, Université de Bordeaux	Invité
M. FLEURY Guillaume, Maitre de conférences, Université de Bordeaux	Directeur de thèse
Mme PONSINET Virginie, Chargée de Recherches, Université de Bordeaux	Directrice de thèse

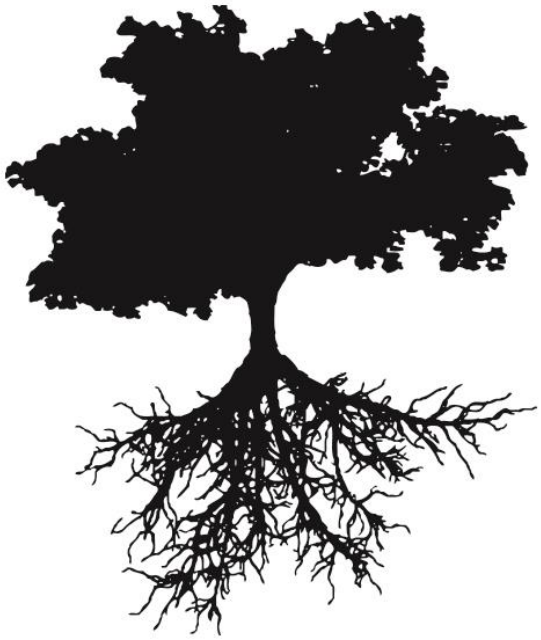

Na mio tierra d'Asturies hai un dichu que diz asina: Un árbol pue crecer abondu mas sin bonos raigaños, l'oral más nidiu valtaralu. D'esta miente los mios agradecimientos van escomenzar pol principiu, polos mios raigaños, los mios güelos. D'ellos aprendí munches coses, la más valiosa, a ser una bona persona. Oxalá estuviérais toos equí, de xuru sentiríes-vos el 10% d'arguyosos de lo que siento-me yo agora mesmu de vós. Y nun escaezo-me de ti, tú enseñástime Burdeos antes siquier de velo, ente otres munches coses. Siempres, siempres, siempres, vais tar conmigo allá ónde vaya.

Con estos raigaños un tueru con bones cañes salió. De que xorreciera encargaronse dos persones maraviyoses. Pá, ma, gracies. Gracies por enseñame a pensar, por tar siempres ellí onde vos precisara, por sofitame y dame impulso, por reñeme, por inclusive dar la vida por mi si vos-lo pidiera, por dame muncho más de lo que yo vos di, por dame al mio hermanu, la persona que más quiero nesti mundo. Quiéro-vos enforma anque nun vos lo diga bien amenudo. Tengo amás la suerte de tener unos tios que bien valen por padres y de un primu que val más qu'una ayalga.

Nesti puntu prestaríame abondu también recordar a tola xente qué formó y forma parte de la mio vida n'Uviéu. Gracies per tou, llévome munches bones alcordances. Del colexu a l´universidá y dempués el cambéu. Cambéu de país, cambéu de xente…cambéu a Burdeos.

Y equí atopé otra familia. Xente qu'en trés años dexa una buelga enorme en mí. Xente d'equí y dellí. Los nomes nun son la mio especialidá, asina que pido perdón por escaecer

daquien antes incluso d'escomenzar. Cuando xuno ta llueñe, dase cuenta que nun ye preciso conocer daquién de tola vida pa sentila como de la familia. Alexandra, Cintia, David, Laura, Jon, Leire, Marina, Miguel, Magdalena, Noelia vos fuisteis la mio familia equí, deséu de veres que sigámos atopándonos allá onde nos lleve la vida. Échovos y voi echavos de menos. Ensín vós nunca pudiera acabar esto, teneilo claro.

Hai dos persones nel llaboratoriu Ariana y Nicoletta, dos amigos, collacios nesta aventura. Nun sé si quiera cómo voi poder trabayar ensin tenevos ende, con quién voi rir, con quien voi aldericar y a quién voi quexame. Gracies per tantu.

A lo llargo d´estos trés años conoci a muncha xente que merecería tar equi, los míos colegues del B8, Konstantinos, Cian, Florian, Soléne, Cindy, Tommaso, Muriel Daniele, Federico, Ségolene, Benjamin, Cezar…, los que tán y los que tuvieron, toda la xente del CRPP y del LCPO. Prestaríame da-yos les gracies también a los míos dos supervisores Guillaume y Virginie, a lo cimeru por dame la oportunidá de trabayar nesta tesis y dame la llibertá y enfotu para llevar a cabu la xera. Gracies.

Para concluyir, a todes les persones coles que concidí equí namá puedo dicivos gracies.

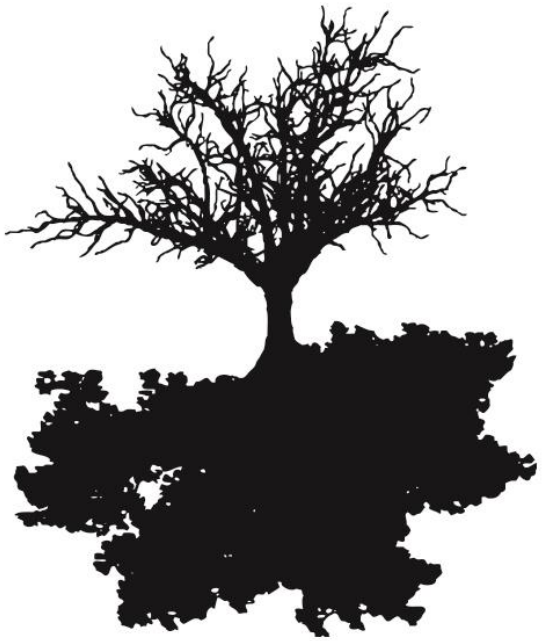

This PhD work could not be finished without the contribution of many people. I would like to thank specially Philippe Barois for his kindness and for helping me with the X-ray reflectivity and during the synchrotron beamtime, Morten Kildemo from NTNU for his help on the analysis of optical properties and Georges Hadziioannou for giving me the opportunity to work in his lab and for his support during these three years.

Thanks also to all the members of the Metamaterials group, specially Alexandre Baron, Philippe Richetti and Romain Dezert. Frederic Nallet for his help during the synchrotron beamtime. Philippe Fontaine from SOLEIL and Guiseppe Portale from Groningen University for giving me the opportunity to perform my GISAXS experiments and for their help during them.

I am deeply grateful to all members of the jury for agreeing to read the manuscript and to participate in the defence of this thesis.

Finally, I would like to address special thanks to the LabEx AMADEus and the Université de Bordeaux for the financial support during these three years.

Abstract

The concept of metamaterials appeared in the years 2000 with the achievement of artificial structures enabling nonconventional propagation of electromagnetic waves. The electromagnetic response of metamaterials is based on the presence of optically resonant elements of sub-wavelength size and well-designed morphology and organization.

In order to create controlled geometrical structures inherent to metamaterials design, block copolymer self-assembly constitutes an emerging strategy. Indeed, the periodic structures inherent to their segregation behavior can be used as scaffolds to create various regular or ordered nanoparticles arrays. The main objectives of this study is to demonstrate that block copolymer self-assembly can indeed lead to a high level of control for a variety of designed nanostructures, in an easy and scalable way, and to correlate the structural parameters of the nanoparticles arrays with their optical properties.

As a first demonstration, a lamellar-forming (poly(styrene)-*block*-poly(2-vinylpyridine) was used to create high refractive index surfaces. The selective and customizable metal incorporation within the out-of-plane lamellae produces azimuthally isotropic metallic nanostructures of defined geometries, for which a clear relationship between the gold content and the refractive index was established. Further studies were dedicated to the correlation between the geometrical parameters of the nanoparticles arrays and the optical properties through the macromolecular engineering of a series of cylinder-forming block copolymers having a wide range of molecular weights. Through this strategy, the particle diameter and the inter-particle distance were tuned leading to the production of metasurfaces with various optical characteristics. More complex metasurface designs were also obtained using a layer-by-layer self-assembly strategy, *i.e.*, bimetallic raspberry nanoclusters or layered hybrid (metallic/polymer) structures. In all cases, the nanoparticles arrays were thoroughly analyzed using microscopy and small-angle X-ray scattering techniques in order to better apprehend the optical properties derived from variable-angle spectroscopic ellipsometry analysis.

Résumé

Le concept de metamatériaux est apparu au cours des années 2000 avec la réalisation de structures artificielles permettant une propagation non-conventionnelles des ondes électromagnétiques. La réponse électromagnétique des metamatériaux est liée à la présence d'éléments optiquement résonants, de dimensions inférieures aux longueurs d'onde d'excitation, arrangés dans une structure périodique prédéfinie.

Afin de produire les structures géométriques inhérentes au design de metamatériaux, l'auto-assemblage des copolymères à blocs constitue une méthodologie émergente. En effet, les structures périodiques produites lors de la séparation de phase de ces matériaux peuvent être utilisées en tant que canevas pour la création de réseaux périodiques de nanoparticules. L'objectif principal de ces travaux de thèse a ainsi été de démontrer la validité de cette stratégie pour la réalisation, d'une manière simple et reproductible, d'une large gamme de nanostructures et de corréler les paramètres structuraux de ces réseaux de nanoparticules aux propriétés optiques.

Une première démonstration de ce concept a été obtenue en utilisant un copolymère à blocs formant une structure lamellaire afin de réaliser des surfaces possédant des indices de réfraction élevés. La formation contrôlée de particules métalliques au sein de cette structure a permis de produire des surfaces décorées par ces nanoparticules, pour lesquelles une corrélation entre la teneur en or et l'indice de réfraction résultant a pu être établie. Ce concept a été poussé plus en avant en utilisant une gamme de copolymères à blocs de différentes masses molaires et formant une morphologie cylindrique. En effet, un contrôle accru des paramètres structuraux des réseaux de nanoparticules (diamètre et distance inter-particules) a permis la réalisation de metasurfaces aux propriétés optiques variées. Enfin la mise au point d'une stratégie d'auto-assemblage itérative nous a permis d'obtenir des metasurfaces au design complexe, avec notamment la production de surfaces décorées par des clusters bimétalliques ou des multicouches hybrides polymère/métal. Dans l'ensemble des cas, les surfaces décorées de nanoparticules ont été minutieusement caractérisées par des techniques de microscopie et de diffraction RX afin de mieux appréhender les propriétés optiques dérivées d'analyses d'ellipsométrie spectroscopique à angle variable.

Table of contents

CHAPTER 2: High refractive index in low metal content nanoplasmonic surfaces from self-assembled block copolymer thin films

CHAPTER 3: Controlling the optical response through the macromolecular engineering of cylinder-forming block copolymers

General Introduction

Nanotechnology is defined as the manipulation of matter on an atomic, (macro)molecular and supramolecular scale. By the precise manipulation of nanoscale building blocks, novel “engineered” materials, exhibiting significantly different physical properties than the bulk counterparts, are at the core of new devices finding applications in medicine, electronics or energy production. The underlying concept was first introduced by Richard Feynman in a talk entitled “*There's Plenty of Room at the Bottom*” in which he described the possibility to directly manipulate individual atoms as a design tool more powerful than conventional chemistry. Relying on the invention of scanning tunnelling and atomic force microscopies in the 1980’s and on the development of powerful lithographic tools, two main approaches, *i.e.*, "bottom-up" and “top-down”, are used in nanotechnologies to produce the artificial features inherent to the engineering of functional systems. Recently, explorations of artificial materials for manipulating electromagnetic waves obtained through structural engineering at the nanoscale have attracted a lot of attention, with notably the first demonstration of an invisibility cloak at microwave frequencies by Schurig, Pendry, and Smith. This class of artificial materials defined thus a novel interdisciplinary research field, called metamaterials.

Metamaterials (from the Greek word μετά *meta*, meaning "beyond") are novel artificial materials with unusual electromagnetic properties that are not found in naturally occurring materials. The concept of metamaterials appeared in the 2000’s, with the achievement of artificial structures showing a frequency band with a negative refraction index. In such metamaterials, an unconventional propagation of electromagnetic waves is enabled. The peculiar electromagnetic response is based on the presence of optically resonant elements of sub-wavelength size with tailor-made shape and organization. More generally, metamaterials exhibit the potential to control the light propagation from the precise design of nanoscale features. These tailor-made resonant nanostructures might exhibit properties such as negative refractive index, electromagnetic bandgap or optical magnetism. However, the fabrication routes of metamaterials are still cumbersome and constitute a bottleneck for the widespread development of such nanotechnologies. Indeed, most demonstrators have

been produced by lithographic techniques which require expensive tools and strong environmental management.

An alternative would be to develop bottom-up approaches able to produce the tailor-made geometrical structures. In particular, block copolymer self-assembly applied to the definition of nanoscale features constitutes an emerging strategy with recent industrial breakthroughs in microelectronics. The periodic structures inherent to their segregation behaviour can be used as scaffolds to create regular and ordered arrays. Consequently, the main objective of this Ph.D. is to translate block copolymer fabrication strategies to the field of metamaterials. More precisely, the self-assembly of block copolymers in thin films will be used to gain a high level of control in the design of nanostructures, in an easy and scalable way. The resulting structures (denominated metasurfaces) will further be probed as regards to their optical properties with the challenge to originate unconventional responses.

The **Chapter 1** of this manuscript will describe the general context of this study. The paradigm of metamaterials and their classification into different classes depending on the final structure will be introduced. Since the properties of these materials strongly depend on the arrangement of the constitutive units at the nanoscale, the different fabrication strategies will be presented. As this Ph.D. thesis is focused on the bottom-up strategies, the most relevant ones will be introduced with a strong emphasis on the phenomenon leading to the block copolymer self-assembly into ordered structures. Furthermore, the techniques leading to the hybridization of block copolymer structures with metals or dielectrics will be reviewed as such strategies will be used to tune the optical responses of the block copolymer arrays. Finally, some pioneer works concerning the application of block copolymer templates to the design of metamaterials will be presented.

In **Chapter 2,** a first geometry of metasurfaces will be designed using the self-assembly of poly(styrene)-*block*-poly(2-vinylpyridine) (PS-*b*-P2VP) into out-of-plane lamellar morphology. The selective impregnation of the block copolymer domains with metallic salts will be pursued in a controlled manner in order to tune the shape and size of the particles formed from the block copolymer template. Indeed, a progressive evolution from isolated spherical nanoparticles to continuous metallic nanowires will be observed. Finally, the geometrical library of objects will allow us to correlate the optical response of the different metasurfaces with the structural design leading to high refractive index surfaces.

The **Chapter 3** will be dedicated to the correlation between the geometrical parameters of the nanoparticles arrays and the optical properties through the macromolecular engineering of a series of cylinder-forming block copolymers having a wide range of molecular weights. Through this strategy, the particle diameter and the inter-particle distance can be tuned leading to the production of metasurfaces with a very strong optical anisotropy.

In **Chapter 4**, more complex designs of metasurfaces will be introduced, taking advantage of the library of bottom-up strategies developed during this Ph.D. to build tailor-made geometrical structures. In particular, a promising strategy based on iterative self-assembly, *i.e.*, a layer-by-layer methodology, allow us to produce bimetallic raspberry nanoclusters or layered hybrid (metallic/polymer) structures. Preliminary results concerning the optical properties of these structures will be as well presented.

Finally, an **Annex** with all the experimental details and the description of the techniques used during this study is provided at the end of this manuscript.

List of abbreviations

1D: One dimension

2D: Two dimensions

3D: Three dimensions

AFM: Atomic Force Microscopy

ALD: Atomic Layer Deposition

AMR: Aqueous Metal Reduction

ATPR: Atom Transfer Radical Polymerization

BCP: Block Copolymer

BSE: Back-Scattering Imaging

$\mathbf{D_{c\text{-}c}}$: Centre-to-centre distance

D: Polydispersity

e: Ellipsoidal eccentricity

EMA: Effective Medium Approximation

FFT: Fast Fourier Transform

FWHM: Full Width at Half Maximum

$\mathbf{G^A}$: Alternating gyroid structure

GBSH: High Resolution Gentle Beam

GISAXS: Grazing Incident Small Angle X-ray Scattering

IR: Infrared

IPVs: Inorganic Photovoltaics

k: Absorption coefficient

$\mathbf{k_B}$: Boltzmann constant

KPFM: Kelvin Probe Force Microscopy

L: Depolarization factor

$\mathbf{L_0}$: Polymer domain spacing

LSPR: Localized Surface Plasmon Resonance

$\mathbf{M_n/M_w}$: Molecular weight dispersity

$\mathbf{M_n}$: Number-average molecular weight

$\bar{\boldsymbol{n}}$: complex refractive index

n: Optical refractive index

N: Degree of polymerization

$\mathbf{N_a}$: Avogadro's number

NMR: Nuclear Magnetic Resonance

NPs: Nanoparticles

ODT: Order-Disorder Transition

OPVs: Organic Photovoltaics

P2VP: poly(-2-vinylpyridine)

P4VP: poly(-4-vinylpyridine)

PCE: Power Conversion Efficiency

PDMS: poly(dimethyl siloxane)

PGMEA: Propylene glycol monomethyl ether acetate

PI-*b*-PEO: poly(isoprene-*b*-styrene-*b*-ethylene oxide

PMMA: Poly(methyl methacrylate)

PS: Poly(styrene)

PS-*b*-P2VP: Poly(styrene)-*block*-poly(-2-vinylpyridine)

PS-*b*-PDMS: Poly(styrene)-*block*-poly(dimethyl siloxane)

PS-*b*-PLA: Poly(styrene)-*block*-poly(lactic acid)

PS-*b*-PMMA: Poly(styrene)-*block*-poly(methyl methacrylate)

PSD: Power Spectral Density

RAFT: Reversible Addition-Fragmentation chain Transfer

$\mathbf{r_e}$: Electron radius

RIE: Reactive Ion Etching

RGB: red-blue-green

rpm: Revolutions per minute

SAXS: Small Angle X-ray Scattering

SE: Spectroscopy Ellipsometry

SEC: Size Exclusion Chromatography

SEI: Secondary Electron Imaging

SFM: Scanning Force Microscopy

SEM: Scanning Electron Microscopy

SLD: Scattering Length Density

SLRs: Surface Lattice Resonances

SRR: Split-Ring Resonator

SVA: Solvent Vapour Annealing

T: Temperature

t: Film thickness

TDMAT: Tetrakis(dimethylamino) titanium

TEM: Transmission Electron Microscopy

$\mathbf{T_g}$: Glass transition temperature

THF: Tetrahydrofuran

TMA: Trimethyl aluminium

UV: Ultraviolet

V: Volume

VASE: Variable Angle Spectroscopy Ellipsometry

VCPD: Contact potential difference

W: Work function

XPS: X-ray photoelectron spectroscopy

XRF: X-ray fluorescence

XRR: X-ray reflectivity

Z: Network coordination number

α: Polarizability

Δ: Ellipsometer angle

$\mathbf{\Delta G_m}$: Gibbs free-energy of mixing

$\mathbf{\Delta H_m}$: Mixing enthalpy

$\mathbf{\Delta S_m}$: Mixing entropy

$\bar{\varepsilon}$ **:** Complex electric permittivity

ε: Electric permittivity

$\mathbf{\varepsilon_0}$: Free-space permittivity

λ: Wavelength

$\bar{\mu}$: Complex magnetic permeability

Σ: Grafting density

ϕ: Volume fraction

$\mathbf{\chi_{AB}}$: Flory-Huggins parameter

ψ: Ellipsometer angle

ω: wave frequency

I

CHAPTER 1 | Bibliographical study

1. Optical metamaterials

1.1. A long short history

Metamaterials are a new class of artificial media composites that exhibit exceptional electromagnetic properties not readily observed in nature. These new functionalities are achieved using conventional building blocks through their packing at small length scale. Metamaterials constitute, therefore, an emerging and cross-disciplinary field, going from electromagnetics to material science [1].

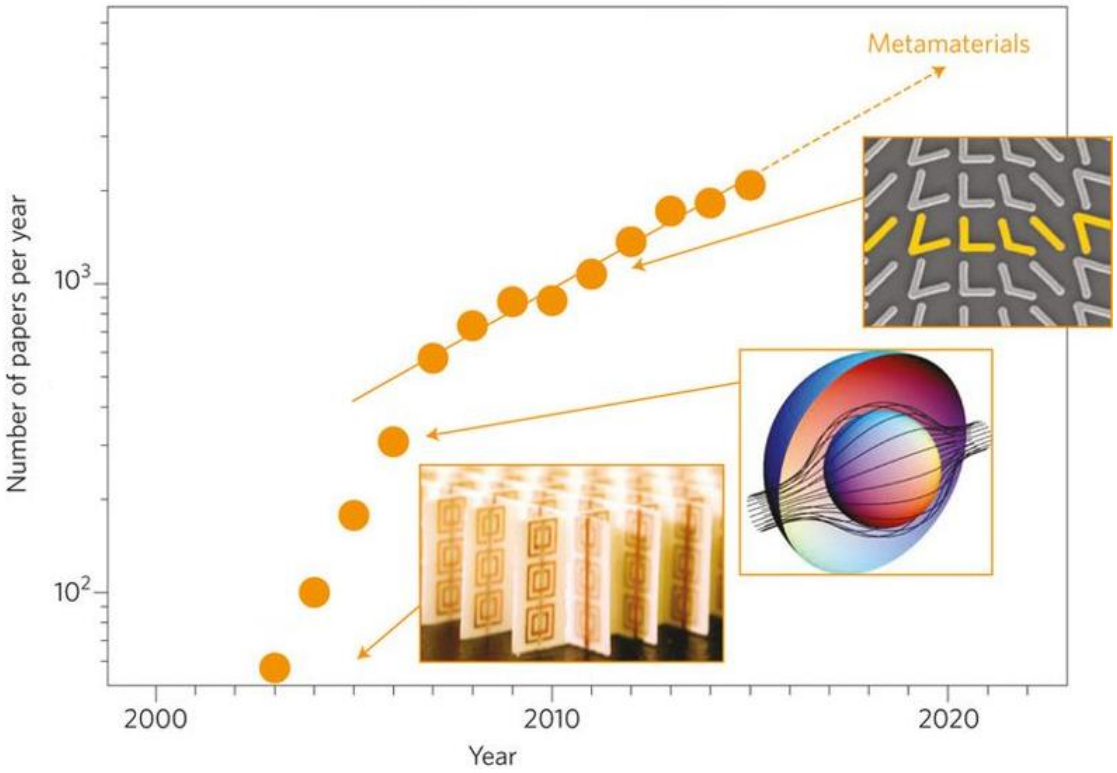

Figure 1.1: *Number of papers published per year in the field of metamaterials between 2000 and 2015. Dashed line is the speculative projection of this trend into the near future[7]. The insets show some of the most relevant marks in the evolution of metamaterial field (from bottom to top) negative refraction[2], cloaking[8] and metasurfaces[9].*

The word metamaterial was used for the first time in 2000. It was defined as *a composite medium, based on a periodic array of interspaced conducting nonmagnetic split ring resonators and continuous wires*[2]. Since that, the definition evolves several times, and all

these modifications are directly related with the necessity to expand the meaning of the term, from something very specific to more general, at the same speed that new discovers and developments were made. For example, in 2010 metamaterials were already defined as *an artificial media structured on a size scale smaller than the wavelength of external stimuli*[3], and finally since 2015 they are simply defined as *man-made media providing electromagnetic properties on-demand*[4]. Nowadays, after more than 20000 research articles published in the field (see **Fig. 1.1**), metamaterials constitute one of the most exciting disciplines, with a wide range of technological applications such as antennas[5] or absorbers[6].

1.2. Optical metamaterials

In this *Ph.D.* thesis, a particular focus was devoted to optical applications of metamaterials. In the following sections, different concepts will be introduced and various strategies for their fabrication will be presented. Nevertheless, a first question should be answered before going further, *i.e.*, why metamaterial design is of interest for optical applications? To answer it, we should go back to 1968. At this time, the seminal work of Veselago *et al.* demonstrated that combining a negative electric permittivity with a negative magnetic permeability could produce a material with a negative refractive index[10]. However, these results were based on theoretical considerations and the conclusion of the manuscript pointed out the absence of such materials in nature. Following this pioneer study, tremendous efforts were devoted by the scientific community towards the fabrication of metamaterials, considering their applications as super-lenses[11] or even in the design of an invisible cloak[12].

A subsequent question is how can we create such materials? Negative permittivity is quite common in metals at optical wavelengths but it is very unusual to find natural materials that exhibit magnetic response at high frequencies[13]. A first answer to this question was given by Pendry and coll. in 1999. They showed that a split-ring resonator (SRR) (**Fig. 1.2A**) with dimension smaller than the excitation wavelength (micro-wave in their study) used as a building block for the fabrication of a textured structure, could lead to a magnetic response at the resonant frequency of this oscillator, even in non-magnetic parent materials[14].

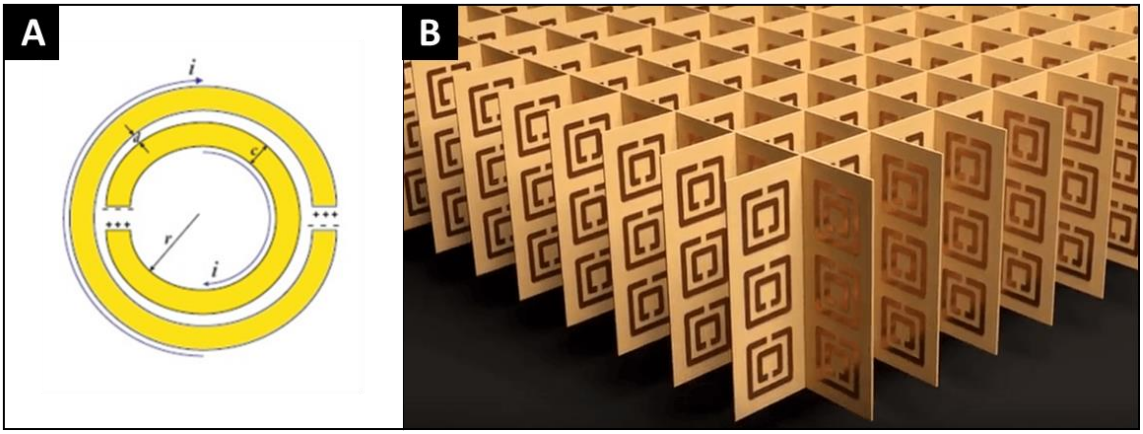

Figure 1.2: *(A) Schematic representation of a split ring resonator (SRR) and (B) of the metamaterial lattice used to demonstrate negative refraction index formed by an array of square split-ring resonators that gives the material a negative magnetic permeability.*

This design allows currents to run in a loop, concentrating the electromagnetic energy in a very small volume (around the gap), thus increasing its density by a huge factor, and greatly enhancing any nonlinear effects. This proof-of-concept opens the way to engineer electromagnetic properties in optical frequency. In other words, it is possible to design materials exhibiting both a negative permeability and a negative permittivity which should subsequently translate into negative refractive index metamaterials (**Fig. 1.2B**). Finally, in 2000, Smith and coworkers[2] demonstrated a negative refractive index material for micro-wave frequencies, using the SRR concept. Other kinds of structures, such as paired nano-rods[15] or metal/dielectric/metal fishnet structures[16], were then proposed, extending the range of structures and giving rise to optical metamaterials with tailored optical properties.

In summary, the metamaterials properties derive not only from the properties of the building block materials, but also from their designed structures. They are generally based on the presence of optically resonant elements of sub-wavelength size of well-designed morphology packed in a defined organization. A precise control of the shape, the geometry, the orientation and the arrangement of the structural units allows to manipulate electromagnetic waves, *i.e.*, by blocking, absorbing, enhancing, or bending waves, thus achieving benefits that go beyond of what is possible with conventional materials. But, what does it mean to be a conventional (unconventional, respectively) material from an optical

point of view? In the following section some basic considerations about material optics will be presented.

1.3. Optics of materials

The optical properties of materials are characterized by the complex refractive index ($\bar{n}$), that is defined as:

$$\bar{n} = n(\lambda) + ik(\lambda) \tag{1.1}$$

Where the real part, *n*, is also called the optical refractive index and the imaginary part, *k*, the absorption coefficient.

This imaginary part represents the energy loss by an electromagnetic radiation passing through a medium. A real refractive index at a defined wavelength means that the electromagnetic wave goes through the medium without being absorbed (k = 0), or in other words, the medium is transparent for this particular wavelength.

For all materials, the complex refractive index can by described by two parameters[14], the electric permittivity, $\bar{\varepsilon}$, and the complex magnetic permeability, $\bar{\mu}$, following the expression:

$$\bar{n} = \sqrt{\bar{\varepsilon}(\lambda)\,\bar{\mu}(\lambda)} \tag{1.2}$$

All the materials can be classified according to these two parameters into four different groups as represented in **Fig. 1.3A**. The first quadrant (I) covers materials with simultaneously positive permittivity and permeability and includes most dielectric materials. The quadrant (II) embraces metals, ferroelectric materials, and doped semiconductors that could exhibit negative permittivity at given frequencies (*i.e.*, below the plasma frequency). The quadrant (IV) describes the behaviour of some ferrite materials with negative permeability at microwave frequencies. Finally, the quadrant (III) is a region of special interest for the metamaterials field, since both the permittivity and the permeability are negative. As mentioned earlier, there is no such material in nature.

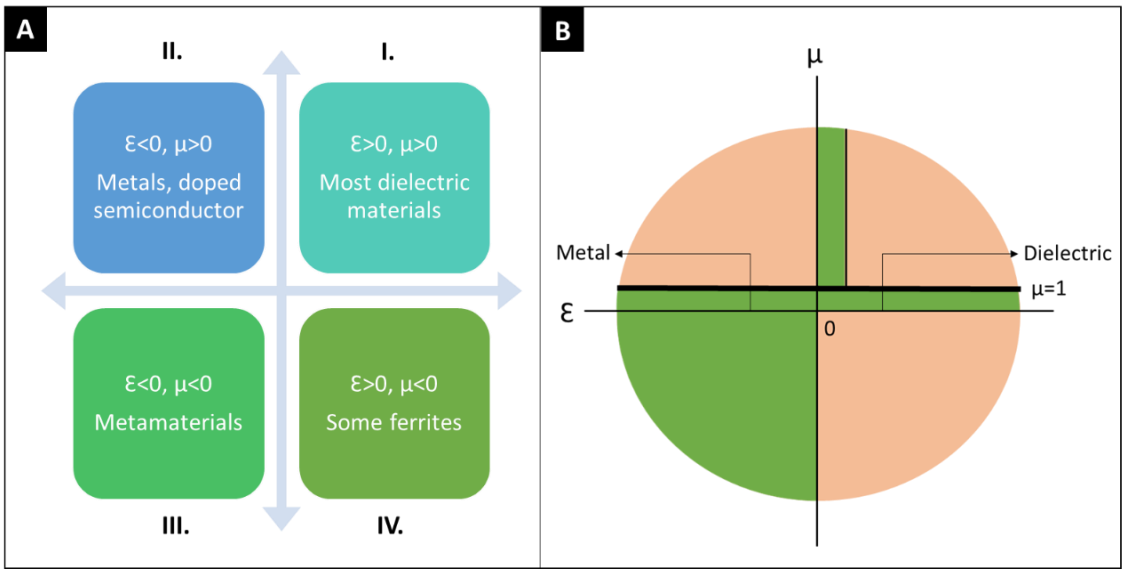

Figure 1.3: *(A) and (B), classification of materials based on the "electric permittivity (Ɛ)" and "magnetic permeability (μ)".*

Thus, the natural materials (orange part in **Fig. 1.3B**) only span a limited region of the theoretically accessible ε and μ values. In the visible range, natural materials have a permeability close to 1. Dielectrics have a positive $\mathcal{E}$ while metals present a negative $\mathcal{E}$. All the other regions (in green) correspond to metamaterials. Thus, designing and engineering metamaterials will open new avenues in order to manipulate the electromagnetic waves, overpassing the constrains of natural materials.

1.4. Nanostructuration is the key

The index of refraction provides a measure of the speed of an electromagnetic wave as it propagates within a material. Additionally, it provides information on the deflection of a light beam when crossing the interface between two materials having different refractive index values. This phenomenon was studied by Willebrord Snell in 1621 and René Descartes in 1637, giving the following relation:

$$n_1 sin\theta_1 = n_2 sin\theta_2 \tag{1.3}$$

Where the indices of refraction of the first and second media are denoted by n_1 and n_2, respectively, and θ_1 and θ_2 are the angles the light makes with the surface normal of each medium.

According to Snell's law, when a light beam is incident from a positive-index medium (n_1) to another positive-index medium (n_2), the light ray is deflected by a positive angle, θ_2, with respect to the perpendicular axis to the interface (**Fig. 1.4A**). On the contrary, when a light beam is incident from a positive-index material to a negative-index one, the refracted beam lies on the same side of the normal as the incident one (**Fig. 1.4B**).

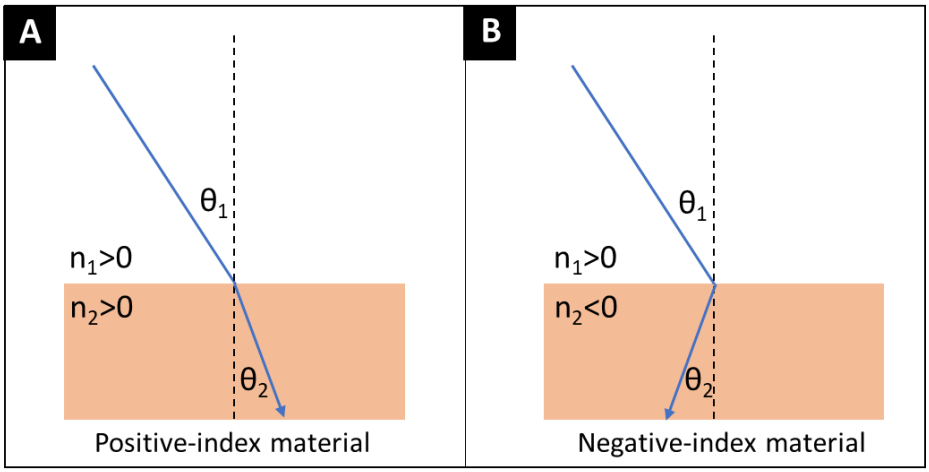

Figure 1.4: *Schematic of refraction of ordinary material medium (A) and negative index material medium (B).*

To obtain a negative refraction in a homogeneous and isotropic material, the refractive index has to be negative, *i.e.*, the electrical permittivity and the magnetic permeability have to be simultaneously negative. Interestingly, for an anisotropic material with a complex refractive index, a negative refraction can be obtained without necessarily having both negative permittivity and permeability[17,18]. In order to engineer such kind of optical properties in the visible range, the basic structures of the anisotropic material should be smaller than the visible wavelengths (400-750 nm).

Consequently, "nanostructuration" is the key to manipulate the electromagnetic properties of materials. Both double negative indexes metamaterials and negative refractive behaviours could be derived from nanostructured materials with appropriate designs as

theoretically predicted in the literature[19]. In the following sections, some of these structures will be explained, starting from the simplest one (meta-atom) to the most complicated (real 3D metamaterials).

2. From metamaterials to metasurfaces

2.1. Metamaterial classification

In the previous sections, optical metamaterials were defined as an artificial material structurally designed with the purpose of producing extraordinary optical properties. An easy and short classification of the different metamaterials can be proposed according to the basic units used to create such materials, the so-called meta-atoms or meta-molecules. They have to be considerably smaller than the operating wavelengths and the distance between the neighbouring meta-atoms should also be in the subwavelength range.

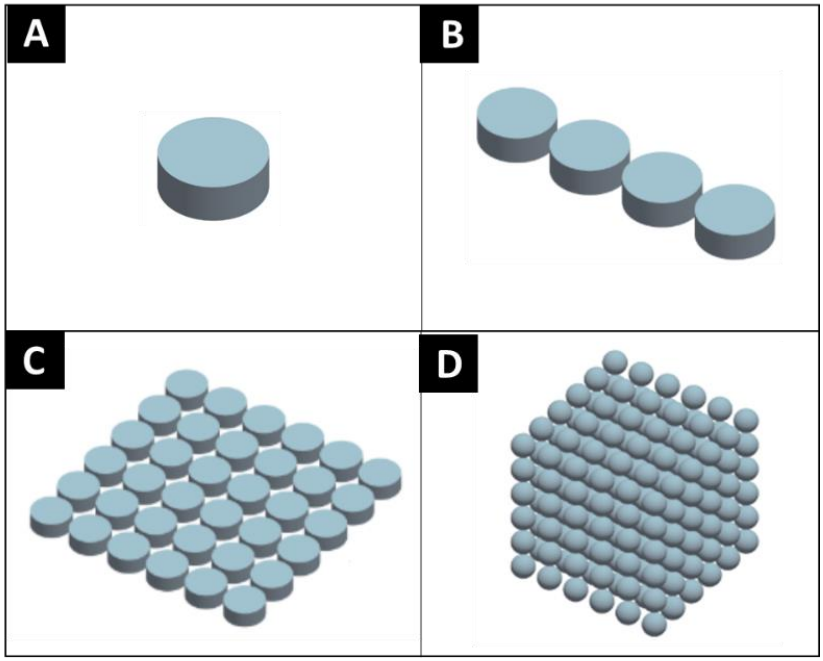

Figure 1.5: *From single meta-atom to 3D metamaterials: A single nanoresonator (A) is arranged at close proximity with several other ones to form chains (B) leading to a planar 2D structure (C). Such structures can be subsequently extended to form a 3D material (D).*

Therefore, depending how these so-called meta-atoms are arbitrarily arranged into periodic arrays, they are classified as one-dimensional (1D) materials (chains), two-dimensional (2D) materials (metasurfaces), and three-dimensional (3D) materials (metamaterials), as shown in **Fig. 1.5**. In the next sections, some theoretical considerations governing the physical properties of metamaterials will be introduced.

2.2. Metasurfaces

Metasurfaces are the two-dimensional version of metamaterials and have attracted increasing attention due to their ability of light manipulation (phase, amplitude or polarization) over subwavelength propagation distances. They are commonly made of structures with specially designed size, geometry, and orientation to generate specific optical responses. Compared with 3D bulk metamaterials, metasurfaces have a negligible layer thickness with respect to the working wavelength, thus occupying much less physical space. Other important advantage is the suppression or the decrease of the undesirable losses, due also to their ultralow thickness. This can be even improved by using appropriately chosen materials and metasurface structures.

Generally, optical metasurfaces can be divided into two main categories, *i.e.*, plasmonic and dielectric, as regards to the material properties used to create the basic unit. For dielectric metasurfaces, the meta-atoms or resonator units are high refractive index dielectric materials such as silicon, germanium or tellurium, which can withstand electric and magnetic dipole responses based on Mie resonances. When a dielectric particle is illuminated by a light wave whose frequency is below or near the bandgap frequency of the material, both the magnetic dipole (first Mie resonance) and the electric dipole (second Mie resonance) are excited. The magnetic and electric Mie resonances can then enhance the magnetic and electric fields at the particle centre at optical frequencies and this enhancement is related to the intrinsic properties of the dielectric particles. On the other hand, plasmonic metasurfaces are made on the basis of metallic meta-atoms whose optical responses are driven by the plasmon resonances supported by metallic particles.

The responses of plasmonic and dielectric metasurfaces are all dependant on the characteristics of the unit structure such as dimensions and materials. Electron-beam lithography is the only technique used to create dielectric metasurfaces[20–22]. Since the objective of this work is to explore the possibility of using block copolymers (BCP) self-assembly to create patterned metasurfaces, we focused on plasmonic metasurfaces. First because BCP can present selective chemical interaction with metallic species and also because the surfaces obtained are more stable (Au *versus* Si).

3. Plasmonic metasurfaces

The starting point of this section is to clearly define the term "plasmonic metasurfaces". Such structure is made of metallic meta-atoms whose optical responses are governed by the particle plasmon resonances. When an electric field is applied to a metallic particle, the conduction electrons (which are loosely bound) are displaced from their equilibrium positions with respect to the core ions, leading to an excess charge at the surface and a polarization of the particle. In a time-varying external field, this collective motion can be described as an oscillator and presents a resonance at a defined frequency. The polarizability of a spherical particle is defined as:

$$\alpha = 3\varepsilon_0 V \frac{\varepsilon - \varepsilon_0}{\varepsilon + 2\varepsilon_0} \quad (1.4)$$

Where V is the volume of the sphere, ε_0 the free-space permittivity and ε the (absolute) permittivity of the spherical object.

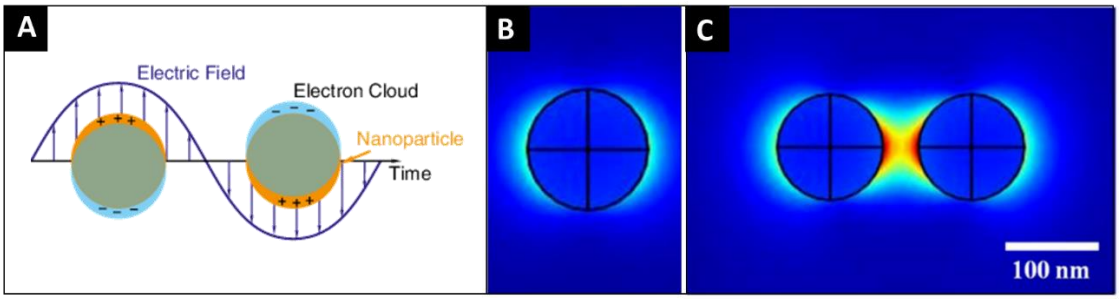

Figure 1.6: *(A) Illustration of surface plasmon resonance (SPR) resulting from the collective oscillations of delocalized electrons in response to an external electric field and the electric field distributions (V/m) of (B) a single Au nanoparticle (NP) and (C) a NP dimer*[23].

For very small particles (less than a few tens of nanometres), the electric field penetrates the whole volume of the particle, polarizing it completely, thereby resulting in a dipolar response whose resonant frequency depends on the particle material, shape and dielectric environment. However, when the particle dimensions are larger, the electric field acts primarily on the surface electrons, giving rise to higher-order multipole resonances (see **Fig. 1.6A**). In both cases this phenomenon is called localized surface plasmon resonance (LSPR). For these larger particles, the plasmon resonance is even more sensitive to the size and shape

of the particle. Even if LSPR is going to affect light propagation even for isolated objects, a crucial question remains; how the arrangement of these meta-atoms into a 2D array is going to affect the optical response of the final material.

In fact, different phenomena take place when these plasmonic meta-atoms are arranged at close proximity. The plasmonic modes (distribution of the polarization charges) supported by an individual meta-atom (**Fig. 1.6B**) are modified by the presence of the other members of the array (**Fig. 1.6C**). Firstly, the proximity of the nearest neighbours modifies the field distribution around a particle, thereby altering its polarizability. Secondly, if the array period is of the order of the wavelength of the particle resonance, the neighbouring particles can coherently interact, leading to collective modes known as surface lattice resonances (SLRs)[24].

Therefore, the response of plasmonic (and also dielectric) metasurfaces are very sensitive to the unit structure characteristics, such as material, shape and size of the resonator but also to the lattice structure. Several types of nanoresonators have been proposed in the literature and some of them will be presented in the next section.

3.1. Plasmonic meta-atoms

Fig. 1.7 shows a library of different plasmonic meta-atoms proposed recently in the literature. The simplest feature consists in spherical or ellipsoidal particles (**Fig. 1.7A**), for which the resonant frequency further depends on the orientation and size of the particle, relative to the driving field[25]. Another example of meta-atom is a metal nanorod with subwavelength dimensions (**Fig. 1.7B**), which acts as a dipole antenna that supports a half-wavelength resonance along its principal axis[26].

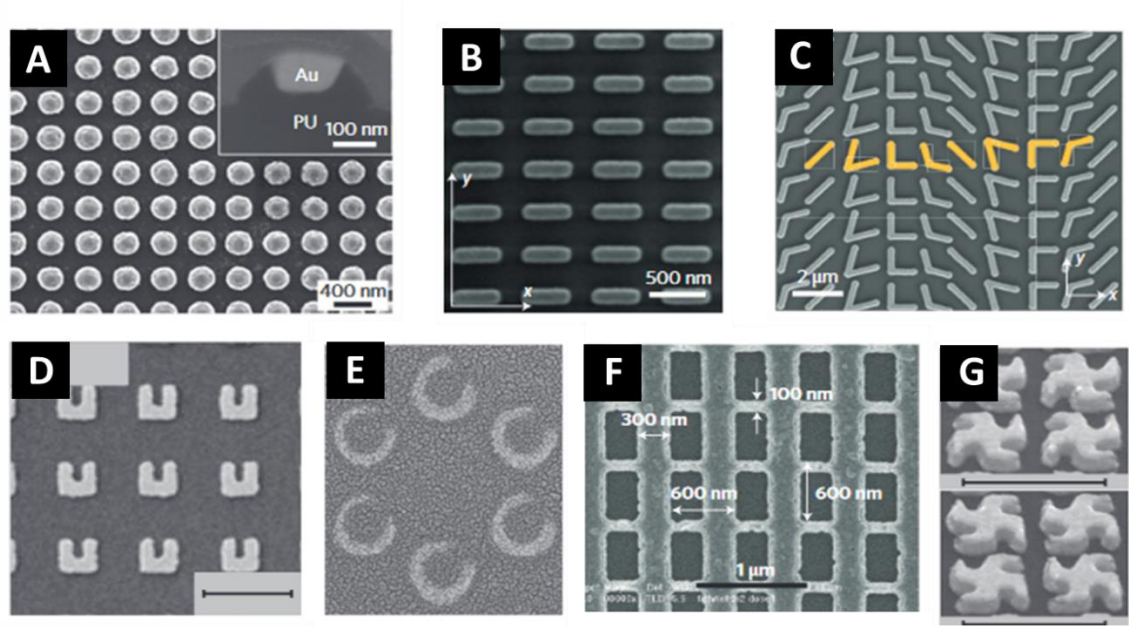

Figure 1.7: *(A) Nanodisks fabricated by template stripping. (B) Rod antennas fabricated by nanoimprint. (C) V-shaped antennas fabricated by electron-beam lithography. (D) U-shape SRR fabricated by electron-beam lithography. (E) C-shape SRR fabricated by nanosphere lithography. (F) Double fishnet structure fabricated by nanoimprint. (G) double-layer right-handed (top) and left-handed (bottom) chiral metamaterials fabricated by electron-beam lithography.*

Using these two basic elements, it is possible to build up more complex meta-atoms. For example, folding a nanorod along its middle creates a V-shaped[9] antenna (Fig 7C). Such geometrical configuration has two main effects: a frequency tunability due to the dipolar interactions between both ends of the nanorod, and the creation of a new symmetry allowing dark (non-radiating) modes to couple the incident light for appropriate directions of the incident electric field. As the magnetic moment for a V-shaped antenna is weak, U-shaped[27] (**Fig. 1.7D**) split-ring resonators or C-shaped[28] (**Fig. 1.7E**) were further designed to enhance the aforementioned phenomena.

To achieve a negative-index material, fishnet structures (**Fig. 1.7F**) were designed with long wires inducing a metallic response[29]. Thus, electric and magnetic field components can be designed to couple, enabling near fields to take on a chiral character (**Fig. 1.7G**). This can ultimately result in chiroptical far-field effects like optical activity or circular dichroism, far stronger than anything observed in natural materials[30].

As presented above, there is a great variety of meta-atoms which can be used for the design of different plasmonic metasurfaces. The next question is then related to how they can be prepared. Which techniques can be used? A quick survey of the literature shows that techniques such as electron beam lithography, focused ion beam or nanoimprinting lithography were employed, since they allow a precise design of the shape and orientation of the meta-atoms, as well as of the lattice structure. This highlights the necessity to develop techniques that allow us to obtain very well-ordered and controllable structures on a large scale. For that, two different methodologies have been used in the literature, top-down and more recently bottom-up approaches. In the next section, the advantages and drawbacks of each one will be discussed.

3.2. Top-down vs bottom-up

There are two different strategies to obtain the required ordering of the meta-atoms, *i.e.*, the top-down and bottom-up methods. Top-down approaches can be likened to sculpting from a block of stone in order to obtain the desired shape. Nanoscale features are commonly produced using lithographic techniques such as conventional photolithography, e-beam lithography, focused ion-beam etching or nanoimprint lithography. With these techniques, patterns with controllable dimensions and shapes are prepared with a nanometric periodicity. Photolithography is the most widely used for fabricating large-area integrated devices. Briefly, it consists in the transfer of geometric patterns in a substrate using optical radiation and photosensitive resins (**Fig. 1.8**)[31].The main disadvantage of photolithography is related to the diffraction limit, which restricts the feature resolution to around 40 nm using 193 nm immersion lithography. With newly developed techniques such as e-beam lithography, it is possible to produce feature sizes around 20 nm, but the cost of production grows exponentially, and such process is constrained to very small scale due to the sequential nature of the pattern formation.

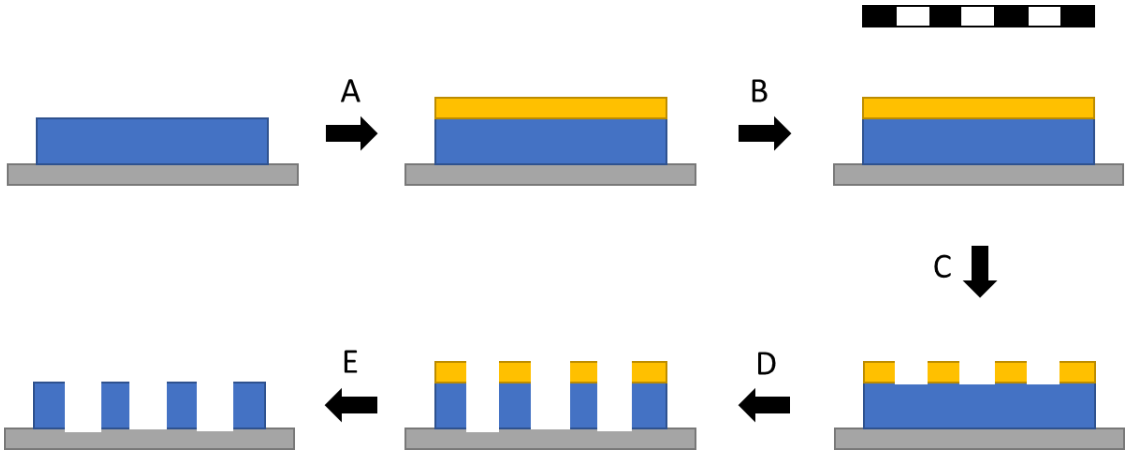

Figure 1.8: *Schematic representation of a photolithography process. (A) The photoresist layer is deposited on top of the substrate of interest. (B) A pattern is transferred using a mask into the photosensitive resist. (C) The photoresist layer is developed using plasma or wet chemistries. (D) An etching step is used to transfer the pattern into the substrate. (E) The removal of the residual photoresist layer is obtained by plasma or wet chemistries.*

As opposed, "bottom-up" approaches can be likened to building a house with bricks, taking advantage of the self-organization of atomic, molecular or even colloidal building blocks to provide access to nanostructures with a corresponding range of characteristic length scales. Self-assembly of colloidal particles (**Fig. 1.9A**) has proven to be an inexpensive method to fabricate nanometric structures, from monolayers to 3D materials. Controlled drying of NP suspensions can produce 3D dense assemblies of resonators of interest[32–34]. Controlled 2D assemblies are less accessible using capillary effects unless template substrates are used to direct the NPs organization, as in the so-called "capillary force assembly"[35]. Recently other methodologies such as the synthesis of patchy particles (**Fig. 1.9B**) have been developed in order to create more complex structures[36]. Nevertheless, the complexity of the synthesis and assembly also increased, limiting the application to small scales.

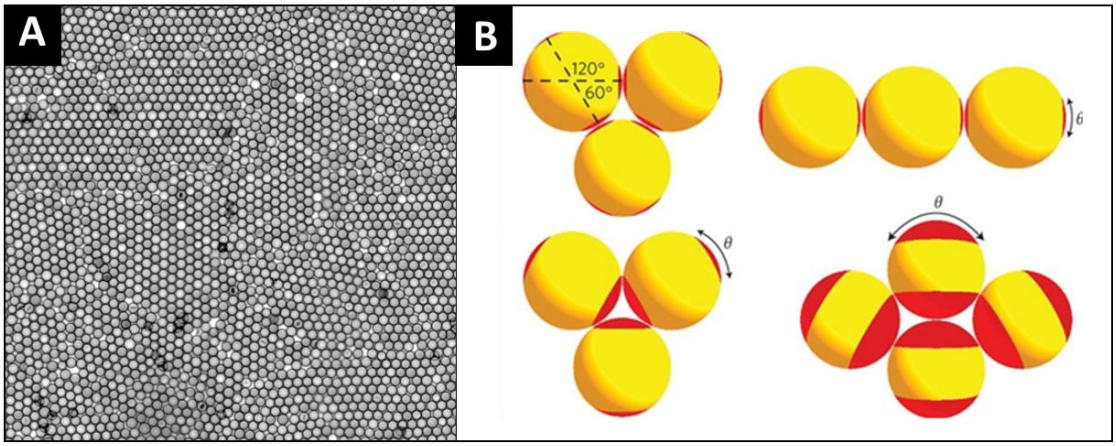

Figure 1.9: *(A) Self-assembly of colloidal nanospheres and (B) different self-assembly of patchy particles proposed in the literature*[36]*.*

BCP self-assembly in the thin film configuration is another promising method to create highly ordered structures. It is based on the segregation behaviour of sequenced polymers (and more particularly BCPs) leading to the formation of periodic structures with nanometric periodicity. This thermodynamically driven fabrication process through solution wet processes offers unique opportunities to design large structured areas of nanometric features with controlled periodicity. In the following sections, some considerations about BCP materials and their self-assembly behaviour will be presented, both in bulk and in thin film.

4. BCP self-assembly

A BCP is a macromolecule formed by two or more chemically different polymers, called the blocks, covalently linked together. Depending on the connectivity between the blocks, various macromolecular architectures have been developed, such as diblock, triblock, star or graft copolymers (**Fig. 1.10**). A rich variety of nanostructures have been produced by self-assembly of these macromolecules. Indeed, several geometrical structures, *i.e.*, lamellae, cylinders or spheres have been obtained controlling the BCP phase behaviour[37].

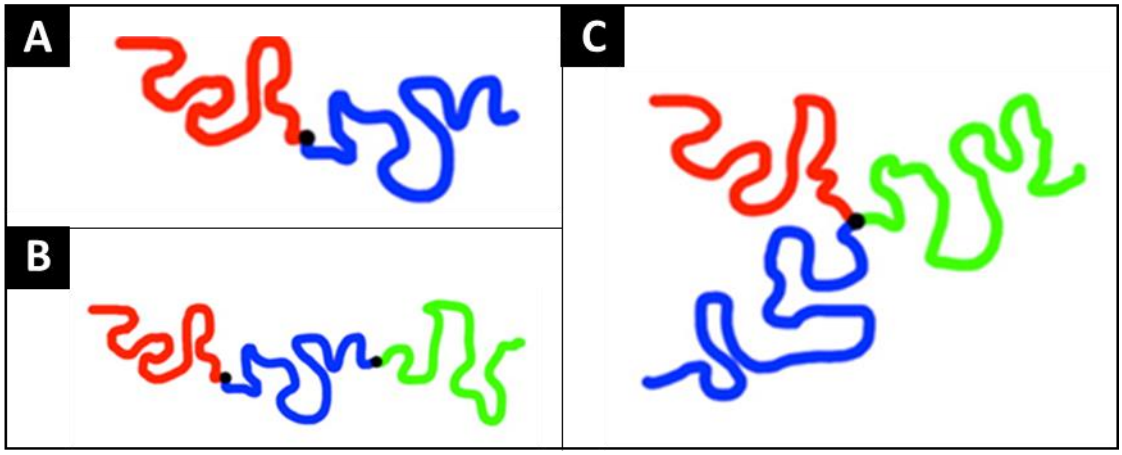

Figure 1.10: *Schematic representation of different BCP configurations: (A) diblock copolymer, (B) linear triblock copolymer and (C) miktoarm terpolymer.*

4.1. Thermodynamics of BCP segregation behaviour in bulk

4.1.1. Phase separation and Flory-Huggins theory

The phase separation process leading to the formation of nanostructures in BCP is driven by the combination of an unfavourable mixing enthalpy coupled to a small mixing entropy of the two polymer components. Assuming a BCP structure formed of two blocks A and B, an unfavourable mixing Gibbs free energy between the A and B blocks, will lead to a phase separation into different domains containing the A and B chains. As the chemical bond between the blocks prevents a separation at the macroscopic scale, the separation appears

locally, and the periodic structures formed from the phase separation process has a length scale related to the radius of gyration of the polymer chains.

Flory and Huggins currently developed a lattice theory to describe the thermodynamics of binary polymer solutions in the early 1940s[38,39]. Using the Stirling's approximation, Flory and Huggins obtained the following expression for the entropy of mixing:

$$\Delta S_m = k_B(-Nln\Phi_A - Nln\Phi_B) \quad (1.5)$$

Where k_B is the Boltzmann constant, ϕ the volume fractions of each block and *N* the degree of polymerization of each block. The microphase separation occurring in BCP systems is controlled by the free energy of the system (ΔG_m) which can be written as:

$$\Delta G_m = \Delta H_m - T\Delta S_m \quad (1.6)$$

Where ΔH_m is the heat of mixing. Flory and Huggins introduce a new parameter, the so-called Flory-Huggins interaction parameter.

It can be seen as measurement gauge of the degree of incompatibility between the A and B blocks, and can be written as:

$$\chi_{AB} = \frac{\Delta H_m}{N k_B T \Phi_a \Phi_b} = \frac{Z}{k_B T}\left[\varepsilon_{AB} - \frac{(\mathcal{E}_{AA}+\mathcal{E}_{BB})}{2}\right] \quad (1.7)$$

Where k_B is the Boltzmann constant, *T* is the temperature, *Z* is the network coordination number, and ε are the interaction energies between two monomers.

Finally, the free energy of mixing of the system (ΔG_m) is obtained by combining the entropic and enthalpic terms:

$$\frac{\Delta G_m}{kT} = \frac{\Phi_A}{N_A}\ln(\Phi_A) + \frac{\Phi_B}{N_B}\ln(\Phi_B) + \chi_{AB}\Phi_a\Phi_b \quad (1.8)$$

According to this equation, the microphase separation mainly depends on three parameters, the volume fractions of each block (ϕ), the degree of polymerization of each block (*N*), and the Flory-Huggins parameter, χ_{AB}. The enthalpy change of the process, ΔH_m, is largely determined by the Flory-Huggins parameter, χ, while the change in entropy of the process, ΔS_m, mainly depends on the polymerization degree of the chain, *N.* Thereby, the product of the interaction parameter with the overall degree of polymerization, $\chi_{AB}N$, as well as the BCP

composition, ϕ, regulates the phase behaviour of BCPs. Self-assembly of the AB-type BCP (demixing) spontaneously occurs if ΔG_m is positive (generally accompanied by an entropy loss).

The $\chi_{AB}N$ product will additionally dictate the phase separation threshold, *i.e.*, the frontier between a mixed phase (referred to as the disordered state) and a phase separated state (referred to as the ordered state). Indeed, an increase of the interaction parameter will further accentuate the block incompatibility, thus favouring an extended phase separation. An increase of the degree of polymerization parameter favours the phase separation as well, since the entropy gain occurring through mixing of the A and B blocks will be further reduced. Consequently, a critical value of the $\chi_{AB}N$ product, denoted as $(\chi_{AB}N)_{ODT}$, demarcates the frontier (order-disorder transition) between a homogeneous and a segregated BCP system (**Fig. 1.11**).

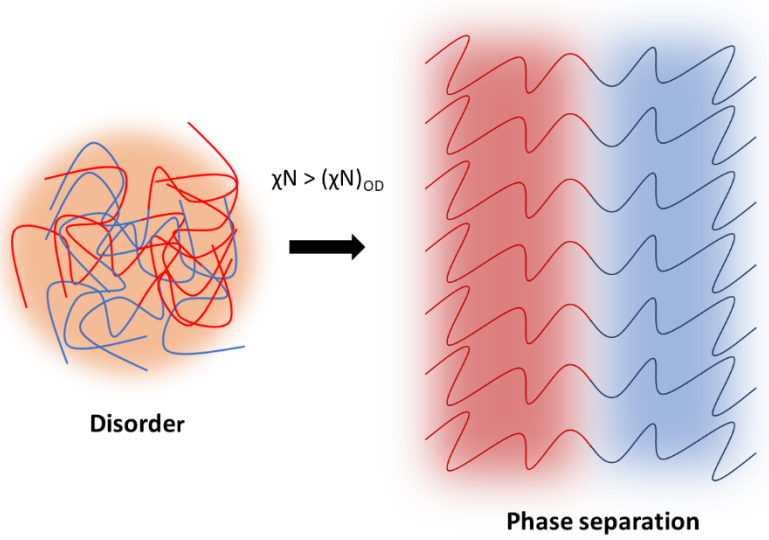

Figure 1.11: *Schematic representation of the order-disorder transition for a diblock copolymer.*

As the interaction parameter is inversely proportional to the temperature, this order-disorder transition can be triggered by a modification of the temperature. An increase of the temperature induces larger thermal fluctuations and reduces the repulsive interactions between the A and B segments. Beyond a certain temperature, denoted as order-disorder transition temperature T_{ODT}, the system is thus in a disordered state (mixed state). On the

opposite, when the temperature is lower than T_{ODT}, the blocks are segregated into microdomains.

As previously introduced, a third factor allows tuning the order-disorder transition: the relative volume fraction of the blocks (ϕ). The theoretical phase diagram of an A-B BCP is plotted as function of the volume fraction in **Fig. 1.12**. It shows how the boundary between the ordered and disordered states varies with the composition of the BCP and further details will be given in the next section.

4.1.2. Phase diagram of diblock copolymers

Extensive research works over the last 50 years led to the definition of the BCP phase diagrams in the ϕ/χN referential (**Fig. 1.12**). When a BCP is in an ordered state, the morphology of the segregated structures depends on the ϕ and χN values. The Flory-Huggins parameter, the degree of polymerization and the volume fraction affect the conformation of the polymer chains and, more importantly, have a strong impact on the spontaneous curvature adopted by the interface between the two blocks. This leads to the definition of a library of morphologies based on the minimization of the free energy of the BCP system depending on the macromolecular parameters of the BCP.

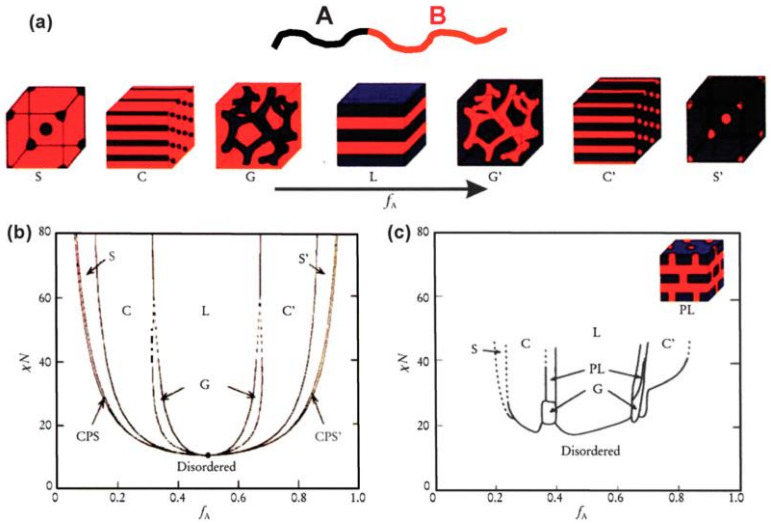

Figure 1.12: *(A) Equilibrium morphologies of A-B BCPs in bulk: S and S' = body-centred-cubic spheres, C and C' = hexagonally packed cylinders, G and G' = bicontinuous gyroids, and L = lamellae. (B) Theoretical phase diagram of A-B BCPs predicted by the self-consistent mean-field theory; CPS and CPS' = close-packed spheres*[40]*. (C) Experimental phase diagram of poly(styrene)-b-poly(isoprene), PL = perforated lamellae*[41]*.*

Thus, for a BCP with values of $\chi_{AB}N$ much smaller than 10.5, the blocks are homogeneously mixed (**Fig. 1.13A**). As $\chi_{AB}N$ approaches 10.5, the chains of the A and B blocks start to segregate. As the incompatibility between the blocks is not very high, the segregation is weak, with not clearly-defined interfaces. This stage is named fluctuating disordered state (**Fig. 1.13B**). For values of $\chi_{AB}N$ larger than 10.5, an ordered mesophase is formed (**Fig. 1.13C** and **D**), with a morphology depending on the volume fraction of the blocks. Therefore, for a symmetric BCP where $\phi \approx 0.5$, the system will adopt a lamellar (L) configuration, increasing ϕ_a or ϕ_b results in more curved interfaces as gyroids (G) $\phi \approx 0.38$, cylinders (C) $\phi \approx 0.15$-0.37 and spheres (S) $\phi \approx 0.05$-0.15, are sequentially obtained. For values larger than 10.5, but close to it, weakly segregated structures will be obtained (**Fig. 1.13C**). Diffuse interfaces with sinusoidal density profiles of A and B blocks in the domains are observed. Increasing the $\chi_{AB}N$ value will further drive the incompatibility between the blocks resulting in a strong segregation regime, with sharp interfaces between the domains (**Fig. 1.13D**).

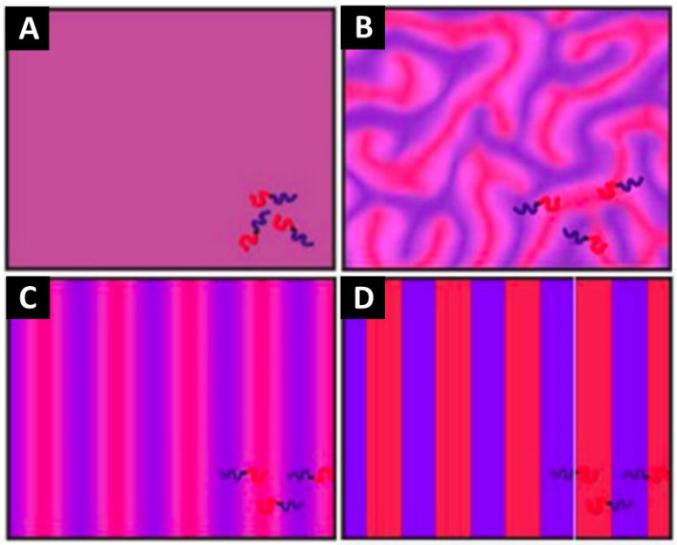

Figure 1.13: *Phase separation regimes for diblock copolymers. (A) homogeneous disordered state at $\chi N << (\chi N)_{ODT}$,(B) fluctuating disordered state at $\chi N < (\chi N)_{ODT}$ (C) weakly segregated lamellae at $\chi N > (\chi N)_{ODT}$, and (D) strongly segregated lamellae at $\chi N >> (\chi N)_{ODT}$.*

Finally, we should note that there are significant differences between the theoretical and the experimental phase diagrams, the most important one is the asymmetry with respect to ϕ_A due to the different volumes and persistence lengths of the two monomer units (**Fig. 1.12C**).

4.2. BCP thin films

As described in the last section, BCP are a class of self-assembling materials that spontaneously segregate at nanometre length scales, making them ideal for the definition of nano-patterns in the thin film configuration. Thin film applications of BCP span the nano-templating, separation, optoelectronic and coatings fields[42–45]. As previously explained, the phase separation in the bulk state mainly depends on three fundamental factors: the incompatibility between the blocks (χ); the degree of polymerization (N) and the volume fraction (ϕ). In thin films, other parameters have to be taken into account such as the interactions with the substrate and the free surface or the confinement effects. But before explaining the influence of these parameters, some experimental details about how BCP thin films are prepared will be provided.

4.2.1. From bulk to thin films

BCP thin films are usually prepared by spin-coating, where drops of a polymer solution dissolved in a volatile organic solvent are deposited on a spinning solid substrate (often silicon wafers, chosen for their flatness) The polymer film spreads by centrifugal forces and the volatile solvent is rapidly driven off (**Fig. 1.14**). With this technique films with a low surface roughness over areas of square millimetres or centimetres are obtained. The film thickness can be controlled through the spin speed and acceleration, the concentration of the BCP solution or the volatility of the solvent[46].

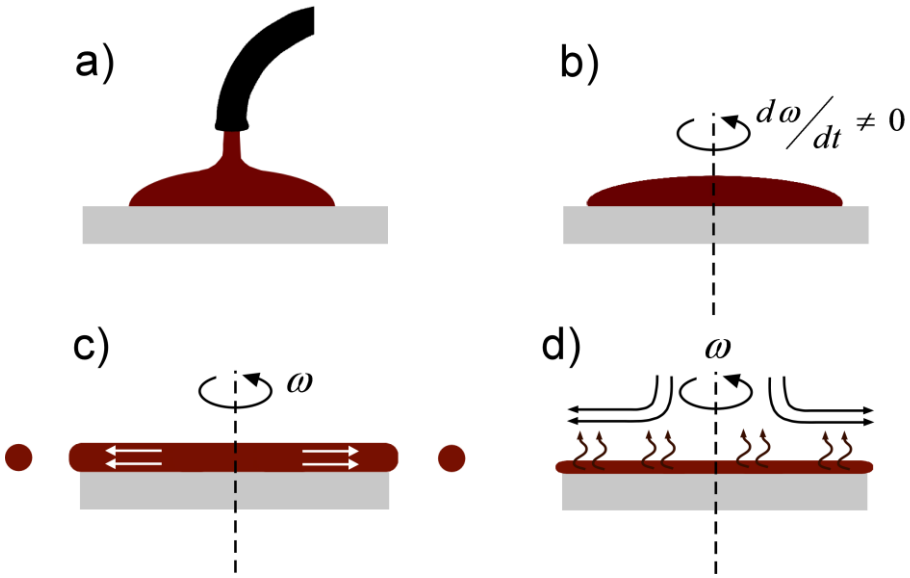

Figure 1.14: *The different "stages" of spin-coating process. (A) Deposition of the solution on the wafer. (B) Starting of the rotational movement. (C) Spreading of the solution in all the wafer thanks to the centrifugal forces. (D) Evaporation of the solvent and end of the process.*

4.2.2. Surface substrate effect

The substrate surface energy and the surface chemistry are important parameters for controlling BCP thin film self-assembly, both with regards to microstructure stability[47] and microstructure orientation (essentially for lamellae and cylinders)[48]. For example, if the surface is preferential for one of the blocks, this block domain will tend to wet the surface and *in-plane* orientations will be preferentially obtained (parallel to the substrate). On the contrary, if the surface of the substrate is neutral for both blocks, *out-of-plane* orientation can be obtained, depending on the film thickness and its commensurability as regards to the BCP period[49].

The most common strategy to modify the substrate surface, and therefore to control the microstructure orientation, is the use of grafted random copolymers (**Fig. 1.15**). The random copolymer methodology relies on the statistical composition of the copolymer to tune the substrate surface energy/chemistry generating neutral or preferential surfaces. The copolymers can be end-grafted[50] or side-grafted[51] to substrates to form a brush layer covering the substrate (**Fig. 1.15B**). This strategy not only allows controlling the orientation but also guiding the azimuthal orientation of the morphology, using chemical patterned surfaces[52].

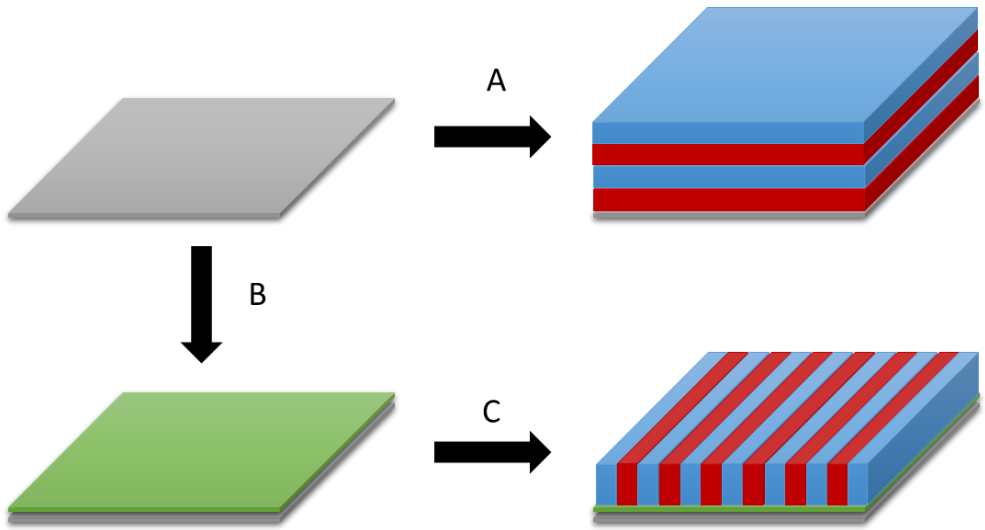

Figure 1.15: *Effect of the surface fields on the BCP domain orientation. (A) preferential surface for one of the blocks leads to an in-plane orientation while (B) the grafting of a neutral layer grafting can induce (C) an out-of-plane orientation.*

4.2.3. Free surface effect

The domain affinity at the free surface (surface in contact with the air) is a similar field effect to that emanating from the substrate surface discussed in the last section. Preferential or neutral interactions also affect both microstructure orientation and stability. This surface property can be tuned by two different strategies, thermal or solvent vapour annealing. For some systems with block surface energies approximately equal, a neutral free surface can be created by heating the samples at the right temperature[49]. But the temperature window between the T_g (glass transition temperature) of the blocks and the degradation temperature of the involved components might only be very small. Thus in order to avoid polymer degradation, solvent vapour annealing can provide a powerful alternative[53–55]. In this case, since a solvent swells the BCP thin film , the final morphology can also be affected by the interactions between the solvents and polymers, leading to structures that cannot be achieved by thermal annealing[56].

Solvent vapour exposure was widely used during this work, since it could be used for multiple purposes. Firstly the vapour establishes surface preferentiality at the free surface of the film[53,57,58]. Besides, by swelling the BCP film, such treatment effectively lowers the glass

transition temperatures (T_g) of the blocks, increasing chain mobility and promoting thus the ordering of the BCP structure[53,57]. Additionally, the presence of solvent in the film affects the interactions between the blocks (χ) and potentially the relative volume fractions, leading to changes in the phase diagram[53,57]. Additionally, the solvent and solvent-swollen polymer interactions with the substrate surface can lead to the screening of undesirable surface interactions[53] or film dewetting[48]. Finally, the swelling followed by the rapid drying quench of the film, leads to an effective polymer domain spacing (L_0) that can be greater[55] or lower[57,58] than the bulk L_0, affecting commensurability considerations.

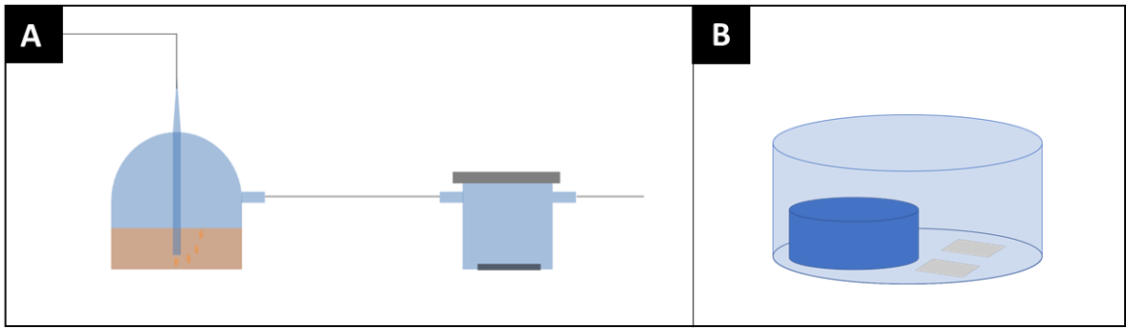

Figure 1.16: *Schematic representation of both types of solvent annealing: (A) dynamic and (B) static.*

Experimentally, two different types of solvent annealing can be distinguished, dynamic or static. In the first case, a continuous gas flow passes through a reservoir of solvent and is then introduced in another chamber containing the polymer film (**Fig. 1.16A**). In the static case (**Fig. 1.16B**), a reservoir of solvent is enclosed in a "bell jar" with the polymer film for a certain period of time. In both cases, the solvent is removed quickly to trap the non-equilibrium, but often well-ordered structures[57,59]. In both cases numerous parameters should be investigated including solvent affinity towards the blocks, annealing time, swollen film thickness, and solvent removal rate.

4.2.4. Confinement effect

The confinement of the BCP thin film between the substrate and the surface in contact with air is a very important parameter to take into account and can induce significant deviations from the predicted bulk structures. As an example, Bai *et al*.[60] showed that starting

from a bulk-gyroid forming polystyrene-*block*-polydimethylsiloxane (PS-*b*-PDMS), it was possible to obtain various thin film morphologies , only by controlling the film thickness (**Fig. 1.17A**). Another example of the importance of the film thickness on the final morphology in thin films was presented by Knoll *et al.*[58] In their work, they studied the different morphologies obtained from a cylindrical BCP as a function of the film thickness. Perforated lamellae, different orientations of the cylindrical structure as well as coexistence between two different morphologies were demonstrated for different sample thicknesses. (**Fig. 1.17B**). The confinement effect, *ergo* the film thickness, is controlled through the deposition methods and, as it has been presented here, constitutes one of the most critical parameters in order to control the final morphology in thin films.

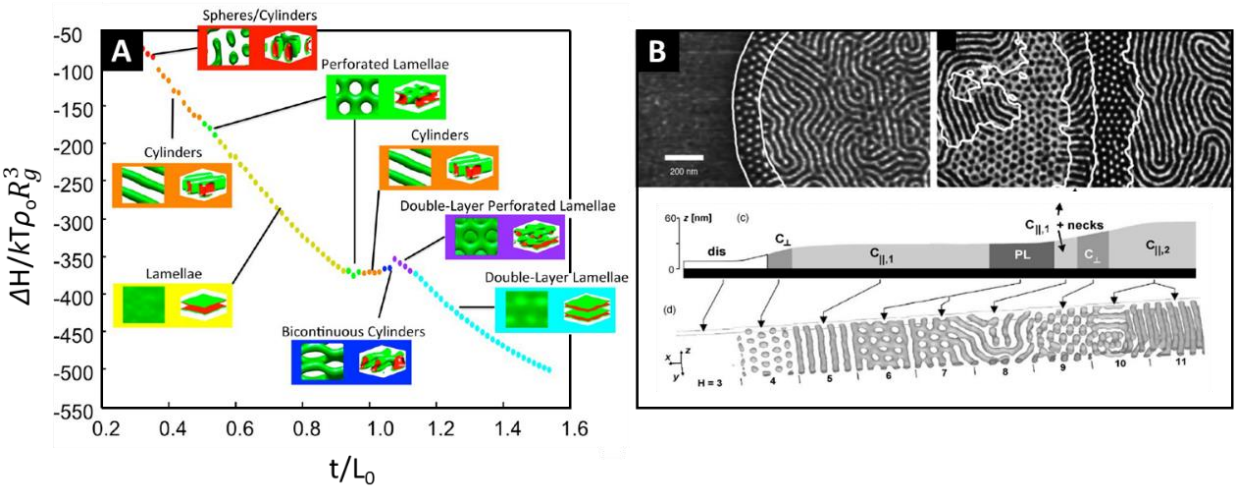

Figure 1.17: *The self-assembly of BCP is fundamentally influenced by the boundary conditions and confinement effects (film thickness). (A) and (B) poly(styrene-b-butadiene-b-styrene) SFM images. (C) height profile of the phase images shown above. (D) simulated morphologies as function of the film thickness.*

In the following sections, we will discuss how these well-ordered structures could be used as a template in order to obtain inorganic or metallic arrays, useful for the formation of metasurfaces.

5. Strategies for inorganic or metallic incorporation into BCP films

Generally, two different strategies have been used to obtain inorganic replicas using BCP films as a template: in situ and ex situ methods. In ex-situ method, pre-synthesized objects are incorporated in the BCP structure mostly through their dispersion in the BCP solution before deposition. As opposed, for the in-situ methods, metallic or inorganic precursors are selectively infiltrated into one of the blocks. In the next sections, the various techniques allowing to hybridize BCP structure will be introduced, starting from the ex-situ and finishing with the in-situ methodologies.

5.1. Ex-situ techniques

As previously introduced, this strategy consists in the incorporation of NPs (NPs) into the initial BCP solution leading to NPs-BCP composite thin films. The successful incorporation of NPs into polymer matrices is the result of a balance between the polymer conformational entropy, enthalpy of the insertion into the polymer matrix (due to the creation of polymer-NPs interfaces), and NP translational entropy. Different parameters such as the NP size, shape, concentration, surface chemistry or the BCP length scales and architectures have a huge influence on the distribution of these NPs inside the polymer matrix [61–63]. Nevertheless, this strategy suffers from the disruptive effect of the NPs on the BCP self-assembly. Li and co-workers[64], for example, have shown the possibility of selectively incorporating P2VP functionalized gold NPs in P2VP polystyrene-*block*-poly-2-vinylpyridine (PS-*b*-P2VP) domains. The particles used for that study present a diameter around 2-3 nm to avoid disturbing the polymer structure (**Fig. 1.18AB**). Indeed, with this strategy only small objects, with a diameter less than 10 nm, have been successfully incorporated[62]. For bigger particles, important disruptions of the BCP structure have been observed, limiting greatly the density of incorporated NPs[63], making it not interesting for the purpose of this study

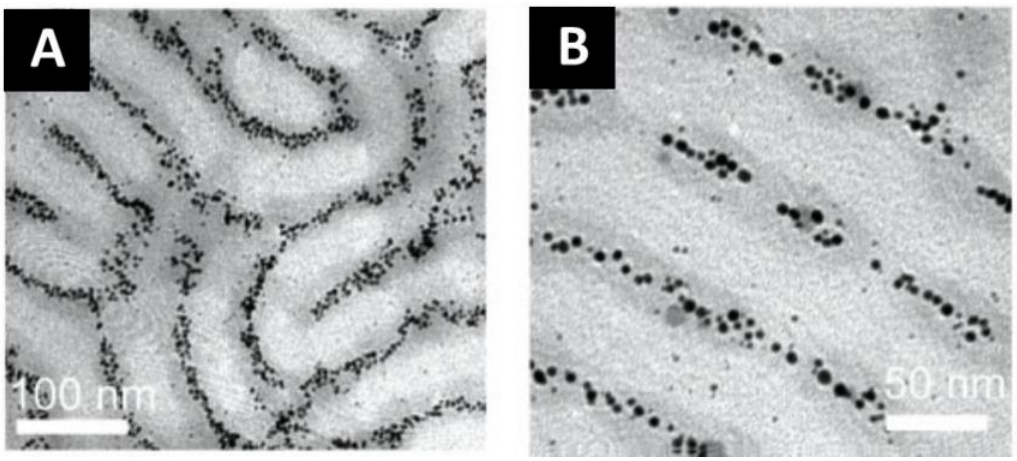

Figure 1.18: *TEM of PS-b-P2VP/gold NPs: A (1:1) and B (3:1) mixtures*[64].

5.2. In-situ techniques

On the other hand, in situ techniques, as they are inherently post self-assembly fabrication methods, avoid large perturbations of the BCP self-assembly and have been shown to be excellent methodologies for inorganic or metallic nanofeature fabrication. In the following section, some of the most important strategies, such as evaporation, ALD or aqueous metal reduction, will be introduced.

5.2.1. Evaporation and sputtering of metals on BCP templates

A straightforward strategy consists in using the nanostructured BCP films as a template by selectively etching one of the BCP domains. This step is followed by the evaporation, the electroplating or the sputtering of a metal through the BCP template in order to define geometrical features with defined periodicity. A final step consisting in the removal of the BCP template is often required to obtain the metallic pattern (see **Fig. 1.19**).

In 1997, Park *et al*., reported the first demonstration of pattern transfer using a BCP[65]. This opens new avenues to use these porous polymer films in order to create patterned metallic structures[66]. Even if the earliest works were done using PS-*b*-poly(butadiene) or PS-*b*-poly(isoprene), further studies using this evaporation technique largely concern PS-*b*-

poly(methyl methacrylate) systems due to the introduction of directed self-assembly methodologies.

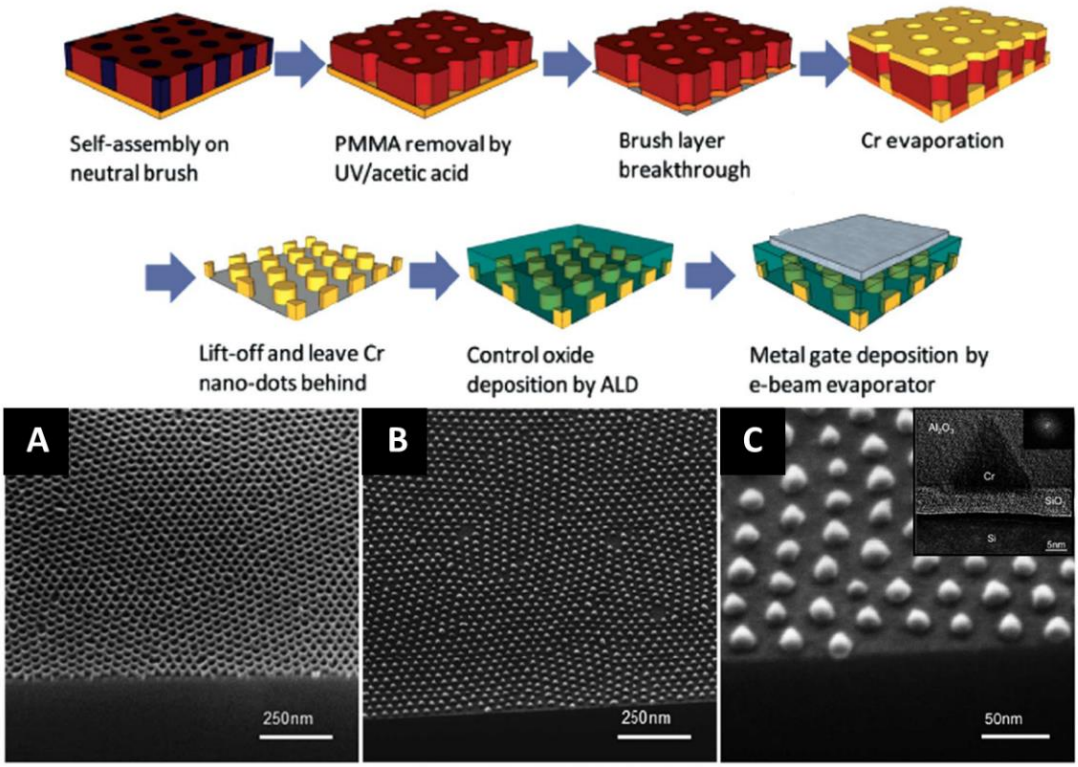

Figure 1.19: *Schema of the process of fabrication of metal nanodots using PS-b-PMMA and Cr evaporation. (A) Side-view scanning electron microscopy (SEM) image of porous PS matrix following selective PMMA removal. (B) Top-down and (C) side-view SEM images of evaporated Cr nanoarrays using a host PS matrix. Inset in (C) shows the transmission electron microscopy (TEM) image of gate oxide on Cr dot*[67].

Another interesting example was reported by Russel and coll. in 2002. They demonstrated the fabrication of an high areal density ($10^{11}cm^{-2}$) metallic array using PS-*b*-PMMA templates and Cr evaporation[68]. The PMMA domains were selectively removed by UV exposure/acetic acid washing protocol (dry plasma etching can also be used[69]). Metal evaporation leads to the formation of Cr nanodots after the PS matrix removal. Magnetic Co nanodots[70], Ag nanowires[71] and Au NPs[72] were also obtained by such methodology underlining its high versatility. More recently PS-*b*-P4VP[73], PS-*b*-PDMS[74] or PS-*b*-PLA[75] have also be used as templating materials as their higher χ parameter allows the definition of metallic structure of lower periodicity.

5.2.2. Atomic layer deposition

Atomic layer deposition (ALD) is a versatile technique for the deposition of inorganic materials with the controlled formation of uniform layers via vapour phase precursors[76]. ALD relies on the alternate pulsing of precursor and reactant gases, separated by purge steps, resulting in self-limiting surface reactions[76,77]. Due to the cyclic nature of the process, the reactants are deposited layer-by-layer, which gives an unparalleled control of the thickness at the atomic level. The BCP self-assembly combined with ALD is a functional route to create porous host materials with a high control, uniformity, and precision in the incorporation of inorganic species.

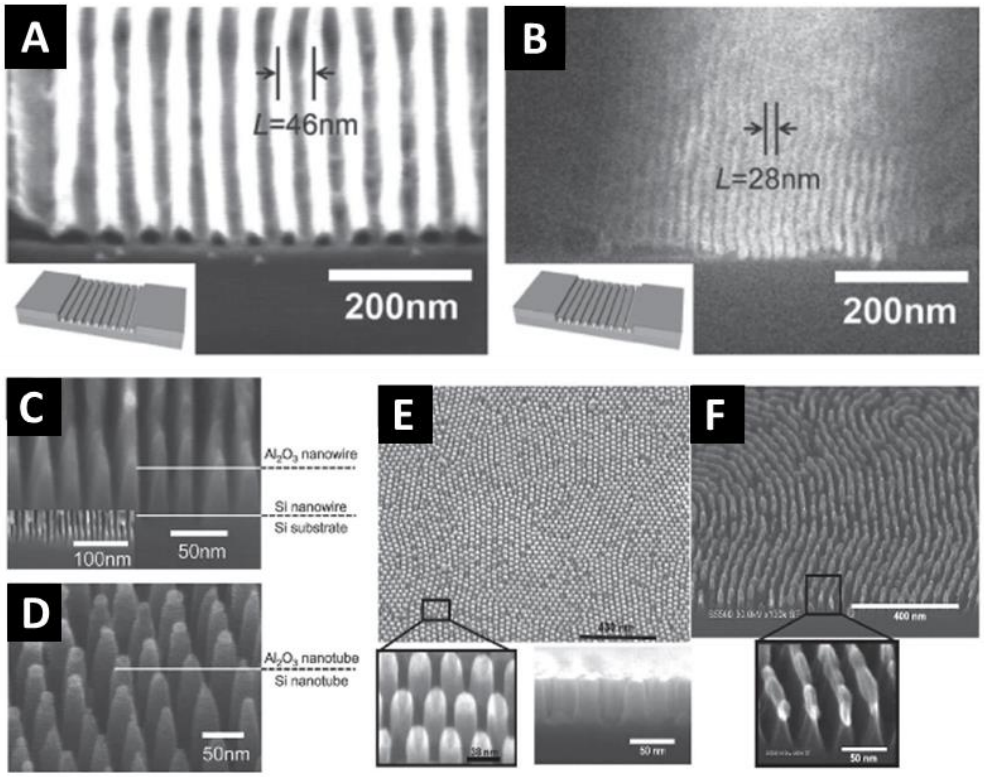

Figure 1.20: *(A) and (B)* Al_2O_3 nanowire features following ALD spacer deposition, *(C) and (D) Si nanostructure and nanotubes after Si etching. Side view and high-resolution SEM images of (E) nanopillars and (H) nanofin features using robust ALD Al_2O_3 mask patterns for enhanced pattern transfer. (a-f)*[78]*(g, h)*[79]

A good example of the potential of this technique was recently showed by Moon *et al*[80]. Line space features or perpendicular cylinders of Al_2O_3 on silicon were obtained by the deposition

of a uniform 5 nm thick Al_2O_3 layer within the grooves produced by removing the PMMA domains of a nanostructured PS-b-PMMA film (**Fig. 1.20**). Another interesting application is to use this porous PS film combined with ALD as a hardmask, producing high-fidelity silicon nanostructures[79].

Peng et al[81] introduced a new strategy for the use of ALD combined with BCP self-assembly (in later publications, this methodology is called sequential infiltration synthesis or SIS). The SIS process involves the initial exposure of the PS-*b*-PMMA films to the precursor molecules (trimethyl aluminium (TMA) or titanium tetrachloride($TiCl_4$) / water), which show a high affinity toward the PMMA domains. Indeed, the PMMA domains behave as selective growth sites for subsequent ALD cycles, due to the selective reaction between the carbonyl groups and the TMA or $TiCl_4$ molecules[82]. A final etching step leading to the removal of the BCP matrix leads to the formation of Al_2O_3 or TiO_2 arrays. Other BCPs such as PS-*b*-P2VP, PS-*b*-P4VP or PS-*b*-PLA can be also used in this approach[83,84], due to the presence of reactive moieties, e.g. carbonyl groups or pyridine sites.

5.2.3. Aqueous metal reduction

Another route for the metal inclusion into polymer films, directly related to the SIS methodology, is the aqueous metal reduction (AMR). It consists in the immersion of a BCP thin film in an aqueous acidic metal containing solution. In 2007, Chai *et al*.[85] reported highly defined Au, Pd and Pt nanowires obtained from metal ions loading into a cylinder-forming PS-*b*-P2VP followed by the subsequent reduction with O_2 plasma (**Fig. 1.21**). This strategy represents a versatile, straightforward and inexpensive approach in comparison with the others presented is the previous sections, since no High-Tech equipment is needed. This ease and low-cost make it the ideal candidate for highly scalable process[86].

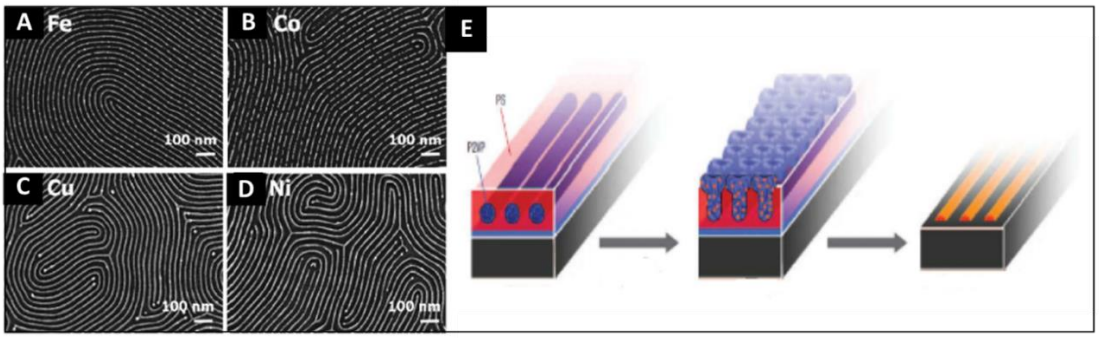

Figure 1.21: *(A–D) Top-down SEM images of Fe, Co, Cu and Ni metallic lines fabricated via aqueous metal reduction and O_2 plasma, (E) Scheme of metal ion reduction after immersion of a PS-b-P2VP film into an acidic medium forming mushroom caps followed by O_2 plasma revealing metallic lines*[85].

It is noteworthy that AMR is directed by the chemical interactions (in that case, the acid-basic interaction) between the polymer and the metal ions present in the aqueous solution. Following this report, several protocols have been developed in order to obtain Fe_2O_3[87] or TiO_2[88] NPs or even more complex systems like Pt-Au binary NPs[89].

In all these reports, an O_2 plasma treatment after the metal incorporation was necessary for both the removal of the polymer matrix and the reduction of the metallic precursors into their metallic state. Even if thermal annealing, UV/ozone or selective solvent sonication[90] could be used for this purpose, O_2 plasma is one of the most effective strategies for the reduction of noble metals such as Au, Pt or Pd[91]. This could be explained taking into account the high abundance of high energy electrons formed during the plasma (independently of the plasma-forming gas) which act as reducing species[91].

To summarize this section, we can stress that the AMR strategy is an effective way to incorporate metal precursors inside a BCP template, maintaining the well-ordered structure produced at the time of the self-assembly. This is clearly emphasized by the large variety of metals that could be incorporated into a nanostructured BCP thin film. Consequently, the AMR methodology is one of the most promising and straightforward techniques in order to create plasmonic metasurfaces consisting of metallic NPs arrays. In the next sections, several examples of this type of structures made by combining BCP self-assembly and AMR will be presented.

6. Metasurfaces based on block-copolymer self-assembly

The use of BCPs to design metamaterials has been mainly focused on the study of 3D structures and has only very recently been devoted to 2D structures and metasurfaces. This section will start introducing how and why the BCPs have been employed in this field, giving some examples of 3D metamaterials and their properties. Finally, a few examples of 2D structures obtained from BCP self-assembly will be described.

6.1. 3D metamaterials based on BCP self-assembly

In the early 2010's, several theoretical studies showed the potential of BCP nanocomposites with different morphologies, like in-plane lamellar or double gyroid, to obtain 3D metamaterials at visible wavelengths[92–94]. In the case of the gyroid structure, the chirality of the structure resulting from the BCP templating leads to a potential negative refractive index. For the in-plane lamellar structure, the anisotropy between the metallic-dielectric layers formed from the two BCP domains can be responsible for unconventional optical behaviours leading to a hyperbolic effect. In the following sections, these two examples will be discussed in more details.

6.1.1. Double gyroid based 3D metamaterials

The gyroid morphology is particularly interesting due to its potential to create metamaterials at visible wavelengths. This type of structure is accessible from a AB BCP, but the structure is achiral and centrosymmetric. Nevertheless, by using an ABC triblock terpolymer, chiral spirals composed of the A and C domains are obtained from the phase separation process. A chirality can lead to a cross-coupling between electric and magnetic dipoles, breaking the degeneracy between two circularly polarized waves and giving rise to a negative refractive index. Particularly, the alternating gyroid structure (G^A) obtained with the ABC terpolymers presents chiral spirals along seven axes, <100> and <111>. Using this type of structure, Vignolini *et al.* demonstrated in 2012 the first 3D chiral metamaterial made by self-assembly[95]. The alternated gyroid structure was created using poly(isoprene-*b*-styrene-*b*-

ethylene oxide) PI-*b*-PS-*b*-PEO. Polyisoprene was selectively removed by UV-ozone treatment. The resulting pores were filled by electro-deposition of gold into the voided template. A subsequent plasma etch was used to remove the remaining polymer template leading to a free-standing single gyroid network of gold that replicated the original structure (see **Fig 1.22A-D**) with a unit cell of size ≈ 50 nm, which is far below optical wavelengths.

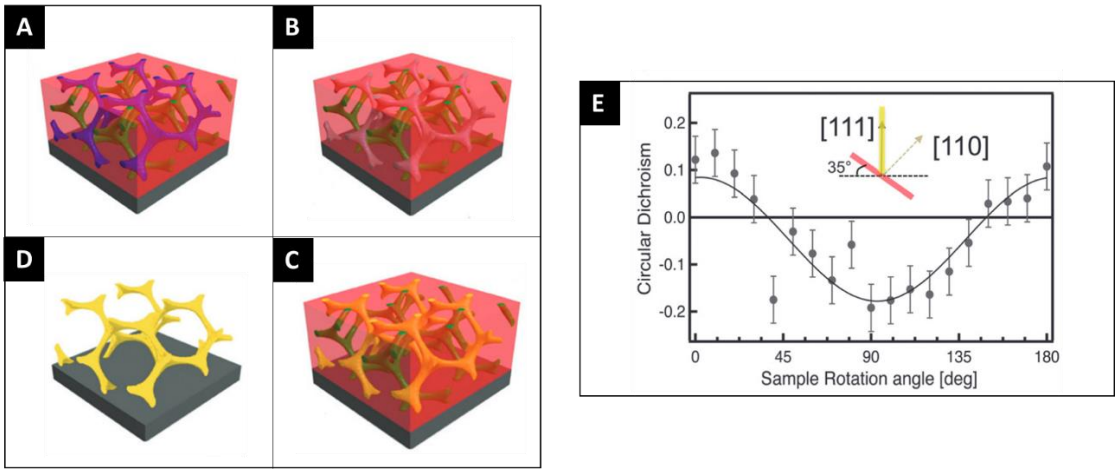

Figure 1.22: *Self-assembly of a 3D chiral metamaterial using a BCP template. (A) BCP was assembled into a G^A morphology. (B) Selective etching of one of the domains. (C) Selective deposition of Au in the porous structure. (D) Polymer removal resulted in a free-standing single-gyroid network of gold. (E) The anisotropic sample exhibited gyrotropic transmission that selectively allowed the passing of circularly polarized light corresponding to the structural chirality*[95].

Optical measurements showed the internal chirality by exhibiting an anisotropic gyrotropic transmission, thus left or right circularly polarized light was preferentially transmitted, depending on the chirality of the morphology. Besides, an orientation-dependent colour under linearly polarized incident light was observed (**Fig. 1.22E**). Other examples of this type of structures were created using hollow alternating gyroid structures[96] or gyroids loaded with gold and platinum NPs[97]. Although this approach has not yet demonstrated a negative refractive index, gyroid metamaterials strongly affect light propagation beyond standard dichroism and pave the way for the potential mass production of optical metamaterials, which can lead to a variety of large-scale applications.

6.1.2. Hyperbolic metamaterials based on lamellar self-assembled BCPs

Hyperbolic metamaterials represent the ultra-anisotropic limit of traditional uniaxial crystals and are usually composed of multi-layered metal-dielectric composites. In such metamaterials, one of the principal components of their permittivity (ε) tensors is opposite in sign to the other two principal components[98–100]. In short, they are materials which behave like a metal in one or two directions (ε < 0) and like a dielectric (ε > 0) in the orthogonal directions. This behaviour makes them ideal for different applications such as negative refraction[101], super-resolution[102] or biosensing[103] materials.

Basic electromagnetic properties of hyperbolic metamaterials may be understood by considering a non-magnetic uniaxial anisotropic material with principal axes (*x*, *y*, *z*) and a permittivity tensor:

$$\varepsilon = \begin{pmatrix} \varepsilon_1 & 0 & 0 \\ 0 & \varepsilon_1 & 0 \\ 0 & 0 & \varepsilon_2 \end{pmatrix} \text{ with } \varepsilon_x = \varepsilon_y = \varepsilon_1 \text{ and } \varepsilon_z = \varepsilon_2 \tag{1.9}$$

The iso-frequency dispersion relation in these materials is given by:

$$\left(k_x^2 + k_y^2 - \varepsilon_1\varepsilon_0\mu_0\omega^2\right)\left(\left(k_x^2 + k_y^2\right)\varepsilon_1 + k_z^2\varepsilon_2 - \varepsilon_2\varepsilon_1\varepsilon_0\mu_0\omega^2\right) = 0 \tag{1.10}$$

Where k_x, k_y and k_z are respectively the *x*, *y* and *z* components of the wave vector and ω is the wave frequency.

The two terms describe the behaviour of waves of different polarizations: polarization in the (*x*, *y*) plane for the first term and polarization in a plane containing the *z* direction for the second. When set to zero, the two terms correspond respectively to a spherical and an ellipsoidal isofrequency surface in the *k*-space, this is normally what occurs in the natural materials (**Fig. 1.23Ai**). As opposed, in hyperbolic metamaterials, the anisotropy is very strong and the two components ε_1 and ε_2 have opposite signs, thus the product verifies $\varepsilon_1\varepsilon_2 < 0$. Then, the first term defines either an isotropic propagation or vanishes because it is algebraically impossible. The second term results in a hyperboloidal isofrequency surface, which defines a hyperbolic medium. Two different possibilities exist, if $\varepsilon_1>0$ and $\varepsilon_2<0$ the

hyperbolic medium is called dielectric hyperbolic or Type I hyperbolic (**Fig. 1.23Aii**). If $\varepsilon_1<0$ and $\varepsilon_2>0$, the hyperbolic medium is called metallic or Type II hyperbolic (**Fig. 1.23Aiii**)[104,105].

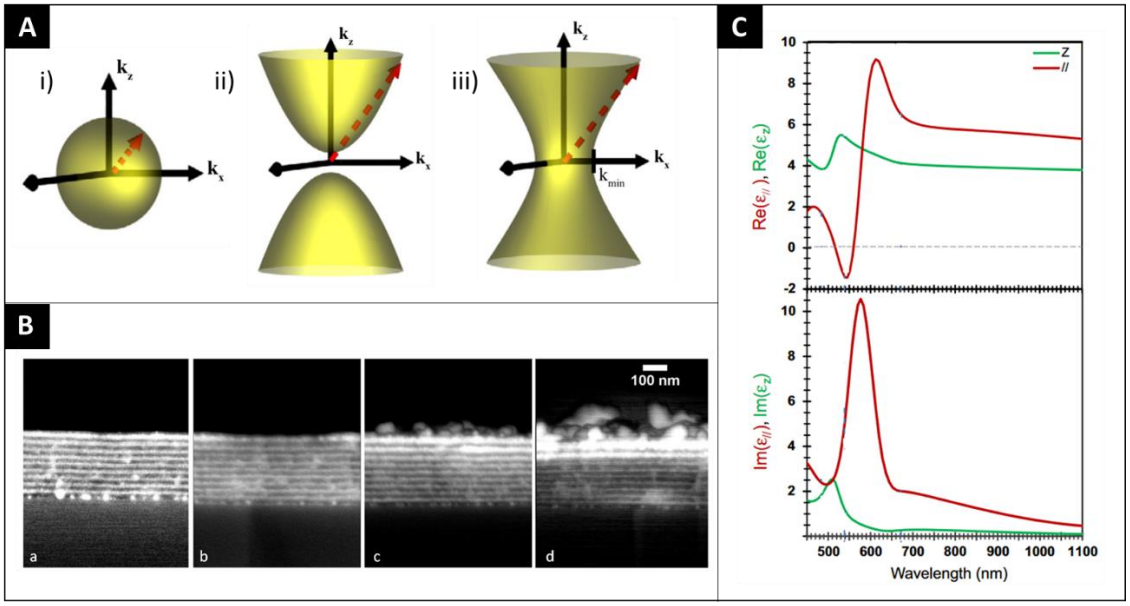

Figure 1.23: *(A) The isofrequency contour for (i) an isotropic dielectric, for (ii) hyperboloid of a type I ($\varepsilon_1>0$ and $\varepsilon_2<0$) and (iii) hyperboloid of a type II metamaterial ($\varepsilon_1<0$ and $\varepsilon_2>0$). (B) Backscattering scanning electron microscopy side-view image (SEM) of the 265 nm-thick film of alternating layers of pure polymer (PS, appearing black) and of Au NPs:P2VP nanocomposite, appearing white, for a number of cycles of gold impregnation and reduction of 5 (a), 10 (b), 20 (c), 30 (d). (C) Parallel (red line) and perpendicular (green line) components of the uniaxial dielectric function of the lamellar nanoplasmonic stack*[100]*.*

Nanocomposites based on metal NPs embedded in a dielectric host, present a strongly anisotropic structure. BCP self-assembly has been revealed as a promising strategy to obtain large scale 3D multi-layered materials. Wang *et al.*[100] have recently demonstrated the possibility of using a self-assembly methodology for the fabrication of bulk hyperbolic material. First of all, self-assembled PS-*b*-P2VP lamellar films were obtained. This structure consists in in-plane alternated PS and P2VP layers. When the film was dipped into $HAuCl_4$ solution and then into a reducing agent ($NaBH_4$) solution, Au NPs were formed selectively within the P2VP layers, due to the strong affinity between the P2VP domains and the Au precursors. The final structure consists of alternating pure PS and Au NPs:P2VP layers (**Fig. 1.23B**). Variable-angle spectroscopic ellipsometry and several theoretical models were used

in order to extract the permittivity tensor in the two polarizations. The results show the possibility to obtain a hyperbolic effective medium in a given region of the visible spectrum ($520 < \lambda < 560$ nm) (**Fig. 1.23C**).

6.2. BCP based metasurfaces

The use of BCP templates to create and design metasurfaces is a novel and promising strategy. In 2016, Young Kim *et al*.[106] demonstrated the potential application of this technique. High and tuneable refractive index materials were created by modifying the inter-objects distance. PS-*b*-PMMA films with hexagonal cylindrical packing were created on silicon substrates. After etching of the PMMA domains by immersion in acetic acid and UV exposure, hexagonal gold nanodots were obtained by e-beam evaporation onto the PS porous film (**Fig. 1.24A**).

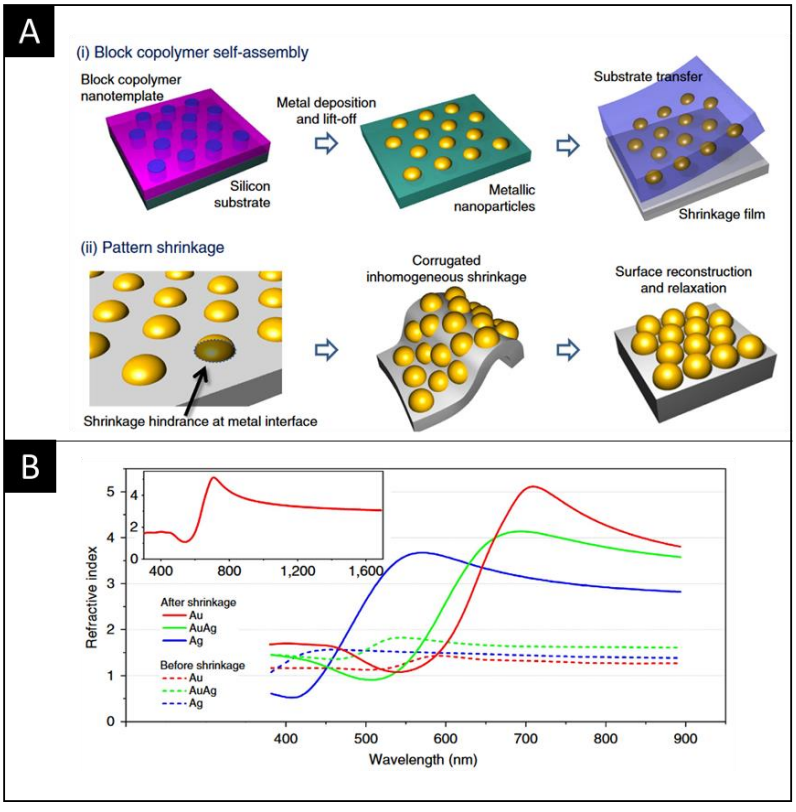

Figure 1.24: *(A) Schematic for metal NP ensemble preparation by (i) BCP self-assembly and substrate transfer and (ii) pattern shrinkage. (B) Ellipsometry measurements of refractive indices of Au, Ag and Au–Ag alloy NP ensembles before (dashed line) and after (solid line) pattern shrinkage*[106].

In order to modify the inter-particle distance, the gold structure was transferred to a PMMA substrate by a lift-off process, and then deposited onto a PDMS stamp allowing a shrinkage of the inter-objects distance through thermal annealing. A heat treatment at 180°C for 3 min promotes a film shrinkage of 40%, with a subsequent decrease of the inter-objects distance from 33 nm to 2.8 nm. Since the inter-objects distance and the particle size are the two significant parameters in order to control the refractive index[107], the precise manipulation of the inter-objects distance allowed to increase the refractive index of such metasurfaces up to 5.10 (natural materials have around 2 as maximum), as is shown in **Fig. 1.24B**.

Lamarre *et al.*[108] have proposed also another strategy using the BCP to organize Au NPs in colloidal solutions. Gold NPs are dispersed in a chloroform PS-*b*-PMMA solution and then spread at the air–water interface in a Langmuir–Blodgett set-up[109]. Based on the higher affinity of water for PMMA, PMMA thin films on the water surface decorated with PS islands were obtained. Depending on the ligand and size of the particles, they are located in the PS part or in the air/PS/PMMA triple interface, forming nanorings. Then these features were deposited on a solid substrate and their optical properties were studied. Interestingly, they have shown the possibility of tuning the optical resonances from visible to near IR spectrum, based on the ring organization of the particles.

7. Conclusions

During this bibliographical chapter, the concept of metamaterial has been introduced. The electromagnetic response of metamaterials is based on the presence of optically resonant elements of sub-wavelength size and well-designed morphology and organization. As it was presented, the arrangement of these meta-atoms into 1D, 2D or 3D structures leads to different classes of metamaterials. One of the most promising fields is devoted to the design of different metasurfaces. Up to now, the top-down approach is the reference in order to obtain controlled geometrical structures. But some examples have recently revealed BCP self-assembly as an emerging strategy. Indeed, the periodic structures inherent to their segregation behavior can be used as scaffolds to create various regular or ordered NPs arrays. Several strategies for inorganic or metallic incorporation into BCP films have been presented.

For all the reasons presented in this chapter, the main objective of this study is to demonstrate that BCP can indeed lead to a high level of control of a variety of designed nanostructures, in an easy and scalable way, and to correlate the structural parameters of the NPs arrays and their optical properties.

During the next chapters several examples of metasurfaces prepared using straightforward methodology based on the selective hybridization of BCP self-assembled film will be presented. The great degree of structural control achieved on 2D structures allows us to create also layer-by-layer 3D structured metallic materials. The optical properties of all the structures created are presented along this manuscript.

1. Zouhdi, S., Sihvola, A. H. & Vinogradov, A. P. *Metamaterials and plasmonics : fundamentals, modelling, applications*. (Springer, 2009).

2. Smith, D. R., Padilla, W. J., Vier, D. C., Nemat-Nasser, S. C. & Schultz, S. Composite Medium with Simultaneously Negative Permeability and Permittivity. *Phys. Rev. Lett.* **84,** 4184–4187 (2000).

3. Zheludev, N. I. The Road Ahead for Metamaterials. *Science (80-.).* **328,** 582–583 (2010).

4. Zheludev, N. I. Obtaining optical properties on demand. *Science (80-.).* **348,** 973–974 (2015).

5. Yuandan Dong & Itoh, T. Metamaterial-Based Antennas. *Proc. IEEE* **100,** 2271–2285 (2012).

6. Landy, N. I., Sajuyigbe, S., Mock, J. J., Smith, D. R. & Padilla, W. J. Perfect Metamaterial Absorber. *Phys. Rev. Lett.* **100,** 207402 (2008).

7. Fernández-Domínguez, A. I., García-Vidal, F. J. & Martín-Moreno, L. Unrelenting plasmons. *Nat. Photonics* **11,** 8–10 (2017).

8. Pendry, J. B. Controlling Electromagnetic Fields. *Science (80-.).* **312,** 1780–1782 (2006).

9. Yu, N. *et al.* Light Propagation with Phase Discontinuities: Generalized Laws of Reflection and Refraction. *Science (80-.).* **334,** 333–337 (2011).

10. Veselago, V. G. The electrodynamics of substances with simultaneously negative values of epsilon and mu. *Fiz. Nauk* **92,** 517–526 (1968).

11. Wang, R., Wang, B.-Z., Gong, Z.-S. & Ding, X. Far-field subwavelength imaging with near-field resonant metalens scanning at microwave frequencies. *Sci. Rep.* **5,** 11131 (2015).

12. Gharghi, M. *et al.* A Carpet Cloak for Visible Light. *Nano Lett.* **11,** 2825–2828 (2011).

13. Yen, T. J. Terahertz Magnetic Response from Artificial Materials. *Science (80-.).* **303,** 1494–1496 (2004).

14. Pendry, J. B., Holden, A. J., Robbins, D. J. & Stewart, W. J. Magnetism from conductors and enhanced nonlinear phenomena. *IEEE Trans. Microw. Theory Tech.* **47,** 2075–2084 (1999).

15. Shalaev, V. M. *et al.* Negative index of refraction in optical metamaterials. *Opt. Lett.* **30,** 3356 (2005).

16. Zhang, S. *et al.* Experimental Demonstration of Near-Infrared Negative-Index Metamaterials. *Phys. Rev. Lett.* **95,** 137404 (2005).

17. Zhang, Y., Fluegel, B. & Mascarenhas, A. Total Negative Refraction in Real Crystals for Ballistic Electrons and Light. *Phys. Rev. Lett.* **91,** 157404 (2003).

18. Hoffman, A. J. *et al.* Negative refraction in semiconductor metamaterials. *Nat. Mater.* **6,** 946–950 (2007).

19. Cui, T. J., Smith, D. R. & Liu, R. *Metamaterials*. (Springer US, 2010). doi:10.1007/978-1-4419-0573-4

20. Yu, Y. F. *et al.* High-transmission dielectric metasurface with 2π phase control at visible wavelengths. *Laser Photon. Rev.* **9,** 412–418 (2015).

21. Khorasaninejad, M., Zhu, W. & Crozier, K. B. Efficient polarization beam splitter pixels based on a dielectric metasurface. *Optica* **2,** 376 (2015).

22. Lin, D., Fan, P., Hasman, E. & Brongersma, M. L. Dielectric gradient metasurface optical elements. *Science (80-.).* **345,** 298–302 (2014).

23. Chung, T., Lee, S.-Y., Song, E. Y., Chun, H. & Lee, B. Plasmonic Nanostructures for Nano-Scale Bio-Sensing. *Sensors* **11,** 10907–10929 (2011).

24. Kravets, V. G., Schedin, F. & Grigorenko, A. N. Extremely Narrow Plasmon Resonances Based on Diffraction Coupling of Localized Plasmons in Arrays of Metallic Nanoparticles. *Phys. Rev. Lett.* **101,** 087403 (2008).

25. Zhou, W. & Odom, T. W. Tunable subradiant lattice plasmons by out-of-plane dipolar interactions. *Nat. Nanotechnol.* **6,** 423–427 (2011).

26. Vecchi, G., Giannini, V. & Gómez Rivas, J. Shaping the Fluorescent Emission by Lattice Resonances in Plasmonic Crystals of Nanoantennas. *Phys. Rev. Lett.* **102,** 146807 (2009).

27. Decker, M., Feth, N., Soukoulis, C. M., Linden, S. & Wegener, M. Retarded long-range interaction in split-ring-resonator square arrays. *Phys. Rev. B* **84,** 085416 (2011).

28. Gwinner, M. C. *et al.* Periodic Large-Area Metallic Split-Ring Resonator Metamaterial Fabrication Based on Shadow Nanosphere Lithography. *Small* **5,** 400–406 (2009).

29. Wu, W. *et al.* Optical metamaterials at near and mid-IR range fabricated by nanoimprint lithography. *Appl. Phys. A* **87,** 143–150 (2007).

30. Decker, M., Klein, M. W., Wegener, M. & Linden, S. Circular dichroism of planar chiral magnetic metamaterials. *Opt. Lett.* **32,** 856 (2007).

31. Sanders, D. P. Advances in Patterning Materials for 193 nm Immersion Lithography. *Chem. Rev.* **110,** 321–360 (2010).

32. Angly, J. *et al.* Microfluidic-Induced Growth and Shape-Up of Three-Dimensional Extended Arrays of Densely Packed Nanoparticles. *ACS Nano* **7,** 6465–6477 (2013).

33. Baron, A. *et al.* Bulk optical metamaterials assembled by microfluidic evaporation. *Opt. Mater. Express* **3,** 1792 (2013).

34. Gomez-Graña, S. *et al.* Hierarchical self-assembly of a bulk metamaterial enables isotropic magnetic permeability at optical frequencies. *Mater. Horizons* **3,** 596–601 (2016).

35. Gordon, M. J. & Peyrade, D. Separation of colloidal nanoparticles using capillary immersion forces. *Appl. Phys. Lett.* **89,** 053112 (2006).

36. Romano, F. & Sciortino, F. Colloidal self-assembly: Patchy from the bottom up. *Nat.*

Publ. Gr. **10,** (2011).

37. Leibler, L. Theory of Microphase Separation in Block Copolymers. *Macromolecules* **13,** 1602–1617 (1980).

38. Flory, P. J. Thermodynamics of High Polymer Solutions. *J. Chem. Phys.* **9,** 660–660 (1941).

39. Huggins, M. L. Some Properties of Solutions of Long-chain Compounds. *J. Phys. Chem.* **46,** 151–158 (1942).

40. Bates, F. S. & Fredrickson, G. H. Block Copolymers—Designer Soft Materials. *Phys. Today* **52,** 32–38 (1999).

41. Khandpur, A. K. *et al.* Polyisoprene-Polystyrene Diblock Copolymer Phase Diagram near the Order-Disorder Transition. *Macromolecules* **28,** 8796–8806 (1995).

42. Ruiz, R. *et al.* Density Multiplication and Improved Lithography by Directed Block Copolymer Assembly. *Science (80-.).* **321,** 936–939 (2008).

43. Phillip, W. A., O'Neill, B., Rodwogin, M., Hillmyer, M. A. & Cussler, E. L. Self-Assembled Block Copolymer Thin Films as Water Filtration Membranes. *ACS Appl. Mater. Interfaces* **2,** 847–853 (2010).

44. Segalman, R. A., McCulloch, B., Kirmayer, S. & Urban, J. J. Block Copolymers for Organic Optoelectronics. *Macromolecules* **42,** 9205–9216 (2009).

45. Joo, W., Park, M. S. & Kim, J. K. Block Copolymer Film with Sponge-Like Nanoporous Strucutre for Antireflection Coating. *Langmuir* **22,** 7960–7963 (2006).

46. Strawhecker, K. E., Kumar, S. K., Douglas, J. F. & Karim, A. The Critical Role of Solvent Evaporation on the Roughness of Spin-Cast Polymer Films. *Macromolecules* **34,** 4669–4672 (2001).

47. Segalman, R. A. Patterning with block copolymer thin films. *Mater. Sci. Eng. R Reports* **48,** 191–226 (2005).

48. Epps, T. H., DeLongchamp, D. M., Fasolka, M. J., Fischer, D. A. & Jablonski, E. L. Substrate Surface Energy Dependent Morphology and Dewetting in an ABC Triblock Copolymer Film. *Langmuir* **23,** 3355–3362 (2007).

49. Han, E. *et al.* Perpendicular Orientation of Domains in Cylinder-Forming Block Copolymer Thick Films by Controlled Interfacial Interactions. *Macromolecules* **42,** 4896–4901 (2009).

50. Mansky, P. Controlling Polymer-Surface Interactions with Random Copolymer Brushes. *Science (80-.).* **275,** 1458–1460 (1997).

51. Ji, S. *et al.* Generalization of the Use of Random Copolymers To Control the Wetting Behavior of Block Copolymer Films. *Macromolecules* **41,** 9098–9103 (2008).

52. Li, W. & Müller, M. Directed self-assembly of block copolymers by chemical or topographical guiding patterns: Optimizing molecular architecture, thin-film properties, and kinetics. *Prog. Polym. Sci.* **54–55,** 47–75 (2016).

53. Cavicchi, K. A., Berthiaume, K. J. & Russell, T. P. Solvent annealing thin films of poly(isoprene-b-lactide). *Polymer (Guildf).* **46,** 11635–11639 (2005).

54. Sinturel, C., Vayer, M., Morris, M. & Hillmyer, M. A. Solvent Vapor Annealing of Block Polymer Thin Films. *Macromolecules* **46,** 5399–5415 (2013).

55. Di, Z., Posselt, D., Smilgies, D.-M. & Papadakis, C. M. Structural Rearrangements in a Lamellar Diblock Copolymer Thin Film during Treatment with Saturated Solvent Vapor. *Macromolecules* **43,** 418–427 (2010).

56. Park, S. *et al.* Lateral Ordering of Cylindrical Microdomains Under Solvent Vapor. *Macromolecules* **42,** 1278–1284 (2009).

57. Horvat, A., Lyakhova, K. S., Sevink, G. J. A., Zvelindovsky, A. V. & Magerle, R. Phase behavior in thin films of cylinder-forming ABA block copolymers: Mesoscale modeling. *J. Chem. Phys.* **120,** 1117–1126 (2004).

58. Knoll, A. *et al.* Phase Behavior in Thin Films of Cylinder-Forming Block Copolymers. *Phys. Rev. Lett.* **89,** 035501 (2002).

59. Rodwogin, M. D., Spanjers, C. S., Leighton, C. & Hillmyer, M. A. Polylactide−Poly(dimethylsiloxane)−Polylactide Triblock Copolymers as Multifunctional Materials for Nanolithographic Applications. *ACS Nano* **4,** 725–732 (2010).

60. Bai, W. *et al.* Thin Film Morphologies of Bulk-Gyroid Polystyrene- *block* -polydimethylsiloxane under Solvent Vapor Annealing. *Macromolecules* **47,** 6000–6008 (2014).

61. Lo, C.-T., Chang, Y.-C., Wu, S.-C. & Lee, C.-L. Effect of particle size on the phase behavior of block copolymer/nanoparticle composites. *Colloids Surfaces A Physicochem. Eng. Asp.* **368,** 6–12 (2010).

62. Chiu, J. J. *et al.* Distribution of Nanoparticles in Lamellar Domains of Block Copolymers. *Macromolecules* **40,** 3361–3365 (2007).

63. Laicer, C. S. T., Chastek, T. Q., Lodge, T. P. & Taton, T. A. Gold Nanorods Seed Coaxial, Cylinder-Phase Domains from Block Copolymer Solutions. *Macromolecules* **38,** 9749–9756 (2005).

64. Li, Q. *et al.* Responsive Assemblies: Gold Nanoparticles with Mixed Ligands in Microphase Separated Block Copolymers. *Adv. Mater.* **20,** 1462–1466 (2008).

65. Park, M. Block Copolymer Lithography: Periodic Arrays of 1011 Holes in 1 Square Centimeter. *Science (80-.).* **276,** 1401–1404 (1997).

66. Park, M., Chaikin, P. M., Register, R. A. & Adamson, D. H. Large area dense nanoscale patterning of arbitrary surfaces. *Appl. Phys. Lett.* **79,** 257–259 (2001).

67. Hong, A. J. *et al.* Metal Nanodot Memory by Self-Assembled Block Copolymer Lift-Off. *Nano Lett.* **10,** 224–229 (2010).

68. Shin, K. *et al.* A Simple Route to Metal Nanodots and Nanoporous Metal Films. *Nano Lett.* **2,** 933–936 (2002).

69. Borah, D. *et al.* Plasma etch technologies for the development of ultra-small feature size transistor devices. *J. Phys. D. Appl. Phys.* **44,** 174012 (2011).

70. Xiao, S., Yang, X., Edwards, E. W., La, Y.-H. & Nealey, P. F. Graphoepitaxy of cylinder-forming block copolymers for use as templates to pattern magnetic metal dot arrays. *Nanotechnology* **16,** S324–S329 (2005).

71. Park, S., Kim, B., Cirpan, A. & Russell, T. P. Preparation of Metallic Line Patterns from Functional Block Copolymers. *Small* **5,** 1343–1348 (2009).

72. Zschech, D. *et al.* High-temperature resistant, ordered gold nanoparticle arrays. *Nanotechnology* **17,** 2122–2126 (2006).

73. Park, S., Wang, J.-Y., Kim, B. & Russell, T. P. From Nanorings to Nanodots by Patterning with Block Copolymers. *Nano Lett.* **8,** 1667–1672 (2008).

74. Hosaka, S., Akahane, T., Huda, M., Zhang, H. & Yin, Y. Controlling of 6 nm Sized and 10 nm Pitched Dot Arrays Ordered along Narrow Guide Lines Using PS–PDMS Self-Assembly. *ACS Appl. Mater. Interfaces* **6,** 6208–6211 (2014).

75. Baruth, A. *et al.* Non-lift-off Block Copolymer Lithography of 25 nm Magnetic Nanodot Arrays. *ACS Appl. Mater. Interfaces* **3,** 3472–3481 (2011).

76. George, S. M. Atomic Layer Deposition: An Overview. *Chem. Rev.* **110,** 111–131 (2010).

77. Richard W.Johnson A brief review of atomic layer deposition: from fundamentals to applications. *MaterialsToday* **7,** 236–246 (2014).

78. Moon, H.-S. *et al.* Atomic Layer Deposition Assisted Pattern Multiplication of Block Copolymer Lithography for 5 nm Scale Nanopatterning. *Adv. Funct. Mater.* **24,** 4343–4348 (2014).

79. Gay, G. *et al.* CMOS compatible strategy based on selective atomic layer deposition of a hard mask for transferring block copolymer lithography patterns. *Nanotechnology* **21,** 435301 (2010).

80. Moon, H.-S. *et al.* Atomic Layer Deposition Assisted Pattern Multiplication of Block Copolymer Lithography for 5 nm Scale Nanopatterning. *Adv. Funct. Mater.* **24,** 4343–4348 (2014).

81. Peng, Q., Tseng, Y.-C., Darling, S. B. & Elam, J. W. Nanoscopic Patterned Materials with Tunable Dimensions via Atomic Layer Deposition on Block Copolymers. *Adv. Mater.* **22,** 5129–5133 (2010).

82. Elam, J. W. *et al.* New Insights into Sequential Infiltration Synthesis. *ECS Trans.* **69,** 147–157 (2015).

83. Yin, J., Xu, Q., Wang, Z., Yao, X. & Wang, Y. Highly ordered TiO 2 nanostructures by sequential vapour infiltration of block copolymer micellar films in an atomic layer deposition reactor. *J. Mater. Chem. C* **1,** 1029–1036 (2013).

84. Li, F. *et al.* Highly Porous Metal Oxide Networks of Interconnected Nanotubes by Atomic Layer Deposition. *Nano Lett.* **12,** 5033–5038 (2012).

85. Chai, J., Wang, D., Fan, X. & Buriak, J. M. Assembly of aligned linear metallic patterns on silicon. *Nat. Nanotechnol.* **2,** 500–506 (2007).

86. Li, X. *et al.* From Precision Synthesis of Block Copolymers to Properties and Applications of Nanoparticles. *Angew. Chemie Int. Ed.* **57,** 2046–2070 (2018).

87. Shin, D. O. *et al.* Sub-Nanometer Level Size Tuning of a Monodisperse Nanoparticle Array Via Block Copolymer Lithography. *Adv. Funct. Mater.* **21,** 250–254 (2011).

88. Mayeda, M. K., Hayat, J., Epps, T. H. & Lauterbach, J. Metal oxide arrays from block copolymer thin film templates. *J. Mater. Chem. A* **3,** 7822–7829 (2015).

89. Shin, D. O. *et al.* Multicomponent Nanopatterns by Directed Block Copolymer Self-Assembly. *ACS Nano* **7,** 8899–8907 (2013).

90. Mokarian-Tabari, P. *et al.* Large Block Copolymer Self-Assembly for Fabrication of Subwavelength Nanostructures for Applications in Optics. *Nano Lett.* **17,** 2973–2978 (2017).

91. Zou, J. J., Zhang, Y. P. & Liu, C. J. Reduction of supported noble-metal ions using glow discharge plasma. *Langmuir* **22,** 11388–11394 (2006).

92. Oh, S. S., Demetriadou, A., Wuestner, S. & Hess, O. On the Origin of Chirality in Nanoplasmonic Gyroid Metamaterials. *Adv. Mater.* **25,** 612–617 (2013).

93. Hur, K. *et al.* Three-Dimensionally Isotropic Negative Refractive Index Materials from Block Copolymer Self-Assembled Chiral Gyroid Networks. *Angew. Chemie Int. Ed.* **50,** 11985–11989 (2011).

94. Wood, B., Pendry, J. B. & Tsai, D. P. Directed subwavelength imaging using a layered metal-dielectric system. *Phys. Rev. B* **74,** 115116 (2006).

95. Vignolini, S. *et al.* A 3D Optical Metamaterial Made by Self-Assembly. *Adv. Mater.* **24,** OP23-OP27 (2012).

96. Salvatore, S. *et al.* A high transmission wave-guide wire network made by self-assembly. *Nanoscale* **7,** 1032–1036 (2015).

97. Li, Z. *et al.* Linking experiment and theory for three-dimensional networked binary metal nanoparticle–triblock terpolymer superstructures. *Nat. Commun.* **5,** (2014).

98. Belov, P. A. Backward waves and negative refraction in uniaxial dielectrics with negative dielectric permittivity along the anisotropy axis. *Microw. Opt. Technol. Lett.* **37,** 259–263 (2003).

99. Smith, D. R. & Schurig, D. Electromagnetic Wave Propagation in Media with Indefinite Permittivity and Permeability Tensors. *Phys. Rev. Lett.* **90,** 077405 (2003).

100. Wang, X. *et al.* [INVITED] Hyperbolic-by-design self-assembled metamaterial based on block copolymers lamellar phases. *Opt. Laser Technol.* **88,** 85–95 (2017).

101. Yao, J. *et al.* Optical negative refraction in bulk metamaterials of nanowires. *Science* **321,** 930 (2008).

102. Narimanov, E. E. & Shalaev, V. M. Beyond diffraction. *Nature* **447,** 266–267 (2007).

103. Guo, Y., Cortes, C. L., Molesky, S. & Jacob, Z. Broadband super-Planckian thermal emission from hyperbolic metamaterials. *Appl. Phys. Lett.* **101,** 131106 (2012).

104. Rytov, S. M. Electromagnetic Properties of a Finely Stratified Medium. *J. Exper. Theor. Phys. USSR* **2,** 605–616 (1956).

105. Cortes, C. L., Newman, W., Molesky, S. & Jacob, Z. Quantum nanophotonics using hyperbolic metamaterials. *J. Opt.* **14,** 063001 (2012).

106. Kim, J. Y. *et al.* Highly tunable refractive index visible-light metasurface from block copolymer self-assembly. *Nat. Commun.* **7,** 12911 (2016).

107. Agranovich, V. M. & Ginzburg, V. Spatial Dispersion in Crystal Optics. in 136–270 (1984). doi:10.1007/978-3-662-02406-5_4

108. Lamarre, S. S. *et al.* Optical properties of Au colloids self-organized into rings via copolymer templates. *J. Nanoparticle Res.* **15,** 1656 (2013).

109. Lamarre, S. S., Lemay, C., Labrecque, C. & Ritcey, A. M. Controlled 2D Organization of Gold Nanoparticles in Block Copolymer Monolayers. *Langmuir* **29,** 10891–10898 (2013).

II

CHAPTER 2 | High refractive index in low metal content nanoplasmonic surfaces from self-assembled block copolymer thin films

1. Introduction

Going beyond the physical limit attainable with natural materials is the purpose of the design of metamaterials[1]. As discussed in the last chapter, the experimental realization of a negative refractive index has been one of the main focus in this field[2–4]. But it is also important to note that the value of the refractive index is also limited in the positive regime[5]. At visible frequencies, most materials show a threshold value of the refractive index around 2. Thus, the realization and the modification on demand of the refractive index towards high positive values constitutes a challenge to be addressed.

In this chapter, we propose a straightforward fabrication technique of high-refractive index surfaces based on the hybridization of an out-of-plane PS-*b*-P2VP lamellar morphology with metallic precursors. The selective metal incorporation into the P2VP domains (as exemplified for gold in this chapter) allows us to obtain multiple arrays of defined geometries: from discrete gold NPs to continuous gold lines with tailored shapes and periodicity. First, we will start describing the preparation and the structural characterization of the BCP nanocomposite films to better apprehend the formation of these hybridized structures. Key stages in this process are:

i. the formation of BCP nanostructured thin films with controlled orientation with respect to the substrate, which has been probed both by imaging (AFM and SEM) and scattering techniques (GISAXS),
ii. the selective metal precursor incorporation into the BCP structure evidenced by structural and chemical analyses (KPFM and XPS),
iii. the reduction of the metallic salts into metallic particles following two different processes based on reactive ion plasma treatment or UV irradiation.

The resulting decorated surfaces with nanometer periodicities will further be studied as regards their optical properties, using variable-angle spectroscopic ellipsometry. Such characterization will allow us to determine the structure/properties relationships between the critical geometrical parameters of the metallic arrays (shape and density of the particles, periodicity of the BCP array) and the resulting refractive indexes extracted from the spectroscopic measurements.

2. Self-assembly of lamellar-forming PS-b-P2VP

The objective of this study is to obtain a lamellar morphology with an out-of-plane orientation, *i.e.*, perpendicular to the substrate. In the previous chapter, several parameters inherent to the formation of the desired BCP morphology were highlighted, such as the incompatibility between the blocks (χ), the degree of polymerization (*N*) and the volume fraction of each block (ϕ). In thin films, two new critical parameters need to be taken into consideration: the interactions with the two interfaces (substrate/BCP film and air/BCP film) and the film thickness (and in particular its commensurability with the BCP periodicity). In order to have a better control of the morphology and its orientation, several strategies have been proposed in the literature, *i.e.*, solvent vapor annealing[6], grafted layers of statistical copolymers[7] and variation of the BCP film thickness[8]. For that reason, in a preliminary study, we have explored these different techniques applied to our BCP system, in order to optimize the targeted BCP structure, which is an out-of-plane lamellar morphology.

2.1 Solvent vapor annealing

Solvent vapor annealing (SVA) consists in exposing the as-prepared BCP thin film to vapors of one (or more) solvent. As introduced in **Chapter 1**, the main effect of the SVA is to swell the BCP film and to give mobility to the polymer chains in order to form well-organized structures[9].

The polymer used in this study is a PS_{102k}-*b*-$P2VP_{97k}$ material. Small-angle X-ray scattering (SAXS) experiment was performed in the bulk and Bragg peaks characteristic of a lamellar order at positions q/q^* = 1:2:3:4 (q is the scattering vector and q^* the position of the first Bragg peak) corresponding to a period of L_0 = 63nm were observed. The molecular weight and dispersity were determined by SEC and ^{1}H-NMR (see experimental section). **Table 2.1** lists the most relevant macromolecular parameters of the BCP structure.

Polymer	M_n (kg/mol^{-1})	M_w/M_n	ϕ_{P2VP}	BCP morphology
PS-block-P2VP	*199*	*1.12*	*0.49*	*Lamellar (L_0=63 nm)*

Table 2.1: *Molecular characteristics of the PS-b-P2VP copolymer used in this work*

A 1 wt.% solution of PS_{102K}-*b*-$P2VP_{97K}$ in toluene was spin coated (30 s, 2000 rpm) onto bare silicon wafers to give a film thickness of 38 nm. The film thickness was determined using a spectral reflectometer (see **Section 4.6** of **Annex)** for experimental details). The self-assembly of the BCP thin films was promoted by exposing samples for different times (ranging from 15 min to 5 h) to a continuous stream of THF or toluene vapors produced by bubbling nitrogen gas through the liquid solvent. The evolution of the nanostructure during SVA strongly depends on the affinity between the solvent and the copolymer blocks. The Hansen solubility parameters (reported in **Table 2.2**) can be used to evaluate these affinities. A solvent is considered as good solvent for a given polymer when the difference between the Hansen solubility parameters of the solvent and the polymer is low. As shown in **Table 2.2**, toluene is a poor solvent for P2VP chains due to its low polarity. This is why, we observed during preliminary experiments, that SVA with toluene failed to produce the desired out-of-plane orientation. In contrast, THF is a neutral solvent for the PS-*b*-P2VP since it presents dispersion component similar to that of PS as well as an important polar component close to that of P2VP. Due to its non-selectivity, it has been revealed as one of the most efficient solvents to obtain out-of-plane lamellar orientation for the system under study[9–11] as the use of THF in the annealing process provides "neutral" interfaces to a certain extent that promote the vertical orientation of the lamellae.

Material	Dispersion ($MPa^{1/2}$)	Polarity ($MPa^{1/2}$)	Hydrogen ($MPa^{1/2}$)
Toluene	*18.0*	*1.4*	*2.0*
THF	*16.8*	*5.7*	*8.0*
PS	*18.6*	*0.2*	*0.0*
P2VP	*18.1*	*6.8*	*7.2*

Table 2.2: *Hansen solubility parameters ($MPa^{1/2}$) for the materials used in this work.*

Atomic force microscopy (AFM) was used to probe the resulting structure after THF vapor annealing. Topographical images for several annealing times are presented in **Fig. 2.1**. For each time, the sample was quickly removed from the chamber, in order to quench the state reached during the SVA. After the spin-coating, a poorly-defined BCP structure is obtained (see **Fig. 2.1A**). After only 15 min in the solvent annealing chamber, (**Fig. 2.1B**) small

out-of-plane domains (lamellae or in-plane cylinders) start to be formed. After 1 h of solvent annealing (**Fig. 2.1C**), the structure has evolved to a clear out-of-plane lamellar structure indicated by the presence of characteristic out-of-plane orientation defects, *i.e.*, dislocations or tilted domain[12,13]. The reason for the well-ordered nature of the system clearly relates to the neutrality of the THF solvent which lowers the interactions between the PS and P2VP by effectively separating the blocks and increasing the chain mobility, allowing defect annihilation. Finally, after 5 h of exposure to THF vapors, some islands, characteristic of the formation of an in-plane lamellar structure[14,15], start to appear and the out-of-plane orientation is partially lost.

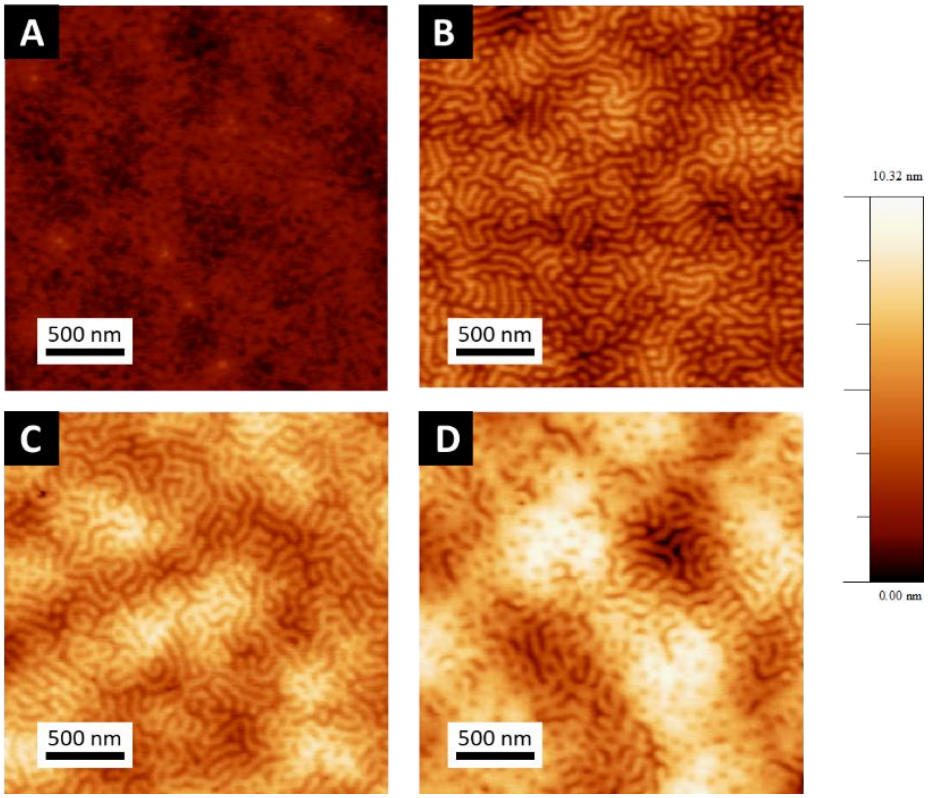

Figure 2.1: *AFM topographical images of PS-b-P2VP films, immediately after spin-coating (A), and after 15 min (B), 1 hour (C) and 5 hours (D) of solvent annealing treatment.*

Therefore, during the THF annealing process, two different phases can be distinguished. During the spin-coating, the diffusion process of the BCP chains is limited due to its high molecular weight. Thus, the sample is kinetically trapped into a non-equilibrium ill-defined structure (**Fig. 2.2A**). THF, being a good solvent for both blocks, swells the film giving

mobility to the polymer chains to diffuse and a reorganization of the segregated structure occurs. As THF is a non-selective solvent, the BCP morphology predicted for a symmetric composition is adopted (**Fig. 2.2B**). This structure is then quenched when the solvent annealing chamber is open due to the quick evaporation of the solvent from the film, leading to well-defined out-of-plane lamellae (**Fig. 2.2C**).

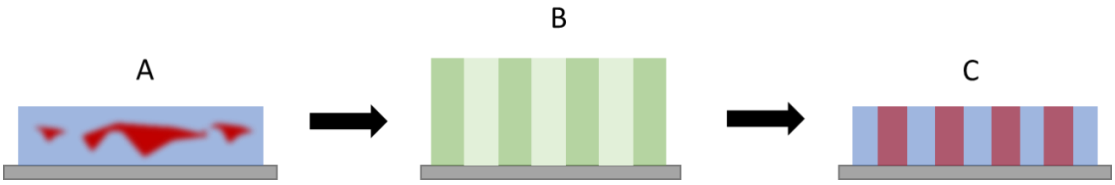

Figure 2.2: *Schematic illustrations of the changes occurring in the film of PS-b-P2VP during the annealing process. (A) Ill-defined structure obtained after spin-coating. (B) Homogeneous swelling of the film due to the solvent exposure leading to the self-assembly of the BCP chains into a lamellar morphology. (C) Quick evaporation of the solvent freezing the film morphology.*

Longer exposure times in the solvent chamber have shown undesirable effects. In our case, an exposure time longer than 5 h starts to damage the film with some partial dewetting. Besides, with a prolonged annealing time, the thermodynamically stable orientation of the BCP morphology, *i.e.*, in-plane lamellae, is partially retrieved, as both interfaces are fundamentally non-neutral to the BCP domains. Other solvents, such as $CHCl_3$ or PGMEA, were tested to prepare the initial BCP solution. Additionally, $CHCl_3$ has been used as an alternative solvent for the SVA process. In all cases, the final results were similar, and we thus choose to use for all the studied BCP films the protocol described beforehand.

To summarize, out-of-plane oriented lamellar structures were obtained using THF solvent vapor annealing. Nevertheless, we opted to optimize further the quality of the BCP structure and we thus considered a strategy involving the use of grafted copolymers layers to tune the surface energy between the substrate and the BCP thin film.

2.2 Control of the surface energy by a grafted layer

Fig. 2.3A shows a schematic representation of the process followed to obtain the desirable out-of-plane lamellar orientation. In order to neutralize the effect of the surface of the substrate during the microphase separation process, a solution of 1.5 wt.% PS-*stat*-PMMA with 73 wt.% PS was prepared in PGMEA and spin-coated (30 s, 1500 rpm) on the silicon wafer. Thermal treatment at 240°C for 10 minutes was carried out in order to promote the copolymer grafting onto the silicon surface. After rinsing with PGMEA to remove the excess of polymer not grafted onto the silicon surface, the thickness (t) of the remaining grafted layer was measured by ellipsometry and found to be 7 nm. The grafting density (Σ) was calculated from the measured brush thickness, as follows:

$$\Sigma = \frac{t\rho N_a}{M_n} \tag{2.1}$$

Where ρ is the polymer density, N_a is the Avogadro's number, and M_n is the number–average molecular weight[16]. **Table 2.3** lists the set of parameters concerning the statistical copolymer used in this study.

Polymer	Styrene (%)	M_n (g/mol^{-1})	M_w/M_n	Σ (nm^{-2})	t (nm)
PS-stat-PMMA	*73%*	*14620*	*1.8*	*0.317*	*7*

Table 2.3: *Material characteristic, M_n and M_w are the average number and mass molecular weights, respectively, Σ is the grafting density and t the thickness obtained by ellipsometry.*

In order to better understand the effect of this layer on the self-assembly, we have determined the surface energy of the grafted PS-*stat*-PMMA film by surface tension measurements obtained using a contact angle goniometer. The results as well as their comparison with the tabulated surface energies[17] of PS and P2VP are summarized in **Table 2.4**. It appears that the surface energy of the grafted layer lies between those of the PS and P2VP domains. Even if such analysis has to be used with caution, such grafted layer with an intermediate surface energy as regards to both BCP blocks is expected to promote an out-of-plane orientation of the lamellae[7,18].

Polymer	Surface energy ($mN.m^{-1}$)
PS-stat-PMMA	*43±1*
PS	*41.5*
P2VP	*46.7*

Table 2.4: *Surface energy values for the PS-stat-PMMA, PS and P2VP.*

In a subsequent step, 1 wt.% solution of PS_{102K}-*b*-$P2VP_{97K}$ in PGMEA was cast upon the grafted substrate. The AFM topographic image presented in **Fig. 2.3B** shows the well-defined out-of-plane lamellar structure obtained, with a periodicity, L_0 = 64 nm. It is important to note that the periodicity extracted from the AFM data (64 nm) is in a good agreement with the bulk SAXS periodicity (63 nm).

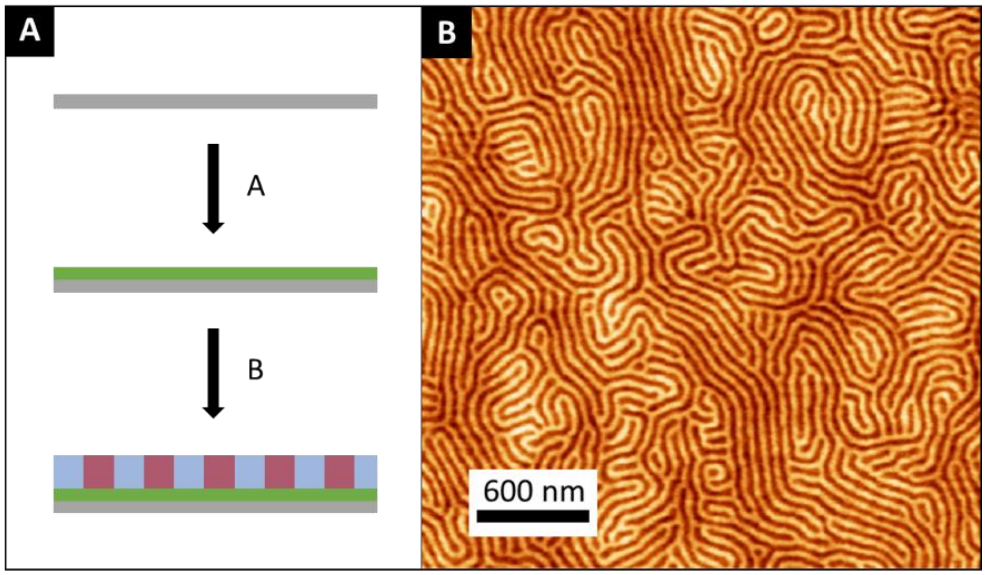

Figure 2.3: *(A) schematic illustration of the fabrication process of out of plane lamellar structures, in the first step a PS-stat-PMMA is grafted to the silicon surface and in a second step the PS-b-P2VP BCP is deposited onto the grafted neutral substrate. (B) AFM image of PS-b-P2VP out of plane lamellar structures, immediately after spin-coating.*

In this case, the solvent used for the thin film deposition was PGMEA. This solvent has a high boiling point, 146°C, in contrast with 66°C of THF. This means that the solvent evaporation during the spin-coating process is slower, giving more mobility to the polymer chains and allowing them to have a better diffusion into well-defined structures[19]. As it was previously

introduced, the film thickness is also a very important parameter to consider. Several solutions with concentrations from 1 to 3 wt.% were prepared in PGMEA, and spin-coated onto PS-*stat*-PMMA grafted silicon substrates. Thickness measurements by spectral reflectometry were carried out on the thin films obtained, giving thicknesses, *t*, from 37 nm (1 wt.%), 56 nm (2 wt.%) and 71 nm (3 wt.%) respectively. **Fig. 2.4** shows the AFM topography images of the different results obtained after the spin-coating.

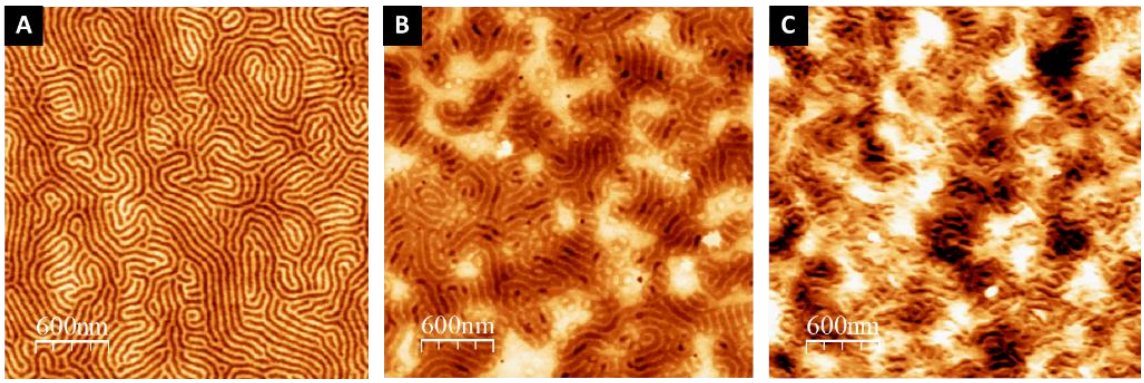

Figure 2.4: *AFM topographical images of PS-b-P2VP film obtained from different concentration solutions: (A) 1 wt.%, (B) 2 wt.% and (C) 3 wt.%.*

The observed behavior can be separated in different regimes depending on the comparison between the BCP film thickness and the periodicity of the BCP (L_0 = 64 nm). As the film thickness is close to ½ L_0 (for the 1 wt.% solution), the out-of-plane orientation is favored (**Fig. 2.4A**). As opposed, when the thickness is close to L_0 (2 wt.%), some islands appear (**Fig. 2.4B**), and with a thickness larger than L_0, the out-of-plane orientation is lost (**Fig. 2.4C**). This is in accordance with previous observations made by Ham and coworkers[20], where for PS-*stat*-PMMA grafted layers with a high PS content, the out-of-plane orientation is limited to a very narrow window in composition and always for a relationship $t/L_0 << 1$.

Nevertheless, the use of this particular grafted layer for BCP film thickness lower than L_0 leads to the formation of well-defined out-of-plane structure with increased correlation length (grain size) as shown in **Fig. 2.4**. Further treatment by SVA of the as-cast films, as performed in the previous section, revealed unsuccessful for the improvement of the BCP structure (in particular the grain size).

GISAXS experiments were also performed to confirm the lamellar orientation of the structure. As shown in **Fig. 2.5**, the GISAXS pattern mainly consists of intense Bragg rods

inherent to the in-plane organization of the BCP domains produced during the PS-*b*-P2VP spin-coating. The GISAXS pattern line-cut along q_y integrated around the Yoneda band confirms the lamellar structure for the neat BCP thin film since a first Bragg rod maximum at q^*=0.103 nm^{-1} (period, L_0 = 61 nm in accordance with the AFM and SAXS characterizations) and higher order Bragg rods at q/q^* = 1, 2, 3 are clearly visible (see **Fig. 2.5A-B**).

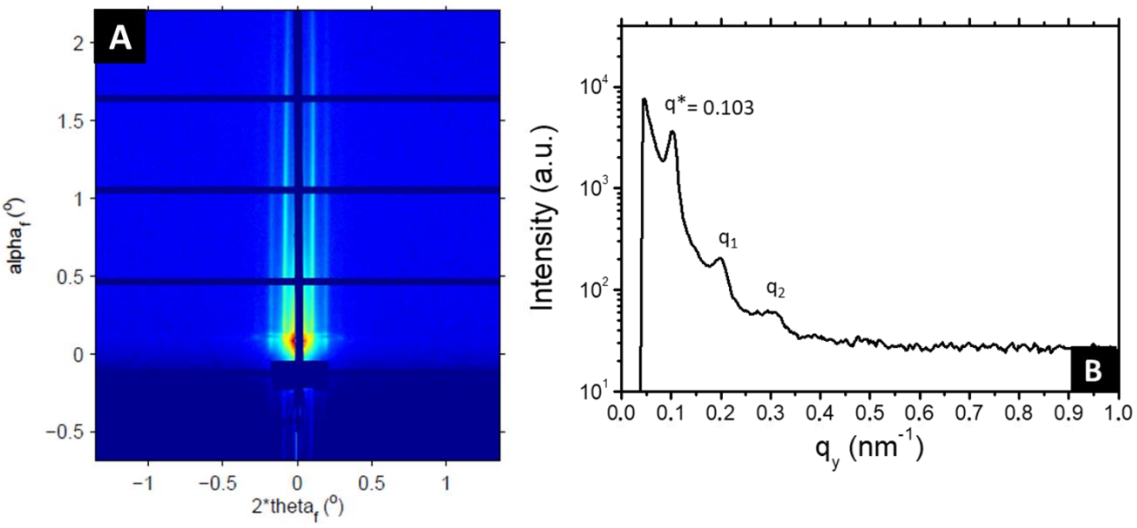

Figure 2.5: *(A) GISAXS pattern of the PS-b-P2VP film obtained by spin-coating on a grafted silicon substrate and (B) GISAXS pattern line-cut along q_y integrated around the Yoneda band.*

To conclude this section, well-defined out-of-plane self-assembled lamellar films were obtained directly by spin-coating the BCP solution onto the grafted substrate. In contrast, the SVA approach was not as efficient in this particular case since some dewetting and inhomogeneities were observed for long treatments. In the next section, we will focus on the selective impregnation of the P2VP blocks with a metallic salt.

3. Selective impregnation of the block copolymer structure

3.1 Fabrication of decorated surfaces: a structural study

Nanoparticles (NPs) decorated surfaces were produced by combining thin film BCP self-assembly and selective hybridization of the BCP domains with metallic precursors following a methodology described in **Fig. 2.6**.

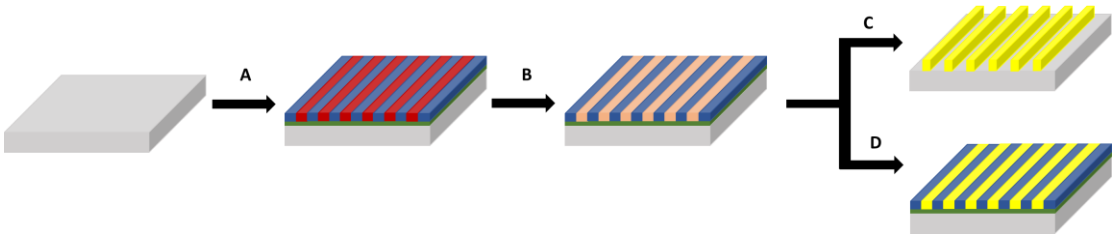

Figure 2.6: *Scheme of the fabrication of nanoplasmonic surfaces. (A) An out-of-plane lamellar BCP thin film can be obtained directly by spin-coating using a grafted layer. (B) These nanostructures are then used as a platform to selectively introduce the gold salt. Finally, gold NPs arrays were obtained by two different strategies, either (D) by O_2 RIE or (C) by UV irradiation.*

The AFM topographic image presented in **Fig. 2.7A** shows the out-of-plane lamellar structure (periodicity, L_0 = 64 nm) obtained from PS_{102K}-*b*-$P2VP_{97K}$ self-assembly in thin film (thickness, t = 32 nm) after casting from PGMEA upon a PS-*stat*-PMMA layer. The subsequent spin-coating of a $HAuCl_4$ solution leads to the selective hybridization of the P2VP domains by the Au salts as attested by the topographical contrast inversion inherent to the swelling of the P2VP domains observed in **Fig. 2.7B** (the circles in **Fig. 2.7A-B** highlight the contrast inversion).

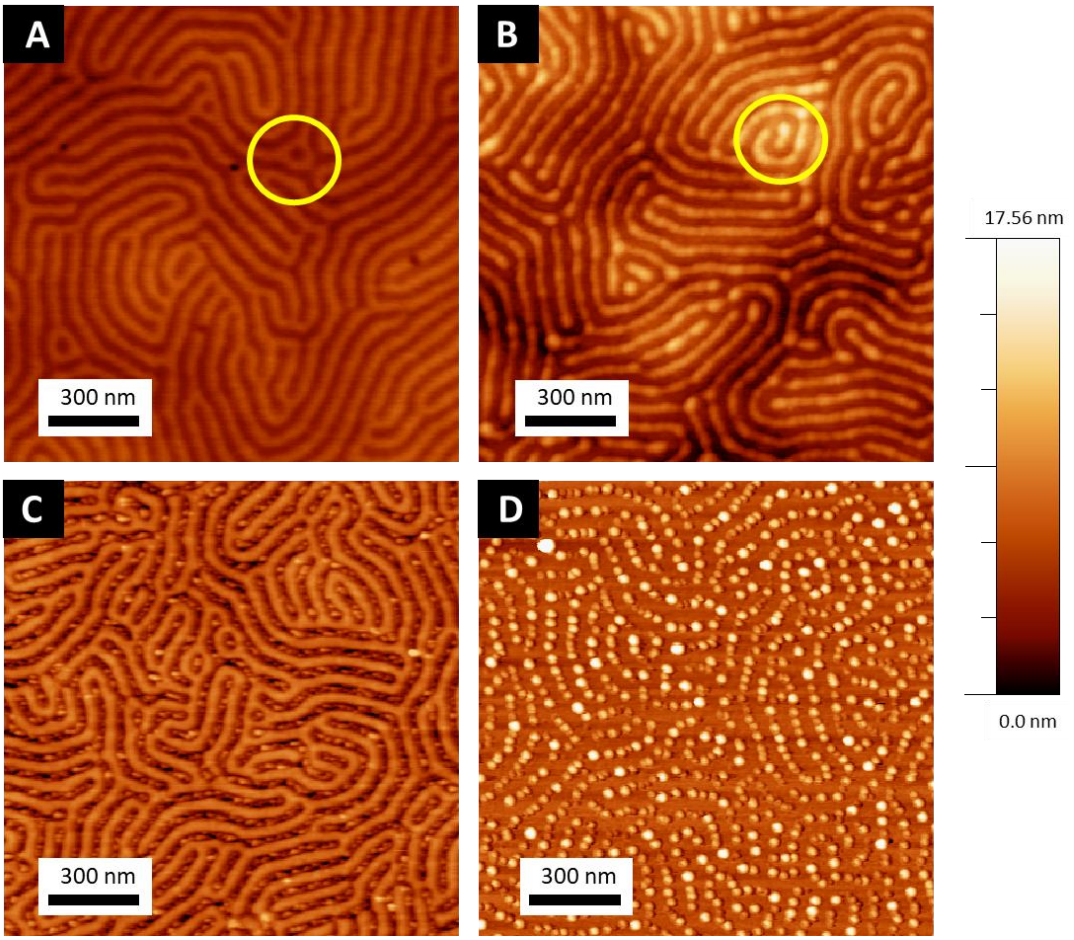

Figure 2.7: *(A) AFM images of PS-b-P2VP out of plane lamellar structures, immediately after spin-coating. (B) Gold-loaded P2VP domains by spin-coating of 1 wt.% gold precursor solution, and arrays of gold NPs obtained by (C) 10 seconds or (D) 60 seconds of oxygen plasma treatment.*

The SEM image of the same sample (**Fig. 2.8A**) also confirms the selective loading of the Au salts into the P2VP domains, since a high contrast between the PS (black) and the loaded P2VP/Au (white) domains is retrieved due to their different electron density. A RIE O_2 plasma was then used to reduce the Au salts sequestered in the P2VP domains into metallic Au. Interestingly, tuning the plasma treatment affords an additional lever for the production of complex plasmonic surfaces[21], as both Au dots confined between PS walls (10 s, 60 W, 10 sccm O_2) and individualized Au dots (60 s, 60 W, 10 sccm O_2) were produced as shown in **Fig. 2.8B** and **Fig. 2.8C**, respectively. This can be explained by the different etching ratios between the two blocks (PS 13 nm/min and P2VP 29 nm/min[22]) leading to a faster degradation of the P2VP domains under the O_2 RIE plasma. It is noteworthy that the control of the plasma

treatment duration allows obtaining an intermediate structure (**Fig 2.8B**). For longer plasma treatment, both PS and P2VP domains are etched (**Fig 2.8C**) and only spherical gold NPs are observed[23].

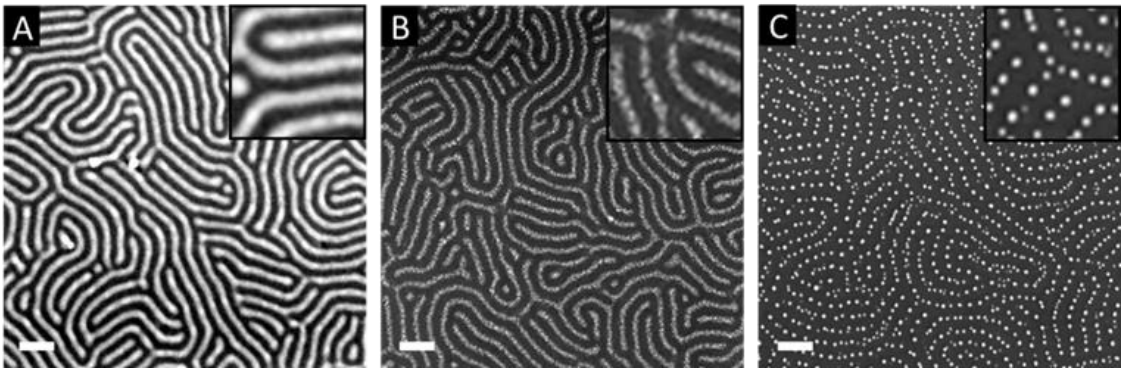

Figure 2.8: *SEM images of gold lines and discreet gold NPs arrays formed on a silicon substrate using a PS-b-P2VP copolymer template: (A) immediately after gold deposition, (B) after 10 s and (C) 60 s of oxygen plasma treatment.*

The associated GISAXS patterns presented in **Fig. 2.9** give access to further insight in the structure of the Au decorated surfaces. They mainly consist of intense Bragg rods related to the in-plane organization of the periodic BCP domains produced during the PS-*b*-P2VP spin-coating as was already described in the **section 2.2** of this chapter. Following the hybridization of the BCP structure with the Au salts, a strong increase of the scattering contrast is noticed due to the high scattering cross-section of Au atoms as shown in **Fig. 2.9C**. Higher order Bragg rods become visible (up to the 5th order), but the lamellar signature remains otherwise unchanged (L_0 = 61 nm, see **Fig. 2.9D**). In addition, the same sequence of Bragg rods is observed, although dominated by a signal attributed to the form factor of NPs, for the Au dots obtained after complete reduction of the gold salt and removal of the BCP template by plasma etching (**Fig. 2.9E-F**). This allows us to conclude on the stability of the nanostructure during the treatment.

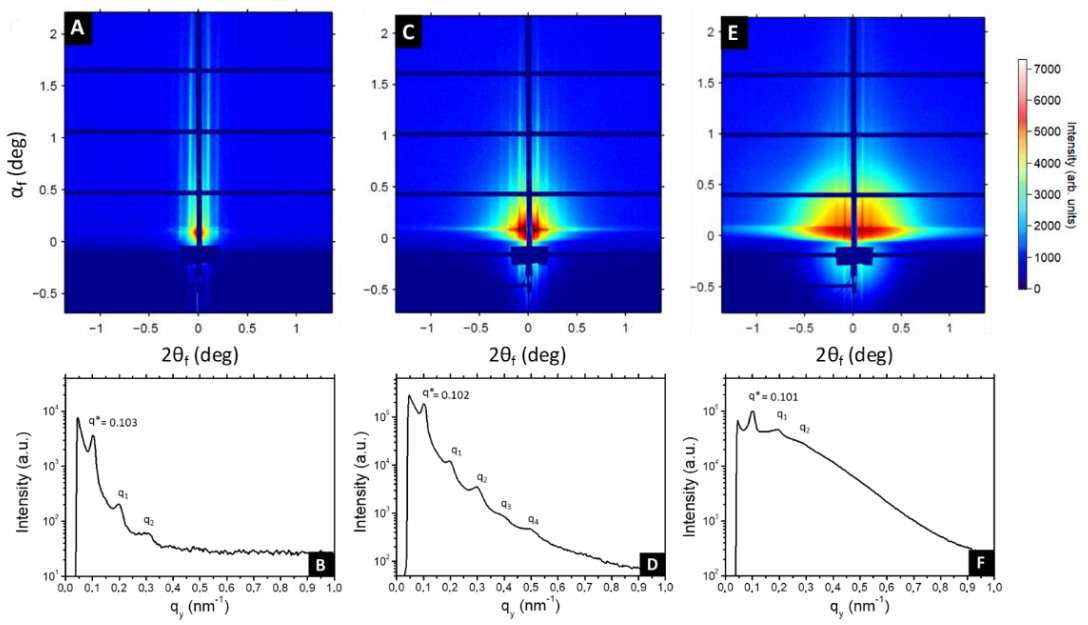

Figure 2.9: *GISAXS patterns and their corresponding line-cuts along q_y integrated around the Yoneda band at different steps of the process: (A-B) after polymer deposition, (C-D) with the gold salt selectively incorporated into the P2VP domains and (E-F) after 60s of O_2 RIE.*

Interestingly, the GISAXS pattern presented in **Fig. 2.9E** contains additional information about the Au NPs. Indeed, a strong contribution of the form factor of the NPs is visible in the form of an intense halo. Simulations using the FitGISAXS software[24] allow us to gain additional insights on the form of the Au NPs. As shown in **Fig. 2.10**, a simulated GISAXS pattern of truncated spheres (diameter d = 11.5 nm and height h = 7.8 nm) arranged in a 1D paracrystalline array with L_0 = 53 nm) shows strong similitudes with the experimental pattern.

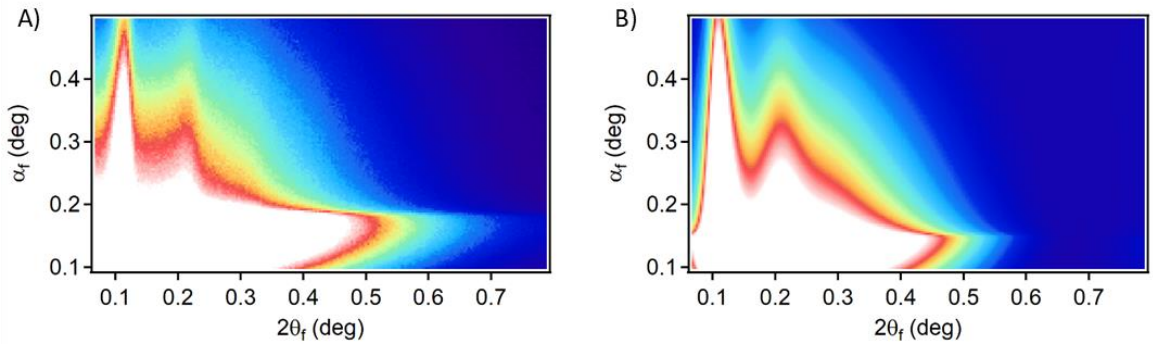

Figure 2.10: *(A) Experimental and (B) simulated GISAXS patterns. The simulated GISAXS pattern corresponds to truncated spheres arranged in a 1D paracrystalline array and was obtained using FitGISAXS.*

The reduction of the Au salts sequestered in the P2VP domains into metallic gold was followed using X-ray photoelectron spectroscopy (XPS). The Au 4f XPS spectrum of the BCP thin film loaded with the Au salts is presented in **Fig. 2.11A**. Two chemical gold states are detected, corresponding to Au(III) (90.6 and 87.0 eV – blue dotted line in **Fig. 2.11A**) and to Au (I) (88.2 and 84.8 eV – green dotted line in **Fig. 2.11A**). The amount of Au(I) is significant, suggesting that the gold salt was already partially reduced by either the contact with the polymer pyridine functions or the effect of ambient light. After the 60 s plasma treatment, the Au 4f XPS spectrum is consistent with Au(0) with characteristic binding energies of 87.6 eV and 83.9 eV (see **Fig 2.11B**)[44].

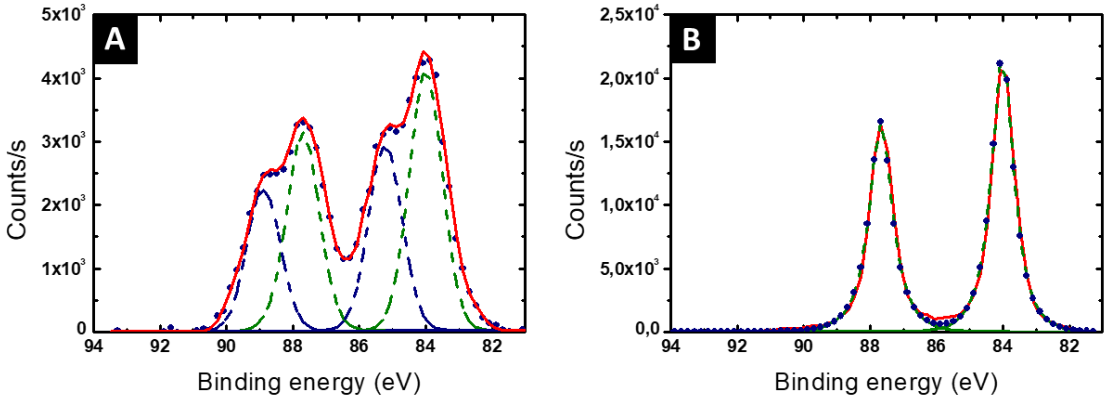

Figure 2.11: *High resolution XPS of Au 4f. (A) After impregnation with the gold salt. This profile is indicative of a mixture of Au(I) and Au(III). (B) After reduction of Au ions via 60 s O_2 plasma treatment. This profile indicates Au(0) exclusively.*

Further evidence of the reduction of the Au salts was obtained by Kelvin Probe Force Microscopy (KPFM) by measuring the contact potential difference, V_{CPD}, between the work functions of the sample and the tip. The topography and contact potential difference (V_{CPD}) images of the surface decorated by Au dots obtained after complete removal of the BCP template (see **Fig. 2.12A-B**) are in good accordance and allow retrieving a precise mapping of the work function of the surface (W) for a known tip work function as shown in **Fig. 2.12C**. A good agreement between the experimental and theoretical work functions for Au (W_{Au} = 5.1

eV) and SiO_2 (W_{SiO2} = 4.3 eV) is obtained showing the strong potential of KPFM for the characterization of decorated surfaces.

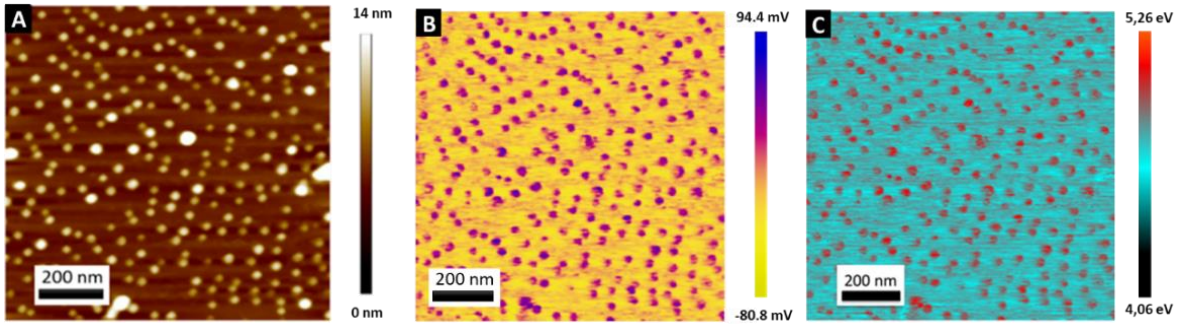

Figure 2.12: *(A) Topography and (B) CPD images obtained using the frequency modulation mode of gold NPs on Si substrate after 60 s of O_2 plasma. (C) Work function map (in eV) of the sample surface retrieved from the composite topographical and CPD images.*

3.2 Alternative reduction method by UV irradiation

UV irradiation, known for triggering the photo-decomposition of $HAuCl_4$ into metallic Au in Au-loaded polymer composite film[25,26] was used as an alternative to the plasma treatment in order to preserve the BCP template. **Fig. 2.13 s**hows SEM and AFM topographical images of PS-*b*-P2VP sample immersed in the gold precursor solution and exposed to UV irradiation for 24 h. A three-color pattern attributed to the PS, P2VP and Au can be observed in the SEM image. The AFM micrograph and N_2 XPS spectra confirm that the polymer film has not been damaged during the exposure (for comparison, the N_2 XPS spectrum of PS-*b*-P2VP sample immersed in the gold precursor and exposed to 60 s of O_2 RIE is provided). Besides the Au XPS spectrum confirms the gold reduction during the UV irradiation treatment.

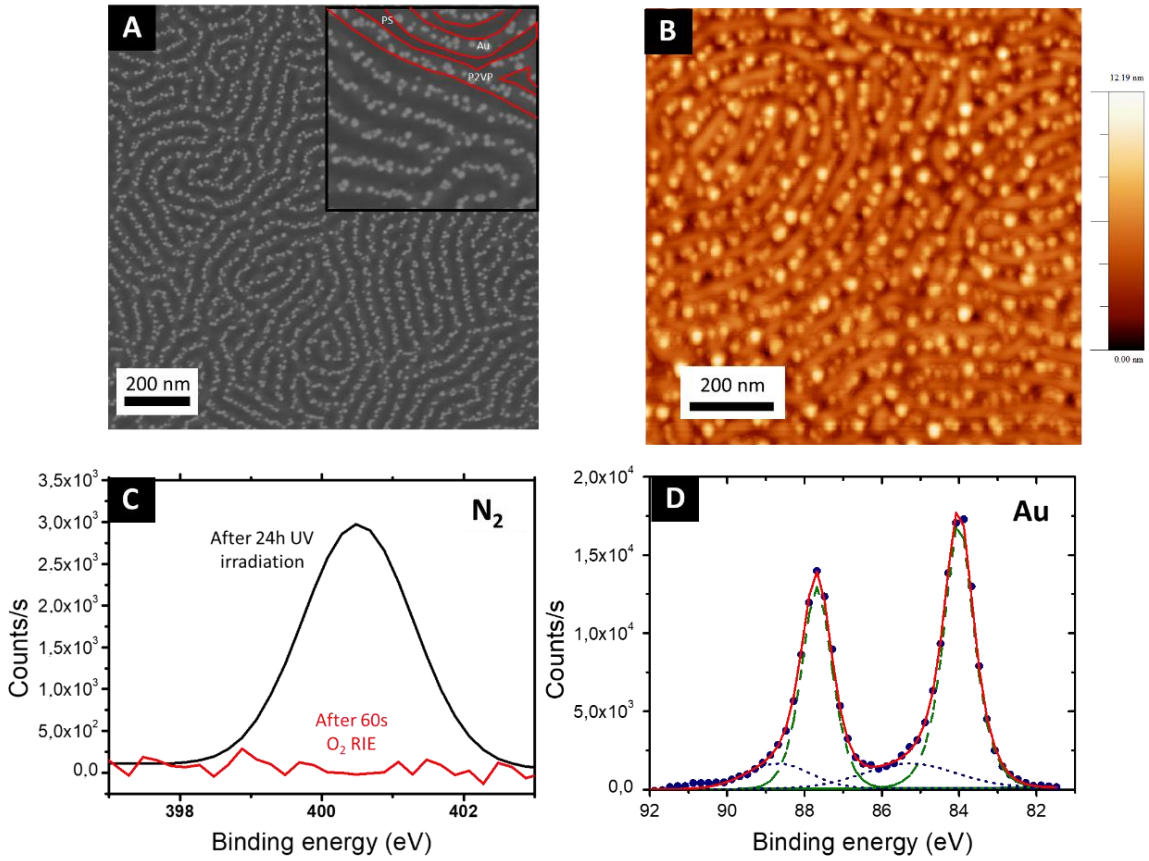

Figure 2.13: *(A) SEM and (B) AFM topographical images and the corresponding (C) N_2 and (D) Au XPS spectrum of PS-b-P2VP sample immersed in the gold precursor solution and exposed to UV irradiation for 24 h.*

The final structures are shown in **Fig. 2.14** for 6, 24 and 48 hours of UV exposure (λ = 254 nm, 6 W) and demonstrate that an additional lever is provided by this methodology as different UV irradiation exposure times result in gold NPs of different sizes. After 6 h of exposure (**Fig. 2.14B**), the TEM image shows ill-defined agglomerates localized in the P2VP lamellar domains. Further exposure to UV light (see **Fig. 2.14C-D**) leads to larger NPs with a size distribution centred on 7 nm after 24 h of exposure (see **Fig. 2.14C** and **E)** and a bimodal size distribution centred on 10 and 15 nm after 48 h of exposure (**Fig. 2.14D** and **F**). Gold reduction was also further confirmed by XPS (see **Fig. 2.13D**)

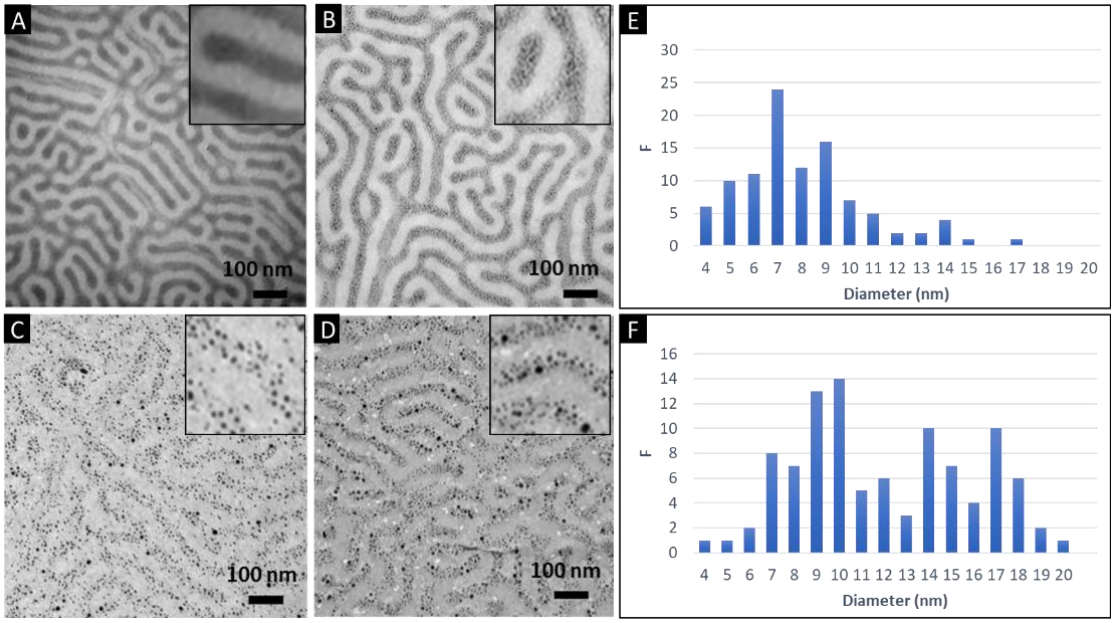

Figure 2.14: *TEM micrographs of the gold NPs obtained inside the BCP matrix at different times of UV irradiation. (A) Neat BCP film, (B) 6 h UV irradiation, (C) 24 h UV irradiation and (D) 48 h UV irradiation. Size distribution diagrams of the gold NPs obtained from the micrographs of the (E) 24 h and (F) 48 h irradiated samples.*

3.3 Monitoring the gold volume fraction. From spheres to continuous lines

As the plasmonic properties of decorated surfaces are strongly influenced by the gold content, a substantial gold salt incorporation in the BCP template is highly desired. Therefore, the BCP thin films were immersed in an aqueous $HAuCl_4$ solution for different times in order to swell the P2VP domains. Water was chosen as the solvent to avoid surface reconstruction of the BCP thin film structure observed by using ethanol. The SEM images presented in **Fig. 2.15** show the different Au structures obtained after plasma treatment (60 s, 60 W, 10 sccm O_2 or Ar) for immersion time ranging from 5 h to 120 h (for comparison the Au structure obtained via the spin-coating methodology is also included in **Fig. 2.15A**). After 1 h of immersion, well defined Au dots with a 20 nm diameter were obtained, while, for 48 h of immersion, rod-like Au particles are formed after the O_2 plasma treatment (**Fig. 2.15B**). By further increasing the immersion time to 120 h, an increase of the length of the Au rods was observed leading to the formation of Au dashed lines on the SiO_2 surface (**Fig. 2.15C**).

Interestingly, continuous gold lines were produced using an Ar plasma (60 s, 60 W, 10 sccm) for a 120 h immersion time of the BCP thin film (**Fig. 2.15D**).

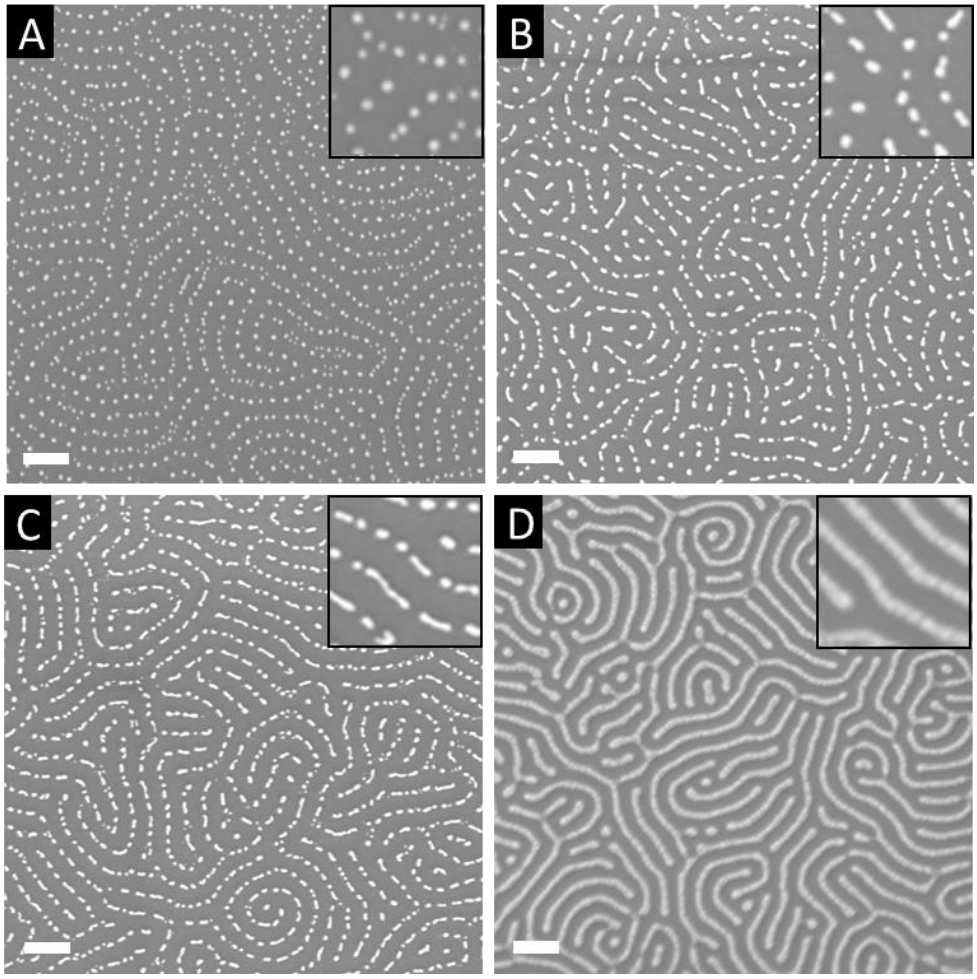

Figure 2.15: *SEM images of discreet gold NPs arrays formed on a silicon substrate using a PS-b-P2VP copolymer template by immersion in an aqueous 1 wt.% gold precursor solution for different times. (A) 1 hour, (B) 48 h and (C) 120 h followed by a subsequent O_2 RIE treatment. (D) SEM image of continuous gold lines formed on a silicon substrate after 120 h of immersion in the gold precursor and a subsequent Ar plasma treatment.*

XPS experiments were performed on the three key samples with different immersion time (1 h, 48 h and 120 h). **Fig. 2.16** shows the Au 4f XPS spectra of the three BCP films immediately after being immersed in the Au salt precursor solution for different times. In all the cases, the two chemical gold states are detected (**Fig. 2.16A**), corresponding to Au(III) (90.6 and 87.0 eV) and to Au (I) (88.2 and 84.8 eV). In order to correlate the immersion time and the quantity of gold present in the sample, the total area corresponding to the different

chemical Au states was calculated for each immersion time. The results are showed in **Fig. 2.16B**, where indeed a clear tendency is observed. Longer immersion time leads to a more intense Au 4f XPS signal, or in other words material present in the sample. A saturation is also observed, which can be understood by the fact that the number of free pyridine moieties is limited.

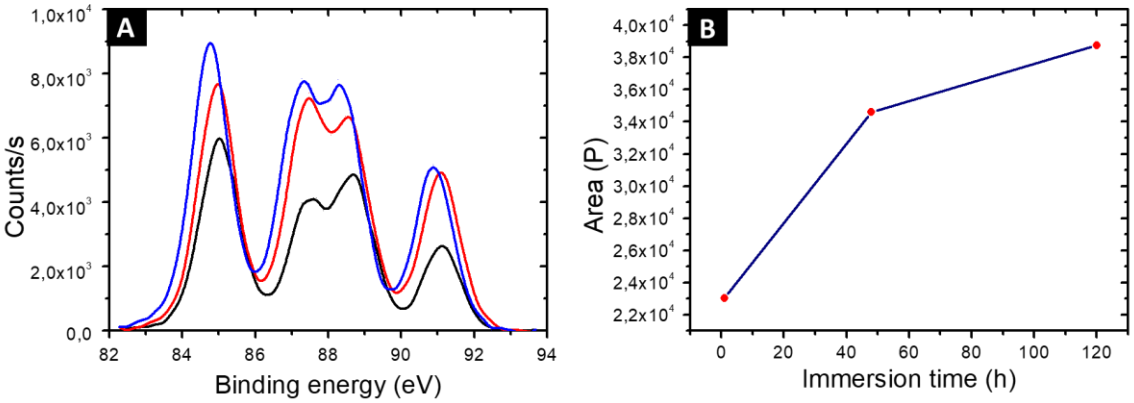

Figure 2.16: *(A) High resolution XPS spectrum of Au 4f for three different polymer films immersed into the gold salt for different times 1 h (black line), 48 h (red line) and 120 h (blue line). (B) Total area of the peaks for the three different immersion times (1 h, 48 h and 120 h)*

3.4 Modulation of the particle size and shape

In order to have a better understanding of the different particles obtained when varying the immersion time of the PS-*b*-P2VP polymer templates into the precursor solution, we decided to do a statistical analysis of the SEM images presented on **Fig. 2.15**. The Vision assistant software of National Instruments was used for that purpose. A first step of image treatment was necessary, to convert the RGB (*red-green-blue*) SEM image to an 8-bits one, with a final conversion into a 2-colored B/N image (**Fig. 2.17A**). Several parameters were studied, the length of the particle in the two different axes, and their ratio called aspect ratio of the particles presented in the three different images. In all the cases, the size and aspect ratio histograms were fitted with a Gaussian distribution (represented in each case by a blue line in **Fig. 2.17**).

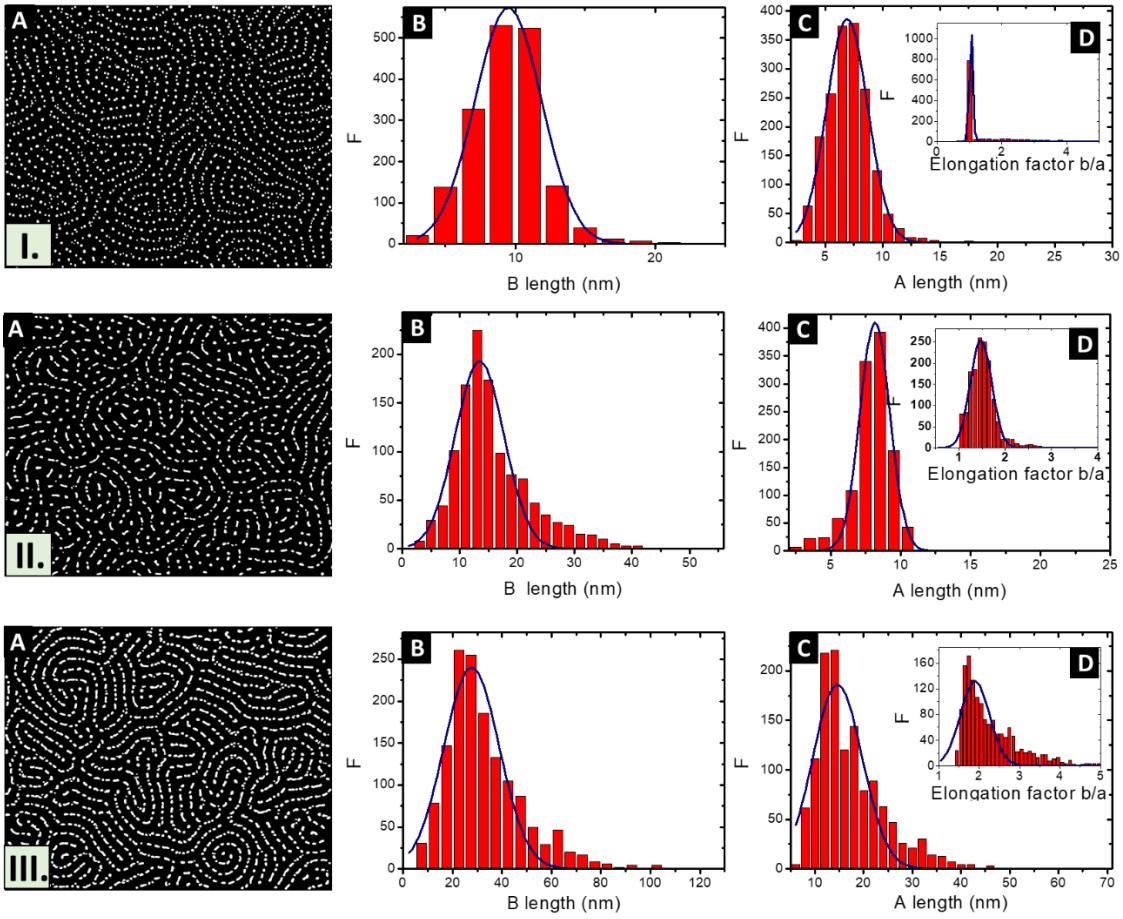

Figure 2.17: *(A) SEM images converted to B/N 8 bits images and treated with Visio Assistant software of discreet gold NPs arrays formed on a silicon substrate using a PS-b-P2VP copolymer template by immersion in an aqueous 1 wt.% gold precursor solution for different times: (I) 1 h, (II) 48 h and (III) 120 h. (B and C) histograms of dimensions of the particles and (D) histogram of the aspect ratio. All distributions were fitted with a Gaussian function of discreet gold NPs arrays formed on a silicon substrate using a PS-b-P2VP copolymer template by immersion in an aqueous 1 wt.% gold precursor solution for different times. 1 hour (I.), 48 h (II.) and 120 h (III.)*

All the obtained values are listed in **Table 2.5**. The shape of the particles clearly changes with the immersion time. One hour of immersion time leads to quasi-spherical particles with a diameter of 9 nm and an aspect ratio of 1.1 (**Fig. 2.17 I.B-D**). After longer immersion times (48 h), the particles elongate, with an aspect ratio around 1.5 (see **Fig. 2.17 II.A-D**). Elongated

particles with an aspect ratio of 1.9 are obtained after 120 h of immersion into the Au precursor solution (**Fig. 2.17 III.A-D**).

Sample	B length (nm)	A length (nm)	Aspect ratio
1 h Au immersion	9.20	9	1.07
48 h Au immersion	13.2	8.7	1.47
120 h Au immersion	27.6	14.5	1.90

Table 2.5: *Structural parameters obtained from the statistical analysis of the SEM images using Visio assistant software.*

In summary, several methodologies for the selective impregnation of PS-*b*-P2VP out-of-plane lamellar films were presented. The first strategy consists of spin-coating the metallic precursor solution on top of the polymer film. The second one involves the immersion of the film into the metallic solution. A controlled metal loading was obtained with the last strategy by monitoring the immersion time. After a subsequent reduction process, this strategy gives access to different particles shapes (from spherical NPs to rod-like ones) or even continuous metallic lines. These changes in the shape, size and inter-distances between the particles are expected to have an important impact on the optical properties.

4. Optical characterization of the decorated surfaces

Key samples (1 h, 48 h and 120 h of immersion followed by an O_2 plasma treatment) were further analyzed by variable angle spectroscopic ellipsometry (VASE) in reflection in order to correlate the geometry of the decorated surfaces with their plasmonic properties. The evolution of the measured ellipsometric angles Ψ and Δ as a function of the photon energy, between 0.6 and 4.8 eV, (see **Fig 2.18**) reveals a clear resonance feature in the region ≈ 2.3 eV, which is attributed to the effect of the localized surface plasmon resonance (LSPR) of the Au NPs templated from the P2VP domains.

A progressive evolution of the resonance band is observed, due to the increase of the gold amount on the surface and the shape evolution of the produced Au NPs. A slight shift in the SPR spectral position is also observed, from 2.30 eV (539 nm) to 2.20 eV (563 nm).

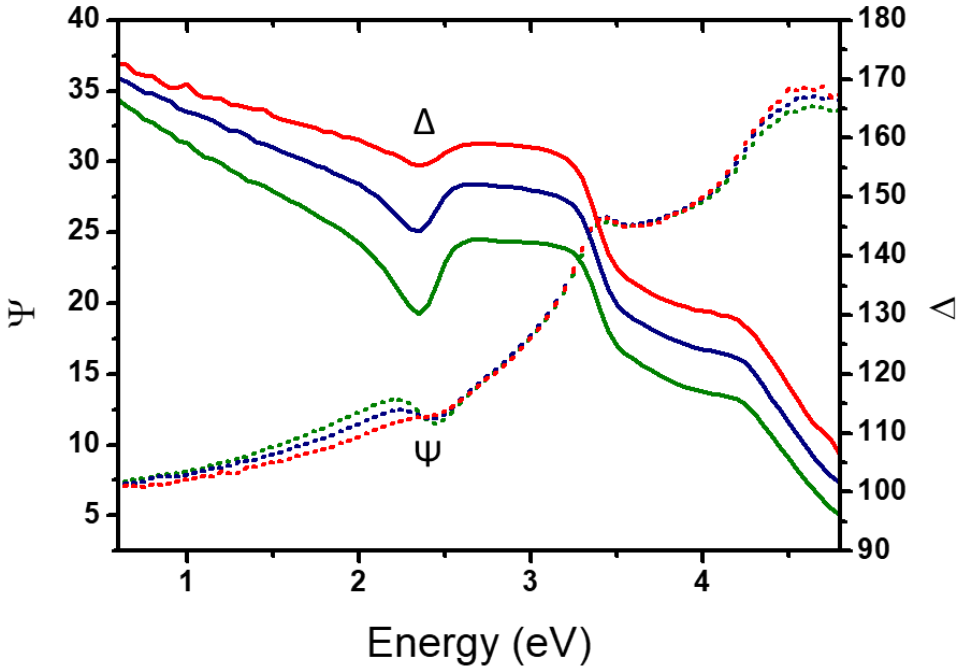

Figure 2.18: *Evolution of the measured ellipsometric angles, Ψ (full lines) and Δ (dotted lines), as a function of the photon energy for an angle of incidence of θ = 70° for three different immersion times 1 h (red), 48 h (blue) and 120 h (green).*

Extracting, from the ellipsometric data, the optical index $\tilde{n} = n + ik$ or the permittivity $\varepsilon = \varepsilon_r + i\varepsilon_i$ of a thin film of material deposited on a substrate requires, on the one hand, a multilayer ellipsometric model representing the sample+substrate system, whereby indices and thicknesses of most layers are known and, on the other hand, an appropriate optical model of the film which can be challenging for nanostructured and anisotropic materials, including some degree of disorder, such as the ones studied here. The studied films are represented by a multilayer ellipsometric model comprising a silicon semi-infinite substrate, a first layer of SiO_2 of thickness 2 nm and the unknown (sample) film of thickness *t*. In a first approximation, nanocomposite materials can be represented with a simple effective medium law, which relates the effective permittivity of the composite medium to the permittivity of the constituent materials, irrespective of the precise structure of the composite provided that the characteristic dimensions are smaller than the wavelength of the incident light. The simplest effective medium law is the Maxwell Garnett formula[27], which is well adapted for dilute spherical inclusions in a matrix and is given by:

$$\frac{\varepsilon_{eff}-\varepsilon_m}{\varepsilon_{eff}+2\varepsilon_m} = f\frac{\varepsilon_{Au}-\varepsilon_m}{\varepsilon_{Au}+2\varepsilon_m} \quad (2.2)$$

where ε_{eff} is the effective permittivity of the gold NP-air composite, ε_m is the matrix permittivity, here for air $\varepsilon = 1$, ε_{Au} is the NP gold permittivity, and *f* is the gold volume fraction in the film.

Equation 2.2 was applied to the set of measured I_s and I_c values over all measured angles of incidence for each sample at different immersion times (1, 48 and 120 h), using for the gold permittivity a function modified from the Johnson and Christy tabulated data[28,29]. The plots of the experimental results, for the incident angle 70°, and the corresponding fits are presented on **Fig. 2.19A-C**.

Two fitting parameters are used: the gold volume fraction *f* (involved in **Equation 2.2**), and the thickness *t* of the film (involved in the ellipsometric model). Fitting is satisfactory for the spectra in the cases of short immersion times (**Fig. 2.19A**) when the produced NPs are spherical. On the opposite, when the NPs are elongated (**Fig. 2.19B-C**) the quality of the fits decreases, particularly in the spectral region of the LSPR of the gold NPs (≈ 2.4eV). In order to obtain better-quality fits, we used a modified Maxwell Garnett formula dedicated to disordered ellipsoids[30,31] defined as:

$$(1-f)\frac{\varepsilon_{eff}-\varepsilon_m}{\varepsilon_{Au}-\varepsilon_{eff}} = \frac{f}{3}\left[\frac{\varepsilon_m}{\varepsilon_m+L[\varepsilon_{Au}-\varepsilon_m]} + \frac{2\varepsilon_m}{\varepsilon_m+\left(\frac{1-L}{2}\right)[\varepsilon_{Au}-\varepsilon_m]}\right] \quad (2.3)$$

This function applies to an assembly of ellipsoids of revolution (or spheroids) of dimensions $a = c \neq b$, with a, b and c the three principal semi-axes of the ellipsoids and L the depolarization factor given by:

$$L = \frac{a^2 b}{3}\int_0^{\infty} \frac{dr}{(b^2+r)^{\frac{3}{2}}(a^2+r)} \quad (2.4)$$

L is related to the aspect ratio, b/a, of the ellipsoids, and values for L with $0 \leq L \leq 1/3$ (prolate ellipsoids), $L = 1/3$ (sphere) and $1/3 \leq L \leq 1$ (oblate ellipsoids) are possible.

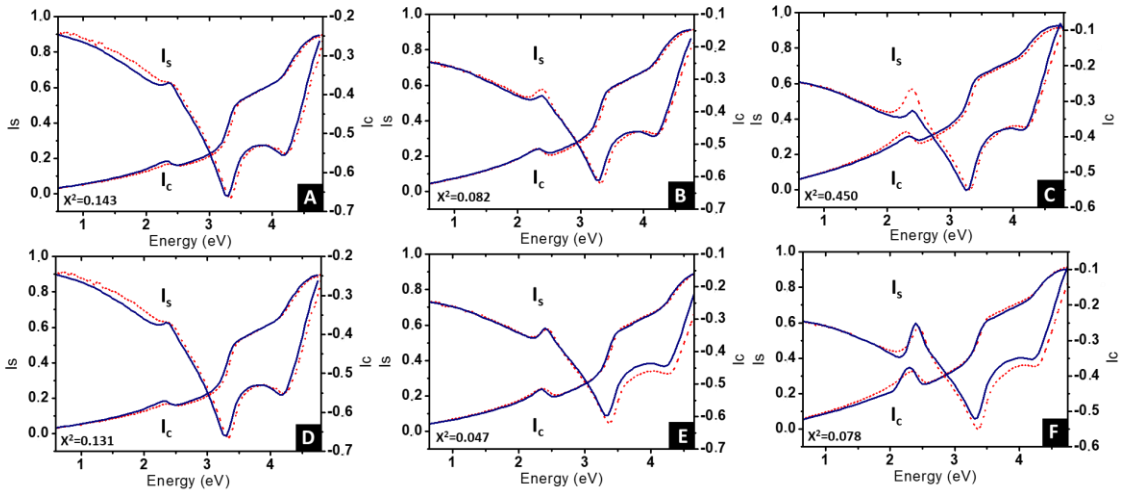

Figure 2.19: *Plots of the experimental ellipsometric quantities, I_s and I_c (red dotted curves) and the corresponding fitting (blue continuo lines) using (A, B, C) spherical Maxwell Garnett formula and (D, E, F) non-spherical Maxwell Garnet formula for three different immersion times: (A, D) 1 h, (B, E) 48 h and (C, F) 120 h. In each graph is given the value of the χ^2 parameter, indicative of the goodness of the fits.*

Using this effective medium law, three parameters were fitted, the gold volume fraction f, the depolarization factor L, and the film thickness t. **Equation 2.3** was applied to the set of measured I_s and I_c values over all measured angles of incidence for each sample at different immersion times (1, 48 and 120 h). The plots of the experimental results, for the incident angle 70°, and the corresponding fittings are presented on **Fig. 2.19D-F**. The fit quality is dramatically improved, especially around the LSPR of the gold NPs. The resulting structural

fitting parameters are presented in **Table 2.6**, in which is also reported the height of the gold NPs measured on the profiles of the AFM topographic images. Both extracted values are in very good agreement, which underlines the robustness of the treatment. The values of *L* extracted from the ellipsometry data fits, for samples with immersion times 48 and 120 hours, are smaller than 1/3 and therefore indicate prolate ellipsoids, as expected from the elongated shapes visible on the SEM images. We can then extract the corresponding aspect ratio, *b*/*a*, using the equation:

$$L = \frac{1-e^2}{e^2}\left[-1 + \frac{1}{2e} ln\left(\frac{1+e}{1-e}\right)\right] \quad (2.5)$$

with $e = \sqrt{1 - \frac{a^2}{b^2}}$ the eccentricity of the ellipsoids.

Fig. 2.17 presents the aspect ratio obtained by analyzing the SEM images of the Au structures obtained. All parameters are listed in **Table 2.6**. The good agreement of the ellipsoidal Maxwell Garnett model, applying to non-interacting NPs, with both the ellipsometric data and the structural analysis indicates that plasmonic couplings are not significant in the optical response of the nanostructured film.

Immersion time	t_{MG} (nm)	t_{AFM} (nm)	f_{MG} (%)	L_{MG}	b/a_{MG}	b/a_{SEM}
1 hour	8	8.5	5.1	0.3	1	1.1
48 hours	9.3	9.7	10.3	0.23	1.5	1.4
120 hours	10.1	10.4	15.7	0.18	1.9	2

Table 2.6: *Sample structural parameters with t_{MG} the film thickness extracted from the fit of the ellipsometry data to the modified Maxwell Garnett formula, t_{AFM} the film thickness obtained from the AFM topographical profiles. f_{MG} the gold volume fraction and L_{MG} the depolarization factor are both extracted from the fit of the ellipsometry data to the modified Maxwell Garnett formula (**Equation 2.3**). From L_{MG}, we can extract an aspect ratio, b/a_{MG}, and compare it to the mean aspect ratio b/a_{SEM} given by statistical analysis of the SEM images.*

Once the parameters *f* and *L* have been determined, the Maxwell Garnett formula (**Equation 2.3**) gives access to the optical index of the composite film. **Fig. 2.20** shows the

values of *n* and *k*, as a function of the photon energy, for the samples with immersion times 1, 48 and 120 h. The precise control on the shape, structure and volume fraction obtained with the fabrication process along with the effect of the localized surface plasmon allows modulating the optical response, while keeping a low gold content and little plasmonic coupling effects.

All films present a resonant behavior, but the amplitude of this resonance greatly increases with immersion time, and its spectral position shifts to lower energy; the shift goes from wavelength of 506 to 576 nm. These evolutions are related to the controlled increment in the gold volume fraction and the increased aspect ratio of the elongated produced NPs. High-refractive index surfaces (n = 3.2) with relatively low extinction coefficient (1.4) are obtained at the maximum time of immersion (120 h). It is useful to note that an application of the simple spherical Maxwell Garnett model with similar gold volume fraction values would provide significantly lower values of *n* (n_{max}= 1.4 vs 1.8 for 10.3 vol.% and n_{max}= 1.6 vs 3.2 for 15.7 vol.%). It is noteworthy that the nanoplasmonic gold decorated surfaces with the highest *n* values reported in the literature[32] (*n* = 5) required a gold content above 40 vol%.

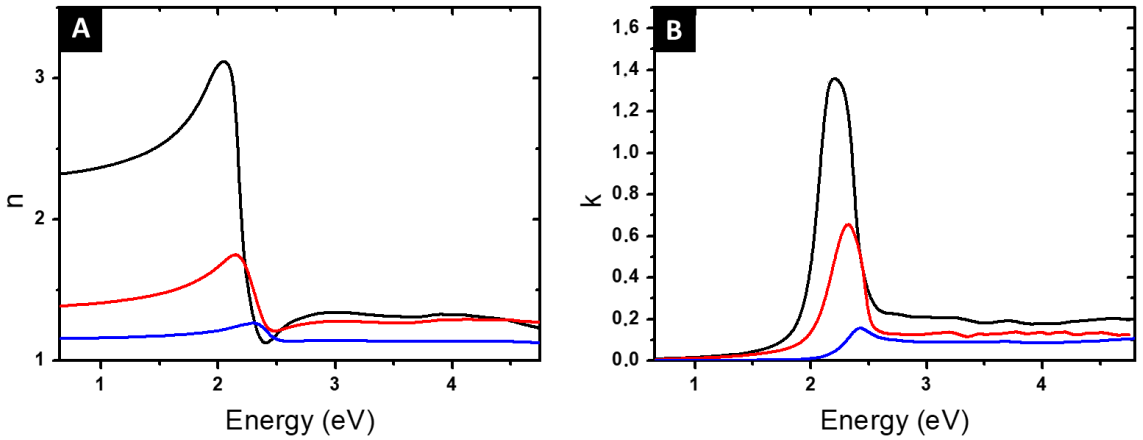

Figure 2.20: *Optical index of the studied films obtained by the modified Maxwell Garnett formula. The blue, red and black curves correspond to the samples obtained from immersion time of 1 h, 48 h and 120 h respectively.*

5. Conclusions

In summary, a straightforward strategy enabling the fabrication of nanostructured plasmonic surfaces with a high refractive index was demonstrated by using BCP thin films as periodic patterned templates. Reproducible spherical and rod-like gold NP arrays over large surface area were produced by varying the surface preparation parameters, which allows to tailor the material refractive index. The effective optical properties of this type of samples were reproduced by the classical Maxwell Garnett model, adapted for non-spherical objects. Finally, high refractive index values were obtained, due to the nanoparticle shape rather than plasmonic couplings.

1. Veselago, V. G. The electrodynamics of substances with simultaneously negative values of epsilon and mu. *Fiz. Nauk* **92,** 517–526 (1968).

2. Smith, D. R., Padilla, W. J., Vier, D. C., Nemat-Nasser, S. C. & Schultz, S. Composite medium with simultaneously negative permeability and permittivity. *Phys. Rev. Lett.* **84,** 4184–4187 (2000).

3. Shalaev, V. M. *et al.* Negative index of refraction in optical metamaterials. *Opt. Lett.* **30,** 3356 (2005).

4. Yao, J. *et al.* Optical negative refraction in bulk metamaterials of nanowires. *Science* **321,** 930 (2008).

5. Wei, X., Shi, H., Dong, X., Lu, Y. & Du, C. A high refractive index metamaterial at visible frequencies formed by stacked cut-wire plasmonic structures. *Appl. Phys. Lett.* **97,** 011904 (2010).

6. Di, Z., Posselt, D., Smilgies, D.-M. & Papadakis, C. M. Structural Rearrangements in a Lamellar Diblock Copolymer Thin Film during Treatment with Saturated Solvent Vapor. *Macromolecules* **43,** 418–427 (2010).

7. Mansky, P. Controlling Polymer-Surface Interactions with Random Copolymer Brushes. *Science* **275,** 1458–1460 (1997).

8. Knoll, A. *et al.* Phase Behavior in Thin Films of Cylinder-Forming Block Copolymers. *Phys. Rev. Lett.* **89,** 035501 (2002).

9. Sinturel, C., Vayer, M., Morris, M. & Hillmyer, M. A. Solvent Vapor Annealing of Block Polymer Thin Films. *Macromolecules* **46,** 5399–5415 (2013).

10. Ghoshal, T. *et al.* Morphological evolution of lamellar forming polystyrene-block-poly(4-vinylpyridine) copolymers under solvent annealing. *Soft Matter* **12,** 5429–5437 (2016).

11. Yang, Q. & Loos, K. Perpendicular Structure Formation of Block Copolymer Thin Films during Thermal Solvent Vapor Annealing: Solvent and Thickness Effects. *Polymers* **9,** 525 (2017).

12. Song, J.-Q., Liu, Y.-X. & Zhang, H.-D. Removal Pathways of Out-of-Plane Defects in Thin Films of Lamellar Forming Block Copolymers. *Macromolecules* **51,** 4201–4212 (2018).

13. Kim, S. O. *et al.* Defect Structure in Thin Films of a Lamellar Block Copolymer Self-Assembled on Neutral Homogeneous and Chemically Nanopatterned Surfaces. *Macromolecules* **39,** 5466–5470 (2006).

14. Maher, M. J. *et al.* Interfacial Design for Block Copolymer Thin Films. *Chem. Mater.* **26,** 1471–1479 (2014).

15. Kim, S. *et al.* Consequences of Surface Neutralization in Diblock Copolymer Thin Films. *ACS Nano* **7,** 9905–9919 (2013).

16. Guo, R. *et al.* Perpendicular orientation of microdomains in PS-b-PMMA thin films on the PS brushed substrates. *Soft Matter* **7,** 6920 (2011).

17. Sauer, B. B. & Dee, G. T. Surface tension and melt cohesive energy density of polymer melts including high melting and high glass transition polymers. *Macromolecules* **35,**

7024–7030 (2002).

18. Keen, I. *et al.* Control of the orientation of symmetric poly(styrene)-block-poly(D,L-lactide) block copolymers using statistical copolymers of dissimilar composition. *Langmuir* **28,** 15876–88 (2012).

19. Spangler, L. L., Torkelson, J. M. & Royal, J. S. Influence of solvent and molecular weight on thickness and surface topography of spin-coated polymer films. *Polym. Eng. Sci.* **30,** 644–653 (1990).

20. Ham, S. *et al.* Microdomain Orientation of PS- *b* -PMMA by Controlled Interfacial Interactions. *Macromolecules* **41,** 6431–6437 (2008).

21. Kim, S.-S. & Sohn, B.-H. Template-assisted self-assembly of diblock copolymer micelles for non-hexagonal arrays of Au nanoparticles. *RSC Adv.* **6,** 41331–41339 (2016).

22. Xiao Cheng, Christian Lewin, Anja Stenbock, Larisa Tsarkova, Jenny Tempeler, Sascha Brose, S. D. Plasma etch resistivity of high molecular weight microphase separated PS-b-PVP block copolymers. in *DSA 2017* (2017).

23. Gu, X. *et al.* High Aspect Ratio Sub-15 nm Silicon Trenches From Block Copolymer Templates. *Adv. Mater.* **24,** 5688–5694 (2012).

24. Babonneau, D. FitGISAXS: Software package for modelling and analysis of GISAXS data using IGOR Pro. *J. Appl. Crystallogr.* **43,** 929–936 (2010).

25. Alexandrov, A. *et al.* UV-initiated growth of gold nanoparticles in PMMA matrix. in *Applied Surface Science* **248,** 181–184 (2005).

26. Abyaneh, M. K., Paramanik, D., Varma, S., Gosavi, S. W. & Kulkarni, S. K. Formation of gold nanoparticles in polymethylmethacrylate by UV irradiation. *J. Phys. D. Appl. Phys.* **40,** 3771–3779 (2007).

27. Garnett, J. C. M. Colours in Metal Glasses and in Metallic Films. *Philos. Trans. R. Soc. A Math. Phys. Eng. Sci.* **203,** 385–420 (1904).

28. Johnson, P. B. & Christy, R. W. Optical constants of the noble metals. *Phys. Rev. B* **6,** 4370–4379 (1972).

29. Vieaud, J. *et al.* Effective medium description of plasmonic couplings in disordered polymer and gold nanoparticle composites. *Thin Solid Films* **603,** 452–464 (2016).

30. Cohen, R. W., Cody, G. D., Coutts, M. D. & Abeles, B. Optical Properties of Granular Silver and Gold Films. *Phys. Rev. B* **8,** 3689–3701 (1973).

31. Heilmann, A. Nanostructure and Optical Properties. in *Polymer Films with Embedded Metal Nanoparticles* 149–197 (Springer, 2003). doi:10.1007/978-3-662-05233-4_6

32. Kim, J. Y. *et al.* Highly tunable refractive index visible-light metasurface from block copolymer self-assembly. *Nat. Commun.* **7,** 12911 (2016).

III

CHAPTER 3 | Controlling the optical response through the macromolecular engineering of cylinder-forming block copolymers

1. Introduction

In **Chapter 2** the control of the packing and the shape of the "meta-atoms" was shown to yield an important effect on the optical properties of the final material. Using nanostructured out-of-plane lamellar block copolymer (BCP) thin films, selectively hybridized with different amounts of gold, allowed us to gain a precise control of their refractive index. Gold nanoparticles (NPs) with different shapes were obtained, ranging from spherical to continuous lines, passing by ellipsoids with different eccentricity.

Nevertheless, the lamellar BCP configuration only offers the possibility to have a control of the structural parameters in one dimension, determined by the periodicity of the BCP (which is related with the molecular weight of the BCP (**Fig. 3.1A**)). In order to go further and have a better control of our assembled structure, we decided to explore cylindrical morphologies. This BCP morphology offers the possibility of a two-dimensional control of the resulting hybridized structure determined by both the molecular weight of the polymer (inter-cylinder distance) and the BCP composition (diameter of the "meta-atoms") as shown in **Fig. 3.1B**.

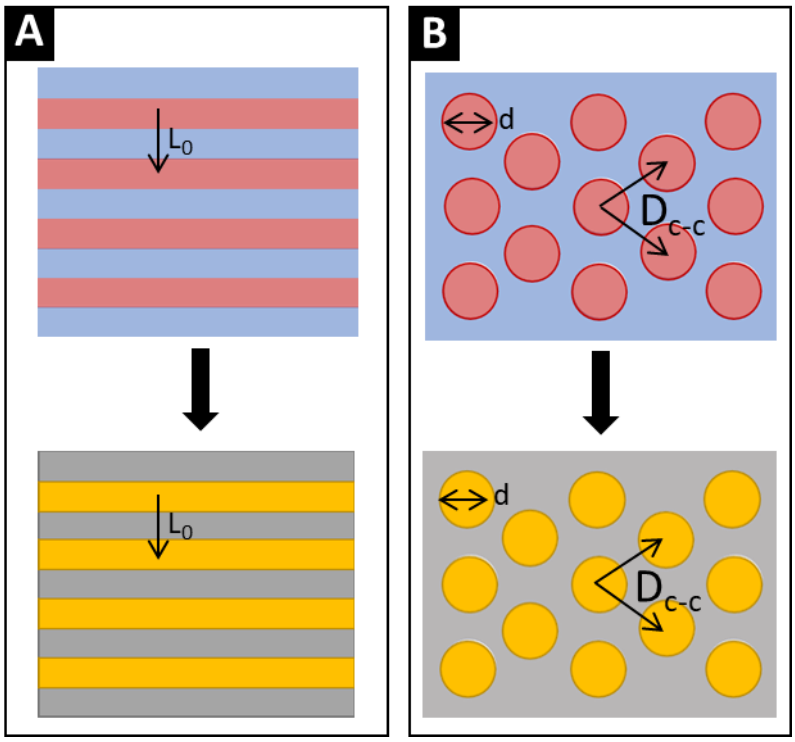

Figure 3.1: *Scheme of (A) BCP out-of-plane lamellar system (top) and the particles obtained after the selective hybridization followed by the reduction process via O_2 RIE plasma (down)*

and (B) BCP cylindrical system (top) and the particles obtained after the selective hybridization followed by the reduction process via O_2 RIE plasma (down).

In this chapter, we propose a straightforward fabrication technique of hexagonal ordered NPs arrays, based on the selective hybridization of an out-of-plane PS-*b*-P2VP (or PS-*b*-P4VP) cylindrical morphology obtained from BCPs of various molecular weights. Several metals or dielectric species are selectively incorporated into the P2VP (or P4VP) domains leading to the production of arrays of meta-atoms with different structural parameters.

First, we will describe the synthesis of the BCPs with different molecular weights *via* sequential anionic polymerization. After that, we will present the preparation and the structural characterization of the nano-composite BCP films to better apprehend the formation of these hybridized structures. Key stages in this process are:

iv. the formation of the nanostructured BCP thin films which has been probed by both imaging (AFM and SEM) and scattering techniques (GISAXS),
v. the selective precursor incorporation into the BCP structure by different techniques depending of the precursor nature (ALD, aqueous metallic salt immersion…),
vi. and, the reduction of the metallic salts into metallic particles.

The resulting decorated surfaces with nanometer periodicities will further be studied as regards to their optical properties, mainly by variable-angle spectroscopic ellipsometry. Such characterization will allow us to determine the structure/properties relationships between the critical geometrical parameters of the metallic arrays (size of the particles, periodicity of the BCP array) and the resulting optical properties extracted from the spectroscopic measurements.

2. Synthesis of BCPs with different molecular weights

The design of macromolecular architectures is one of the most active fields in polymer chemistry[1]. Several synthetic approaches have been developed over the years to control the production of well-defined polymers including BCPs, *i.e.*, reversible addition-fragmentation chain transfer (RAFT)[2], atom transfer radical polymerization (ATRP)[3] or anionic polymerization[4]. All of them show some advantages and drawbacks[1] (for instance, versatility as regards to the available monomers for radical controlled polymerization *versus* unmatched polymerization control for anionic polymerization).

The anionic polymerization technique is a well-established method for the synthesis of well-defined BCPs, as it yields BCPs with controlled molecular weight and low dispersity. It requires high purity reagents and the use of vacuum or controlled atmosphere procedures to prevent chain termination during the polymerization due to the presence of impurities (protic impurities, H_2O or O_2). This technique has been the work-horse of the BCP scientific community for the production of BCPs since clear relationships between the macromolecular parameters and the self-assembly behavior can be readily established.

During this work, several PS-*b*-P4VP and PS-*b*-P2VP BCPs were synthesized by living anionic polymerization, according to the standard procedure reported in the literature[5,6] and presented in **Fig. 3.2**. Sec-butyllithium (Sec-BuLi) was used to initiate the polymerization of the styrene monomers in THF at -78°C. After complete conversion of the styrene monomers (about 30 min), the reactivity of the active species was decreased using 1,1-diphenylethylene (DPE) followed by the subsequent polymerization of the 2VP or 4VP monomers.

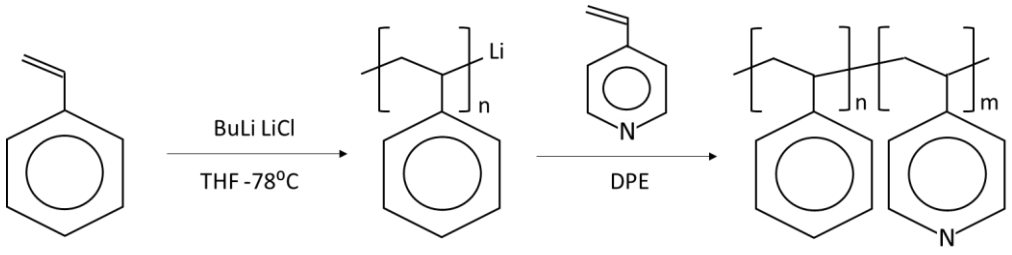

Figure 3.2. *Scheme of the reaction. Polystyrene is obtained in THF at -78°C in the presence of LiCl as additive. Polystyrene living chains were end-capped with a unit of diphenyl ethylene (DPE) before adding 4-vinylpyridine (4VP).*

The typical polymerization procedure was as follows. In a 500 mL flamed dried round flask equipped with magnetic stirrer, tetrahydrofuran (THF, 400mL) was introduced. The solution was cooled to -78°C. Sec-BuLi was charged followed by the addition of styrene. The reaction mixture was stirred for 30 min and the living polystyryl lithium anions were end-capped with 1,1-diphenylethylene. 4-vinylpiyridine monomers were added after 30 min and the reaction mixture was kept stirring for 30 min. Finally, the reaction was terminated by the addition of degassed methanol, concentrated, precipitated in cyclohexane and dried in vacuum oven at 35°C. The different BCPs were characterized by ^{1}H NMR (δ (ppm), 400 MHz, THF), and size exclusion chromatography (SEC) in THF. The elution times were converted to molecular weights using a calibration curve based on low dispersity polystyrene standards. **Table 3.1** lists the macromolecular parameters of the various BCPs: M_n and M_w were extracted from the SEC analysis while the S and P molar fractions were extracted from the NMR analysis. NMR spectra and SEC analysis graphs are provided in the Annex at the end of this thesis.

Sample	M_n (kg/mol)	M_w	M_w/M_n	Fraction S (molar ratio)	Fraction P
PS-b-P4VP-21k	21,0	25,9	1,23	69,9	30,1
PS-b-P2VP-183k	182,7	248,7	1,36	81,9	18,1
PS-b-P4VP-444k	443,9	500,3	1,13	58,3	41,7

Table 3.1: *Macromolecular characteristics of the synthetized PS-b-P4VP BCPs.*

As previously presented, the objective of having different molecular weight BCPs was to control the structural parameters of the BCP arrays, *i.e.*, the center-to-center distance and the diameter of the cylinders. Indeed, after the metallic impregnation, these two parameters are the critical parameters for the definition of the geometry of the decorated surfaces (pattern symmetry, size and inter-object distance).

3. BCP self-assembly

The self-assembly of BCPs with periodicity higher than 100 nm remains challenging because of the difficulties in the synthesis of ultrahigh molecular weight BCPs (> 200 $kg.mol^{-1}$) and the related low chain mobility[7–9]. In the previous section, we described the synthesis of different molecular weight PS-*b*-P4VP BCPs, with molecular weights ranging from 26 to 500 $kg.mol^{-1}$. Different BCPs lead to different strategies in order to obtain well-ordered self-assembled structures. In this section, we will describe the different procedures followed to self-assemble the synthetized BCPs as well as the characterization methodologies used to obtain the structural parameters (AFM and GISAXS).

3.1. Self-assembly of PS-*b*-P4VP-21k

A 0.5 % wt. solution of $PS_{14.7K}$-*b*-$P4VP_{6.3k}$ in PGMEA was spin-coated (30 s, 2000 rpm) onto bare silicon wafers to give a film thickness of 30 nm. The AFM topographical image obtained immediately after the polymer deposition is showed in **Fig. 3.3A**. We can clearly observe regularly organized dots, which we interpret as the top surface of out-of-plane P4VP cylinders surrounded by a PS matrix. The Fast Fourier Transform (FFT) (inset **Fig. 3.3A**) of the AFM image reveals the hexagonal packing of the P4VP cylinders (P6mm symmetry) in accordance with the BCP phase diagram for this particular BCP composition. The Power Spectral Density (PSD) function calculated as the square of the absolute intensity value of the FFT (**Fig. 3.3B**) shows the position of the correlation peak (1.43), from which we can extract a cylinder centre-to-centre distance of 31 nm. The use of a high boiling point solvent during the spin-coating process (PGMEA, 145°C) limits the solvent evaporation from the wet BCP layer, favouring the polymer chains mobility and allowing them to form well-defined self-assembled structures[10].

The out-of-plane orientation can be explained in relation with the solvent affinity and the solvent evaporation rate during the spin-coating process[11,12]. The Hansen solubility parameters (reported in **Table 3.2**) can be used to evaluate these affinities. A solvent is considered a good solvent for a given polymer when the difference between the Hansen solubility parameters of the solvent and the polymer is low. PGMEA is a neutral solvent for the PS-b-P4VP since it presents dispersion component similar to that of PS as well as an important polar component close to that of P4VP. Non-selective solvents promote the out-of-

plane orientation since the balanced interactions of the solvent with the two blocks increase the solvent evaporation rate during the spin-coating. Additionally, the non-selectivity imparts substantial mobility to the copolymer which enhances lateral order[12].

Material	Dispersion ($MPa^{1/2}$)	Polarity ($MPa^{1/2}$)	Hydrogen ($MPa^{1/2}$)
PGMEA	*15.6*	*6.3*	*7.7*
PS	*18.6*	*0.2*	*0.0*
P4VP	*18.5*	*7.8*	*6.2*

Table 3.2: *Hansen solubility parameters ($MPa^{1/2}$) for the materials used in this work.*

In any case, the out-of-plane structure obtained during the evaporation of the solvent is trapped in a non-equilibrium state, and heating the film above the glass transition temperatures of the blocks would lead to films having cylindrical microdomains oriented parallel to the surface[13]. Summing up, the combination of a small molecular weight BCP with high polymer chain mobility and the use of a non-selective solvent result in well-ordered structures exhibiting out-of-plane orientation, even without any subsequent process, *i.e.*, solvent or thermal annealing.

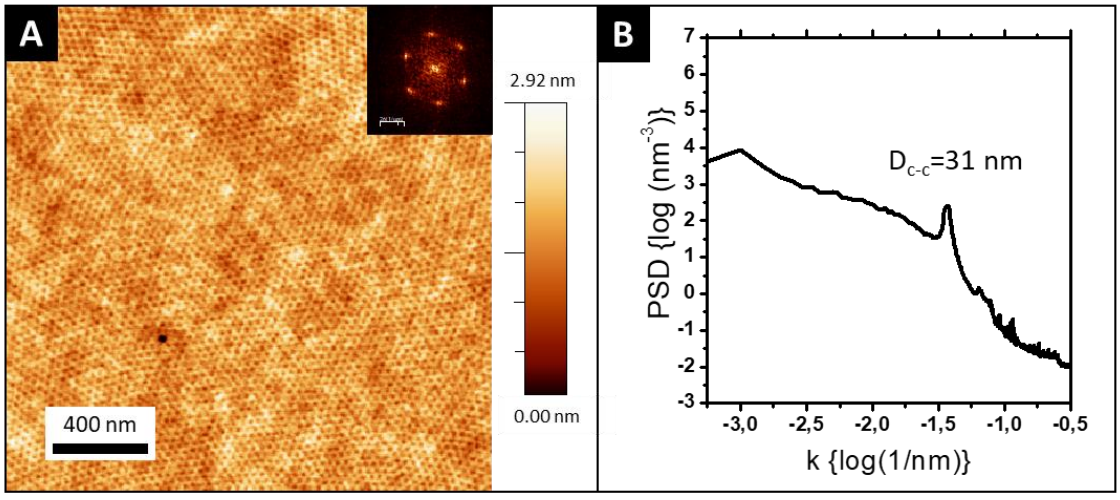

Figure 3.3: *(A) AFM topographical image of the PS-b-P4VP out-of-plane cylinders obtained after casting from a 0.5 wt.% in PGMEA solution (inset correspond to the FFT of the image) and (B) power spectral density function calculated as the square of the absolute intensity value of the FFT.*

GISAXS experiments were carried out to confirm the cylindrical out-of-plane orientation of the BCP structure. While the AFM topographic images present only the top surface of the film, GISAXS probes the in-depth structure. Another important difference is that the GISAXS probes a film surface several orders of magnitude larger than the nanostructure characteristic size since the footprint of the beam at grazing incidence is typically of several mm². A typical scattering pattern (here at incidence angle 0.18°, *i.e.*, between the polymer and substrate critical angles) is shown in **Fig. 3.4A**. It consists in intense Bragg rods along q_z, inherent to the out-of-plane periodic organization of the P4VP cylinders produced during the spin-coating. The GISAXS pattern line-cut along q_y integrated around the Yoneda band (between α_f = 0.20 and α_f = 0.25, see the red lines in **Fig. 3.4A**) is also presented (**Fig. 3.4B**). Polymer periodicity (L_0) and the center-to-center distances ($d_{c\text{-}c}$) between the cylinders can be calculated with respect to the position of the first Bragg peak (q^*) following the **Equations 3.1** and **3.2.**

$$L_0 = \frac{2\pi}{q^*} \tag{3.1}$$

$$d_{c-c} = \frac{4\pi}{\sqrt{3}q^*} \tag{3.2}$$

The position q^* = 0.237 nm^{-1} of the first Bragg peak indicates a period of $L_0 = \frac{2\pi}{q*}$ = 26.5 nm between scattering planes, corresponding to a center-to-center distance of $d_{C\text{-}C}$ = 30.6 nm between cylinders, in accordance with the AFM characterizations. Higher order Bragg rods are observed at $q_y/q_y^* = \sqrt{3}$ indicating the hexagonal ordering of the BCP structure. The low electronic contrast between the BCP domains only yields these two reflections.

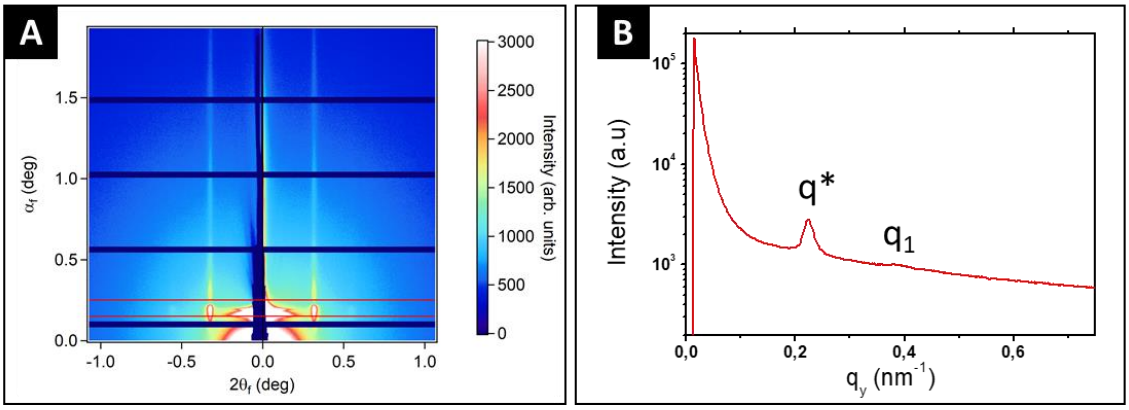

Figure 3.4: *(A) GISAXS pattern and (B) GISAXS pattern line-cut along q_y integrated around the Yoneda band of a $PS_{14.7K}$-b-$P4VP_{6.3k}$ film after spin-coating.*

3.2. Self-assembly of PS-*b*-P2VP-183k

A 2.5 wt.% solution of PS_{150K}-*b*-$P2VP_{32k}$ in PGMEA was spin-coated (30 s, 4000 rpm) onto bare silicon wafers to give a thickness of 80 nm. The AFM topographical image obtained immediately after the polymer deposition is showed in **Fig. 3.5A**. As the molecular weight of this particular BCP is higher, the self-assembled structure after spin-coating is ill-defined due to a lower chain mobility, thus inhibiting a fast microphase separation process. Therefore, a subsequent solvent vapour annealing (SVA) process was necessary to improve the BCP ordering. A scheme of the setup used for the SVA process is shown in the inset of **Fig. 3.5A**. It consists in a closed container, in which is kept the sample and a small vessel containing the solvent. In this case, the chosen solvent was THF, a good solvent for both blocks, as already discussed in **Chapter 2**. The solvent starts to evaporate due to its low boiling point and the partial solvent vapour pressure increases inside the container. THF vapours penetrate into the BCP film, leading to a swelling of the film and allowing a reorganization of the BCP chains due to an increased mobility. After a given SVA duration, the BCP film is removed from the container and the associated fast evaporation process quenches the BCP nanostructure. **Fig. 3.5B** shows the results of the SVA process after 16 h of SVA with THF and we can clearly notice a better ordering of the self-assembled structure with larger grains.

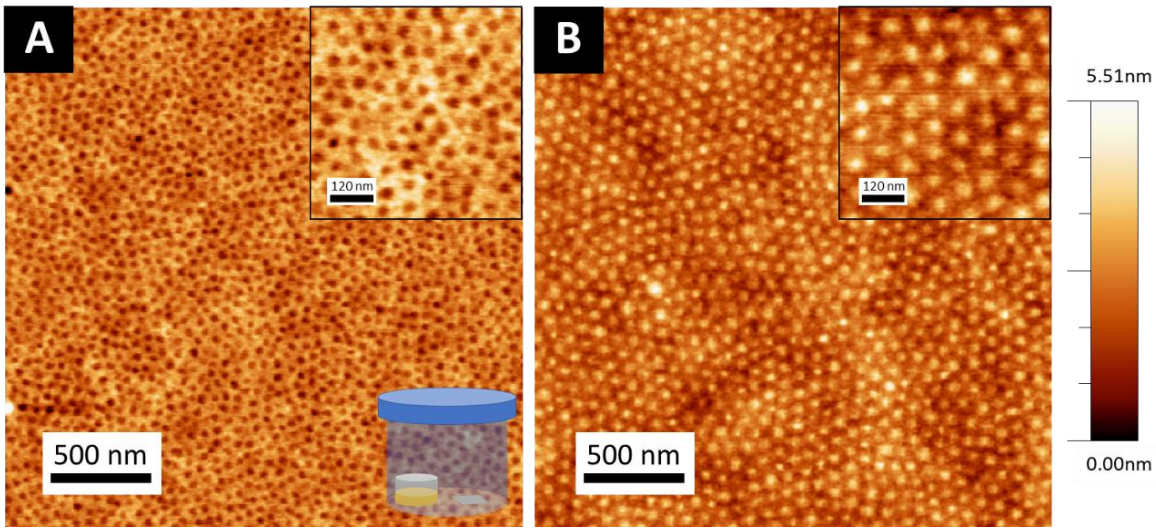

Figure 3.5: *(A) AFM images of PS-b-P2VP film immediately after spin-coating and (B) the same film after 16h under THF solvent vapour annealing.*

GISAXS experiments were performed after different SVA durations to gather more details about the process. The as-cast sample (**Fig 3.6A**) presents a unique large Bragg rod, revealing the out-of-plane orientation of the BCP structure. Nevertheless, as shown in **Fig 3.6E**, no higher order rods were visualized on the GISAXS pattern line-cut along q_y integrated around the Yoneda band (black line **Fig 3.6E**). From this particular line-cut, a periodicity $L_0 = \frac{2\pi}{q*}$ = 57.11 nm with $q*$ =0.110 nm^{-1}, was determined corresponding to a center-to-center distance of $d_{C\text{-}C}$ = 65.95 nm between the cylinders. The lack of higher order reflections hints at the poor quality of the self-assembled structure obtained directly after casting. When the sample is exposed to a SVA, higher order Bragg rods develop, indicating an improved order of the hexagonal BCP structure with $q_y/q_y* = 1, \sqrt{3}$ and $\sqrt{7}$ (see **Fig 3.6C-E)**. Interestingly, an increase of the periodicity of the BCP structure is noticed with annealing time as the value of $q*$ starts to shift to lower q values (**Fig 3.6BCE**). Finally, at the end of the process, the first Bragg rod maximum is positioned at $q*$ =0.091 nm^{-1} (indicating a period of $L_0 = \frac{2\pi}{q*}$ = 69.05 nm between scattering planes, corresponding to a center-to-center distance of $d_{C\text{-}C}$ = 79.7 nm between cylinders in accordance with the AFM characterizations). At the end of the SVA process, higher order Bragg rods at $q_1/q* = \sqrt{3}$ and $\sqrt{7}$ are as well visible (see **Fig. 3.6AE**) and confirm the hexagonal packing.

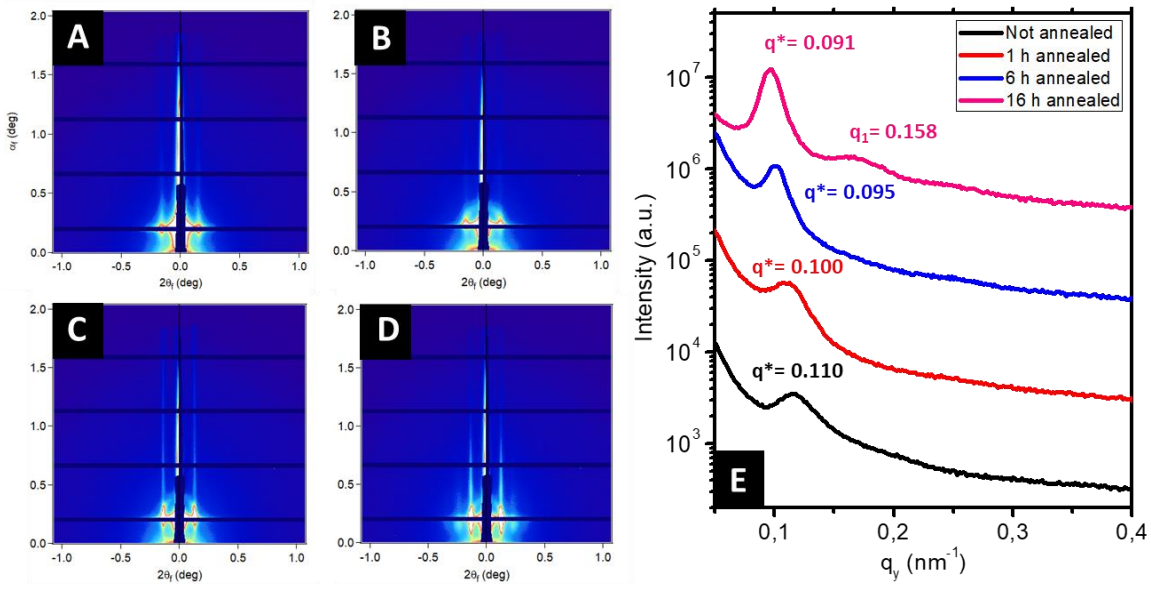

Figure 3.6: *GISAXS patterns of PS-b-P2VP films at different solvent vapour annealing time (A) as-cast, (B) 1h, (C) 6h and (D) 16h. (E) GISAXS pattern line-cut along q_y integrated around the Yoneda band for all the samples.*

The increase in the periodicity of a BCP structure during the SVA or after the quench in ambient air was already reported in the literature[14,15]. Gu *et al.* have realized an in-situ study of the morphological changes occurring on a nanostructured BCP film during SVA by GISAXS[15]. The film thickness gradually increases during the SVA duration due to the swelling of the BCP domains in contact with the solvent vapours. They noticed an increase as well of the BCP periodicity (L_0) during the SVA treatment. At the end of the SVA, the rapid evaporation of the solvent (through the removal of the sample from the solvent atmosphere) leads to a decrease of the BCP film thickness to its original value. Nevertheless, an increase of the BCP period of around 12% was still observed from the as-cast state as regards to the final state of the SVA process. This phenomenon can be understood since the rapid evaporation of the solvent leads to the anisotropic shrinkage of the BCP thin film (important shrinkage in the out-of-plane direction *versus* dimensional stability in the in-plane direction) which does not allow the BCP structure to retrieve its thermodynamic equilibrium periodicity L_0. Besides, due to the thicker films studied in this work and the higher molecular weight of the BCP, some molecules of solvent can also be retained into the film, even after the deswelling process, increasing also the periodicity of the structure.

An indirect proof of the swelling of the BCP film was obtained by analysing the as-cast and after SVA topographical AFM images presented in **Fig. 3.5.** A contrast inversion inherent to the swelling of the P2VP domains (from small depressions (around 2-3 nm) in the as-cast samples (**Fig. 3.5A**) to bumps around 4 nm after 16 h of SVA (**Fig. 3.5B**)) is noticed underlining the presence of solvent in the BCP thin film after the SVA process.

The improvement in the long-range order during the SVA could be also quantified using the full width at half maximum (FWHM) of the first Bragg rod. **Fig. 3.7A** shows the Gaussian fitting obtained of the normalized first Bragg rods for different times of SVA (0 h, 1 h, 6 h and 16 h). The FWHM corresponding to the various SVA duration is presented in **Fig. 3.7A**. The FWHM is related to the grain size (D) (in our case the domain size) following the formula[16]:

$$D = \frac{2\pi K}{FWHM} \tag{3.3}$$

Where K is the Scherrer constant, mostly cited in the literature as having a value of about 0.9, as derived in Scherrer's original paper[17] with

$$K = 2\left(\frac{2\ln(2)}{\pi}\right)^{1/2} = 0.93 \qquad (3.4)$$

Applying **Equation 3.3** to the FHWM values calculated for our samples, we obtain an estimation of the grain size as showed in **Fig. 3.7B.** We can confirm the previous AFM results showing that, with longer SVA duration, larger BCP domains are formed (a decrease of the FWHM). For 16 h SVA, an increase of about 70% in the grain size is consequently noticed as regards to the as-cast state, until reaching almost 400 nm, typically ten times the periodicity of the nanostructure.

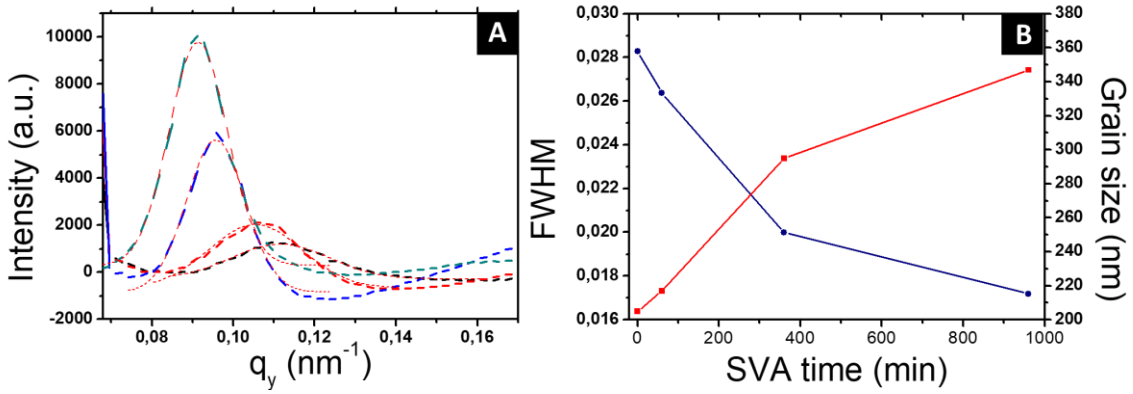

Figure 3.7: *(A) Normalized first brag rod peak of the sample at different SVA times, 0 h (black), 1 h (red), 6 h (blue) and 16 h (green), and the Gaussian fitting of each peak in order to determine the FWHM. (B) FWHM and the grain size values obtained after the Scherrer analysis*[16]*.*

3.3. Self-assembly of PS-b-P2VP-444k

Increasing further the molecular weight of the BCP leads to very low polymer chain mobility. In order to circumvolve this issue, prolonged SVA treatment was used to self-assemble PS_{267k}-b-$P4VP_{177k}$. A 2.5 wt.% BCP solution in toluene was spin-coated (30 s, 4000 rpm) onto bare silicon wafers to give a thickness of 110 nm. SVA treatment was performed in various solvent atmospheres for different durations and conclusive results were obtained for 24 h SVA in THF vapour. The AFM topographical image obtained after a subsequent solvent vapour annealing (SVA) of the sample in THF vapour for 24h is showed in **Fig 3.8A**. Out-of-plane cylinders of P4VP inside of PS matrix are observed. The power spectral density (PSD) of

the Fast Fourier Transform (FFT) of the AFM image gives a centre to centre distance of 110 nm (**Fig 3.8B**).

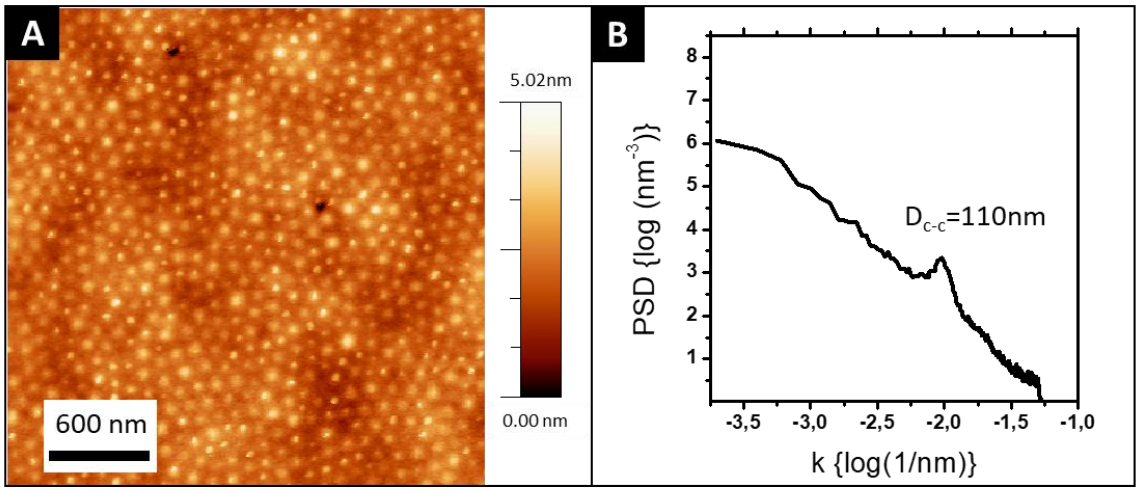

Figure 3.8: *(A) AFM topographical image of the PS-b-P4VP out of plane cylinders obtained after casting from a 2.5 wt.% in toluene solution and after 24 h THF SVA and (B) Power spectral density graph calculated as the square of the absolute value of the FFT.*

4. Selective hybridization

Through this section the different strategies to selectively impregnate BCP domains will be presented. Such methodologies allow obtaining a great variety of both metallic and non-metallic ordered arrays from BCP structures. Since the procedures are independent of the BCP molecular weight, each procedure will be exemplified as regards to a particular case, even if all the techniques and procedures were applied to all the polymers under study.

4.1. Metallic impregnation of nanostructured thin films

In **section 3.1**, we have described the procedure to self-assemble the $PS_{14.7K}$-*b*-$P4VP_{6.3k}$ BCP into well-ordered periodic structure (see **Fig. 3.9A**). In order to produce the desired metallic arrays, the second step of the fabrication process consists in the selective impregnation of the BCP structure. In the case of gold, the selective incorporation into the P2VP domains is insured by the Brønsted base character of the 4VP units forming pyridium salts in the presence of the tetrachloroauric acid ($HAuCl_4$) through the protonation of the pyridine moieties[18]. Thereby, the polymer film was immersed in the metallic salt precursor solution ($HAuCl_4$, 1 wt.% in miliQ H_2O) for a fixed duration (30 min) to facilitate the ionic interaction between the pyridine and the Au(III) ions. The penetration of the gold salts is facilitated by the swelling in water of the P4VP domains and appears to be homogeneous along the whole film thickness. It is noteworthy that the swelling of the P4VP cylinders also induces an increase of the diameter of the cylinders, while keeping the centre-to-centre distance unchanged. This can be clearly observed in the topographical AFM image presented in **Fig. 3.9B**, obtained after a subsequent step of water rinsing. A final step of O_2 RIE (60 W, 60 s, 10 sccm) was performed in order to remove the BCP template and reduce the metallic salts, as already described in the previous chapter. At the end of the process, the decorated surface consists of a hexagonal array of metallic gold NPs deposited on the silicon wafer (see **Fig. 3.9C**), faithfully reproducing the initial BCP pattern.

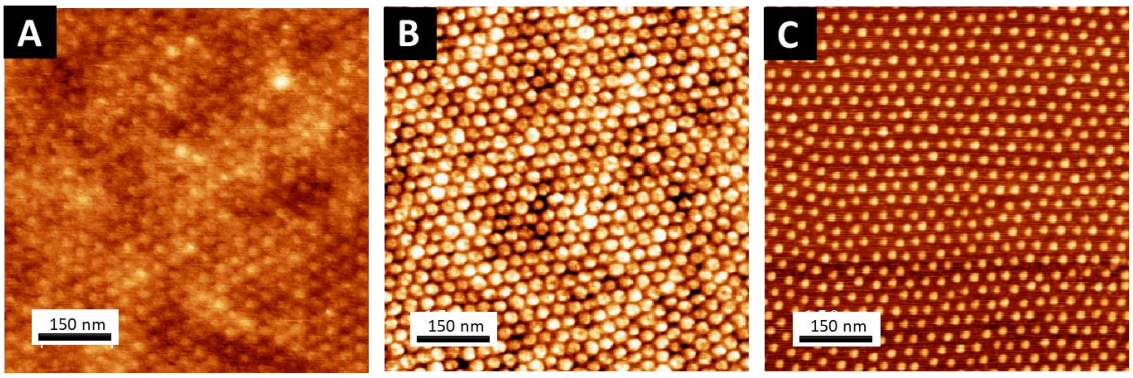

Figure 3.9: *AFM topographical images of (A) pristine PS-b-P4VP film, (B) polymer film after 30 min of immersion in the gold precursor solution and (C) after O_2 RIE reductive process* (60 W, 60 s, *10 sccm).*

Additional insights in the reduction process were obtained using X-ray fluorescence (XRF). XRF consists in the analysis of the emitted fluorescent radiation from a material that has been excited by high-energy X-rays. This emitted radiation is characteristic of each element, thus XRF provides an elementary analysis of the sample[19]. The measurements were carried out on the SIRIUS beamline of the SOLEIL synchrotron, using an energy irradiation of 8 keV and an incidence angle of 0.18°. **Fig. 3.10A** shows the results for the spectral region of interest. The black line represents the results obtained for the pristine polymer film: as expected, no gold or chlorine signals were detected. The signal that appears at 1860 eV corresponds to the Ar filling the sample chamber to minimize the X-ray absorption by ambient air. When the sample was immersed in the gold precursor solution (red line), two new peaks appear, one at 1780 eV assigned to Au and another more intense centred around 1830 eV and corresponding to the chlorine. **Fig. 3.10B** shows a scheme of the interaction between the polymer and the gold salt and allows a better understanding of the XRF spectra. The chloroauric acid first protonates the pyridine function. The tetrachloroaurate ions are then the neutralizing charge associated with the protonated pyridine moieties, leading to the detection of both Au and Cl signals on the XRF spectra. After the O_2 RIE treatment, the signal attributed to the chlorine disappeared, while the gold peak remains, showing the reduction of the gold from Au(III) to Au(0).

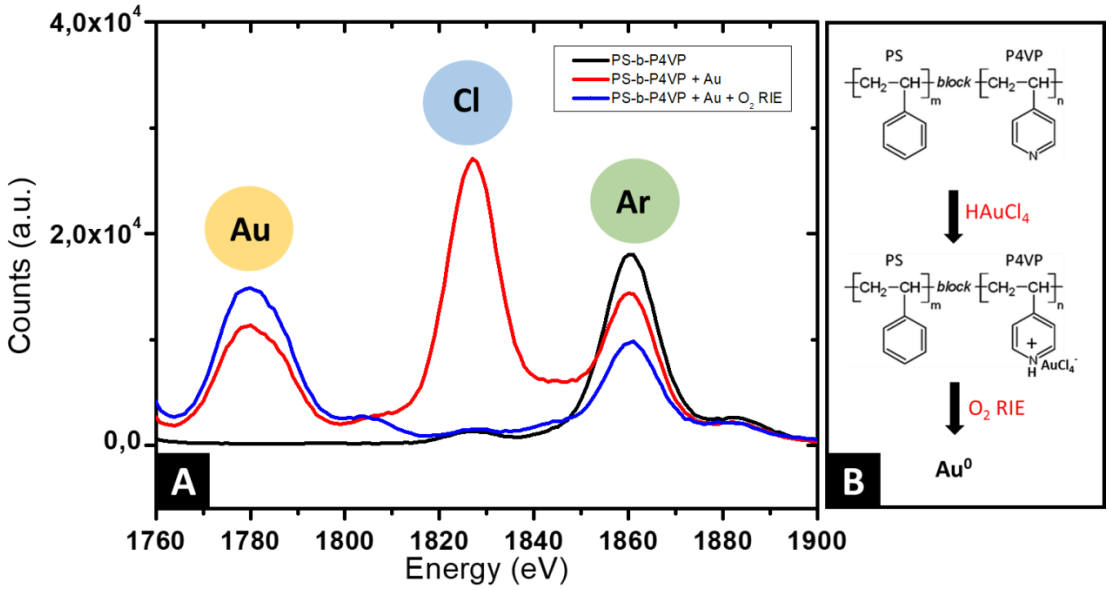

Figure 3.10: *(A) XRF (X-Ray Fluorescence) results of three different samples, PS-b-P4VP pristine film (black), PS-b-P4VP after immersion in the gold precursor solution (red) and after O_2 RIE treatment (blue). (B) scheme of the interaction between the polymer and the metallic salt precursor.*

GISAXS experiments were carried out at each step of the process in order to confirm the stability of the structures created. Three different samples were studied: the pristine BCP film, the BCP film after the selective hybridization with gold salts and the metallic array obtained after the O_2 RIE treatment. Typical scattering patterns (here at an incidence angle of 0.18°) are shown on the **Fig. 3.11A-C**. They all contain intense Bragg rods along q_z, inherent to out-of-plane organization of the BCP domains. The GISAXS pattern line-cut along q_y integrated around the Yoneda band (between α_f = 0.2 and α_f = 0.25, see the red lines in the pattern images) are also presented in the **Fig. 3.11.** They all present a first peak around q^* = 0.23 nm^{-1} and at least one higher order peak at $q/q^* = \sqrt{3}$, confirming the hexagonal packing of the P4VP cylinders (see **Fig. 3.11A**). Following the hybridization of the BCP structure with the Au salts, a strong increase of the scattering intensity is noticed due to the high scattering cross section of Au atoms (see **Fig. 3.11B**), confirming indirectly the selective introduction of the Au salts into the P4VP domains. Inherent to this increase of contrast, both gold containing films present several high order peaks, such as $q/q^* = \sqrt{3}, \sqrt{7}$ for the gold salt loaded BCP film, which

confirms as well the hexagonal packing of the P4VP cylinders and its stability during the process.

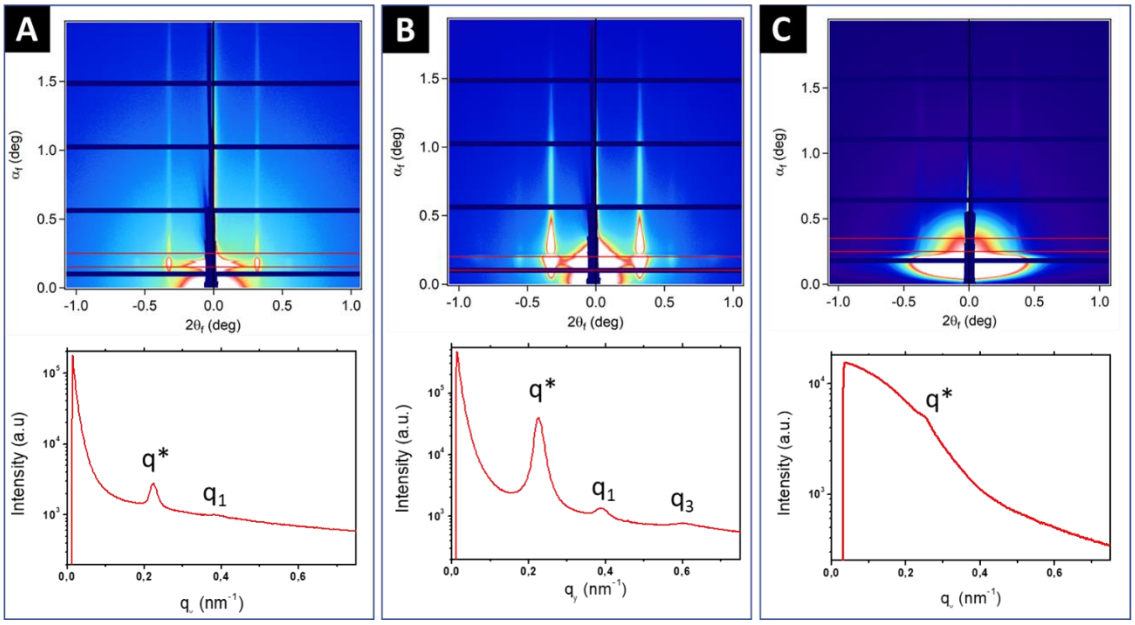

Figure 3.11: *GISAXS patterns (upper panel) and GISAXS pattern line-cut along q_y integrated around the Yoneda band (lower panel) of the BCP film at different steps of the process: (A) BCP template, (B) with the gold salt selectively incorporated into the P4VP domains and (C) after 60 s of O2 RIE.*

4.2. Distribution of the gold salts in the P4VP cylinders during impregnation

X-ray reflectivity (XRR) experiments were also carried out in order to determine the electron density profile along the sample thickness, and to probe the homogeneous distribution of the gold precursor salts along it. XRR constitutes one of the most powerful techniques to characterize thin films with high sensitivity and will be presented with more details in the **Chapter 4**. **Fig. 3.12** shows the XRR reflectivity curves obtained for a pristine polymer film (**Fig. 3.12A**) and after the gold salt impregnation (**Fig 3.12B**). Both of them correspond to a homogeneous film, since highly periodic fringes are obtained as shown in **Fig. 3.12**. The GenX software[20] was used to fit the experimental data and obtain the scattering length density (SLD) profiles of the films. The SLD is a measure of the scattering power of the material, in other words, the more the electron density, the higher the SLD. **Fig. 3.12C** shows the SLD profile obtained after fitting the experimental reflectivity curve corresponding to the pristine polymer. It displays the plot of the electron density as a function of the *z* coordinate

(distance from the substrate). High SLD values are observed at small z due to the silicon substrate but the SLD rapidly decays for higher *z*. A uniform SLD profile consistent with a homogeneous polymer film is observed with a value of 0.31 $Å^{-3}$. At the surface of the film, the SLD decreases to zero with a certain interface thickness, due to roughness and in our case the difference in the height between the two different domains (P2VP cylinders are higher than the PS matrix). In order to compare with the theoretical values expected for a polymer film, the theoretical SLD values were calculated. SLD can be computed from the scattering lengths and material densities as:

$$SLD = \frac{\sum_{i=1}^{N} b_i}{V_m} \tag{3.5}$$

Where we sum the scattering length contributions (b_i) from the *N* atoms, divide by the volume, V_m of this unit cell that can be represented as:

$$V_m = \frac{M}{\rho N_a} \tag{3.6}$$

X-ray scattering length contribution (b_i) can be calculated from the tabulated atomic scattering factors for each atom as:

$$b_i = \frac{e^2}{4\pi\varepsilon_0 m_e c^2} f_1 \tag{3.7}$$

Where f_1 is the real part of the atomic scattering factor (and can be approximated as equal to the atomic number *Z*), *e* is the charge of the electron, ε_0 is the permittivity of free space, m_e is the mass of the electron and *c* is the speed of light. During this section, SLD values will be expressed in $Å^{-3}$, obtained by dividing the SLD value by the Thomson radius (r_e = 2.818x10^{-15} m).

By considering a polymer density of ρ=1.04 g/cm^3 for the BCP, a theoretical SLD value of 0.33 $Å^{-3}$ was predicted for the PS-*b*-P2VP BCP (the calculation can also be done with an online calculator: https://sld-calculator.appspot.com). Therefore, the experimental value is in agreement with the theoretical one, which allows us to confirm the homogeneity of the BCP film.

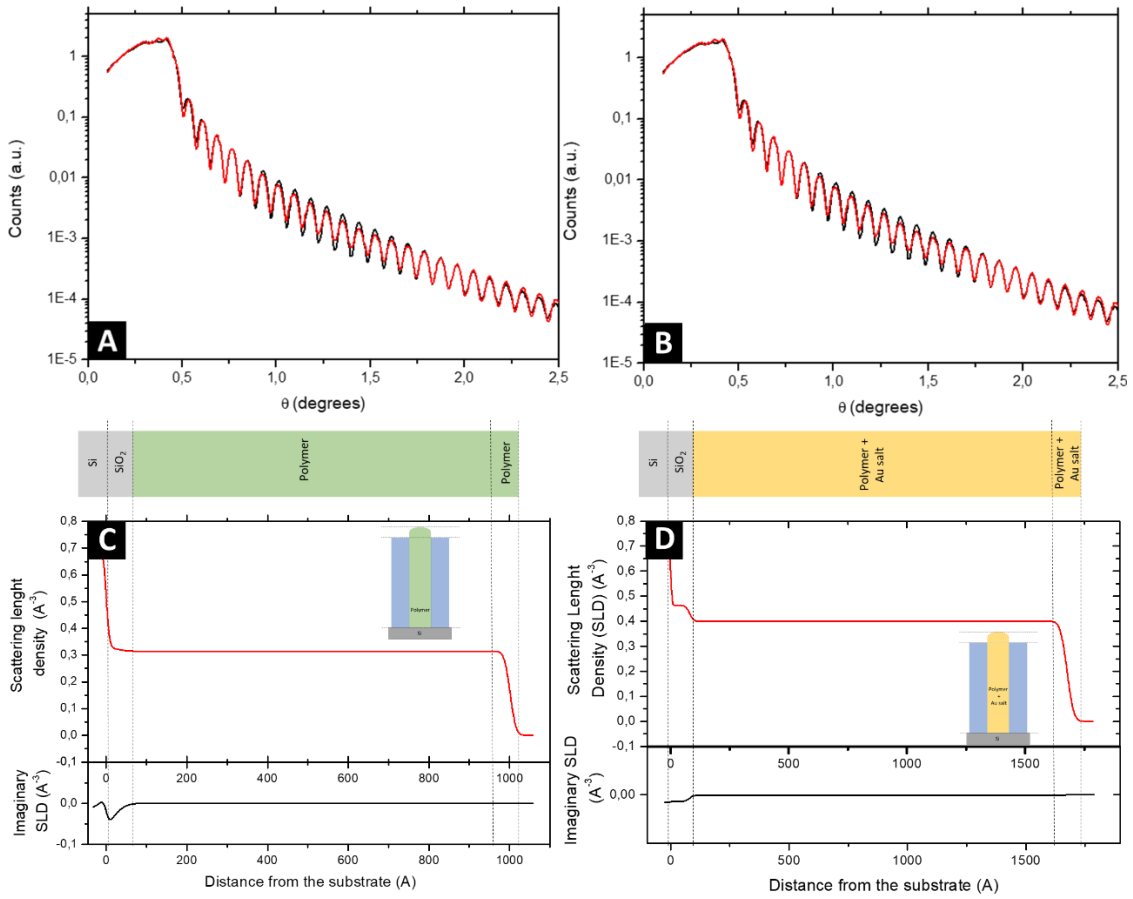

Figure 3.12: *XRR reflectivity data (black line) obtained for (A) PS-b-P2VP pristine film, (B) PS-b-P2VP films impregnated with gold salts. Red lines are the fitting obtained using the GenX software and were used to derive the SLD profiles for both samples (C and D respectively)*

After the immersion in the gold precursor solution, the extraction of the SLD profile from the experimental reflectivity curve also confirms the homogeneity of the gold salt loaded BCP film (**Fig 3.12D**) even if the SLD value increases to 0.41 $Å^{-3}$. Therefore, we can conclude that the gold salts were homogenously distributed along the whole height of the P4VP cylinders. In order to compare and try to extract the gold volume fraction (ϕ_{Au}) in the film, the theoretical values were calculated. Following the **Equation 3.5**, a SLD value of 1.01 $Å^{-3}$ was calculated for $HAuCl_4$. The gold volume fraction was evaluated to 14.28 % from the following expression.

$$SLD_{Composite} = SLD_{polym}\Phi_{polym} + SLD_{Au}\Phi_{Au} \quad (3.8)$$

Where $SLD_{Composite} = 0.41\ Å^{-3}$, $SLD_{polym} = 0.31\ Å^{-3}$, $SLD_{Au} = 1.01\ Å^{-3}$ and $\Phi_{poly} + \Phi_{Au} = 1$.

As was already presented in **Chapter 2**, **Section 3.1**, the gold salt inside the polymer matrix can be partially reduced to Au (I), for that reason the calculated volume fraction presented here could not be completely accurate, lower values can be expected, since the AuCl salt presents higher calculated SLD values (1.81 $Å^{-3}$) than the Au (III) salt (1.01 $Å^{-3}$). Assuming a 30-40% proportion of partially reduced salt, we can estimate a ϕ_{Au} of 10-11%. **Table 3.3** lists all the theoretical SLD values calculated during this section.

Material	Formula	Density ($g.cm^{-3}$)	SLD ($Å^{-2}$)	SLD / r_e ($Å^{-3}$)
Silicon	Si	2.3	$2.0x10^{-5}$ - i $4.6x10^{-7}$	0.71 - i 1.6 $x10^{-2}$
Polymer	$C_{15}H_{15}N$	1.02	9.3 $x10^{-6}$ - i 1.3 $x10^{-8}$	0.33 - i 4.6 $x10^{-4}$
Gold (III)	$HAuCl_4$	3.9	2.8 $x10^{-5}$ - i 2.0 $x10^{-6}$	1.01 - i 0.23
Gold (I)	AuCl	7.6	5.1 $x10^{-5}$ - i 4.6 $x10^{-7}$	1.81 - i 1.64 $x10^{-2}$

Table 3.3: SLD theoretical values for the materials of interest in this study, calculated using https://sld-calculator.appspot.com.

4.3. A versatile strategy: various decorated surfaces using the same templating methodology

One of the great advantages of this approach is its versatility: different metallic salts can be used in order to obtain a wide variety of metallic structures. H_2PtCl_6, for example, can be used as a precursor and, using the same strategy as gold, the process produces metallic Pt arrays (**Fig; 3.13AB**). Other metallic salts such as $AgNO_3$ or H_2PdCl_6 can also be used as precursors to obtain the corresponding metallic arrays (**Fig. 3.13C**). In the case of the silver salts, the procedure is slightly different. The film is immersed into the salt solution ($AgNO_3$ 1 wt.% in H_2O) to obtain the loading of the P4VP cylinders but, as the silver is rapidly oxidised in air, we decided to reduce it without damaging the polymer matrix. For that reason, a chemical route was used to reduce the silver salts by using either an immersion of the film in sodium citrate or citric acid at room temperature[21,22]. Metallic silver was observed by XPS (**Fig. 3.13D**), proving that the polymer matrix acts as a scaffold protecting the silver NPs against the oxidation.

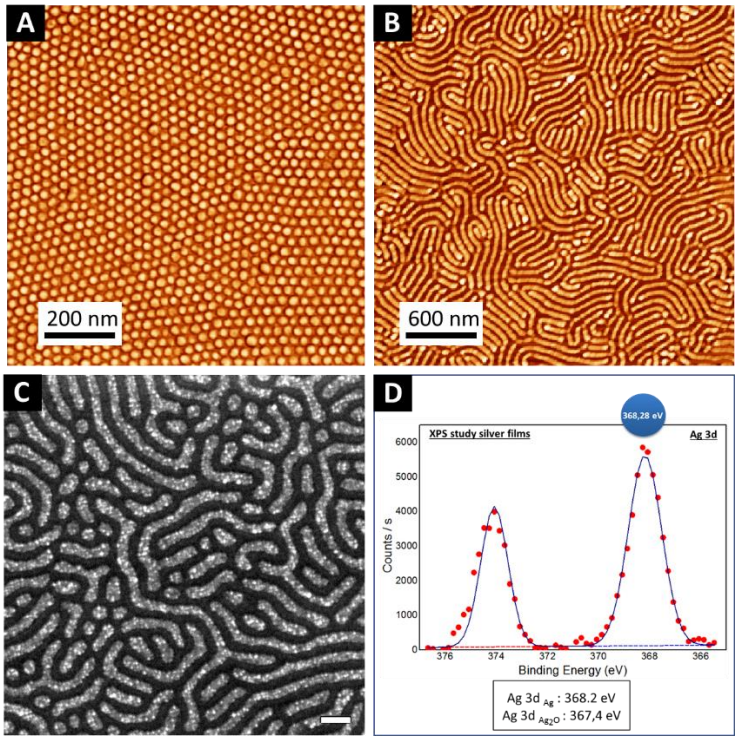

Figure 3.13: *AFM topographical images of different metallic arrays obtained using different BCP as a template. (A) hexagonal ordered arrays using PS-b-P4VP and (B) continuous lines obtained using lamellar PS-b-P2VP. (C) SEM image of Ag metallic NPs synthesis inside the BCP matrix and (D) Ag 3d XPS spectrum of the metallic array.*

Another strategy consists in using the BCP film as a platform to link selectively pre-formed NPs, using specific interactions between the NPs surface and the BCP domains. Non-metallic ordered structures can be obtained as well by using "sequential infiltration synthesis"[23], and, in the following sections, these methodologies will be presented in greater details.

4.3.1. Hybridization with pre-formed gold NPs

Gold NPs were synthetized by standard Turkevich method[24], consisting in a reduction of gold(III) chloride salt by citrate acid or sodium citrate in water at 80°C, and producing a colloidal suspension of citrated capped spherical gold NPs of 20 nm diameter. A PS-*b*-P2VP thin film was subsequently immersed into the colloidal suspension for 5 hours, then rinsed with water and dried under N_2 flow. The AFM topographical view presented in **Fig. 3.14A** shows that the gold NPs are preferentially deposited onto the P2VP domains. Indeed P2VP

and P4VP have been widely used as surface modifiers for the immobilization of NPs on the surface of different substrates because of the strong affinity of the pyridyl group with metals[25,26]. In this particular case, since the P2VP cylinders have a diameter around 35 nm, only a unique gold NP can bind to the cylindrical domain. Thus, the BCP thin film allow for a spatial ordering of the gold NPs into a hexagonal packing directed by the nanostructured PS-*b*-P2VP thin film. This, was clearly observed on the AFM topographical view presented in **Fig. 3.14A**. The topographical profiles, extracted from the AFM images, of the BCP films before and after immersion in the colloidal gold solution are also provided in **Fig. 3.14B**. A small protuberance, around 2 nm, due to the P2VP cylinders is clearly detected on the pristine BCP film before immersion. After the selective binding of the gold NPs onto the P2VP domains, the height of the protuberances increases to 20 nm, demonstrating the selective binding between the gold NPs and the P2VP cylinders.

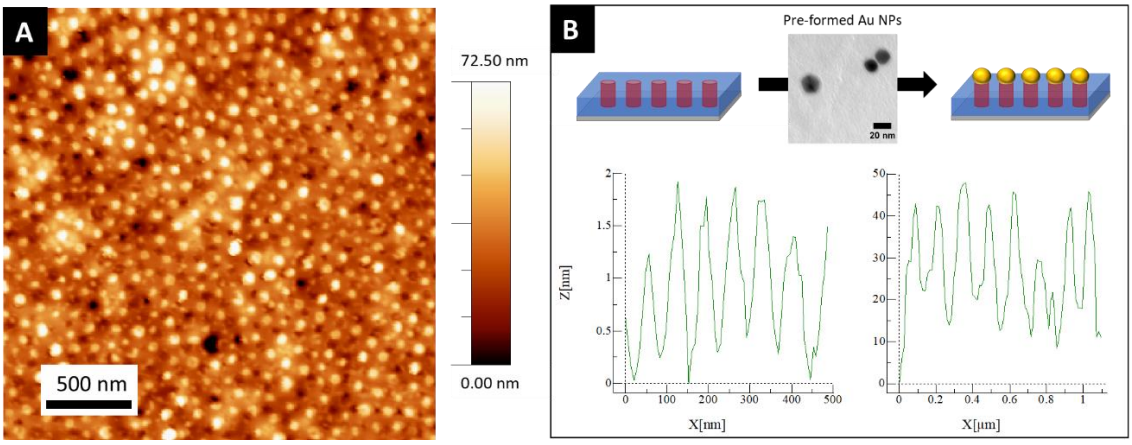

Figure 3.14: *(A) AFM topographical image of the PS-b-P2VP film after immersion in the Au NPs colloidal suspension. (B) Scheme of the process and topographical profiles obtained from the AFM topographical images of pristine polymer (left) and the polymer film with the NPs (right).*

GISAXS experiments were performed to follow the binding of the gold NPs onto the P2VP domains. **Fig. 3.15** shows the 2D GISAXS patterns and the line-cut along q_y integrated around the Yoneda band obtained for the pristine polymer (**A** and **C**) and after the immersion in the gold nanoparticle colloidal solution (**B** and **D**), respectively. For the pristine BCP thin film, an out-of-plane hexagonal structure was observed as previously discussed (see **Section 3.2** of this Chapter). In the case of the sample immersed into the colloidal suspension, the presence of gold NPs on top of the BCP thin film is confirmed by the appearance of a halo, due

to the form factor of the spherical particles. In order to extract the form factor of the particles, the line cut was fitted using FitGISAXS software[27]. The best fit presented in **Fig. 3.15D**, corresponds to spherical objects with a diameter, D = 19.7 nm, which is in agreement with the AFM measurements.

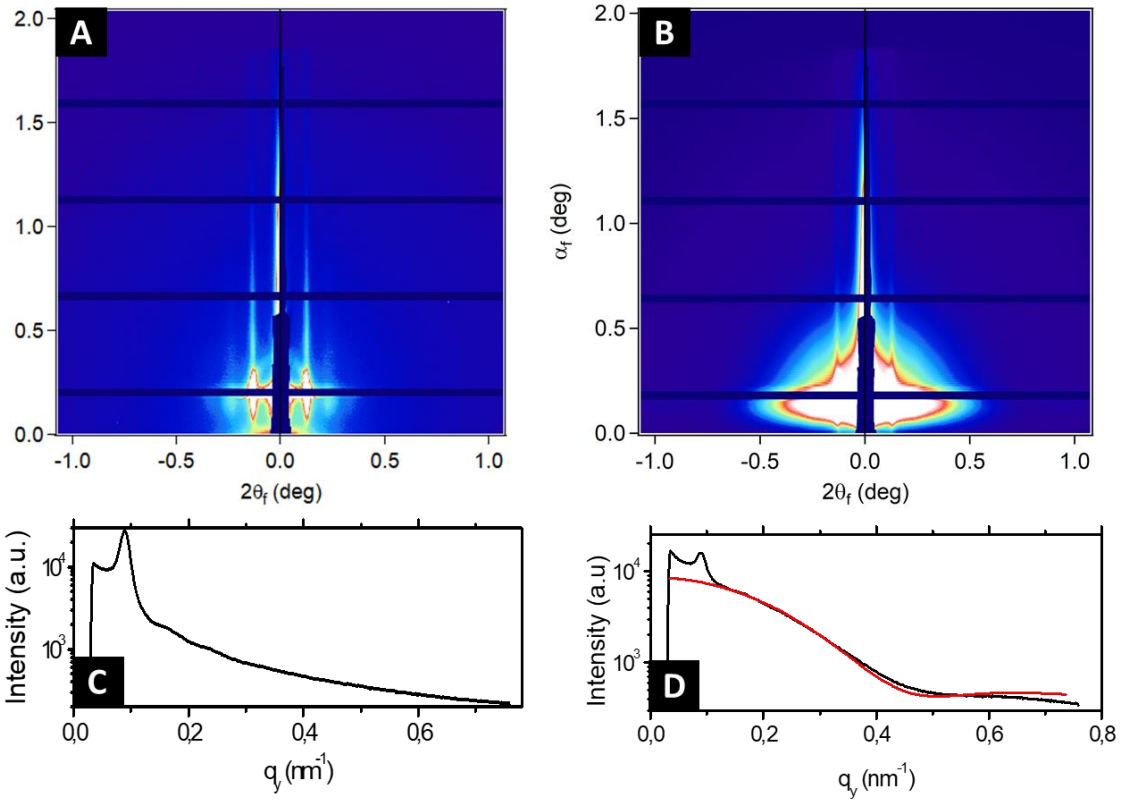

Figure 3.15: *GISAXS patterns of PS-b-P2VP pristine films (A) and hybridized with the Au NPs (B) and their corresponding GISAXS pattern line-cut along q_y integrated around the Yoneda band (C and D). The red line in D represents the curve obtained for spherical objects of 20 nm diameter.*

Once the form factor of the particles is determined, we can obtain the structure factor of the created metallic array. For that, and since the halo due to the form factor scattering of the spherical particles was very intense, we divided the experimental data by the fit data obtained for the spherical particles. **Fig 3.16B** shows the results of this operation, and higher order Bragg peaks appear. Their position at $q/q^* \approx \sqrt{3}, 2$ confirms the hexagonal order of the NPs, and their selective link onto the P2VP cylinders.

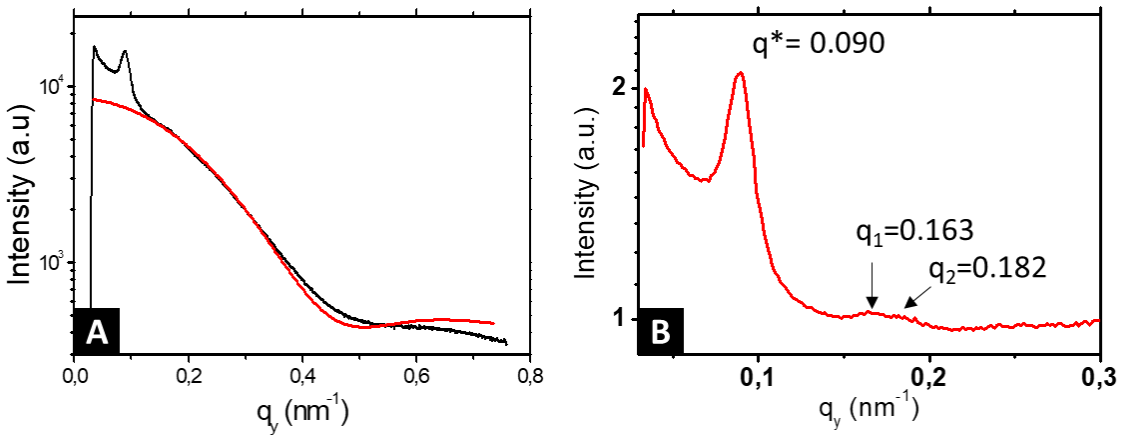

Figure 3.16: *(A) GISAXS q_y line-cut of PS-b-P2VP pristine films and hybridized with the Au NPs (black curve) and the corresponding fitting obtained for spherical objects of 20 nm diameter (red curve). (B) GISAXS pattern line-cut along q_y integrated around the Yoneda band obtained after the division of the curves presented in (A).*

4.3.2. Hybridization of BCP domains using atomic layer deposition

4.3.2.1. Formation of Alumina arrays from nanostructured BCP films

The procedure of exposing nanostructured BCP films to different ALD precursors in vapour phase has several terminologies in literature, but all of them are describing effectively the same process. ‘‘Multiple Pulsed Infiltration’’ (MPI)[28,29] ‘‘Sequential Infiltration Synthesis’’ (SIS)[30,31] or ‘‘Sequential Vapour Infiltration’’ (SVI)[32,33] are based on the ALD technique, relying on the alternating pulsing of precursor and reactant gases, separated by purge steps, resulting in self-limiting surface reactions. Using this approach, different dielectric materials, *i.e.*, Al_2O_3, TiO_2 or SiO_2, can be grown inside BCP domains. A first pulse of the reactive species impregnates selectively a BCP domain. This first pulse is followed by a second oxidative one in order to form the oxide materials. During this section, we will expose the procedures and the results obtained in the objective to create Al_2O_3 NPs arrays using BCPs as template.

A typical procedure is described thereafter. A first pulse of trimethylaluminum (TMA) vapour (0.015 s) is introduced in the vacuum chamber containing the nanostructured BCP sample. TMA selectively “reacts” with carbonyl groups, C=O (PLA or PMMA) and pyridine groups (P2VP or P4VP)[34,35]. The infiltration of the TMA vapours into the P2VP cylinders is promoted by an increase of the pressure in the chamber. After a purge step to remove the

unreacted precursor (2.5 min), a second pulse of H_2O (0.015 s) takes place leading to the formation of Al_2O_3 through the reaction of H_2O with TMA. After a defined number of alternating precursor/oxidant pulses, Al_2O_3 structures templated by the P2VP domains are obtained. **Fig. 3.17A** shows the AFM topographical image of the pristine PS-*b*-P2VP BCP polymer film. After the subsequent infiltration process in the ALD chamber, Al_2O_3 is selectively grown into the P2VP domains (see **Fig. 3.17B**). Finally, the sample is exposed to a UV/O_3 treatment to remove the polymer and only maintain the inorganic part as small dots of Al_2O_3 are clearly observable after this process (see **Fig. 3.17C**).

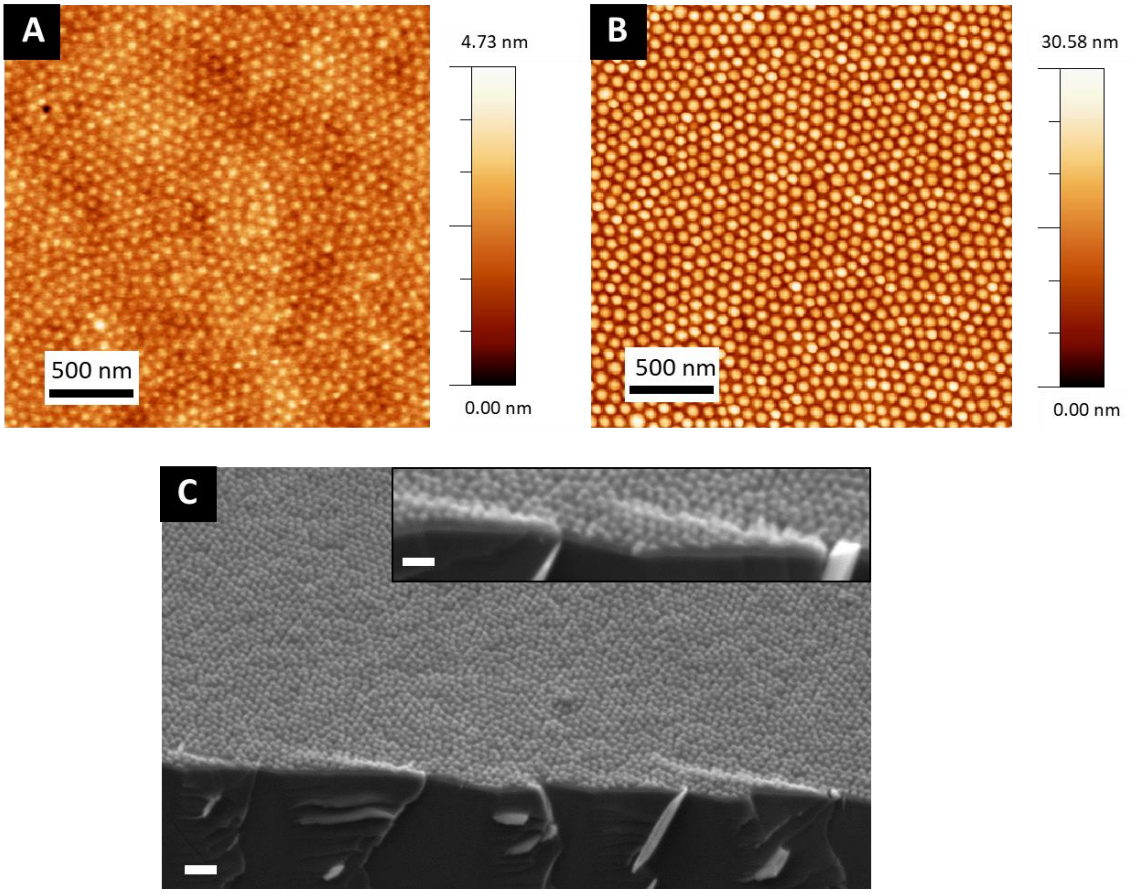

Figure 3.17: *(A) and (B) AFM topographical images of PS-b-P2VP pristine film and after the incorporation of the Al_2O_3, respectively. (C) 45° tilted SEM image of the Al_2O_3 features obtained after removal of the polymer by a UV/O_3 treatment.*

The associated GISAXS pattern presented in **Fig. 3.18A** shows that the out-of-plane orientation of the polymer template is maintained after the infiltration process. Thereby, intense Bragg rods are observed with a first Bragg rod position established at q^* = 0.085 nm^{-1}

(centre-to-centre distance $d_{c\text{-}c}$ = 85 nm) and higher order Bragg rods at q/q^* = √3, 2 and √7 are clearly visible confirming the hexagonal packing of the hybrid structure (**Fig. 3.18B**).

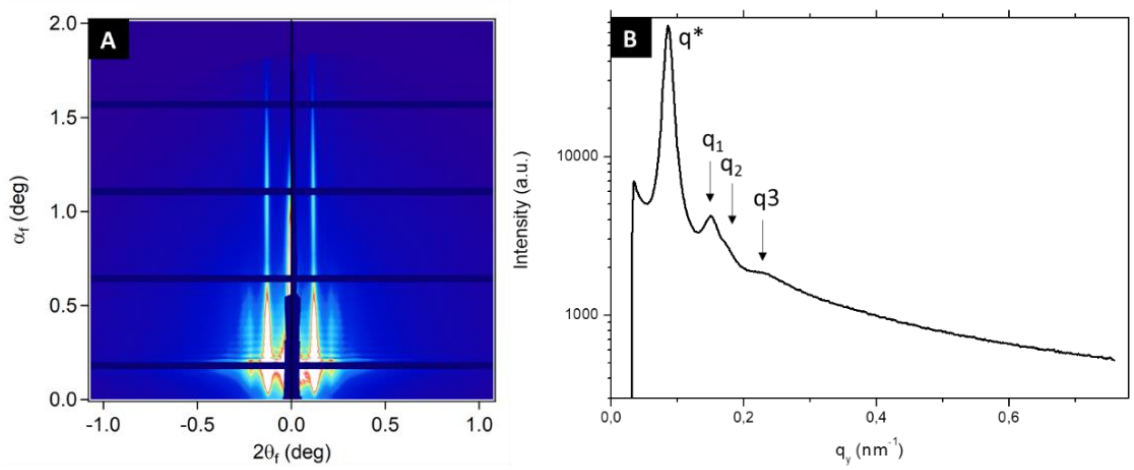

Figure 3.18: GISAXS patterns of PS-b-P2VP films after Al_2O_3 infiltration (A) and its GISAXS pattern line-cut along q_y integrated around the Yoneda band (B)

To gain further insights on the shape of the Al_2O_3 dots produced following this protocol, XRR measurements were carried on and the results will be presented in **Chapter 4**, **Section 3.2.2.3**.

4.3.2.2. Formation of titania (TiO_2) arrays from nanostructured BCP films

In the case of TiO_2, a first pulse of tetrakis(dimethylamino) titanium (TDMAT) vapor (0.015 s) is introduced in the vacuum chamber in which was previously introduced the BCP sample. TDMAT reacts selectively with the P4VP domains and the infiltration into the P4VP cylinders is promoted by an increase in the pressure in the chamber. After a purge vacuum step in order to remove the precursor that did not interact with the P4VP domains, a second pulse takes place, (H_2O 0.015 s) and the molecules of water react with the TDMAT to form TiO_2. After a series of alternating precursor/oxidant pulses, TiO_2 structures were obtained **(Fig. 3.19F**).

4.4. Different sizes, different metals, a large library of decorated surfaces

All the different strategies that were presented in this chapter were applied to all the synthetized polymers, giving rise to a great variety of different structures as shown in **Fig. 3.19**. Our objective to control the different center-to-center distances and the size of the meta-

atoms was, therefore, fulfilled. The next step is to determine how this structural control affects the optical properties of these decorated surfaces. This will be analyzed and presented in the next section.

Besides, this structural control and the versatility in the materials that can be produced will allow us to create more complex structures using a multilayered strategy[36], not accessible by conventional BCP self-assembly. This will be the topic of **Chapter 4**.

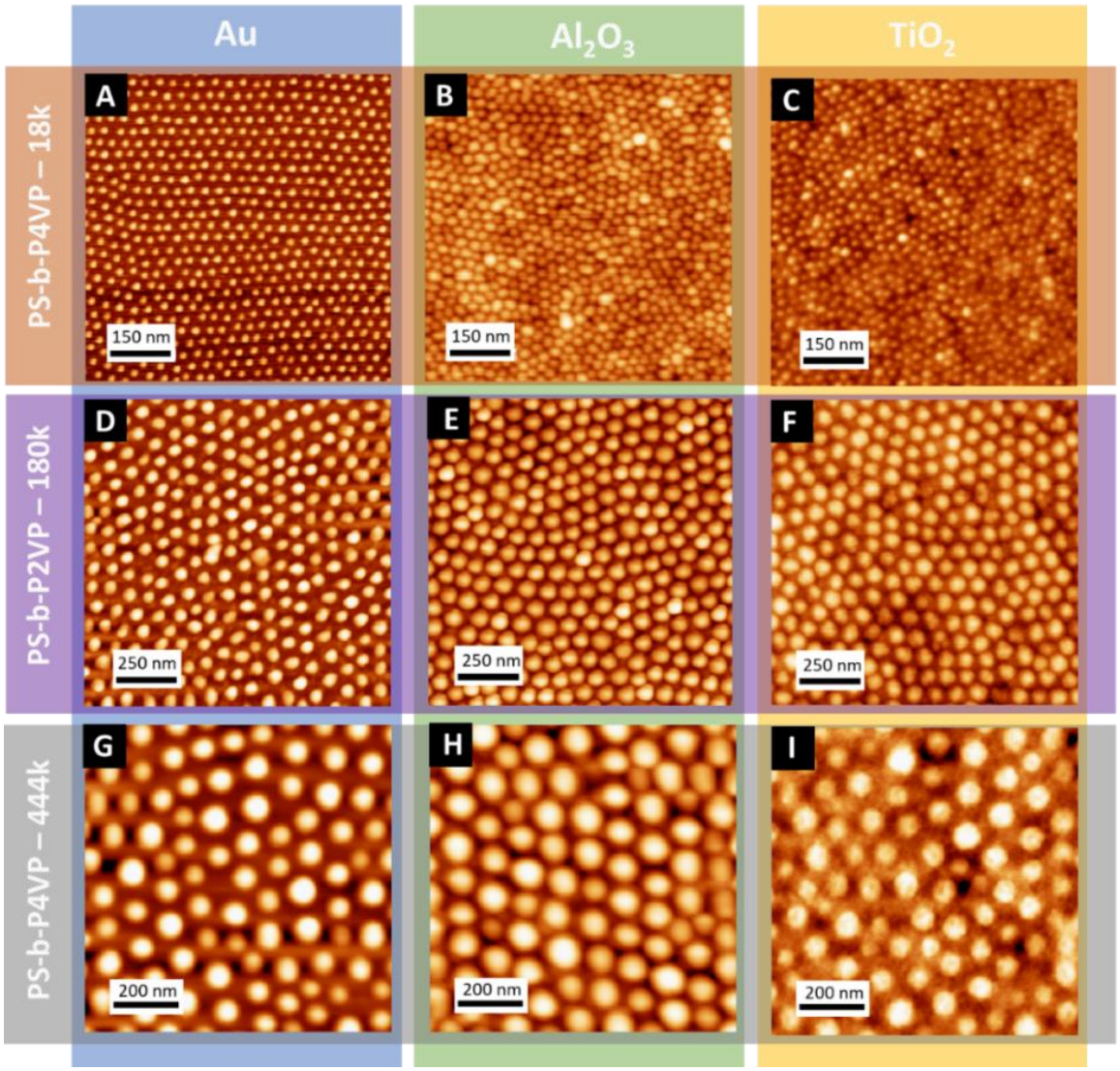

Figure 3.19: *AFM topographical images of all the possible structures created using the three different BCPs as a template (A-C) $PS_{14.7K}$-b-$P4VP_{6.3k}$, (D-F) PS_{150K}-b-$P4VP_{32k}$ and (G-I) PS_{267k}-b-$P4VP_{177k}$, and using metallic salt impregnation (A, D, G) or ALD (B, C, E, F, H, I)*

5. Optical characterization of the decorated surfaces

5.1 Influence of the structural parameters on the optical properties.

The gold NPs arrays with different structural parameters (diameter and centre-to-centre distance) synthetized using the different molecular weight BCP templates were further analyzed by variable angle spectroscopic ellipsometry (VASE) in reflection in order to correlate the geometry of the decorated surfaces with their plasmonic properties. The evolution of the measured ellipsometric parameters I_s and I_c as a function of the photon energy, between 0.6 and 4.8 eV, is shown on the **Fig. 3.20**. It reveals a clear resonance feature in the region ≈ 2.3 eV, which is attributed to the effect of the localized surface plasmon resonance (LSPR) of the Au NPs templated from the P2VP or P4VP domains. The ellipsometric parameters I_s and I_c are related to the ellipsometric angles Ψ and Δ by the following expressions

$$I_s = sin(2\psi)sin(\Delta) \tag{3.9}$$

$$I_c = sin(2\psi)cos(\Delta) \tag{3.10}$$

The small gold NPs, produced using PS-*b*-P4VP-21k as a template, gave a very weak plasmonic signal (red line **Fig. 3.20**). With the larger BCP templates, a progressive evolution of the resonance band is observed, due to the increase of the gold amount on the surface and the size evolution of the produced Au NPs. For that reason and since the most intense signals are attributed to the medium and bigger particles, we decided to focus our efforts to study more in details these two samples.

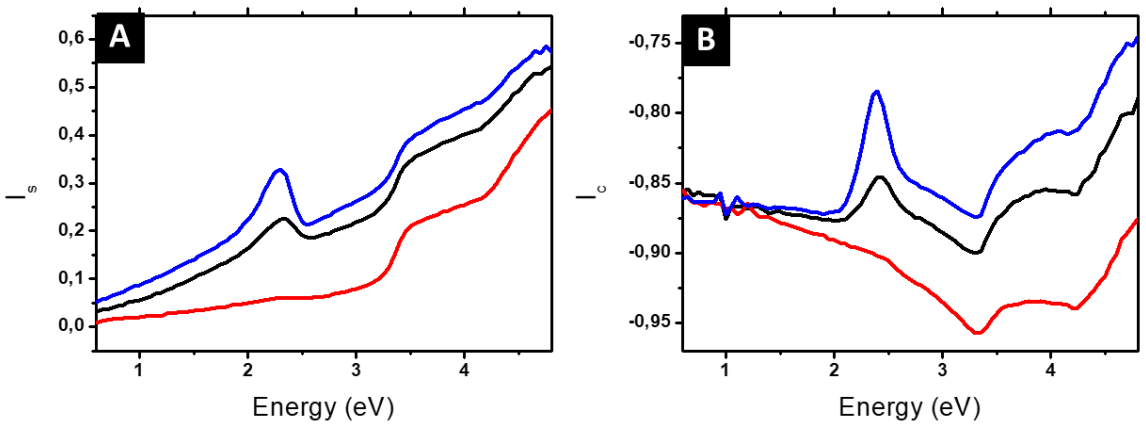

Figure 3.20: *Evolution of the measured ellipsometric parameters, I_s (right) and I_c (left), as a function of the photon energy for an angle of incidence of* θ *= 50° for the three different size*

particles obtained using the three different polymers as a template: $PS_{14.7K}$-b-$P4VP_{6.3k}$ (red line); PS_{150K}-b-$P4VP_{32k}$ (black line) and PS_{267k}-b-$P4VP_{177k}$ (blue line).

With the aim of going further in the tuning of the optical response of the materials, several samples with different thickness were prepared. Consequently, different speeds of deposition were used during the spin-coating process. A 2.5 wt.% solution of PS_{150K}-*b*-$P4VP_{32k}$ in PGMEA was spin-coated (30 s, at 2000, 3000 and 4000 rpm) onto bare silicon wafers, resulting in BCP films with thickness of 140 nm (2000 rpm), 110 nm (3000 rpm) and 80 nm (4000 rpm), respectively. After the subsequent immersion in the aqueous gold salt solution, all of them were exposed to the same O_2 RIE conditions (60 W, 10 sccm, 60 s), which correspond to a dose large enough to reduce the gold salts but not to remove completely the BCP layer for the thicker films. The samples obtained at the end of the process were further analyzed by VASE in reflection, in order to detect if different film thicknesses lead to different gold objects. **Fig. 3.21** shows the evolution of the measured ellipsometric parameters I_s and I_c as a function of the photon energy, between 0.6 and 4.8 eV. A clear difference in the amplitude of the resonant band attributed to the LSPR of the gold NPs is observed, related with the original thickness of the polymer film used as a template.

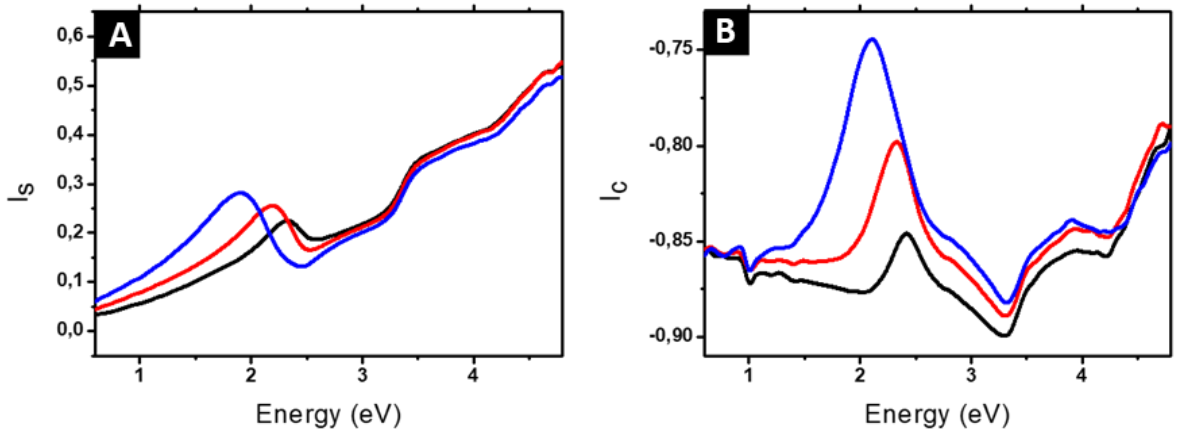

Figure 3.21: *Evolution of the measured ellipsometric parameters, I_s (right) and I_c (left), as a function of the photon energy for an angle of incidence of θ = 50° for the gold NPs obtained using three different PS_{150K}-b-$P4VP_{32k}$ BCP film thicknesses, 80 nm (black line), 110 nm (red line) and 140 nm (blue line).*

Indeed, a more intense band corresponds to the particles obtained using the thicker film as template, indicating that the thicker the BCP film is, the larger the particles are. This is also indicated by the shift in the maximum values of the plasmonic resonance, from a peak centered at 2.33 eV in the case of NPs obtained using the thinner film to a maximum centered at 1.90 eV in the case of the NPs obtained using the thicker one. This means that we are passing from quasi-spherical NPs for the low thickness film, to cylindrical (rods, columns) particles for the thicker one. Unfortunately, this assumption could not be confirmed by the AFM measurements (see schema in **Fig. 3.22**), since harsher plasma conditions for the thicker films lead to the collapse of the structure because high elongated objects cannot maintain the vertical orientation.

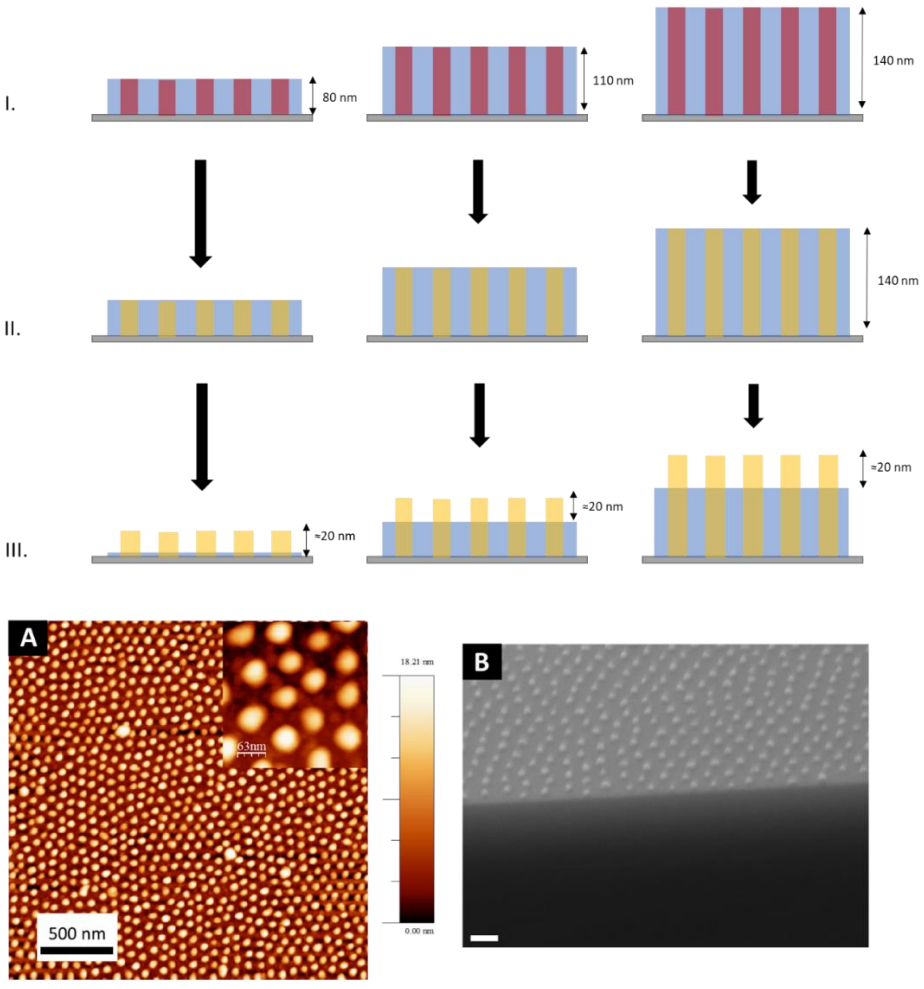

Figure 3.22: *Scheme of the different structures obtained using different PS_{150K}-b-$P4VP_{32k}$ BCP film thickness. I. Self-assembly, II. Selective impregnation with gold salts, III. O_2 RIE treatment (60 W, 10 sccm, 60 s). (A) AFM and (B) 45° tilted SEM image of the gold NPs obtained using the 80 nm thick film.*

For the thinner film (80 nm), the AFM and SEM images (**Fig. 3.22 A-B**) show that most of the polymer has been degraded during the O_2 RIE. In the initial stage, the gold atoms are homogeneously distributed along the P2VP cylinders, but during the reduction process of the plasma, an increase of the gold density is observed to form the particle (height of the particle ≈ 18 nm vs 80 nm height of the BCP cylinder). Since the conditions of the plasma are always the same, a similar polymer thickness will be degraded in the initially thicker films, causing that some of the height of the gold cylinder will remain cover by the polymer (helping also in the stability of the structure). In the ellipsometric measurements, the whole film will impact the data.

To conclude this section, the optical response of the samples can be completely tuned, first using different BCPs as a template, creating NPs arrays with different structural parameters in each case. Secondly, using the same template but modifying the film thickness gives us the opportunity to tune the optical response of the metallic features obtained on top of the surfaces, since the morphology of the objects change to more elongated ones.

In the next section, we will present the full analysis realized for the biggest particles created using the PS_{267k}-*b*-$P4VP_{177k}$ BCP as a template.

5.2 Metasurfaces with a strong optical anisotropy

As we have introduced in **Chapter 2**, **Section 4**, it is possible to extract the optical index $\tilde{n} = n + ik$ or the permittivity $\varepsilon = \varepsilon_r + i\varepsilon_i$ of a thin film of material deposited on a substrate from the ellipsometric data, using a multilayer ellipsometric model. In this case, the studied films are represented by a multilayer ellipsometric model comprising a silicon semi-infinite substrate, a first layer of SiO_2 of 2 nm thickness and the unknown (sample) film of thickness *D*. In a first approximation, nanocomposite materials can be represented with a simple effective medium law, which relates the effective permittivity of the composite medium to the permittivities of the constituent materials, irrespective of the precise structure of the composite provided that the characteristic dimensions are smaller than the wavelength of the incident light.

The Maxwell Garnett formula[37] (introduced in **Chapter 2**, **Section 4**) was applied to the measured I_s and I_c values over all measured angles of incidence for the sample obtained using PS_{267k}-*b*-$P4VP_{177k}$ as a template, using for the gold permittivity a function modified from the Johnson and Christy tabulated data[38,39]. The plots of the experimental results, for the incident angle 50°, and the corresponding fits are presented on **Fig. 3.23A-B**.

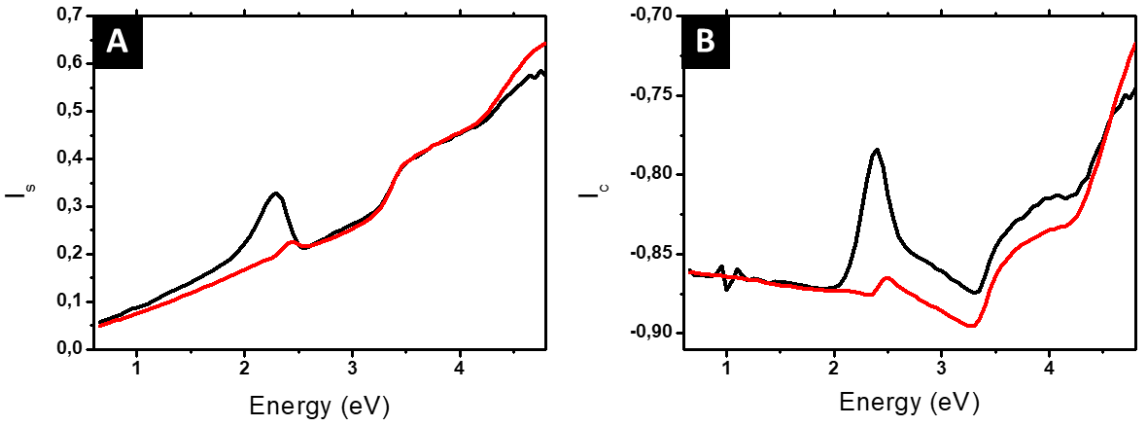

Figure 3.23: *Plots of the experimental ellipsometric quantities, I_s and I_c (black line) and the corresponding fitting using spherical Maxwell Garnett formula (red line) for Au NPs decorated surfaces obtained from PS_{267k}-b-$P4VP_{177k}$ BCP film.*

Two fitting parameters were used: the gold volume fraction *f* (involved in Maxwell Garnett formula), and the thickness *D* of the film (involved in the ellipsometric model). Unfortunately, the fitting was not satisfactory in the spectral region of the localized SPR of the gold NPs (≈ 2.3 eV) using this simple model. By extracting the topographical profiles from the topographical AFM image of the gold NPs obtained using the BCP as a template (**Fig 3.24A-B**), we can see that they are not spherical but rather hemi-ellipsoidal (base diameter of 80 nm with a maximum height of 20-22 nm) as shown on the scheme of **Fig 3.24C**. A 3D AFM image is also provided in order to have a better understanding of the structure under study.

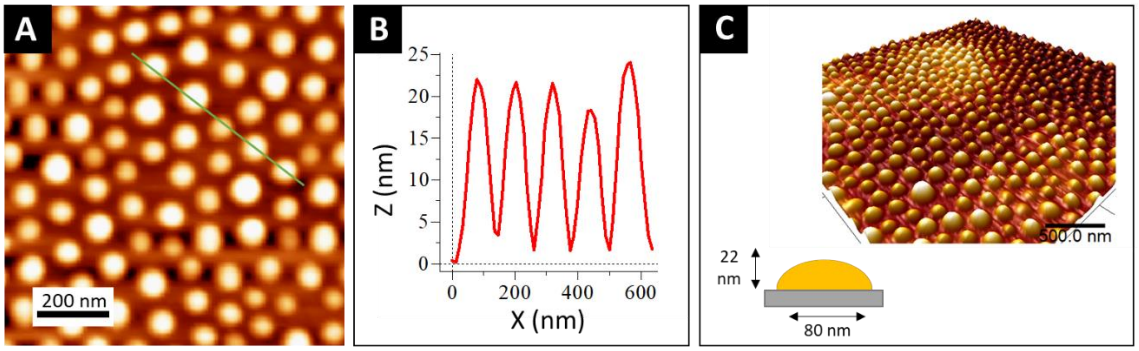

Figure 3.24: *(A) AFM image and (B) topographical profile obtained for the Au NPs created on the silicon surface after etching the PS_{267k}-b-$P4VP_{177k}$ BCP film, selectively charged with metallic salt. (C) Schematic of the particles with the structural dimension, and 45° tilted 3D AFM image of the NPs on top of the silicon substrate.*

Considering the AFM data and noticing that all the ellipsoidal NPs have a parallel major axis oriented perpendicular to the surface of the substrate (**Fig. 3.24C**), we used a modified Maxwell Garnett formula dedicated to oriented ellipsoids, defined as:

$$\frac{\varepsilon_{eff}-\varepsilon_m}{\varepsilon_m+L_z[\varepsilon_{eff}+\varepsilon_m]} = f\frac{\varepsilon_{Au}-\varepsilon_m}{\varepsilon_m+L_z[\varepsilon_{Au}+\varepsilon_m]} \quad (3.11)$$

This function applies to an assembly of oriented ellipsoids of revolution (or spheroids) of dimensions $a = c \neq b$, with a, b and c the three principal semi-axes of the ellipsoids and L_z the depolarization factor given by:

$$L_z = \frac{a^2 b}{3}\int_0^{\infty}\frac{dr}{(b^2+r)^{\frac{3}{2}}(a^2+r)} \quad (3.12)$$

L_z is related to the aspect ratio, b/a, of the ellipsoids, and values for L_z with $0 \leq L_z \leq 1/3$ (prolate ellipsoids), $L_z = 1/3$ (sphere) and $1/3 \leq L_z \leq 1$ (oblate ellipsoids) are possible. Using this effective medium law, four parameters were fitted, the gold volume fraction f, the film thickness D, and the depolarization factor L_z. **Equation (3.11)** was applied, using the DeltaPsi2 software, to the measured I_s and I_c values over all measured angles of incidence for the sample obtained using PS_{267k}-*b*-$P4VP_{177k}$ as a template. The plots of the experimental results, for all the incident angles (50°, 60° and 70°), and the corresponding fittings are presented on **Fig. 2.25A-B**. The fit quality is dramatically improved compared to the case of the spherical Maxwell Garnet model,

especially around the localized SPR of the gold NPs (X^2 = 10.34 *vs* 1.35, respectively). The optimal fitting values obtained are listed in **Table 3.4**.

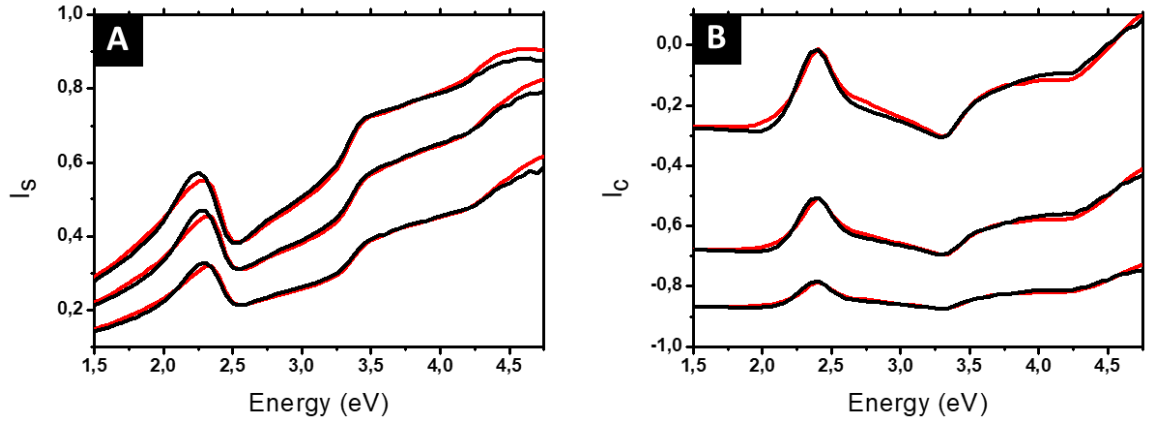

Figure 3.25 *Plots of the experimental ellipsometric quantities, I_s and I_c (black lines) and the corresponding fitting using oriented ellipsoids Maxwell Garnett formula (red lines) for Au NPs decorated surfaces obtained after etching the PS_{267k}-b-$P4VP_{177k}$ BCP film, selectively charged with metallic salt.*

Sample	*t* (nm)	$L_x = L_y$	L_z	f_{Au}
Au NPs 80nm	14.5	0.4225	0.155	18.78

Table 3.4: *Structural parameters extracted from the fit of the ellipsometry data with the oriented ellipsoids Maxwell Garnett formula: t the film thickness. f_{Au} the gold volume fraction and L_x, L_y and L_z the depolarization factors along the three ellipsoidal semi-axes.*

The extracted L_z value (0.155) is related with a prolate spheroid (elongated) which is in contradiction with the AFM data where oblate objects were detected. This contradiction can be explained by two different factors. First, since lateral dimensions are strongly distorted by AFM tip convolution effects, giving the impression of wider features[40] (**Fig. 3.26A**), the lateral dimensions obtained from the topographical profile are not reliable. Secondly, an image dipole effect can also disturb the optical response of the material. Indeed, since the particle is deposited on a substrate, the optical response of the particles can be extremely dependent

on the irradiation conditions and the particle environment[41]. The spherical symmetry of the dipole generated by a plasmon particle is broken by the presence of the nearby interface of a high index substrate, generating an anisotropy and interfering in the final shape of the particle predicted by the ellipsometric model (**Fig. 3.26B**). For these reasons, in this case, we cannot precisely correlate the particle shape given by the ellipsometric model with the one obtained by the experimental results.

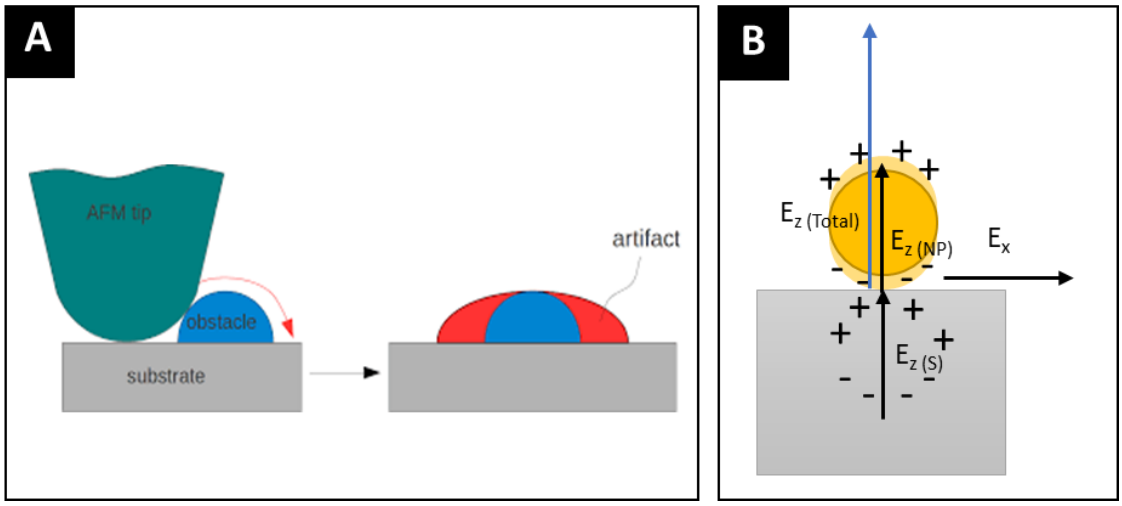

Figure 3.26: (A) an *AFM artefact due to the tip convolution arises from the measurement of small objects deposited on a substrate. (B) Scheme of the image dipole effect produced by the interaction between the particle and the surface of the substrate.*

Once the parameters *f* and *L* have been determined, the oriented ellipsoids modified Maxwell Garnett formula gives access to the anisotropic effective permittivity, $\varepsilon_x = \varepsilon_{r,x} + i\varepsilon_{i,x}$ and $\varepsilon_z = \varepsilon_{r,z} + i\varepsilon_{i,z}$ of the composite film. **Fig. 3.27** shows the values of ε_r and ε_i, as a function of the photon energy for both directions. In all the cases the film presents a resonant behaviour close to the plasmonic resonance of the Au NPs (2.3eV)[39]. Interestingly, we can observe three different regions of strong anisotropy, denoted as (A) $\varepsilon_z > \varepsilon_x > 0$, (B) $\varepsilon_x > \varepsilon_z = 0$ and (C) $\varepsilon_x > \varepsilon_z > 0$, indicated on **Fig. 3.27**. In the regions A and C, ε_x and ε_z present both high positives values. On the contrary, in the region B, the two components of the dielectric permittivity tensor ε have a very different value. Thus, for the spectrum region from 2.1 eV to 2.4 eV (516–590 nm^{-1}) ε_z presents a value close to 0 while ε_x remains with a high value. This is a clear proof of the strong anisotropy of the decorated surfaces obtained following the

hybridization of nanostructured BCP films. Interestingly, very dispersive dielectric permittivity values are obtained in the spectral region around 2.3 eV, due to the LSPR of the Au NPs created.

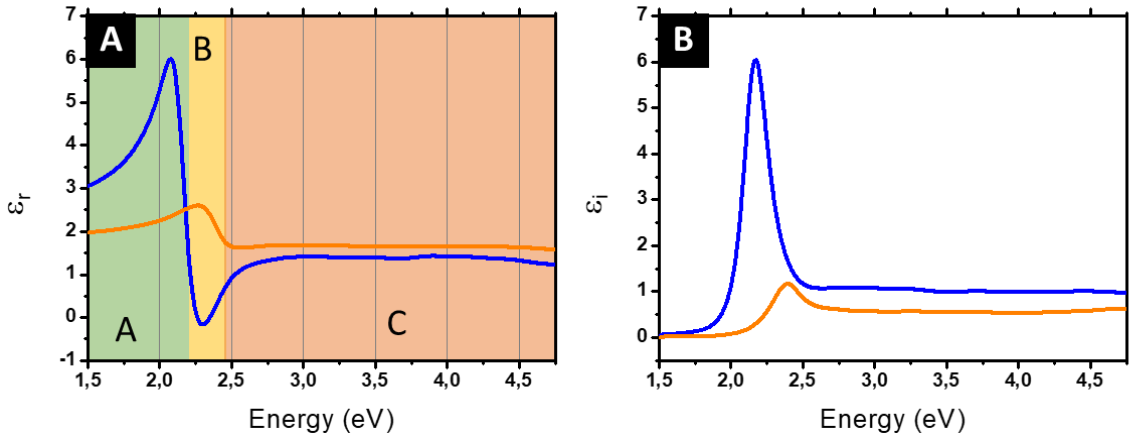

Figure 3.27: *Perpendicular (blue line) and parallel (orange line) components of the (A) real and (B) imaginary dielectric functions of ellipsoidal NPs obtained on top of the silicon substrates. The three different colors indicate the three regions of interest.*

Producing materials with low impedance at fixed frequency is one of the aims pursued for a new generation of antennas and optical circuits[42,43]. Our materials, with an electric permittivity close to 0 in the *z* direction and high optical index contrast, with low losses (**Fig. 3.28A-B**) for the spectral window from 516 to 590 nm, open the door to new metasurfaces for the development of new optical devices such as superlenses, perfect absorbers, or ultrafast switches.

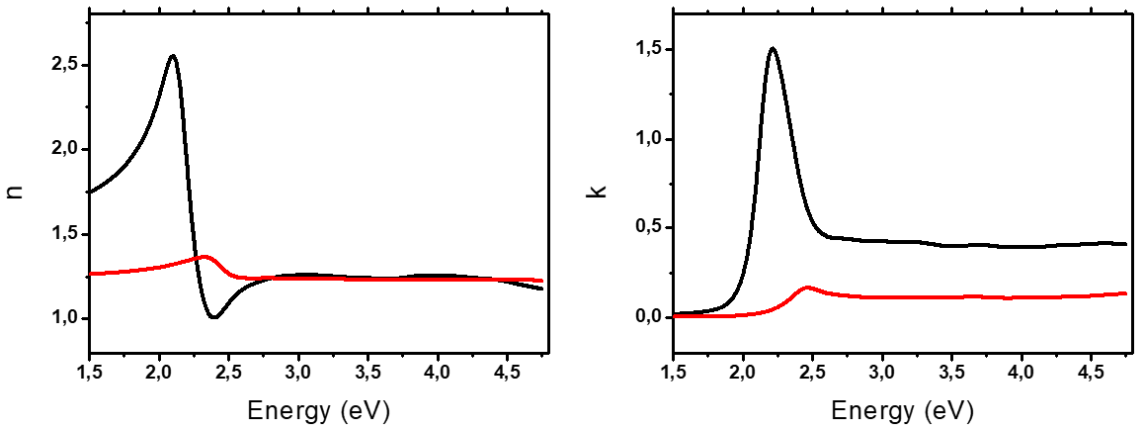

Figure 3.28: *Perpendicular (black line) and parallel (red line) components of the optical index of the studied films obtained by the modified Maxwell Garnett formula for the ellipsoidal NPs on top of the silicon substrates*.

6. Conclusions

In this chapter, BCPs ranging from low to ultra-high molecular weights with low dispersity were synthetized using living anionic polymerization. The self-assembly of these BCPs into cylindrical ordered structures have been studied using several techniques, *i.e.*, AFM and GISAXS in order to obtain the structural parameters inherent to the BCP self-assembly

Several selective hybridization processes have been studied during this chapter, showing the great versatility of the approach developed in this Ph.D. First of all, the gold impregnation procedure was followed at each step of the process by XRF, confirming the final reduction to metallic gold by the O_2 RIE treatment. The homogeneous distribution of the gold salt inside the polymer film was studied by XRR and GISAXS. Other examples of selective impregnations by immersion into metallic precursor solutions were also provided. Indeed, metallic platinum nanowires and metallic silver NPs were obtained using this methodology.

Besides ordered hexagonal structures of pre-synthetized gold NPs were obtained using the BCP film as a spatial registration tool. The immersion of the BCP film in an aqueous colloidal suspension of gold NPs leads to a selective binding of the gold NPs onto the polymer film. The AFM and GISAXS studies corroborate the final structure. Finally, we have showed that Al_2O_3 and TiO_2 NPs arrays could be obtained using the ALD technique and BCP films as template.

The optical properties of the gold NPs arrays were studied with VASE. The modification of the structural parameters by using different BCPs or hybridization methodologies enables us to tune the optical response of the different decorated surfaces. The particle diameter and inter-particle distance have a dramatic effect on the LSPR of the objects created. Also, we have shown the possibility of tune even further the optical response by controlling the film thickness and thus by increasing the volume fraction of gold on the surface. Thicker BCP films produce bigger and more elongated objects with enhanced LSPR effect.

Finally, the effective optical properties of the sample have been modelled using the Maxwell Garnett formalism adapted to oriented ellipsoids. A strong anisotropy has been

observed and an effective electric permittivity close to 0 has been extracted for a region of the spectra. This opens the door for the use of such metasurfaces in the development of new of optical devices.

1. *Developments in Block Copolymer Science and Technology*. (John Wiley & Sons, Ltd, 2004). doi:10.1002/0470093943
2. De Brouwer, H., Schellekens, M. A. J., Klumperman, B., Monteiro, M. J. & German, A. L. Controlled radical copolymerization of styrene and maleic anhydride and the synthesis of novel polyolefin-based block copolymers by reversible addition-fragmentation chain-transfer (RAFT) polymerization. *J. Polym. Sci. Part A Polym. Chem.* **38,** 3596–3603 (2000).
3. Mühlebach, A., Gaynor, S. G. & Matyjaszewski, K. Synthesis of Amphiphilic Block Copolymers by Atom Transfer Radical Polymerization (ATRP). *Macromolecules* **31,** 6046–6052 (1998).
4. Theodosopoulos, G. & Pitsikalis, M. Block Copolymers by Anionic Polymerization: Recent Synthetic Routes and Developments. in *Anionic Polymerization* 541–623 (Springer Japan, 2015). doi:10.1007/978-4-431-54186-8_12
5. Varshney, S. K., Zhong, X. F. & Eisenberg, A. Anionic homopolymerization and block copolymerization of 4-vinylpyridine and its investigation by high-temperature size-exclusion chromatography in N-methyl-2-pyrrolidinone. *Macromolecules* **26,** 701–706 (1993).
6. Gao, Z., Varshney, S. K., Wong, S. & Eisenberg, A. Block Copolymer "Crew-Cut" Micelles in Water. *Macromolecules* **27,** 7923–7927 (1994).
7. Runge, M. B. & Bowden, N. B. Synthesis of High Molecular Weight Comb Block Copolymers and Their Assembly into Ordered Morphologies in the Solid State. *J. Am. Chem. Soc.* **129,** 10551–10560 (2007).
8. Ikkala, O. & ten Brinke, G. Functional Materials Based on Self-Assembly of Polymeric Supramolecules. *Science (80-.).* **295,** 2407–2409 (2002).
9. Kim, E. *et al.* Directed Assembly of High Molecular Weight Block Copolymers: Highly Ordered Line Patterns of Perpendicularly Oriented Lamellae with Large Periods. *ACS Nano* **7,** 1952–1960 (2013).
10. Spangler, L. L., Torkelson, J. M. & Royal, J. S. Influence of solvent and molecular weight on thickness and surface topography of spin-coated polymer films. *Polym. Eng. Sci.* **30,** 644–653 (1990).
11. Park, S., Wang, J.-Y., Kim, B., Chen, W. & Russell, T. P. Solvent-Induced Transition from Micelles in Solution to Cylindrical Microdomains in Diblock Copolymer Thin Films.

Macromolecules **40,** 9059–9063 (2007).

12. Paradiso, S. P., Delaney, K. T., García-Cervera, C. J., Ceniceros, H. D. & Fredrickson, G. H. Block Copolymer Self Assembly during Rapid Solvent Evaporation: Insights into Cylinder Growth and Stability. *ACS Macro Lett.* **3,** 16–20 (2014).
13. Kim, G. & Libera, M. Morphological Development in Solvent-Cast Polystyrene−Polybutadiene−Polystyrene (SBS) Triblock Copolymer Thin Films. *Macromolecules* **31,** 2569–2577 (1998).
14. Kim, S. H., Misner, M. J., Xu, T., Kimura, M. & Russell, T. P. Highly Oriented and Ordered Arrays from Block Copolymers via Solvent Evaporation. *Adv. Mater.* **16,** 226–231 (2004).
15. Gu, X., Gunkel, I., Hexemer, A., Gu, W. & Russell, T. P. An In Situ Grazing Incidence X-Ray Scattering Study of Block Copolymer Thin Films During Solvent Vapor Annealing. *Adv. Mater.* **26,** 273–281 (2014).
16. Smilgies, D.-M. Scherrer grain-size analysis adapted to grazing-incidence scattering with area detectors. *J. Appl. Crystallogr.* **42,** 1030–1034 (2009).
17. Scherrer, P. Bestimmung der Größe und der inneren Struktur von Kolloidteilchen mittels Röntgenstrahlen. *Nachrichten von der Gesellschaft der Wissenschaften zu Göttingen, Math. Klasse* **1918,** 98–100
18. Antonietti, M., Wenz, E., Bronstein, L. & Seregina, M. Synthesis and characterization of noble metal colloids in block copolymer micelles. *Adv. Mater.* **7,** 1000–1005 (1995).
19. Alov, N. V. Total reflection X-ray fluorescence analysis: Physical foundations and analytical application (A review). *Inorg. Mater.* **47,** 1487–1499 (2011).
20. Björck, M. & Andersson, G. GenX : an extensible X-ray reflectivity refinement program utilizing differential evolution. *J. Appl. Crystallogr.* **40,** 1174–1178 (2007).
21. Zhang, Q., Li, N., Goebl, J., Lu, Z. & Yin, Y. A Systematic Study of the Synthesis of Silver Nanoplates: Is Citrate a “Magic” Reagent? *J. Am. Chem. Soc.* **133,** 18931–18939 (2011).
22. Evanoff, D. D. & Chumanov, G. Synthesis and Optical Properties of Silver Nanoparticles and Arrays. *ChemPhysChem* **6,** 1221–1231 (2005).
23. George, S. M. Atomic Layer Deposition: An Overview. *Chem. Rev.* **110,** 111–131 (2010).
24. Turkevich, J., Stevenson, P. C. & Hillier, J. The Formation of Colloidal Gold. *J. Phys.*

Chem. **57,** 670–673 (1953).

25. Dong, H., Fey, E., Gandelman, A. & Jones, W. E. Synthesis and Assembly of Metal Nanoparticles on Electrospun Poly(4-vinylpyridine) Fibers and Poly(4-vinylpyridine) Composite Fibers. *Chem. Mater.* **18,** 2008–2011 (2006).
26. Malynych, S., Luzinov, I. & Chumanov, G. Poly(Vinyl Pyridine) as a Universal Surface Modifier for Immobilization of Nanoparticles. *J. Phys. Chem. B* **106,** 1280–1285 (2002).
27. Babonneau, D. FitGISAXS: Software package for modelling and analysis of GISAXS data using IGOR Pro. *J. Appl. Crystallogr.* **43,** 929–936 (2010).
28. Lee, S.-M. *et al.* Greatly increased toughness of infiltrated spider silk. *Science* **324,** 488–92 (2009).
29. Lee, S.-M. *et al.* Improved Mechanical Stability of Dried Collagen Membrane after Metal Infiltration. *ACS Appl. Mater. Interfaces* **2,** 2436–2441 (2010).
30. Tseng, Y.-C. *et al.* Enhanced polymeric lithography resists via sequential infiltration synthesis. *J. Mater. Chem.* **21,** 11722 (2011).
31. Biswas, M., Libera, J. A., Darling, S. B. & Elam, J. W. Kinetics for the Sequential Infiltration Synthesis of Alumina in Poly(methyl methacrylate): An Infrared Spectroscopic Study. *J. Phys. Chem. C* **119,** 14585–14592 (2015).
32. Gong, B. *et al.* Sequential Vapor Infiltration of Metal Oxides into Sacrificial Polyester Fibers: Shape Replication and Controlled Porosity of Microporous/Mesoporous Oxide Monoliths. *Chem. Mater.* **23,** 3476–3485 (2011).
33. Dandley, E. C. *et al.* Temperature-dependent reaction between trimethylaluminum and poly(methyl methacrylate) during sequential vapor infiltration: experimental and ab initio analysis. *J. Mater. Chem. C* **2,** 9416–9424 (2014).
34. Li, F. *et al.* Highly Porous Metal Oxide Networks of Interconnected Nanotubes by Atomic Layer Deposition. *Nano Lett.* **12,** 5033–5038 (2012).
35. Yin, J., Xu, Q., Wang, Z., Yao, X. & Wang, Y. Highly ordered TiO 2 nanostructures by sequential vapour infiltration of block copolymer micellar films in an atomic layer deposition reactor. *J. Mater. Chem. C* **1,** 1029–1036 (2013).
36. Tavakkoli K. G., A. *et al.* Multilayer block copolymer meshes by orthogonal self-assembly. *Nat. Commun.* **7,** 10518 (2016).
37. Garnett, J. C. M. Colours in Metal Glasses and in Metallic Films. *Philos. Trans. R. Soc. A Math. Phys. Eng. Sci.* **203,** 385–420 (1904).

38. Johnson, P. B. & Christy, R. W. Optical constants of the noble metals. *Phys. Rev. B* **6,** 4370–4379 (1972).
39. Vieaud, J. *et al.* Effective medium description of plasmonic couplings in disordered polymer and gold nanoparticle composites. *Thin Solid Films* **603,** 452–464 (2016).
40. Wong, C., West, P. E., Olson, K. S., Mecartney, M. L. & Starostina, N. Tip dilation and AFM capabilities in the characterization of nanoparticles. *JOM* **59,** 12–16 (2007).
41. Lermé, J. *et al.* Optical Properties of a Particle above a Dielectric Interface: Cross Sections, Benchmark Calculations, and Analysis of the Intrinsic Substrate Effects. *J. Phys. Chem. C* **117,** 6383–6398 (2013).
42. Yun, S. *et al.* Low-Loss Impedance-Matched Optical Metamaterials with Zero-Phase Delay. *ACS Nano* **6,** 4475–4482 (2012).
43. Alù, A. & Engheta, N. Input Impedance, Nanocircuit Loading, and Radiation Tuning of Optical Nanoantennas. *Phys. Rev. Lett.* **101,** 043901 (2008).

IV

CHAPTER 4 | Building complex structures: Bimetallic raspberry-like nanoclusters and on-demand 3D structures

1. Introduction

As presented in **Chapter 1**, controlling independently the dielectric permittivity (ε) and the magnetic permeability (μ) can open the possibility of obtaining materials with extraordinary properties. Double negative materials (simultaneous negative values of ε and μ) have the potential to be integrated in perfect lens, which are of particular interest for lithography and optics[1]. Nevertheless the control of μ is not trivial, since the natural materials have a negligible susceptibility at optical frequencies[2]. Thus, the design, synthesis and assembly of different artificial nanocomposites in order to tailor the magnetic response have been important foci in this field in the last years. Practical fabrication of such designs often involves elaborate chemistry and/or nanofabrication, which limits the capacities of scalability and development. New fabrication methods are needed, which can give access to large scale surfaces with few process steps.

In the first chapter, some examples were given of how artificial optical magnetism has been observed in structures thinner than the wavelength of light as a non-local effect using complex structures, *i.e.*, double fishnet or double ring resonators. Recently other types of nanocomposites were proposed. One of the most promising was presented by Lerond and co-workers in 2011[3]. It consists in the assembly of metallic nanoparticles (NPs) into plasmonic nanorings. Gold NPs are dispersed in a chloroform PS-*b*-PMMA solution and then spread at the air–water interface in a Langmuir–Blodgett set-up[4]. Based on the higher affinity of water for PMMA, PMMA thin film on the water surface decorated with PS islands were obtained. Depending on the ligand and size of the particles, they are located in the PS part or in the air/PS/PMMA triple interface, forming nanorings. Different nanorings with different aspect ratio allow to tune the plasmonic resonances of the material[5].

Another interesting structure is the raspberry-like magnetic nanoclusters, consisting in a dielectric core particle assembled with metallic satellites. The design of this type of meta-atoms was proposed by Simovski-Tretyakov[6] in 2008. The successful synthesis of such objects (presented in **Fig. 4.1**) by bottom-up approach was described recently[7,8]. Silica NPs are coated by polycations (**Fig. 4.1A**) inducing the assembly of negatively charged silver NPs (**Fig. 4.1B**) to form raspberry-like meta-molecules. Finally, an outer silica layer is grown to stabilize the nanostructure (**Fig. 4.1C**). Artificial optical magnetism ($\mu \neq 1$), generated by resonant loops of

plasmonic currents induced by the light wave[9], has been demonstrated recently for these structures[10].

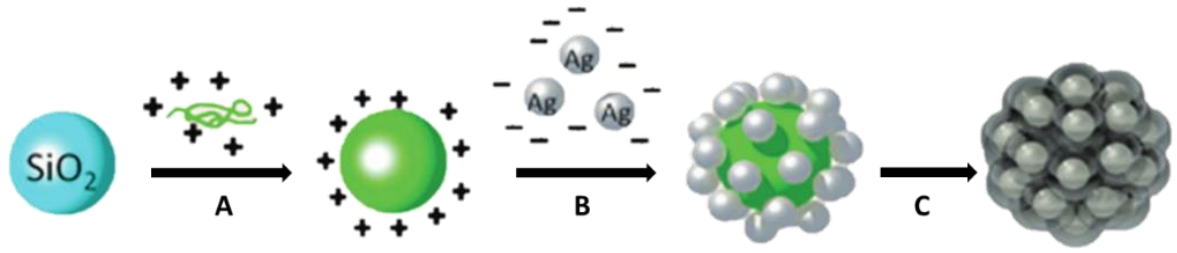

Figure 4.1: *Schematic representation of the hierarchical self-assembly process of raspberry magnetic nanoclusters.*

The self-assembly of these meta-atoms into different 3D structures has been studied using different techniques, *i.e.*, microfluidics[7], DNA interactions[11] or non-specific electrostatic forces[12]. But there is no satisfactory method so far to obtain the ordering of these structures onto a surface monolayer. Another limitation is the necessity to establish a new synthetic route for each desired metal-dielectric combination.

In **Chapters 2 and 3**, we presented the possibility of obtaining several ordered structures made from a large variety of both metallic and dielectric species, using BCPs as templates (**Fig. 4.2**). The synthesis of different molecular weight BCPs gives the opportunity to have a good control of the particle sizes and inter-distances. **Table 4.1** exemplified the versatility of such approach with the characteristics of the NPs arrays formed following this methodology.

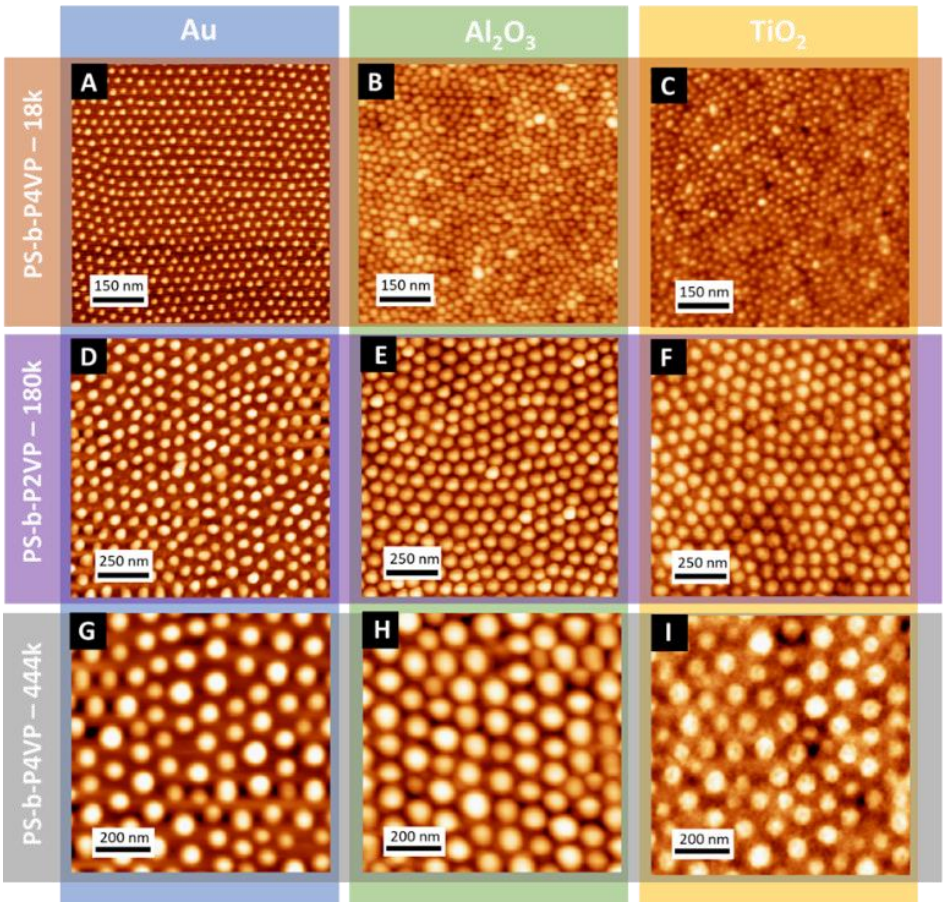

Figure 4.2: *AFM topographical image of hexagonal arrays of different materials obtained after impregnating PS-b-P(4)(2)VP BCPs films: (A,B and C) PS_{26k}-b-$P2VP_{5,7k}$, (D, E and F) PS_{247k}-b-$P2VP_{57k}$ and (G, H and I) PS_{440k}-b-$P2VP_{353k}$.*

Polymer	M_n (kg/mol)	Centre-to-centre distance (D_{c-c})	NP diameter (d)
PS-*b*-P4VP-01	21,0	30 nm	10
PS-*b*-P2VP-02	182,7	79 nm	36
PS-*b*-P4VP-03	443,9	110 nm	50

Table 4.1: *Structural parameters of the polymers used in this study*

In this chapter, a new strategy to obtain bimetallic raspberry-like nanoclusters will be presented. This strategy is inspired by the pioneer works of Majewski et *al*. using an iterative self-assembly to form 3D stuctures[13–15]. We translated this methodology for the formation of complex metallic-dielectric hybrid NPs using the sequential self-assembly of different

molecular weight BCPs selectively impregnated with different metallic-dielectric combinations. Such strategy allows us to obtain more complex metallic structures not directly accessible by BCP self-assembly.

1. Firstly, the fabrication process will be explained step by step. AFM will be used to characterize the sample at each stage of the process while GISAXS and XRR will provide complementary information on the structure of the nanoclusters.
2. As a perspective, some other complex structures will be demonstrated using the same methodology but varying the iterative self-assembly process.

2. Bimetallic raspberry-like nanoclusters

A scheme of the procedure to prepare bimetallic raspberry-like nanocluster arrays using BCPs as template is presented in **Fig 4.3.**

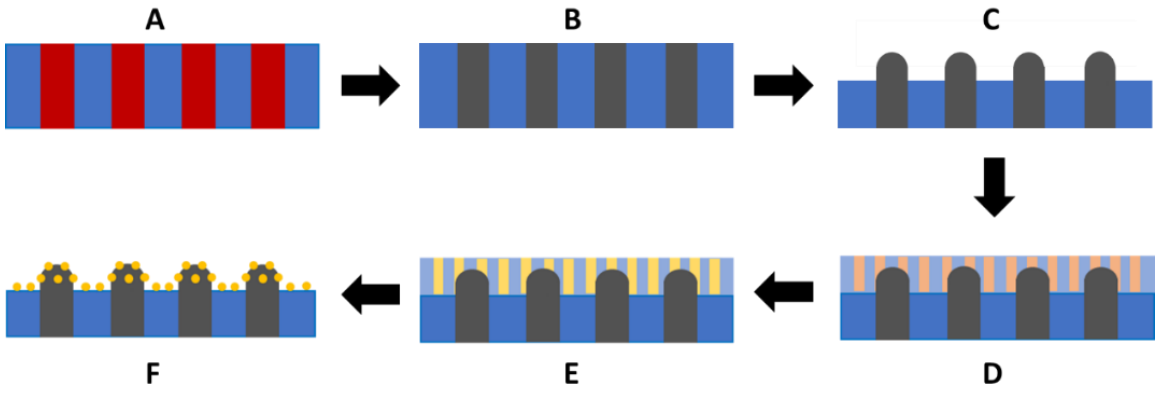

Figure 4.3: *Schematic representation of the process: (A) PS-b-P2VP self-assembly, (B) alumina infiltration by ALD, (C) controlled removal of 30 nm polymer film, (D) self-assembly of a second PS-b-P2VP BCP, (E) metal impregnation, (F) metal reduction.*

In a first step, a 2.5 wt.% solution of PS_{150K}-b-$P2VP_{32k}$ in toluene was spin-coated onto bare silicon wafers (4000 rpm, 30s) leading to a film thickness of 80 nm. After a subsequent static solvent annealing for 8h, well-ordered hexagonal out-of-plane cylindrical arrays of P2VP in a PS matrix were obtained with a centre-to-centre distance of 83 nm and a diameter of 36 nm (**Fig. 4.4A**). The next step was to replicate the BCP structure with Al_2O_3. Therefore, ALD sequential infiltration was carried out. After 10 alternated cycles $Al(CH_3)_3$ / H_2O, Al_2O_3 was selectively introduced into the P2VP domains. In a next step the sample was treated with UV/O3 for 30 min in order to remove 30 nm of the polymer film thickness (**Fig. 4.4B**).

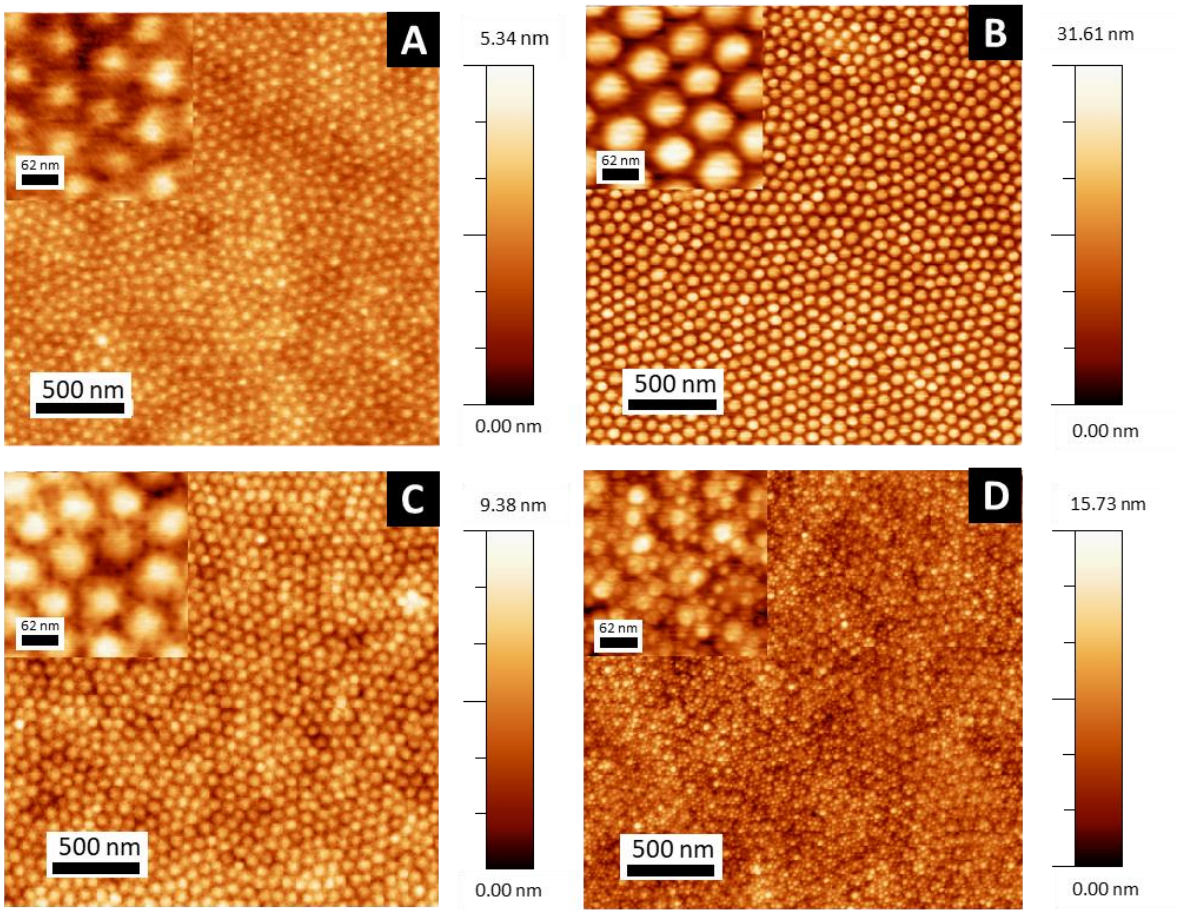

Figure 4.4: *AFM topographical images of the different steps of the process to obtain bimetallic raspberry-like nanoclusters: (A) PS-b-P2VP self-assembled film. (B) Alumina dots obtained after 30 min of treatment with UV/O_3. (C) Self-assembly of the second BCP on top of the Al_2O_3 dots. (D) small gold nanodots obtained on top of the Al_2O_3 particles after impregnation and O_2 RIE.*

This last step is necessary in order to deposit the second BCP on top of the alumina dots, acting thus as a topographical field to guide the next BCP layer self-assembly. After that a 0.5 wt.% solution of $PS_{14.7K}$-*b*-$P4VP_{6.3k}$ in PGMEA (2000 rpm, 30s) was spin-coated on top of the first layer. The thickness of this film is around 30 nm and the BCP used in this step had a centre-to-centre distance of 29 nm and the cylinders formed have a diameter of 12 nm (**Fig. 4.4C**). By a subsequent immersion in an aqueous metallic salt solution ($HAuCl_4$, 1 wt.% in H_2O) for 30 minutes, the gold precursor was selectively incorporated into the P4VP domains. In a final step, the samples were exposed to an O_2 RIE (30 s, 10 sccm and 60 W). Therefore, the gold salt was reduced into metallic gold while the polymer was degraded, resulting in a

structure of Al_2O_3 particles (diameter around 36 nm) decorated by gold dots (diameter around 15 nm).

This approach has as main advantage the high versatility as several metal-dielectric combinations can be derived using always the same strategy (see **Table 4.2**).

Dielectric (core)	Metal (satellites)
Al_2O_3	**Au**
TiO_2	**Pt**
SiO_2	*Ag*
	Pd

Table 4.2: *Dielectric-metal hybrid nanoclusters obtained following the described strategy (bold) and other proposed combinations (italic).*

3. Structural characterization of the nanoclusters

3.1. Direct imaging of the nanoclusters (AFM and SEM)

In a first step, the samples were characterized by AFM (**Fig. 4.5A**) and SEM **(Fig. 4.5B**). In both cases, big dots with a hexagonal order corresponding to the Al_2O_3 cylinders with a diameter around 36 nm are observed. They correspond to the Al_2O_3 particles obtained *via* the self-assembly of the high molecular weight BCP followed by the subsequent sequential infiltration synthesis. On top of these large particles, small satellites corresponding to the Au dots (diameter of 12 nm) formed from the low molecular weight BCP are visible, even if it is difficult to assert the homogeneity of their distribution on top of the large particles.

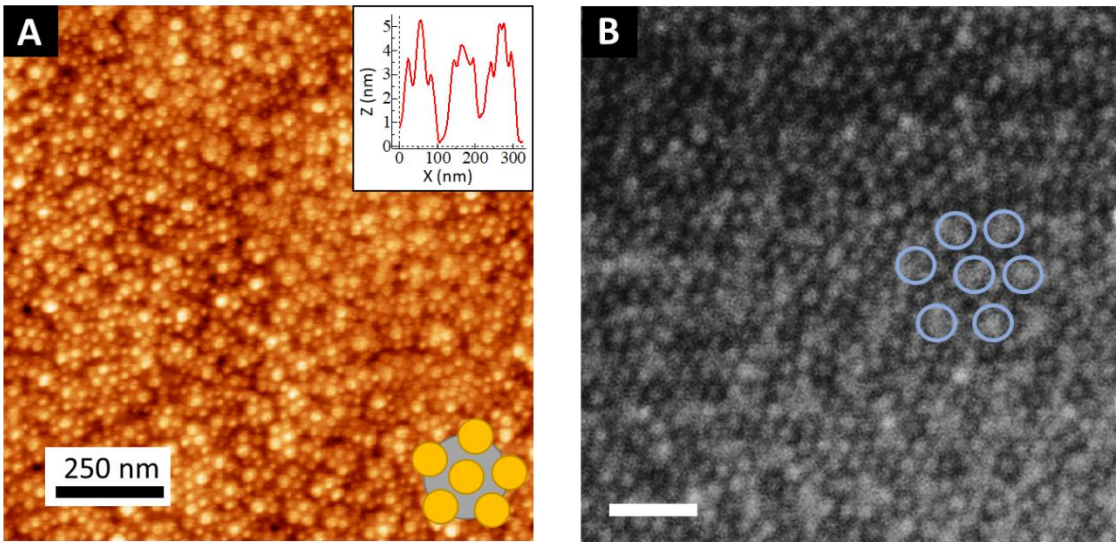

Figure 4.5: *(A) AFM topographical image of the bimetallic nanoclusters formed by a core of Al_2O_3 and gold satellites (see schematic representation and topographical profile in inset) and (B) SEM image of the same sample (the Al_2O_3 dots are marked with blue circles to facilitate their recognition)*

3.2. X-ray characterization

Two different kinds of X-ray experiments were implemented in order to better apprehend the configuration of these decorated surfaces. On one hand, GISAXS experiments

were performed to study the in-plane ordering of the structure. On the other hand, X-ray reflectivity was used to analyse the materials distribution along the out-of-plane direction.

3.2.1. Grazing-incidence small-angle scattering

GISAXS experiments were performed at each step of the process. **Fig. 4.6A** shows the GISAXS pattern obtained for the samples composed of Al_2O_3 particles made by sequential infiltration synthesis with the high molecular weight BCP film acting as a template. It mainly consists of intense Bragg rods inherent to the out-of-plane orientation of the BCP domains produced during the PS_{150K}-b-$P2VP_{32k}$ spin-coating and subsequent solvent annealing. The position of the first Bragg peak (q^*=0.085 nm^{-1}) indicates a period of $L_0 = \frac{2\pi}{q^*}$ = 73.9 nm between scattering planes, corresponding to a centre-to-centre distance of $d_{C\text{-}C}$ = 83.3 nm between cylinders, in accordance with the AFM characterizations. Higher order Bragg rods at $q/q^* = \sqrt{3}$ and $\sqrt{7}$ clearly confirmed the hexagonal order of the cylindrical structure (**Fig. 4.6B**).

When the second BCP layer is deposited on top of the previous one, the GISAXS pattern undergoes drastic modifications (**Fig. 4.6C**). An intense Bragg rod appears at q = 0.241 nm^{-1}. The GISAXS pattern line-cut along q_y integrated around the Yoneda band confirms that the morphological characteristics of the Al_2O_3 under-layer remains unchanged (q^* = 0.086 nm^{-1} with the same sequence of Bragg rods) (**Fig. 4.6D**). Thus, the newly visible Bragg rod observed at q = 0.241 nm^{-1} correspond to the gold dots created on top of the alumina layer. The period, $L_0 = \frac{2\pi}{q^*}$ = 26.1 nm between scattering planes (corresponding to a centre-to-centre distance of $d_{C\text{-}C}$ = 30.1 nm between cylinders) is in accordance with the AFM characterization and with the GISAXS data for the pristine polymer films obtained for this polymer (**Chapter 3**, **Section 4.1**). Therefore, the GISAXS data confirm the AFM and SEM observations, and show that, with the multilayer strategy, it is possible to obtain ordered distributions of bimetallic nanoclusters decorating a surface on a large scale.

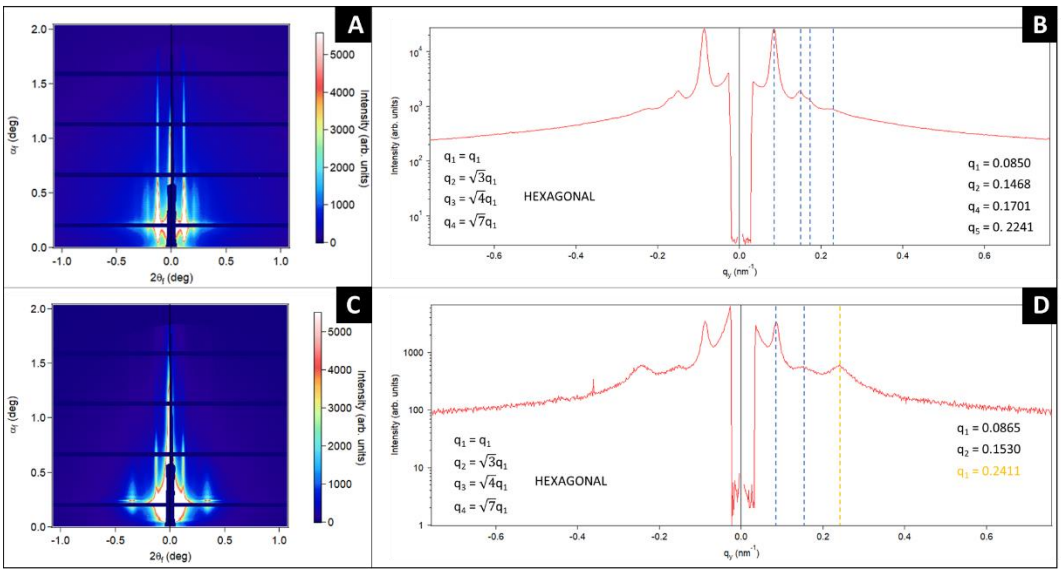

Figure 4.6: *GISAXS patterns of the film in different steps of the process. (A) Al_2O_3 infiltrated into the P2VP domains of the high molecular weight BCP and (C) at the end of the process, with the gold NPs on top of the alumina dots. (B) and (D) correspond to the GISAXS pattern line-cuts along q_y integrated around the Yoneda band of the corresponding samples.*

3.2.2. Specular reflectivity from an interface

The study of the internal structure (perpendicular to the interface) is crucial to have a complete understanding of the obtained morphologies. X-ray reflectivity (XRR) constitutes one of the most efficient techniques to characterize the structure of thin films with high sensitivity. XRR offers some unique advantages of working at the small-length scales because it has a high spatial sensitivity (resolution can be around 0.1 nm), a high penetration and being a non-destructive technique. In the following sections, some theoretical overview is provided and finally the results obtained for the samples studied are presented.

Fig. 4.7A shows the measurement geometry used during the experiment. The measurements were made using the most frequently used geometries in x-ray reflection studies: the so-called θ-2θ scans. During a θ-2θ scan, the sample and the detector are rotated simultaneously so that the angle 2θ between the incident x-ray beam and the reflected beam, is changed twice faster than the angle θ between the incident beam and the sample surface. With this geometry, the curve of specular reflectivity versus incidence angle is measured.

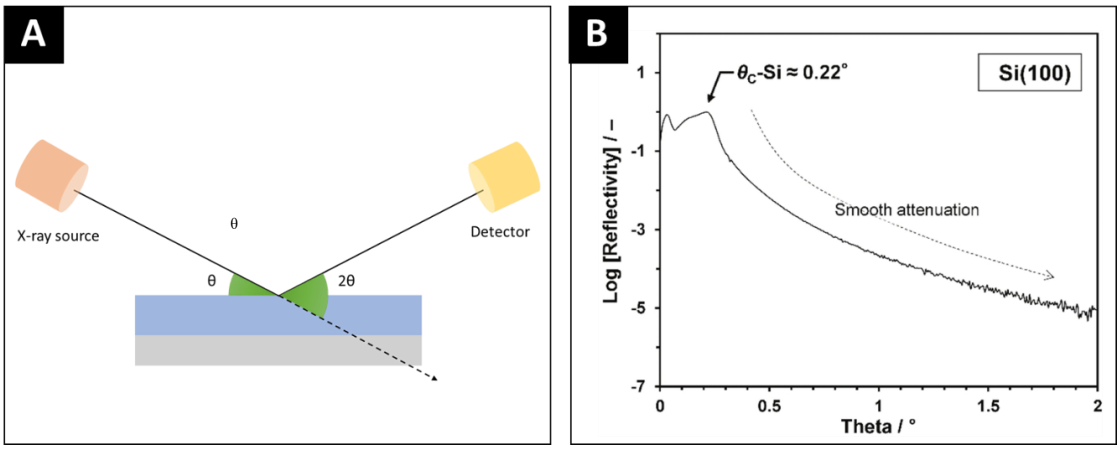

Figure 4.7: *A)* θ-2θ *measurement geometry used during the XRR experiments and B) typical reflectivity curve obtained for an interface specular reflection.*

When an x-ray beam of intensity I_0 interacts with an interface between two media of refractive indices n_1 and n_2, the beam is partially reflected. The intensity, I, of the reflected beam is given by the following formula

$$I = I_0 \, exp\left\{-\frac{4\pi\mu d}{k_{z,1}\,\lambda}\right\} \left|r \, exp\left\{-2k_{z,1}^2\sigma^2\right\}\right|^2 \tag{4.1}$$

Where the first exponential factor accounts for the absorption of x-rays of wavelength λ, traveling a distance d through the first medium with a linear absorption coefficient μ before interacting with the interface of the second medium[16].

The wave vector in the j medium k_j has a component normal to the interface, $k_{z,j}$, given by the following formula:

$$k_{z,j} = \frac{2\pi}{\lambda} n_j \sin\theta_j \tag{4.2}$$

The second exponential factor represents the effect of the roughness σ of the interface on the measured reflectivity. The coefficient r is the Fresnel reflection coefficient of a smooth interface[17] for a beam with an incident angle θ_1, and a refracted angle θ_2 following Snell's law[18] (**Eq. 4.3**).

$$r = \frac{n_1 \sin\theta_1 - n_2 \sin\theta_2}{n_1 \sin\theta_1 + n_2 \sin\theta_2} = \frac{k_{z,1} - k_{z,2}}{k_{z,1} + k_{z,2}} \tag{4.3}$$

$$n_1 cos\theta_1 = n_2 cos\theta_2 \tag{4.4}$$

Fig. 4.7B shows the curve of the reflected intensity versus incidence angle corresponding to a unique interface between air and a homogeneous material. The X-ray reflection intensity is smoothly attenuated, and no oscillation fringes were discernible since there is no interferences between media of different electron densities.

3.2.2.2.- Specular reflectivity produced by a layer

If a second interface is present, the total intensity of the X-rays reflected by the layer is the coherent superposition of the X-ray beams reflected by both interfaces (**Fig. 4.8A**). Fringes characteristic of interference phenomena are clearly observed in the curve of the reflected intensity *versus* incident angle for a film made of one homogeneous layer, as shown in **Fig. 4.8B**.

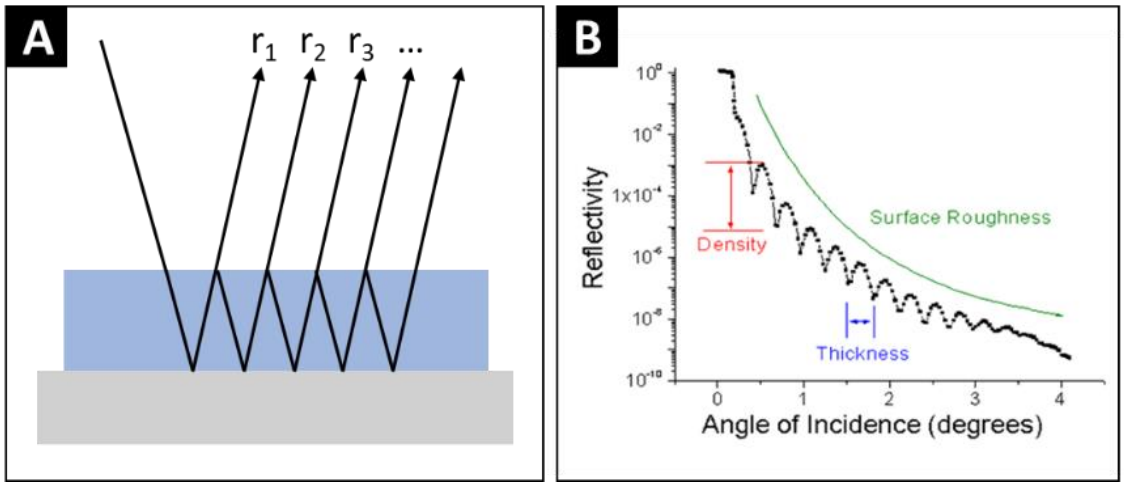

Figure 4.8: *(A) X-ray reflection of a layer and (B) typical reflectivity curve obtained for a layer on top of a substrate and the relation between the profile of the X-ray reflectivity and the structural parameters.*

Some information can be obtained directly from the reflectivity curve, *i.e.*, the thickness and the density of the film. To go further in the analysis and to extract all the information required for a better understanding of the internal structure of the film, it is necessary to establish a model that fits with the experimental data.

In an absorbent medium, the refractive index *n* in the wavelength range of X-rays can be defined as:

$$n = 1 - \delta - i\beta \qquad (4.5)$$

with the real term δ related to the dispersion, and the imaginary term β related to the absorption. In the x-ray wavelength range, both δ and β are small quantities (about 10^{-4} to 10^{-8}).

In order to fit non-homogeneous density profiles, one usual approach consists in splitting the whole thickness of the film in a certain number of independent homogeneous layers. This can be done through building the complex sample layer by layer, using a software called GenX[19]. δ and β are constant in each of these created layers. The fit uses the Parrat formalism which iterates the calculation of the transmission and reflection at each interface to obtain at the end of the process an adjusted profile of the scattering length density (SLD) of the whole film thickness. The SLD obtained by the GenX software is related with δ and β by the following expressions, were re is the Thomson radius with a value of 2.818×10^{-15} m.

$$\delta = r_e \frac{\lambda^2}{2\pi} Re(SLD) \tag{4.6}$$

$$\beta = r_e \frac{\lambda^2}{2\pi} Im(SLD) \tag{4.7}$$

3.2.2.3.- Raspberry-like nanocluster XRR characterization

In order to have a better understanding of the nanostructure of the raspberry nanoclusters fabricated by the multi-layered self-assembly, XRR experiments were implemented at each step of the fabrication procedure (see **Fig. 4.9**).

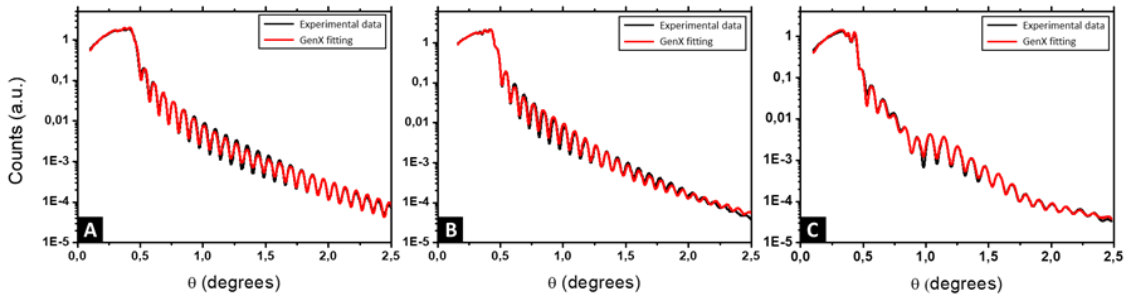

Figure 4.9: *XRR reflectivity data (black line) obtained for (A) PS-b-P2VP pristine film, (B) PS-b-P2VP films infiltrated with Al_2O_3 and (C) PS-b-P2VP infiltrated with Al_2O_3 and with Au NPs on top of the surface. Red lines correspond with fitting obtained by GenX.*

Different structures were created using the GenX software to model the different samples and obtain the best fitting with the experimental results. In order to have a better starting point, some geometrical data derived from the AFM and SEM images as well as some thickness measurements were used. Theoretical values of SLD for the different elements were calculated using the same procedure followed in **Section 4.2.2** of **Chapter 3** and are listed in **Table 4.3**. During this section SLD values will be expressed in $Å^{-3}$, obtained dividing the SLD value by the Thomson radius (r_e).

Material	Formula	Density	SLD ($Å^{-2}$)	SLD / r_e ($Å^{-3}$)
Silicon	Si	2.3	$2.0x10^{-5}$ - i $4.6x10^{-7}$	0.71 - i $1.6x10^{-2}$
Polymer	$C_{15}H_{15}N$	1.02	$9.3x10^{-6}$ - i $1.3x10^{-8}$	0.33 - i $4.6x10^{-4}$
Gold	Au	19.6	$1.25x10^{-4}$ - i $1.3x10^{-5}$	4.44 - i 0.46
Alumina	Al_2O_3	3.95	$3.25x10^{-5}$ - i $3.8x10^{-7}$	1.15 - i $1.3x10^{-2}$

Table 4.3: SLD theoretical values for the materials of interest in this study, calculated using https://sld-calculator.appspot.com.

In case of the pure polymer sample, the best fit with a figure of merit (FOM, quantity used for assessing goodness-of-fit) of $4.26x10^{-2}$ (**Fig. 4.9A** line black and red respectively) correspond to only one homogeneous layer with some roughness at the surface. Once the correct model was established, the scattering length density (SLD) profile was obtained as a function of the height Z (**Fig. 4.10**). For negative Z, a SLD value of 0.71 $Å^{-3}$ is obtained. For comparison with the theoretical values listed in **Table 4.3**, it corresponds to the silicon substrate. At z=0, the SLD rapidly decreases to a uniform SLD value of 0.31 $Å^{-3}$. Since the theoretical SLD value expected for the polymer was 0.33 $Å^{-3}$ we can affirm that we have a homogeneous polymer film. At the upper surface of the film, the SLD decreases with a certain interface thickness, due to the different heights of the polymer (see AFM image and topographical profile in **Fig. 4.10**), the electron density decreases along the z axis while the material quantity present also is diminishing, which we interpreted as related to the quasi-hemispherical shape of the P2VP cylinders. The thickness of the sample is found to be 103 nm, including the small native SiO_2 layer between the silicon and the polymer.

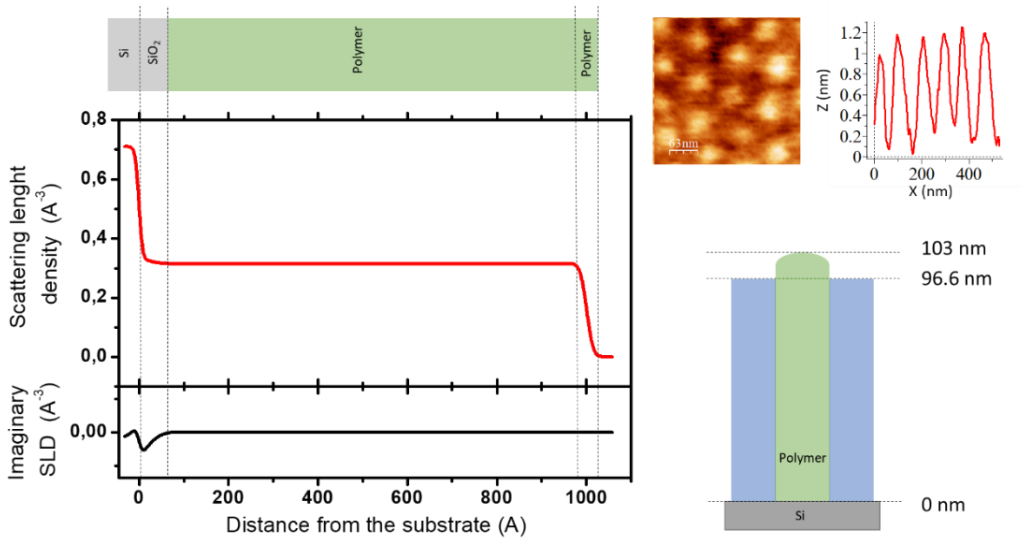

Figure 4.10: *SLD profile obtained after fitting the experimental XRR data for a PS-b-P2VP pristine polymer layer. Some graphical representations, AFM image and topographical profile are also presented to help the data interpretation.*

The fabrication process of the nanoclusters continues with the incorporation of Al_2O_3 into the P2VP domains by ALD (**Fig. 4.3**). In this case, the model that fits better the XRR data is more complicated, consisting in four layers. The FOM of the fit is $5.68x10^{-2}$ showing that the proposed model matches very well the experimental results (**Fig. 4.9B**). The SLD profile obtained is therefore more complex (**Fig. 4.11**). First, like in the previous case, a high SLD value of 0.71 is obtained, which is assigned to the silicon substrate. Then the SLD value decrease until 0,33 $Å^{-3}$. This value is the same as the theoretical one predicted for the pristine polymer.

The following layer has a higher SLD (0.39 $Å^{-3}$), which we interpret as the introduction of Al_2O_3, since the presence of the Al_2O_3 atoms causes an increase of the electron density of the film. Thus, the incorporation of the alumina by ALD does not occur homogeneously in the whole cylinder height: the sample has a thickness around 100 nm and the alumina penetration is found to be 50 nm deep into the polymer film. This is clearly observed in the SLD profile, which increases progressively from around 50 nm from the surface of the substrate, starts to increase until it reaches the maximum value (0,46 $Å^{-3}$ at 100 nm). Thereby, the volume fraction of the Al_2O_3 through the film is not the same. It can be calculated with the following expression.

$$SLD_{Composite} = SLD_{poly}\Phi_{poly} + SLD_{Al_2O_3}\Phi_{Al_2O_3} \quad (4.8)$$

Where $SLD_{polym} = 0.31\ \text{Å}^{-3}$, $SLD_{Al_2O_3} = 1.15\ \text{Å}^{-3}$ and $\Phi_{poly} + \Phi_{Au} = 1$.

A volume fraction of 6.96% of Al_2O_3 is calculated at 70 nm thickness, increasing to 13% close to the film surface. An increase in the thickness is also observed (around 20 nm), which agrees with the AFM observations and is attributed to the Al_2O_3 growth onto the P2VP cylinders (see AFM and topographical profile in **Fig. 4.11**). We suppose this shape explains the smooth decrease of the SLD profile at the upper surface of the film.

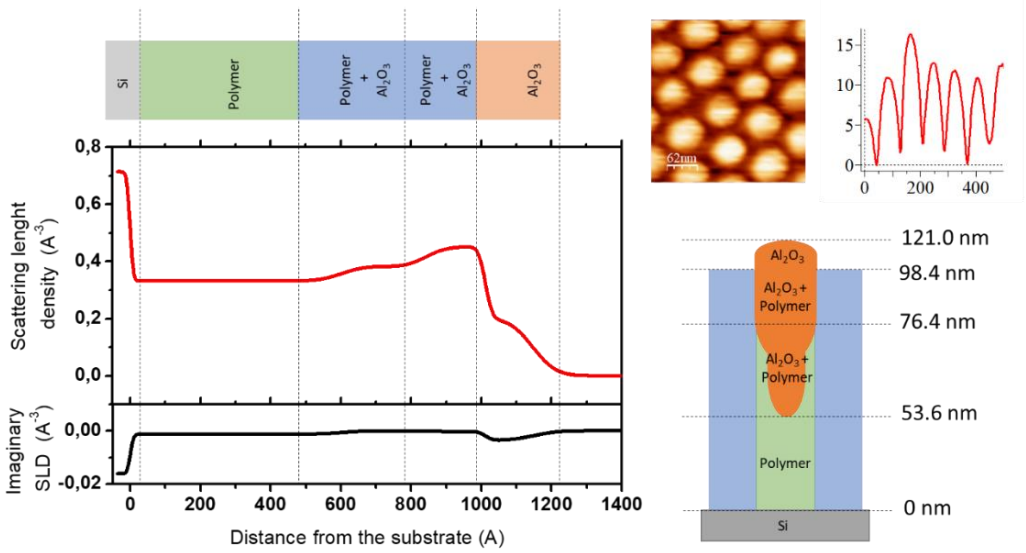

Figure 4.11: *SLD profile obtained after the fitting the experimental XRR data for a PS-b-P2VP impregnated with Al_2O_3. Some graphical representations, AFM image and topographical profile are also presented to help the data interpretation.*

In the next step, the sample was exposed to an UV/O_3 treatment in order to remove partially the BCP layer. Then the second film of BCP (PS_{26k}-*b*-$P4VP_{5.6k}$) was spin-coated on top of the alumina array and impregnated with the gold salt. An O_2 RIE treatment was carried out to remove this second BCP layer and reduce the gold salt to metallic gold. Bimetallic nanostructures composed of an Al_2O_3 core covered by metallic Au satellites were obtained on the top of the surface. XRR was performed at this step of the process, in order to gain some insights on the internal structure of the nanoclusters.

The reflectivity fringes obtained in this case (**Fig. 4.9C**) suggest a more complex structure formed by different objects, as some destructive interferences can be observed. The model requires appropriately adjusting the reflectivity data and is thus more complex, and 12 different layers were necessary to obtain a satisfactory fit of the XRR data. The FOM obtained with this model was established in 3.07×10^{-2} and the SLD profile obtained is presented in **Fig. 4.12**.

At $z < 0$ and $z = 0$, the silicon substrate is observed as well as a thin layer of SiO_2 corresponding to a SLD value of 0.71 $Å^{-3}$, in agreement with the theoretical values listed on **Table 3**. Between $z = 0$ and $z = 20$ nm, three thin layers with SLD values of 0.37 $Å^{-3}$, 0.41 $Å^{-3}$ and 0.37 $Å^{-3}$, respectively. The SLD values, higher than expected for the pristine polymer (0.33 $Å^{-3}$), suggest the presence of some metallic impurity. One possible explanation could be related to the residual BCP layer below the Al_2O_3 particles which is feebly impregnated by the gold salt solution at the time of the formation of the Au dots.

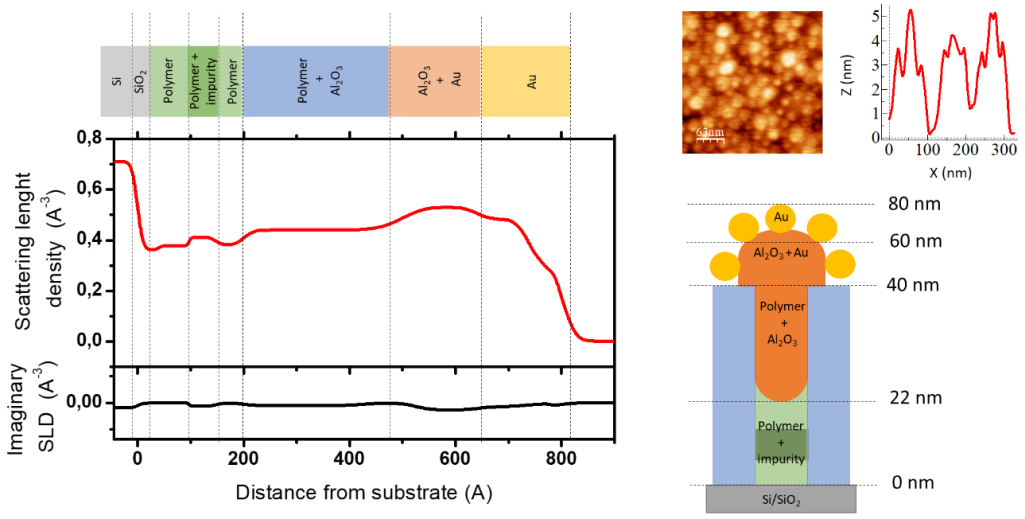

Figure 4.12: *SLD profile obtained after the fitting the experimental XRR data for a PS-b-P2VP layer impregnated with Al_2O_3 and with Au NPs on top of it. Some graphical representations, AFM image and topographical profile are also presented to help the data interpretation.*

Above these copolymer impurity layer, the SLD value increases again due to the presence of the alumina in the polymer. A constant SLD value of 0.44 $Å^{-3}$ is observed from 22 to 44 nm, corresponding to a $\Phi_{Al_2O_3}$ of 11.3%. A higher SLD value (0.53 $Å^{-3}$) is observed in the vicinity of the surface of the film due to the presence of the gold NPs (also the imaginary part

decreases to negative values). Finally, the decrease of the SLD is consistent with the presence of Au NPs on top of the larger alumina dot (see AFM image and topographical profile on **Fig. 4.12**).

4. Other complex structures

In order to generalize this strategy, another type of hybrid nanostructure was studied (see **Fig. 4.13A**). An out-of-plane lamellar structure (periodicity, L_0 = 64 nm) obtained from PS_{102K}-*b*-$P2VP_{97K}$ self-assembly in thin film (thickness, t = 32 nm) after casting from PGMEA was prepared following the procedure explained in **Section 2.1.2** of **Chapter 2**. With a subsequent immersion into an aqueous solution of H_2PtCl_6 (1 wt. %) for 30 min followed by an O_2 RIE (30 s, 10 sccm, 60W), metallic platinum nanowires were obtained (**Fig. 4.13B**.)

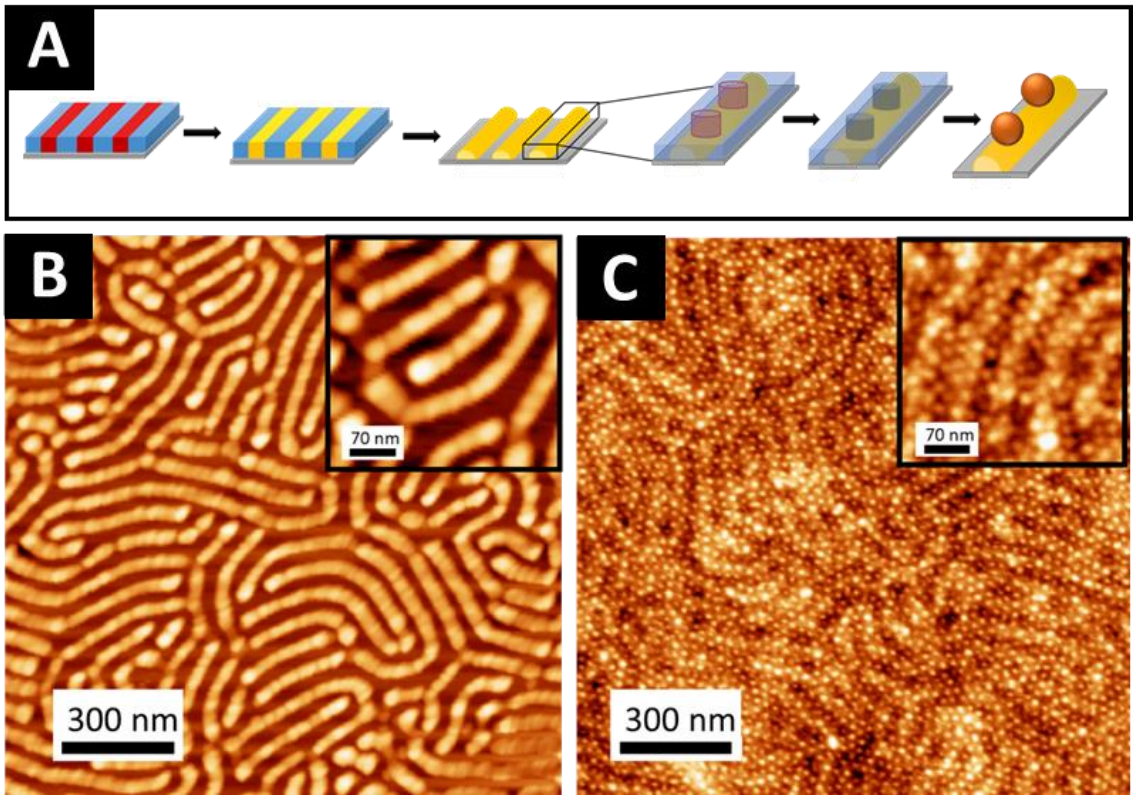

Figure 4.13 *(A) Schematic representation of the process to obtain decorated bimetallic nanowires. AFM topographical images of the different steps of the process to obtain decorated bimetallic nanowires (B) Pt nanowires obtained by selective impregnation of the out-of-plane PS-b-P2VP lamellar films and (C) bimetallic Au-Pt nanowires obtained by self-assembly of cylindrical BCP on top of the Pt nanowires.*

Once the platinum nanowires were obtained, a 0.5 wt.% solution of PS_{26k}-*b*-$P4VP_{5,7k}$ in PGMEA was spin coated on top of it. After a subsequent immersion in a metallic gold solution

($HAuCl_4$ 1 wt.%) and a successive O_2 RIE (30 s, 10 sccm, 60 W), a hexagonal array of gold nanodots was obtained, decorating the platinum nanowires and creating a bimetallic complex structure (**Fig. 4.13C**).

These two examples show the high versatility of this strategy to produce different hybrid structures. During this section the formation of several complex structures, *i.e.*, spheres-on-lines or spheres-on-spheres have been presented. Indeed, a wide variety of metallic-metallic or metallic -dielectric combinations are accessible with this approach, giving rise to the possibility of exploring different surface properties.

5. Optical characterization

The bimetallic raspberry-like nanoclusters consisting in an Al_2O_3 core covered by Au satellites were further analysed by variable angle spectroscopic ellipsometry (VASE) in reflection. **Fig. 4.14** presents the evolution of the measured sample at different incident angles (ranging from 50° to 70°). The two ellipsometric parameters I_c and I_s are presented as a function of the photon energy, between 0.5 and 4.8 eV. I_c and I_s are related to the two ellipsometric angles (Ψ, Δ) by the following equations:

$$I_s = \sin(2\Psi) sin\Delta \tag{4.8}$$

$$I_c = \sin(2\Psi) cos\Delta \tag{4.9}$$

The measurements reveal two clear features. The first one is a maximum in both I_c and I_s in the region ≈ 2.1-2.2 eV, which could correspond to the localized surface plasmon resonance (LSPR) of the Au nanoparticles. At least a second less pronounced bump in I_c, associated with a minimum of I_s, is visible at higher energy (3.0-3.1 eV), and may correspond to another resonant mode of the nanostructure. I_c higher energy resonant modes can be observed at high angles at 3.5 eV.

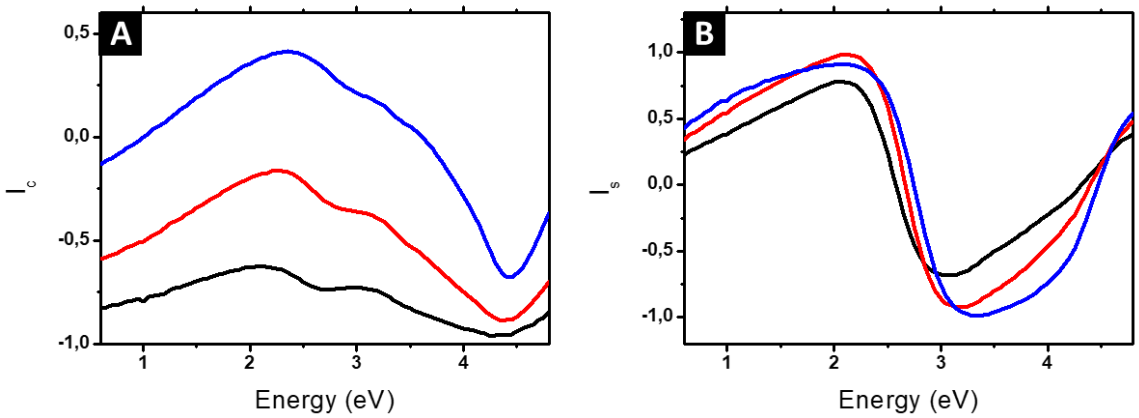

Figure 4.14: *Ellipsometric parameters I_c and I_s as a function of the photon energy for an angle of incidence of θ = 50° (black), 60° (red) and 70° (blue) obtained for the raspberry-like bimetallic nanoclusters formed by a alumina core surronded by gold satellites.*

Raspberry structures have already shown interesting results in colloidal suspensions and 3D assembled materials[10,20]. Indeed, isotropic artificial optical magnetism ($\mu \neq 1$) at visible frequencies was detected using extinction and light scattering. The studied structures consist into a 103 nm silica core, surrounded by gold satellites in an average number of 26 with a diameter of 30 nm. As presented in the introduction of this chapter, no method to obtain an ordered monolayer of these objects has been reported in the literature.

Recent efforts, within a collaborative framework between the MaFIC team at CRPP and the Chemistry of Nanomaterials group at ICMCB, have been devoted to the preparation of monolayers of plasmonic dodecapods, formed by a silica core with twelve gold satellites. The fabrication process of these meta-atoms is as follows. First, silica particles with a controlled number of dimples (12 in the case of the dodecapods) were prepared following a synthetic route developed in the group[21] (**Fig. 4.15A** left). Afterwards, gold NPs are grown in a controlled manner to form patches at the dimples sites (**Fig. 4.15A** right). **Fig. 4.15B** shows the different conditions used in order to control the particle growth.

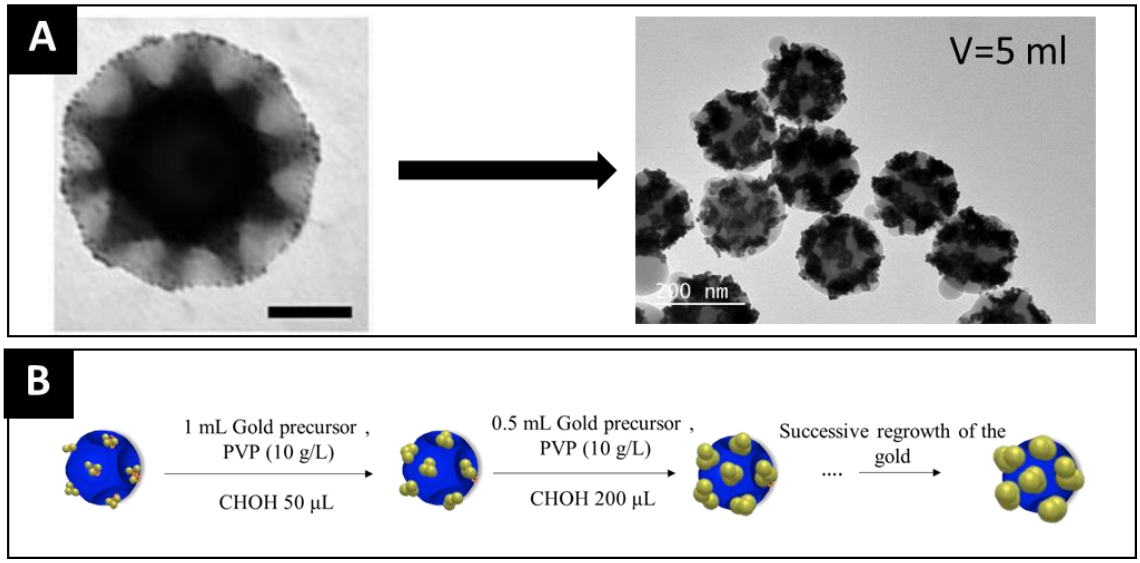

Figure 4.15: (A) *TEM images of the pristine silica particles with the 12 dimples (left) and after growth of the Au NPs in the patches (right). (B) reaction conditions used for the NPs controlled growth.*

Ellipsometric measurements have been performed on one such thin film. The results are presented in **Fig. 4.16** (red line) and compared to the measurements on the templated raspberry-like nanoclusters. The ellipsometric parameter, I_c, shows two clear features as well,

(1.9 and 3 eV respectively) changing in intensity with the incidence angle. I_s shows an incipient S-shape attributed to the resonant behaviour of the sample, which is clearer at high angles.

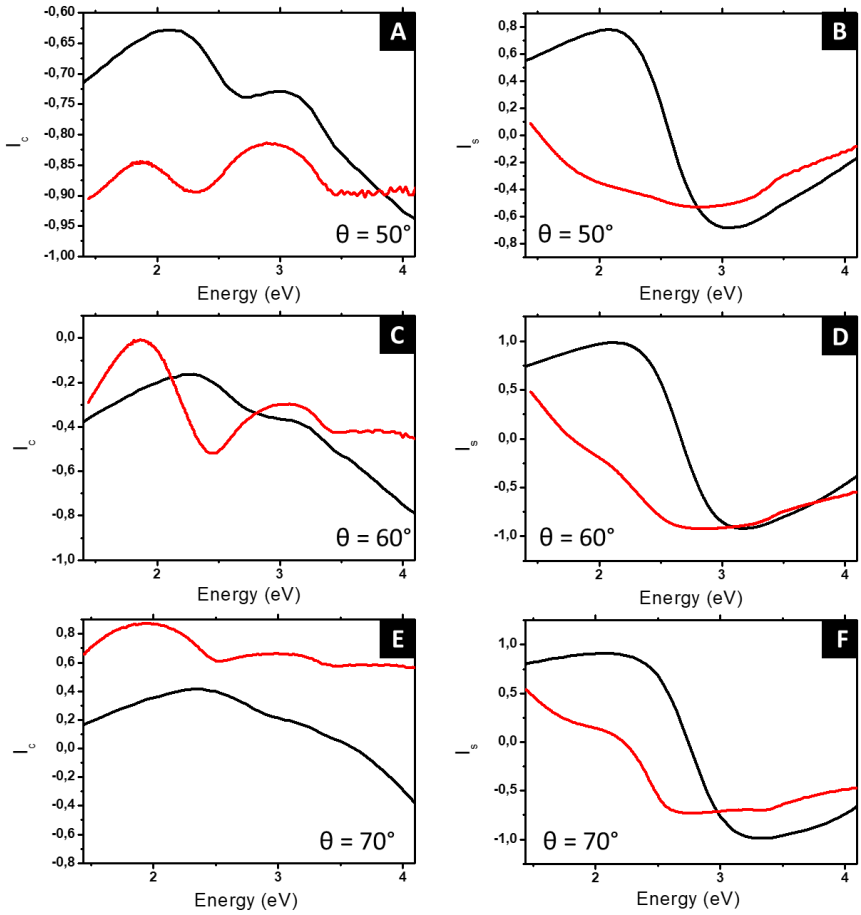

Figure 4.16: *Ellipsometric parameters I_s and I_c as a function of the photon energy for different angles of incidences of θ = 50°, 60° and 70° obtained for the raspberry-like bimetallic nanoclusters formed by an alumina core surrounded by gold satellites (black lines) and the dodecapods consisting in a silica core surrounded by gold satellites (red lines).*

A comparison between the ellipsometric parameters obtained for the bimetallic raspberry-like nanoclusters obtained using BCP multilayer self-assembly (**Fig. 4.16** black lines) and the dodecapods (**Fig. 4.16** red line), suggests that the optical responses are similar. Thereby, we can conclude that the strategy proposed in this section is a straightforward alternative in order to obtain these complex structures, with the additional benefit of providing a well-ordered and defined monolayer organization.

The ellipsometry data of both samples can also be plotted as the ellipsometric angles Ψ and Δ (see **Fig. 4.17**). They show the existence of a maximum of the ellipsometric intensity angle Ψ at Ψ = 90°, while the ellipsometric phase angle Δ jumps abruptly of more than 180° at an incidence angle between 60° and 70° and a photon energy of 2.7 eV. A similar behaviour has been called ''plasmon-induced Brewster'' extinction[22], when the ellipsometric angle Ψ is minimum at Ψ = 0°, while the ellipsometric phase angle Δ jumps abruptly. It has been identified as a method to reach very sensitive plasmonic detection[23] in biological or chemical sensors, thanks to the very large phase jump.

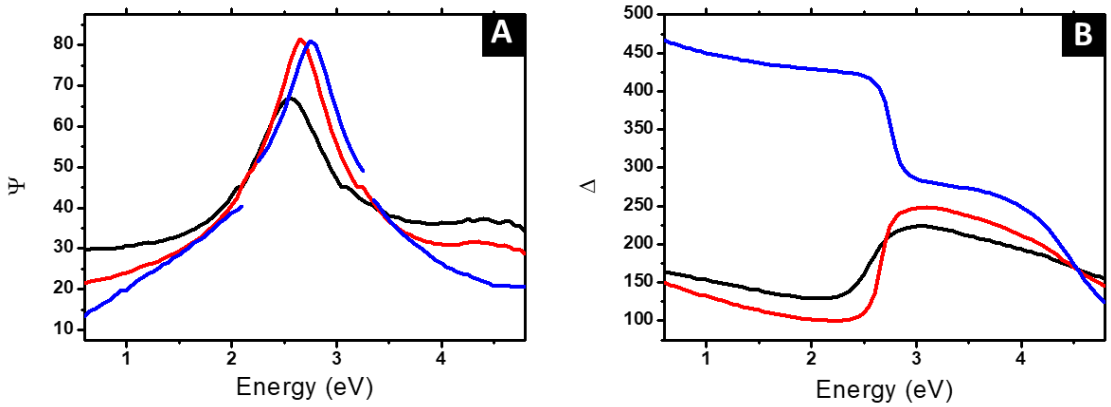

Figure 4.17: *Evolution of the measured ellipsometric angles, Ψ (left) and Δ right), as a function of the photon energy for an angle of incidence of* θ *= 50° (black curve)* θ *= 60° (red curve) and* θ *= 70° (blue curve) for the raspberry-like bimetallic nanoclusters formed by a alumina core surrounded by gold satellites.*

The relation between the ellipsometric angles Ψ and Δ and the reflection coefficients for parallel and perpendicular polarizations is given by the following expression, that constitute the basic equation in ellipsometry

$$\rho = \frac{|r_p|}{|r_s|} e^{i(\delta_p - \delta_s)} = \tan(\Psi) e^{i\Delta}$$

In this case, the remarkable point returned by the ellipsometer as Ψ = 90°, corresponds to the conditions for which the s-polarized light is not reflected (r_s = 0), whereas Ψ = 0° corresponds to r_p=0. For a simple isotropic film, which can be described by a single effective optical index n = *n* + *ik*, the extinction corresponds to a specific combination of the parameters defining r_s,

through the Fresnel coefficients, namely the wavelength λ, the angle of incidence, the index $N = n + ik$ of the film material and those of the ambient (air) and substrate media. Only a limited number of examples of extinction of r_s have been described, so far, in the literature[24], and even less in self-assembled nanostructures.

6. Building a UV transparent absorber

6.1. Introduction

Besides manipulation of light for optical devices, nanoplasmonic surfaces can also find applications in the field of photovoltaics. Indeed, in the last decade, organic photovoltaics (OPVs) has shown impressive progress. Continuous improvements in material synthesis and advancements in cell architecture gave rise to power conversion efficiencies (PCE) of up to 12%[25,26]. Incorporation of plasmonic nanostructures for light trapping in these thin-film devices offers an attractive solution to increase further the PCE of these systems[27].

Various light trapping strategies have been explored to enhance the sunlight absorption in the light-harvesting layer(s) of photovoltaic devices, including front and back surface texturing[28,29] and using photonic crystals[30]. This strategy is well-suited for thick conventional inorganic photovoltaics (IPVs) but not for thin film OPVs. A new method for achieving light trapping in thin-film solar cells is the use of metallic nanostructures that support surface plasmon resonances[31]. But the main problem of these solutions is so far that they require the use of a backing metallic layer (see **Fig. 4.18**). This element, crucial for the proper operation of the absorber, makes the transmission coefficient of the device approximately equal to zero for any frequency and is thus an important restriction limiting the possible application of such devices.

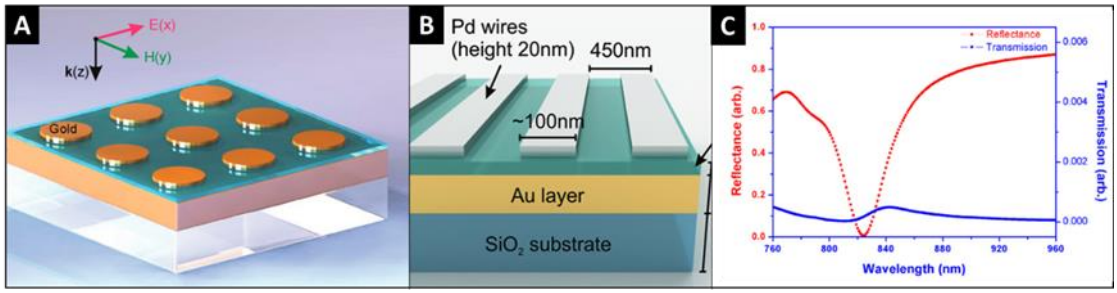

Figure 4.18: *(A and B) examples of stacks leading to optical absorbers with the backing metallic layer leading to (C) zero transmission at any frequency.*

In our case, we consider substituting this metal layer with an optical metasurface, made of plasmonic gold NPs synthetized using a BCP thin film as a template, and then, start

to grow consecutive layers, to create an optical device able to selectively absorb incident light, thanks to the localized surface plasmon resonance (LSPR) of the gold NPs, in a desired frequency range while being almost completely transparent outside this range. During the following sections we will present the fabrication process and the optical characterization of this composite.

6.2. Layer-by-layer deposition

The fabrication process is presented in **Fig. 4.19**. It consists in the deposition of consecutive layers of metallic NPs and polystyrene layers as spacer.

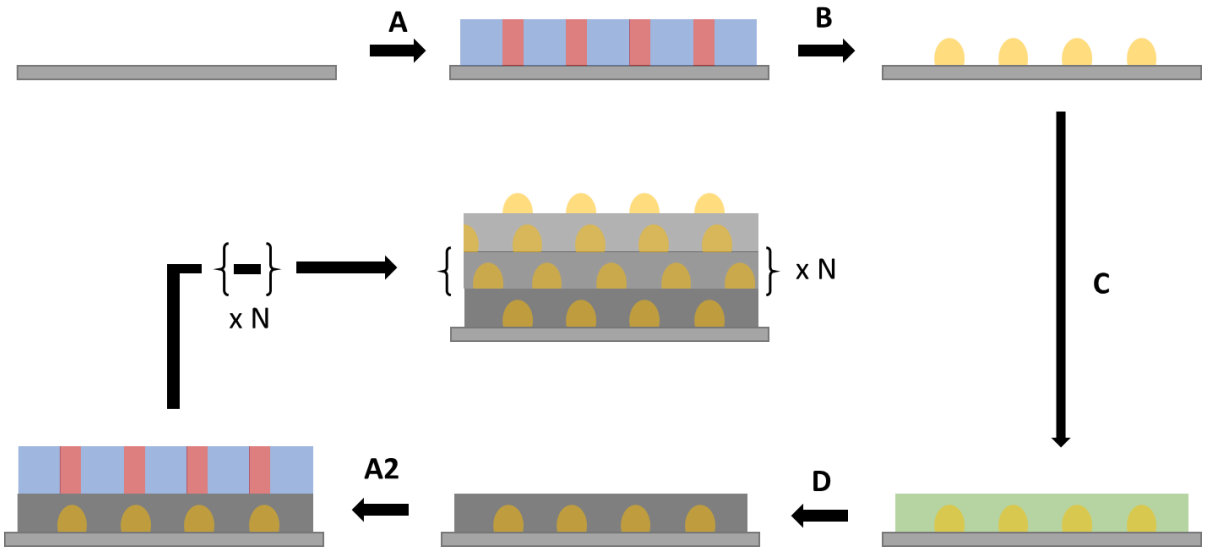

Figure 4.19: *Schematic representation of the fabrication process of transparent UV absorbers. (A) self-assembly of the cylindrical BCP, (B) selective hybridization and O_2 RIE treatment in order to obtain the metallic NPs array, (C) cross-linkable polystyrene layer deposition by spin-coating, (D) cross-link process, (A2) deposition of the second BCP layer. The process continues N times until obtaining the desirable number of layers.*

A 2.5 wt.% solution of PS-b-P4VP in toluene was spin-coated (30 s, 4000 rpm) onto bare glass substrates to give a thickness around 90 nm. Atomic force microscopy (AFM) topographical image obtained after a subsequent solvent vapour annealing (SVA) of the sample in THF vapours for 24 h is showed in **Fig. 4.20A**. Out of plane cylinders of P4VP inside of PS matrix are

observed as it was explained in **Chapter 3**. After the selective impregnation by immersion in a 1 wt.% $HAuCl_4$ aqueous solution and the reduction by O_2 RIE (60 W, 10 sccm, 75 s), gold NPs arrays are obtained on top of the silicon substrate (**Fig. 4.20B**).

The process continues with the deposition of a cross-linkable polystyrene layer of 100 nm on top of the gold NPs (4 wt.% toluene solution, 2000rpm). The PS layer is cross-linked by heating the sample for 10 min at 240°C in a hotplate. After rinsing the sample with toluene, it was observed by AFM (**Fig. 4.20C**). A flat surface without distinct topographical features is obtained, meaning that the PS layer has covered the gold NPs. A second layer of BCP is then spin coated on top of the PS layer (**Fig. 4.20D**), repeating the different steps as previously described, until the desirable number of layers is obtained.

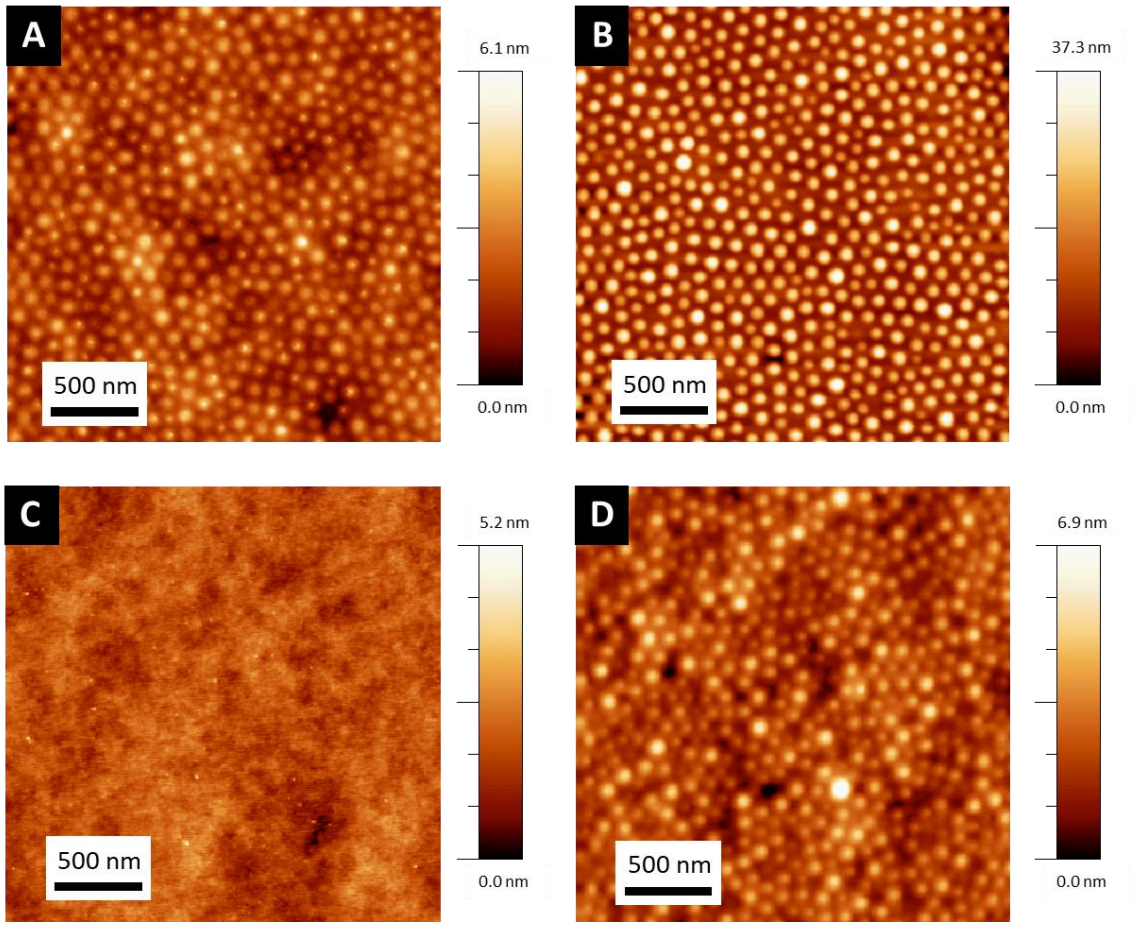

Figure 4.20: *AFM topographical images at different steps of the fabrication process, (A) after casting from a PS-b-P4VP 2.5 wt. % in toluene solution and after 24h THF SVA, (B) after selectively impregnation and O_2 RIE, (C) after deposition of a PS layer, crosslinked by heating at 240°C for 10 min (D) after casting the second layer from a PS-b-P4VP 2.5 wt. % in toluene solution and after 24h THF SVA.*

With the additional layers, the colour of the sample starts to change from transparent to light-purple. After 10 layers of gold NPs the sample presents an intense purple colour (See **Fig. 4.21A**) due to the intense plasmon resonance of the composite created, but the sample is still highly transparent. An AFM image of the last layer is presented in **Fig. 4.21B**, showing the robustness of the fabrication process. In the next section we will present the optical characterization of these films.

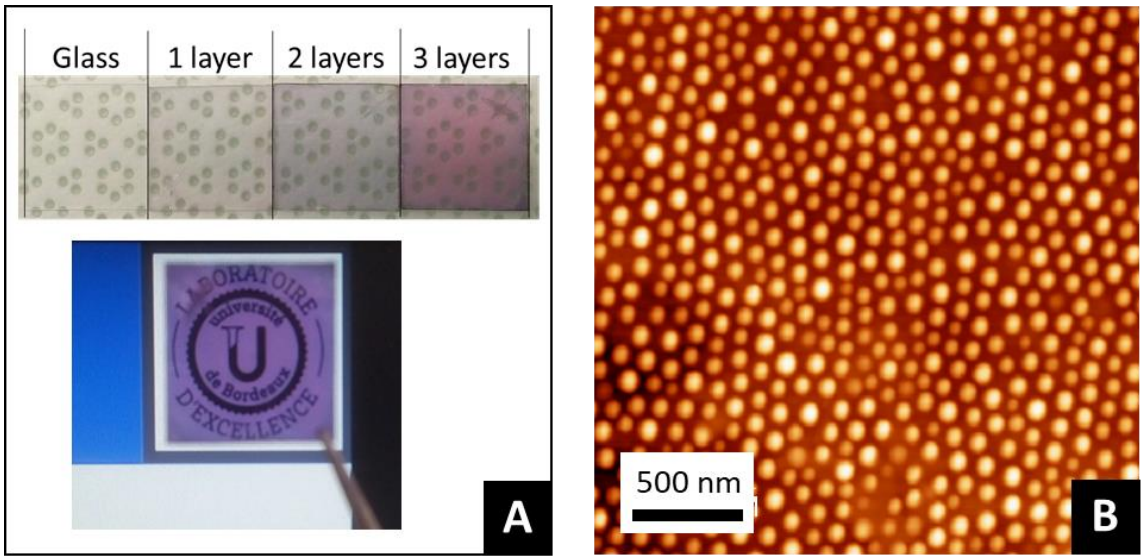

Figure 4.21: *(A) Images of the samples at different steps of the process in front of a white paper with grey dots (upper part) and in front of a white paper with a printed black logo (B) AFM image of the upper surface of the film after the deposition of 10 layers.*

6.3. Optical characterization

6.3.1. Building a selective transparent absorber

In order to quantify and study the light absorption of the samples with the different layers, some near IR-VIS-UV spectrometry measurements were carried out at each deposition step. **Fig. 4.22** shows the transmission (T) measurements obtained for a sample ranging from 1 to 10 layers. A progressive decrease of the transmission in the spectral region from 500-600 nm^{-1} is observed. This is assigned to the surface plasmon resonance of the gold NPs. Each additional layer induces a decrease in the transmission by 8-10%. At the end of the process

(after 10 layers) a transmission of 15% is obtained, that correspond to an absorption of 0.85. At wavelength above 800 nm, the transmission is close to 90%, pointing out the selective absorption of our system.

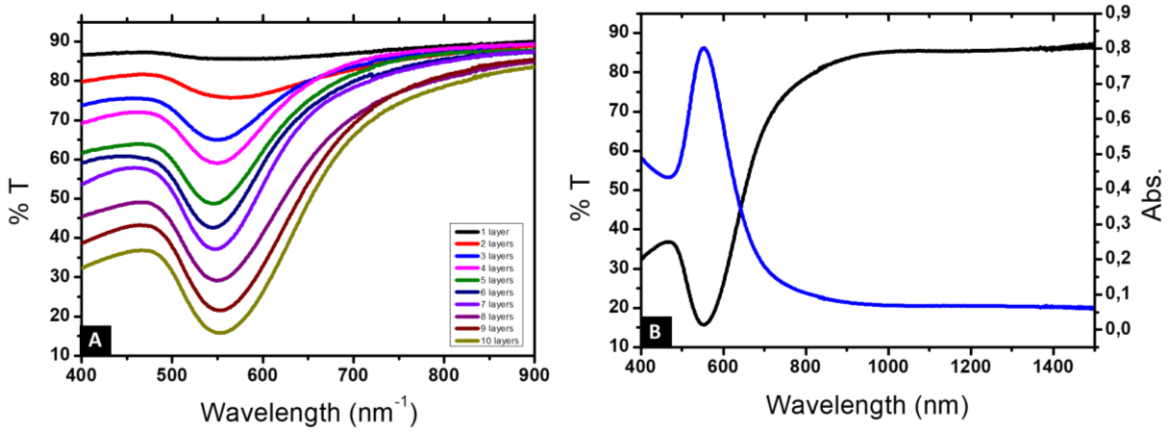

Figure 4.22: *(A) VIS-IR spectrometry measurements in transmission obtained for films from 1 to 10 layers. (B) Transmission and absorption VIS-IR spectrometry data corresponding to the sample after 10 layers.*

This selective and high absorption makes this device very suitable for several applications, from photovoltaics to optical filters. But even more interesting, it could be a platform to build tailored hyperbolic metamaterials.

6.3.2. Towards a 3D metamaterial

During this thesis we have presented the high level of control that we have over 2D structures, and in the last sections we have demonstrated that it is possible to build a 3D material in a controllable way. Recently, as it was presented in **Section 6.1.2** of **Chapter 1**, Wang *et al*.[32] have demonstrated the possibility of using a self-assembly methodology for the fabrication of bulk hyperbolic metamaterial. Using the self-assembly of a lamellar BCP and the selective impregnation with metallic salt, nanocomposites consisting of alternating pure PS and Au NPs:P2VP layers were obtained (**Fig. 4.23**).

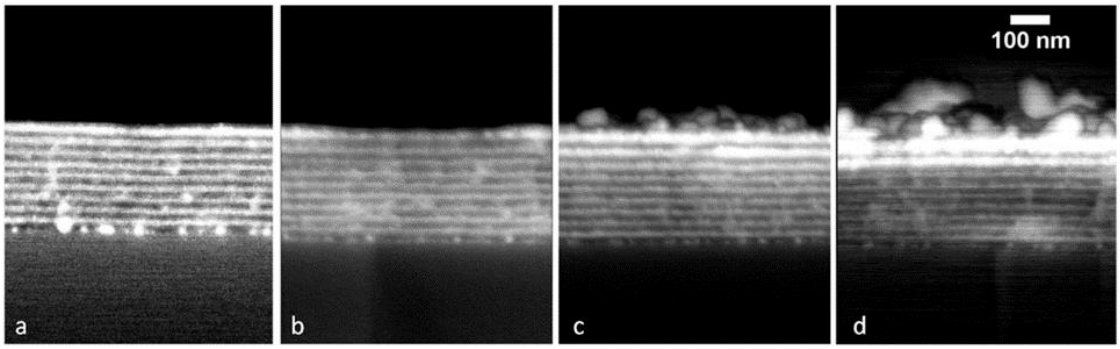

Figure 4.23: *Backscattering scanning electron microscopy side-view image (SEM) of the 265 nm-thick film of alternating layers of pure polymer (PS, appearing black) and of Au NPs:P2VP nanocomposite, appearing white, for a number of cycles of gold impregnation and reduction of 5 (a), 10 (b), 20 (c), 30 (d).*

The in-situ nature of the gold nanoparticles synthesis does not allow a full control on the size, shape and distribution of the particles inside of each layer. The strategy developed herein overpasses this limitation. The sequential growth by a layer-by-layer technique allows us to obtain an unprecedented control over the structural parameters. The size and inter-distances between the particles can be controlled as we have previously showed only choosing the suitable BCP. Different metals or non-metal species can be introduced, only modifying the impregnation process. Besides the interlayer distances can also be tuned by controlling the cross-linkable polystyrene layer thickness.

In order to have a proof-of-concept of the optical properties that could be possible to achieve with this material, the ten layered sample was further analysed by variable angle spectroscopic ellipsometry (VASE) in reflection. **Fig 4.24** presents the evolution of the measured sample at different incident angles (ranging from 50° to 70°). The two ellipsometric parameters I_c and I_s are presented as a function of the photon energy, between 1.4 and 3.3 eV. I_c and I_s are related with the two ellipsometric angles (Ψ, Δ) by **Equation 4.8** and **4.9**.

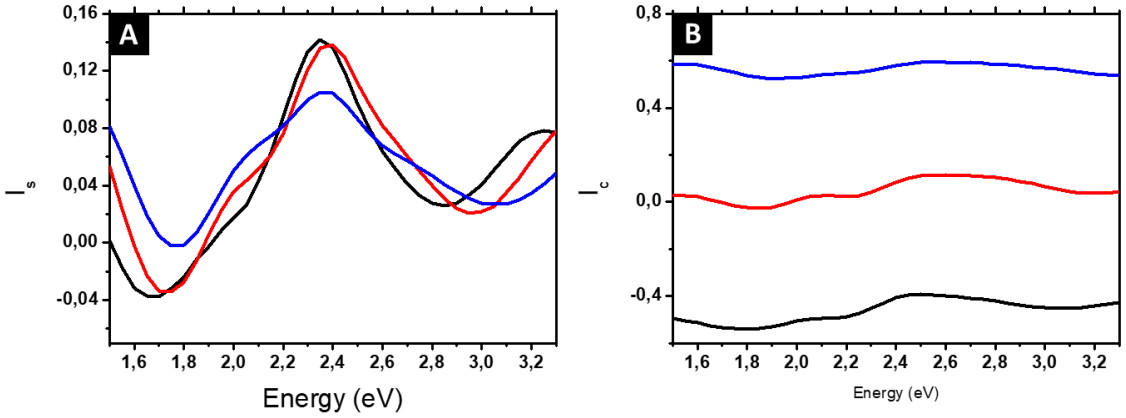

Figure 4.24: *Ellipsometric parameters I_s and I_c as a function of the photon energy for different angle of incidence (ϑ = 50° (black), 60° (red) and 70° (blue) obtained for the 10-layers sample.*

The values (especially of I_s) are very weak which could be explained in part by the use of glass as a substrate. In any case, a clear feature at 2.3 eV is observed and attributed to the LSPR of the Au NPs present in the sample. The weakness of the signal renders very difficult to fit the experimental data with an ellipsometric model. Since this 3D sample is made using 10 consecutive layers of the 2D decorated surfaces analysed in **Chapter 3**, **Section 5.2** we used the same approach. The Maxwell Garnett formula modified for oriented ellipsoids (**Equation 3.11**) was applied to the experimental data (**Fig. 4.25**) and the optimal fitting values are listed in **Table 4.4**.

Sample	*t* (nm)	$L_x = L_y$	L_z	f_{Au}
10 Layers	997	0.39	0.22	19.1

Table 4.4: *Structural parameters extracted from the fit of the ellipsometry data with the oriented ellipsoids Maxwell Garnett formula: t the film thickness. f_{Au} the gold volume fraction and L_x, L_y and L_z the depolarization factors along the three ellipsoidal semi-axes.*

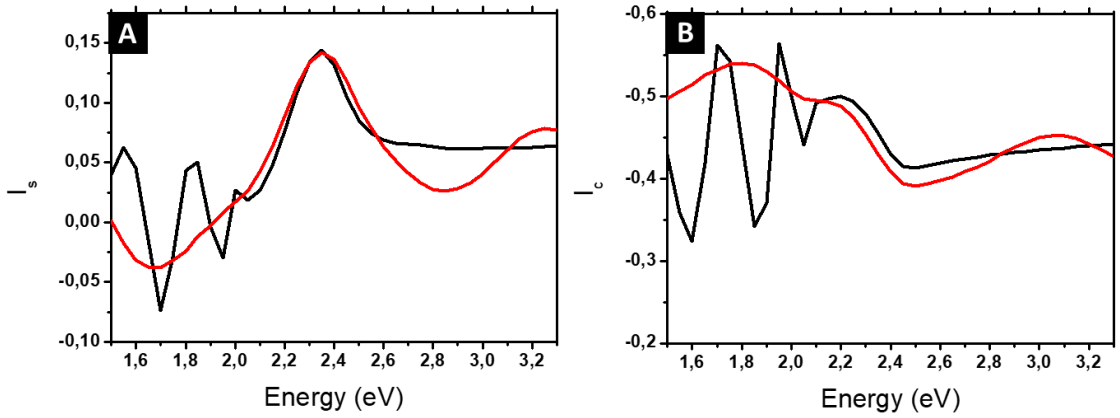

Figure 4.25: *Plots of the experimental ellipsometric quantities, I_s and I_c (red line) and the corresponding fitting using the oriented ellipsoids Maxwell Garnett formula (black line) for an angle of incidence θ = 50°.*

Unfortunately, the fitting was not fully satisfactory, especially for the spectral region below 2 eV. Besides glass can present several backside reflections, that makes even more complicated the fitting and the ellipsometric model analysis (although they can be corrected with the DeltaPsi software). Nevertheless, around the region of the LSPR of the Au NPs (2.3 eV), the quality of the fit is satisfactory, and we decided thus to tentatively extract the anisotropic effective permittivities $\varepsilon_x = \varepsilon_{r,x} + i\varepsilon_{i,x}$ and $\varepsilon_z = \varepsilon_{r,z} + i\varepsilon_{i,z}$ of the composite film (**Fig 4.26**).

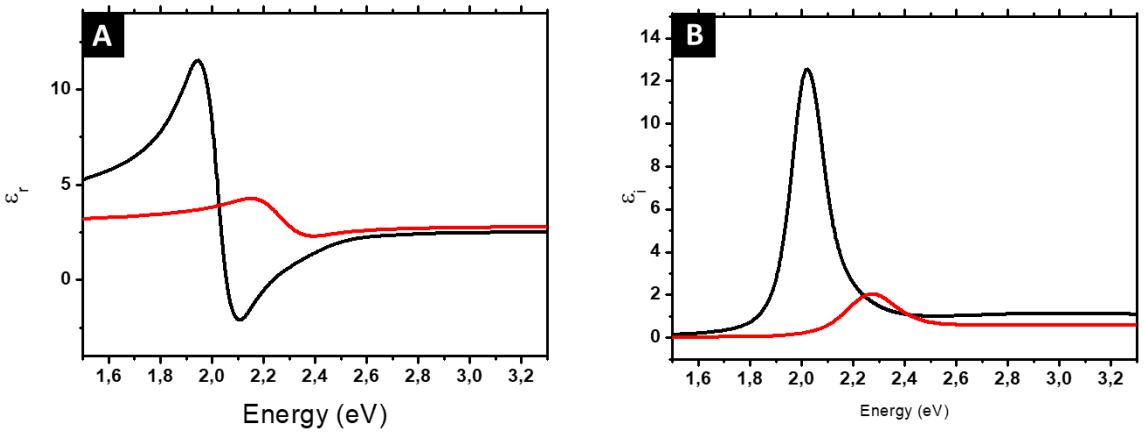

Figure 4.26: *Perpendicular (black line) and parallel (red line) components of the (A) real and (B) imaginary dielectric functions extracted from the MG oriented ellipsoidal formula for the 10 layers sample.*

Fig; 4.26 shows the potential of this strategy to create highly anisotropic 3D metamaterials even if additional and more robust analysis is needed in order to confirm this behaviour.

We can conclude this section pointing out that such strategy is promising even if further studies are needed to completely assess its potential. As a *motto*, this strategy could be summarized as “From 2D to 3D, building on-demand 3D structures”.

7. Conclusions

Through this chapter, we have introduced an interesting type of meta-atoms consisting in a dielectric core surrounded by different metallic satellites. This design leads to structures presenting artificial optical magnetism ($\mu \neq 1$). Due to the final shape, these objects are commonly named as raspberry nanoclusters. We have presented here a versatile and straightforward strategy to obtain on-demand bimetallic raspberry nanoclusters using multi-layered self-assembled BCP films, selectively impregnated with different metallic species. Indeed, for the first time, ordered monolayers of this kind of structures have been obtained. Several techniques, *i.e.*, AFM, SEM, GISAXS and XRR, have been used to characterize the designed structures. Finally, optical measurements by VASE have revealed the similarities between our structures and the ones synthetized by a colloidal chemistry approach.

In the second part of the chapter we have presented how the control obtained in the self-assembly of 2D structures can help us to create on-demand 3D materials, where all the structural parameters can be easily tuned. Layer-by-layer deposition of gold NPs arrays obtained by self-assembled BCP films, allows us to obtain a transparent and selective absorber in the visible region of the spectra, with possible applications in the OPV field. Moreover, this approach constitutes a very promising starting point in the design of new structures for hyperbolic 3D metamaterials.

1. Smith, D. R., Padilla, W. J., Vier, D. C., Nemat-Nasser, S. C. & Schultz, S. Composite Medium with Simultaneously Negative Permeability and Permittivity. *Phys. Rev. Lett.* **84,** 4184–4187 (2000).

2. Landau, L. D. (Lev D., Lifshi͡ts, E. M. (Evgeniĭ M. & Pitaevskiĭ, L. P. (Lev P. *Electrodynamics of continuous media*. (Butterworth-Heinemann, 1984).

3. Lerond, T., Proust, J., Yockell-Lelièvre, H., Gérard, D. & Plain, J. Self-assembly of metallic nanoparticles into plasmonic rings. *Appl. Phys. Lett.* **99,** 123110 (2011).

4. Lamarre, S. S., Lemay, C., Labrecque, C. & Ritcey, A. M. Controlled 2D Organization of Gold Nanoparticles in Block Copolymer Monolayers. *Langmuir* **29,** 10891–10898 (2013).

5. Lamarre, S. S. *et al.* Optical properties of Au colloids self-organized into rings via copolymer templates. *J. Nanoparticle Res.* **15,** 1656 (2013).

6. Simovski, C. R. & Tretyakov, S. A. Model of isotropic resonant magnetism in the visible range based on core-shell clusters. *Phys. Rev. B* **79,** 045111 (2009).

7. Gomez-Graña, S. *et al.* Hierarchical self-assembly of a bulk metamaterial enables isotropic magnetic permeability at optical frequencies. *Mater. Horizons* **3,** 596–601 (2016).

8. Le Beulze, A. *et al.* Robust raspberry-like metallo-dielectric nanoclusters of critical sizes as SERS substrates. *Nanoscale* **9,** 5725–5736 (2017).

9. Alù, A., Salandrino, A. & Engheta, N. Negative effective permeability and left-handed materials at optical frequencies. *Opt. Express* **14,** 1557 (2006).

10. Ponsinet, V. *et al.* Resonant isotropic optical magnetism of plasmonic nanoclusters in visible light. *Phys. Rev. B* **92,** 220414 (2015).

11. Höller, R. P. M. *et al.* Protein-Assisted Assembly of Modular 3D Plasmonic Raspberry-like Core/Satellite Nanoclusters: Correlation of Structure and Optical Properties. *ACS Nano* **10,** 5740–5750 (2016).

12. Qian, Z. *et al.* Raspberry-like Metamolecules Exhibiting Strong Magnetic Resonances. *ACS Nano* **9,** 1263–1270 (2015).

13. Rahman, A., Majewski, P. W., Doerk, G., Black, C. T. & Yager, K. G. Non-native three-dimensional block copolymer morphologies. *Nat. Commun.* **7,** 13988 (2016).

14. Tavakkoli K. G., A. *et al.* Multilayer block copolymer meshes by orthogonal self-assembly. *Nat. Commun.* **7,** 10518 (2016).

15. Majewski, P. W., Rahman, A., Black, C. T. & Yager, K. G. Arbitrary lattice symmetries via block copolymer nanomeshes. *Nat. Commun.* **6,** 7448 (2015).

16. Compton, A. H. *X-rays in theory and experiment,*. (New York, 1935).

17. Pietsch, U., Holý, V. & Baumbach, T. *High-Resolution X-Ray Scattering*. (Springer New York, 2004). doi:10.1007/978-1-4757-4050-9

18. Born, M. & Wolf, E. *Principles of optics : electromagnetic theory of propagation, interference and diffraction of light*. (Cambridge University Press, 1999).

19. Björck, M. & Andersson, G. GenX : an extensible X-ray reflectivity refinement program utilizing differential evolution. *J. Appl. Crystallogr.* **40,** 1174–1178 (2007).

20. Gomez-Graña, S. *et al.* Hierarchical self-assembly of a bulk metamaterial enables isotropic magnetic permeability at optical frequencies. *Mater. Horizons* **3,** 596–601 (2016).

21. Hubert, C. *et al.* Synthesis of multivalent silica nanoparticles combining both enthalpic and entropic patchiness. *Faraday Discuss.* **181,** 139–146 (2015).

22. Toudert, J. *et al.* Plasmonic Optical Interferences for Phase-Monitored Nanoscale Sensing in Low-Loss Three-Dimensional Metamaterials. *ACS Photonics* **2,** 1443–1450 (2015).

23. Kravets, V. G. *et al.* Singular phase nano-optics in plasmonic metamaterials for label-free single-molecule detection. *Nat. Mater.* **12,** 304–309 (2013).

24. Svedendahl, M., Johansson, P. & Käll, M. Complete Light Annihilation in an Ultrathin Layer of Gold Nanoparticles. *Nano Lett.* **13,** 3053–3058 (2013).

25. Yu, J. *et al.* Towards High Performance Organic Photovoltaic Cells: A Review of Recent Development in Organic Photovoltaics. *Polymers (Basel).* **6,** 2473–2509 (2014).

26. Sun, S.-S., Sariciftci, N. S. & Sariciftci, N. S. *Organic Photovoltaics*. **99,** (CRC Press, 2005).

27. Gan, Q., Bartoli, F. J. & Kafafi, Z. H. Plasmonic-Enhanced Organic Photovoltaics: Breaking the 10% Efficiency Barrier. *Adv. Mater.* **25,** 2385–2396 (2013).

28. Yerokhov, V. Y. *et al.* Cost-effective methods of texturing for silicon solar cells. *Sol. Energy Mater. Sol. Cells* **72,** 291–298 (2002).

29. Llopis, F. & Tobías, I. The role of rear surface in thin silicon solar cells. *Sol. Energy Mater. Sol. Cells* **87,** 481–492 (2005).

30. Krc, J., Zeman, M., Luxembourg, S. L. & Topic, M. Modulated photonic-crystal structures as broadband back reflectors in thin-film solar cells. *Appl. Phys. Lett.* **94,** 153501 (2009).

31. Atwater, H. A. & Polman, A. Plasmonics for improved photovoltaic devices. *Nat. Mater.* **9,** 205–213 (2010).

32. Wang, X. *et al.* [INVITED] Hyperbolic-by-design self-assembled metamaterial based on block copolymers lamellar phases. *Opt. Laser Technol.* **88,** 85–95 (2017).

General conclusions

During this Ph.D., plasmonic nanostructured surfaces were created by taking advantage of the BCP segregation behaviour. A straightforward approach was developed based on the selective hybridization by metallic or dielectric precursors of self-assembled BCP films as an alternative to traditional top-down techniques. In the aim of controlling the optical responses by structural design, various metallic or metallic/dielectric arrays (dot arrays, continuous lines and complex multi-component structures) were produced from a library of block copolymers having different macromolecular characteristics. These resulting structures were further probed as regards to their optical properties with the challenge to induce unconventional responses.

Firstly, high refractive index surfaces were obtained using the self-assembly of a lamellar PS-*b*-P2VP. The selective and controllable hybridization of the BCP films with gold salts leads to arrays, after a subsequent O_2 RIE treatment, formed by gold NPs with different aspect ratios. Indeed, decorated surfaces consisting in spherical, rod-like particles with different degree of elongation or even continuous lines were obtained following this methodology. The morphological evolution of the gold NPs has a significant effect on the final optical properties as the gold patterns, formed by elongated spheroids, with a high degree of homogeneity and a gold content as low as 16 vol %, reach a refractive index of more than 3 in the visible domain.

Nanostructured plasmonic surfaces have also been produced through the macromolecular engineering of a series of cylinder-forming block copolymers having a wide range of molecular weights. Arrays of gold dots, regularly organized in a hexagonal lattice, were obtained and the optical properties of these samples were tuned by controlling the structural parameters of the arrays, *i.e.*, the NPs diameter, the interparticle distance or the height of the structures created on top of the surface. A significant and anisotropic plasmon resonance signature was obtained for the gold arrays prepared from the selective impregnation of an ultra-high molecular weight BCP. The spectroscopic ellipsometry data indicated a near-zero effective electric permittivity in the out-of-plane direction in the spectral

region from 516 nm^{-1} to 590 nm^{-1}, leading potentially to the application of such structures as low impedance metasurfaces.

Besides, we extended the variety of hybridized materials to others metals and dielectrics. For instance, metallic Pt and Ag structures were created by immersion of BCP thin films into precursor solutions. In another demonstration, colloidal gold NPs were selectively bound to the BCP domains. Finally, dielectric Al_2O_3 and TiO_2 arrays were produced using the ALD technique adapted to the hybridization of BCP thin films.

All these different combinations of structural parameters and materials allow us to create more complex structures using a layer-by-layer self-assembly strategy. As examples, raspberry-like bimetallic nanoclusters and layered hybrid (metallic/polymer) structures were designed paving the way to the production of on-demand 3D structures from BCP self-assembly. Preliminary optical characterizations also showed the potential of such complex structures for manipulating electromagnetic waves.

The different strategies presented herein are thus promising even if further work is needed to completely assess the potential of these decorated surfaces. A particular point of interest would be to design anisometric plasmonic NPS arrays. Indeed, a recent collaborative project with Pr. Kildemo, from the Norwegian University of Science and Technology, has been launched with the objective of exploring the innovative concept of phase gradients along the surface. Such phase gradients can be produced from gradients in the orientation, size and shapes of the particles along the surface. Such metasurfaces can then be exploited to control properties such as colour and polarization. We believe BCP self-assembly can provide a great alternative in order to create these phase gradient surfaces.

A

ANNEX | Instruments and methods

1. Introduction

In this **Annex**, a description of the structural and optical techniques as well as the experimental conditions used during this study will be presented. We will start by describing the polymer synthesis and the different techniques of characterization to access their macromolecular parameters (NMR and SEC). After that, spin coating will be introduced as it is the main deposition technique used to prepare the thin polymer films. Finally, the different structural and optical techniques used to characterize the properties of the nanostructured thin films will be thoroughly described, including AFM, SEM, XPS, KPFM, GISAXS, Spectral reflectometry and VASE

2. Polymer synthesis

2.1. Materials and purification.

In chapter 3, various PS-*b*-P2VP and PS-*b*-P4VP having different molecular weights were synthetized via sequential anionic polymerization[1]. The monomers and solvents were distilled as previously described in the literature[2,3] in order to remove impurities (mainly protic species). The vinylpyridine monomers were doubly cryo-distilled under vacuum over CaH_2. Styrene was first cryo-distilled over CaH_2 followed by a second cryo-distillation over dibutylmagnesium (1.0 M in heptane, Sigma Aldrich). Tetrahydrofuran (THF, Sigma Aldrich) was obtained from a Braun MB-SPS-800 solvent purification system and stored over sodium benzophenone ketyl under dry atmosphere prior to use.

All the anionic polymerizations were performed in an inert atmosphere of argon using schlenk techniques to avoid the introduction of oxygen in the media. Monomers and solvent were stored in burettes after their cryo-distillation, and the *sec*-BuLi initiator was introduced with a sealed syringe through a septum surrounded by parafilm. The glassware was flame-dried and at least three cycles of vacuum / argon were performed before the beginning of the reaction. The reaction was carried out under a small argon overpressure to limit the risks of contamination.

2.2. Polymer characterization

^{1}H-NMR spectra were recorded using a Bruker AC-400 NMR spectrometer at room temperature. The resonance frequency was at 400 MHz and the solvent used was CD_2Cl_2. Size Exclusion Chromatography (SEC) was performed at room temperature and the samples were prepared in a mixture of THF/trichlorobenzene (1L/2mL) as solvent. Trichlorobenzene is used as a flow marker and the measurements are performed at 30°C at a flow rate of 0.8 mL.min^{-1} using a differential refractometer RI (Varian) and a UV-Visible spectrophotometer (Varian) operating at 260 nm and using 3TSK gel Tosoh columns. The elution times were converted into molecular weights using a calibration curve based on low dispersity polystyrene standards. The shoulders appearing in **Fig. 5.5** and **5.6** are attributed to the presence of some PS homopolymer impurities produced during the reactions (*i.e.*, uncomplete crossover between the styrene and the vinylpyridine blocks).

2.2.1. ^{1}H-NMR characterization

Below are given the ^{1}H NMR spectra of the copolymers synthesized during this study. All the ^{1}H NMR spectra show the characteristic peaks of the P2VP and PS protons and the composition of the BCPs were calculated using the signals at 8-8.5 ppm (m, 1H P2VP) and 6-7.5 ppm (m, 5H PS and m, 3H P2VP).

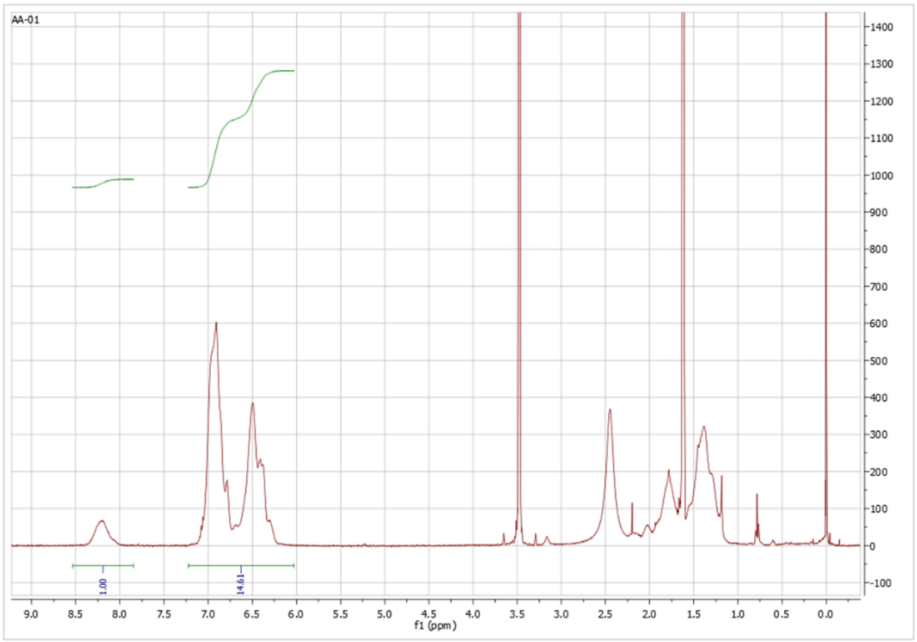

Figure 5.1: *^{1}H-NMR (CD2Cl2, 400 MHz) of the* $PS_{14.7K}$-*b*-$P4VP_{6.3k}$

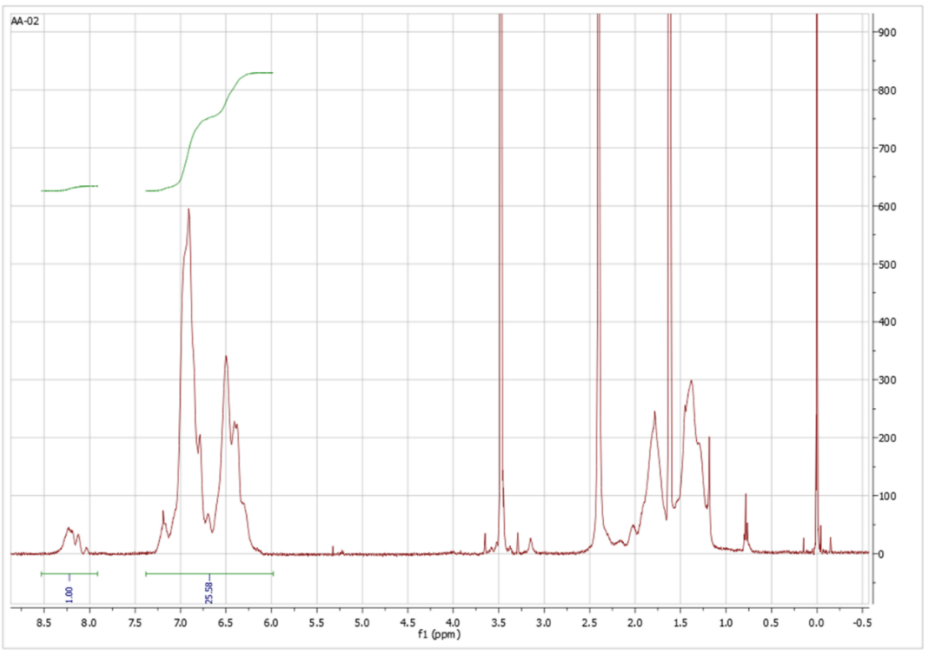

Figure 5.2: *^{1}H-NMR (CD2Cl2, 400 MHz) of the* PS_{150K}-b-$P2VP_{32k}$

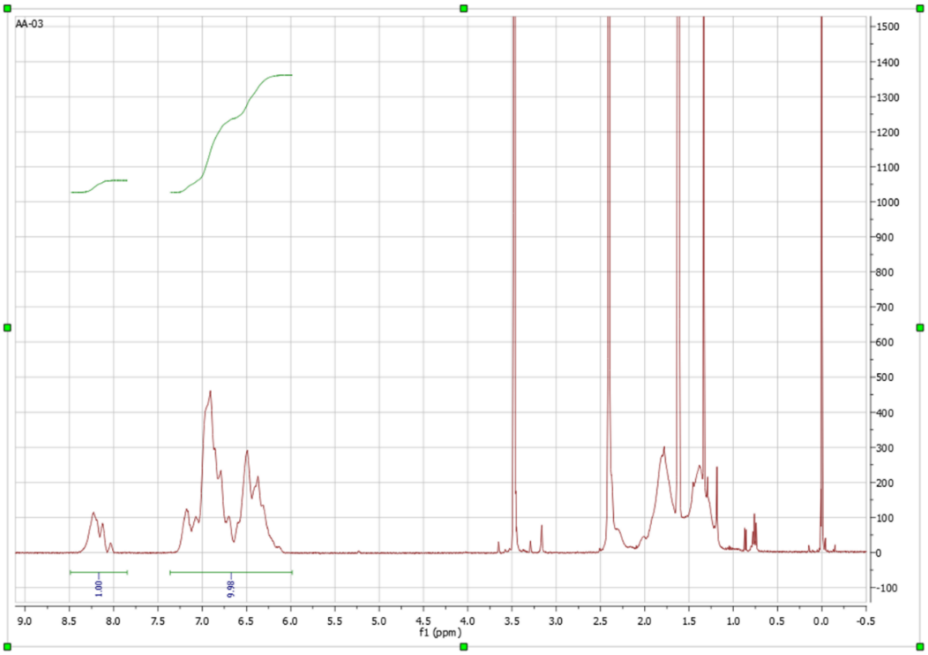

Figure 5.3: *^{1}H-NMR (CD2Cl2, 400 MHz) of the* PS_{267k}-b-$P4VP_{177k}$

2.2.2. SEC characterization

Below are presented the SEC traces for the copolymers synthesized in this study.

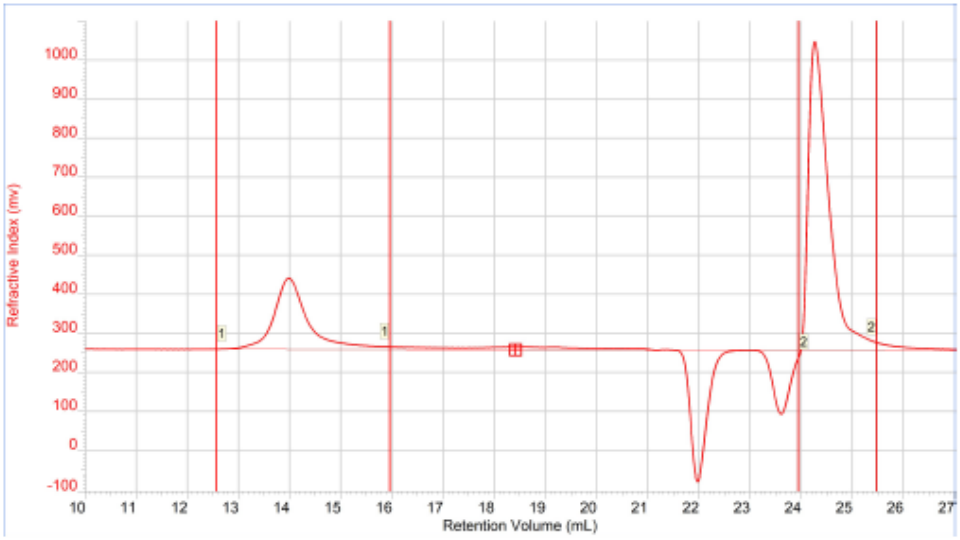

Peak	Mn	Mw	Mz	Mp	Mw/Mn	Ret Vol
1	21 046	25 943	30 461	26 803	1.233	13.976

Figure 5.4: *SEC spectra (UV-vis trace) of* $PS_{14.7K}$-*b*-$P4VP_{6.3k}$

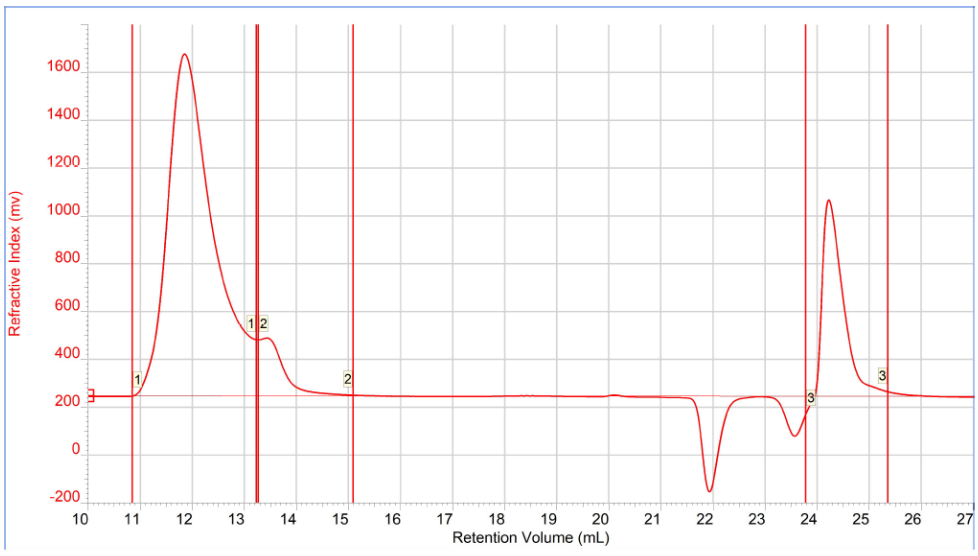

Peak	Mn	Mw	Mz	Mp	Mw/Mn	Ret Vol
1	182 750	248 769	318 579	272 638	1.361	11.845
2	35 068	38 507	40 826	45 110	1.098	13.421

Figure 5.5: *SEC spectra (UV-vis trace) of* PS_{150K}-b-$P2VP_{32k}$

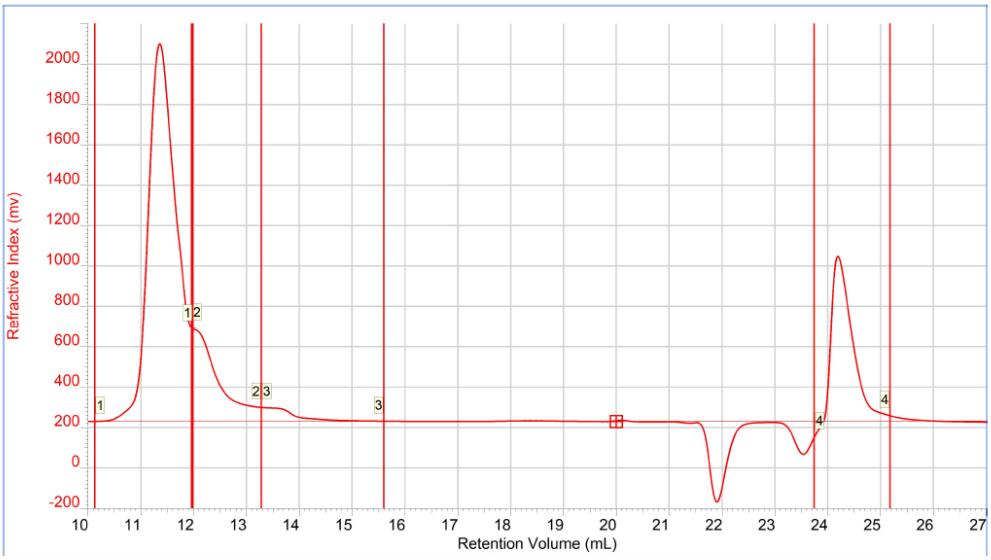

Peak	Mn	Mw	Mz	Mp	Mw/Mn	Ret Vol
1	443 973	500 398	571 469	514 705	1.127	11.352
2	129 442	150 828	167 427	211 008	1.165	12.035
3	28 269	33 717	37 271	46 602	1.193	13.373

Figure 5.6: *SEC spectra (UV-vis trace) of* PS_{267k}-b-$P4VP_{177k}$

3. Thin film process

3.1. Spin-coating

Spin coating is one of the most common techniques for to deposit polymer solutions in thin films. It is used in a wide variety of industrial and technological sectors. The advantage of spin coating is its ability to quickly and easily produce very uniform films, ranging from a few nanometers to a few microns in thickness.

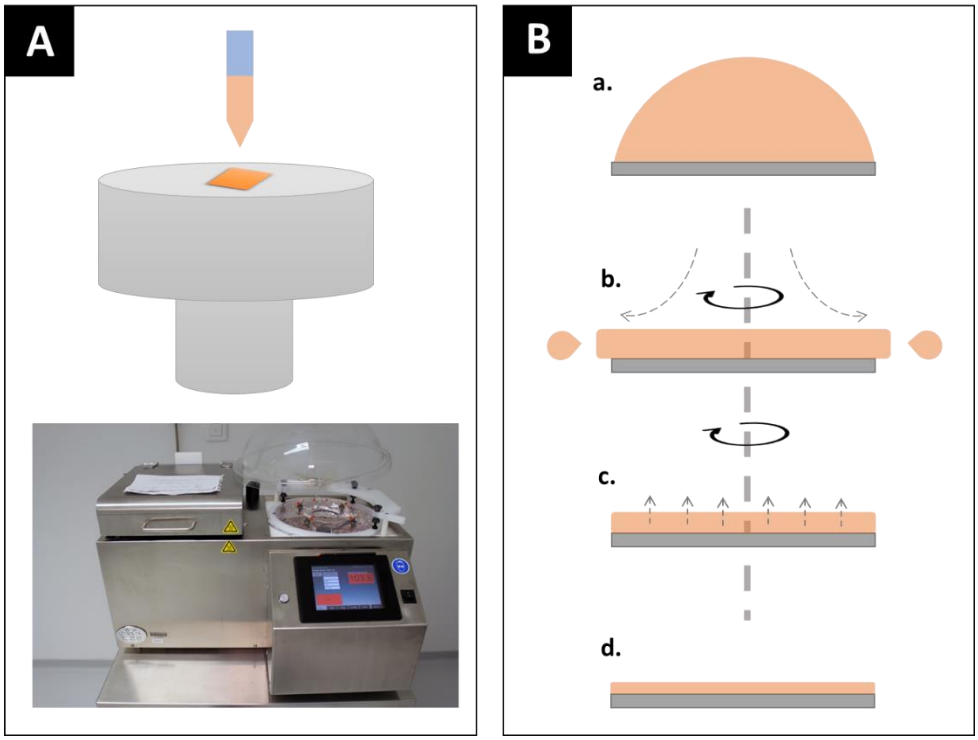

Figure 5.7: *(A) Scheme of the procedure and picture of the spin-coater used during this study. (B) Schematic example of different stages during the spin coating process: a. deposition of the solution, b. and c. evaporation of the solvent during the rotation and d. final film.*

First, the substrate is coated with the solution containing the polymer dissolved in a solvent (**Fig. 5.7A**). The substrate starts to rotate at a constant acceleration rate until the desired rotation speed is reached (in our case 2000-4000 rpm), and the majority of the solvent is evaporated during this process (**Fig. 5.7B**). Varying the rotation speed or the polymer concentration in the solution allows us to control the thickness of the film[4–6].

3.2. Reactive ion etching plasma

Plasma etching has proven to be a great tool for revealing metallic arrays using BCP films as a template[7–9]. The polymer material is chemically etched by reactive species of the plasma (*i.e.*, radicals or ions created in the plasma), inducing the formation of volatile products in the plasma chamber (**Fig. 5.8A**). It is also a good method to reduce noble metal salts to their metallic state (Au, Ag and Pt)[10]. For these reasons, it was used during this study in order to remove the polymer and reduce the gold or platinum salts selectively loaded in one of the BCP domains. The plasma etcher used in this study is a PE-100 Benchtop Plasma System (**Fig. 5.8B**)

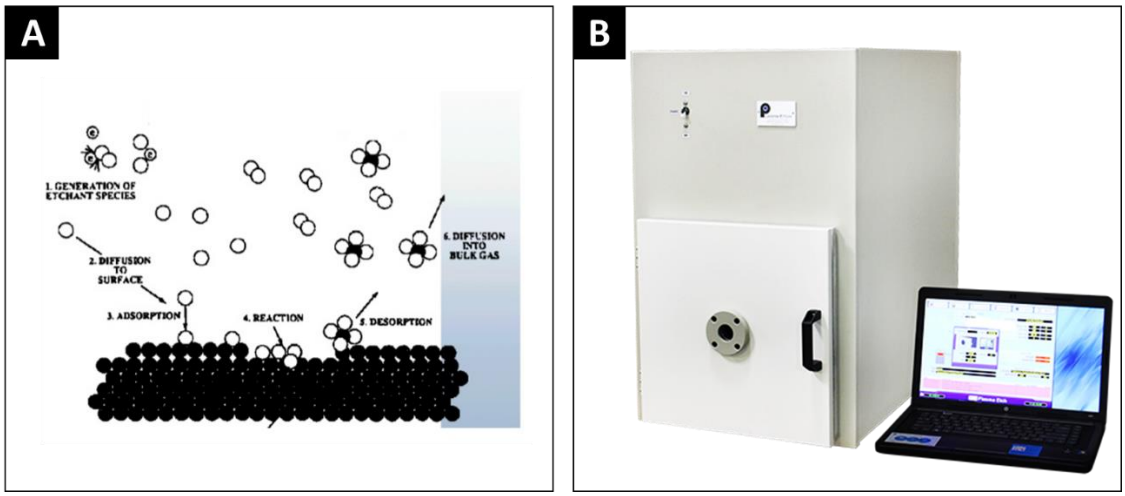

Figure 5.8: *(A) Schema of the plasma etching steps and (B) plasma etcher used during this study.*

4. Thin film characterization

4.1. Atomic force microscopy (AFM)

Atomic force microscopy (AFM) is a very high-resolution type of scanning probe microscopy technique. It is one of the foremost tools for imaging, measuring and manipulating surface features at the nanoscale level. Information is gathered by "feeling" the surface with a mechanical probe. It operates by measuring the attractive or repulsive forces between a tip and the sample surface. The tip is mounted on a reflective cantilever (the cantilever and the tip together are known as the probe) made of silicon nitride, silicon oxide or pure silicon fabricated with standard techniques used in semiconductor industry. A laser beam is focused onto the back of the reflective cantilever (**Fig. 5.9A**). As the tip scans the surface of the sample, the tip deflects, and the laser beam is bounced of the cantilever. Depending on the interaction between the tip and the sample, there will be a difference in the intensity of the reflected light. This difference is measured by the photodetector and the signal is sent off to the controller feedback loop. The feedback loop will attempt to keep the cantilever deflection constant by maintaining a constant distance between the cantilever and the sample. This can be done by moving the piezoelectric scanner (by applying a voltage) in the Z direction at each point. The voltage is then converted to a cantilever deflection.

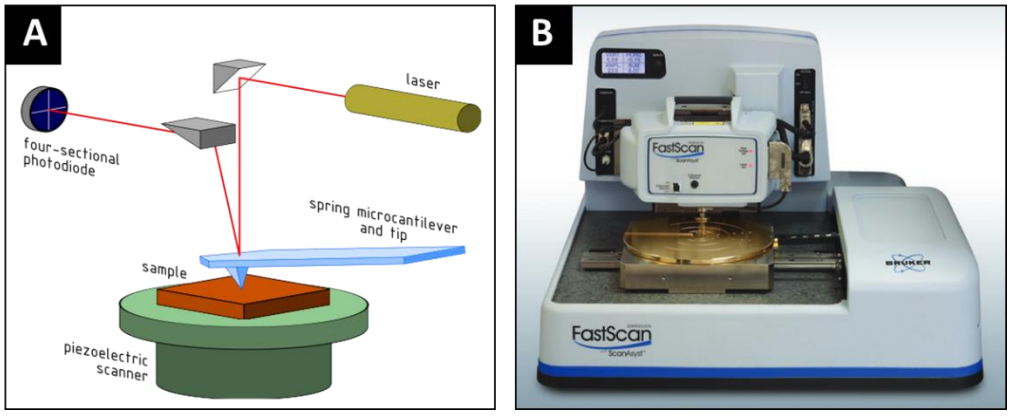

Figure 5.9. *(A) Schematic illustration of the principles of AFM. The scanner is composed of three piezo components, which control the horizontal (x and y) and vertical (z) movement of the sample. (B) AFM used during this study.*

Depending on the type of sample-tip interaction, there are three operation modes: contact mode, non-contact mode and tapping mode. In contact mode, the tip constantly touches the sample surface and scans across the surface. The contact mode microscopy gives an accurate image with high resolution, but both the sample and the tip may be damaged due to the direct contact. Such damage can be avoided by using the non-contact mode; however, the resolution is decreased. Hence, the tapping mode, a combination of contact and non-contact mode, appears to be a good solution. In tapping mode, the tip is alternatively placed in contact with the surface to provide a high resolution and lifted above the surface to avoid dragging the tip across the surface. The cantilever oscillates close to its resonant frequency with an amplitude between 20 and 100 nm.

In this work, a Dimension Fast Scan AFM from Bruker was used in tapping mode to characterize the surface morphology of the different films (**Fig. 5.9B**). Silicon cantilevers (Fastscan-A) with a nominal tip radius of 5 nm and a spring constant of 18 N/m were used. The resonance frequency of the cantilevers was 1400 KHz. The images were analysed using the WSxM software[11].

4.2. Scanning electron microscopy

The signals used by a scanning electron microscope to produce an image result from interactions of the electron beam with atoms at various (small) depths within the sample. The observation can be performed in two different imaging modes: SEI and BSEI.

SEI refers to the most common SEM mode, which is detection of secondary electrons emitted by surface atoms excited by the electron beam. By scanning the sample and collecting the emitted secondary electrons using a specific detector, an image displaying the topography of the surface is created. BSEI refers to backscattered-electron imaging (**Fig. 10A**), which is formed using an optional backscattered-electron detector and is mostly sensitive to the chemical contrast in the sample, with heavier and electron-rich elements scattering more, and appearing brighter in the images[12].

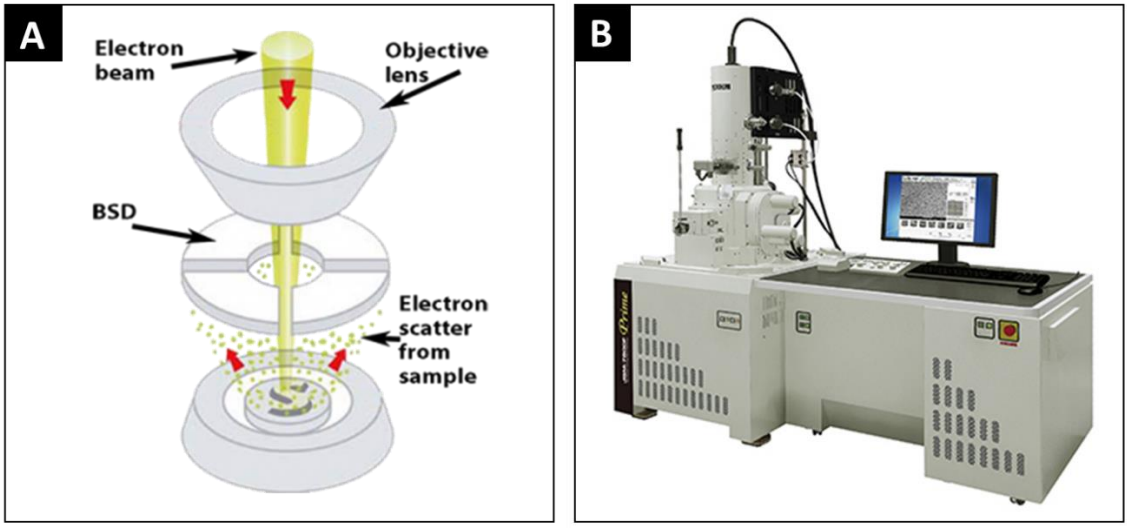

Figure 5.10: *(A) Schematic of backscattered electron image and (B) SEM used during this study*

During this study, a Jeol 7800-E Prime microscope at low acceleration voltage (1 kV) in the super high resolution gentle beam mode (GBSH) was used to characterize the structure of the metallic patterns (**Fig. 5.10B**). Gentle Beam (GB) is a technique of applying a bias voltage to the sample to reduce the speed of the incident electrons and increase the speed of the emitted electrons. The low acceleration voltages used in this study allows us to measure the samples without any metallization.

4.3. X-ray photoelectron spectroscopy (XPS)

X-ray photoelectron spectroscopy (XPS) is a surface-sensitive quantitative spectroscopic technique that measures the elemental composition at the parts per thousand range, empirical formula, chemical state and electronic state of the elements that exist within a material. XPS spectra are obtained by irradiating a material with a beam of X-rays while simultaneously measuring the kinetic energy and number of electrons that escape from the material being analyzed. XPS requires high vacuum (P ~ 10^{-8} millibars) or ultra-high vacuum (UHV; P < 10^{-9} millibars) conditions.

During this study, XPS analysis was carried out using a Thermo Fisher Scientific K-Alpha spectrometer with a monochromatic Al K_α source (E = 1486.6 eV). The X-ray spot size was 200 µm. The spectrometer was calibrated with monocrystalline gold and silver foils. Spectra were

acquired at a 200 eV pass energy and the high resolution spectra were acquired with a pass energy of 40 eV. Thermo Scientific Avantage software was used for fitting and quantification.

4.4. Kelvin probe force microscopy (KPFM)

The Kelvin probe force microscopy (KPFM) is a noncontact variant of atomic force microscopy (AFM) (**Fig. 5.11**). The KPFM technique consists in the measure of the V_{CPD} (contact potential difference) that is defined as

$$V_{CPD} = \frac{(W_{sample} - W_{tip})}{e} \quad (5.1)$$

Where W_{sample} and W_{tip} are the work functions of the sample and tip respectively, and e is the electronic charge[13]. As the charge state of the sample is not modified during the KPFM measurements (the electrical force is compensated with an application of an external V_{bias}), the work function of the sample can be calculated as the tip work function is known.

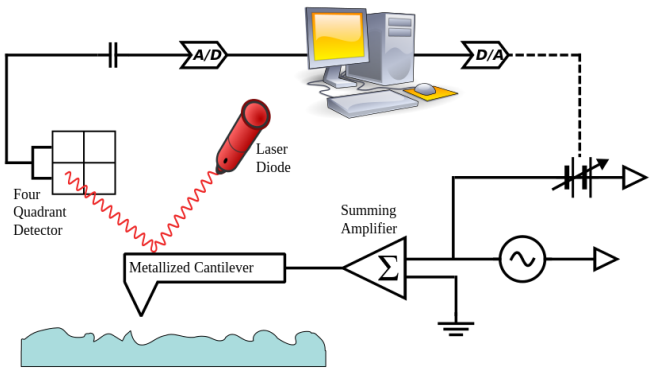

Figure 5.11: *Schematic of the KPFM technique, a conducting cantilever is scanned over a surface at a constant height in order to map the contact potential difference.*

In our case, KPFM experiments were performed in ambient conditions using a commercial AFM (Dimension Icon, Bruker) in frequency modulation mode (FM-Kelvin Probe Force Microscopy) with highly doped Si probes (PFQNE-AL, Bruker). For KPFM experiments, AC voltages of 5 V were applied to the sample. In FM-KPFM, the contact potential difference (CPD) is measured simultaneously to the surface imaging. KPFM images were analysed with Nanoscope analysis software (v1.8, Bruker).

4.5. Grazing-Incidence Small-Angle X-ray Scattering (GISAXS)

Grazing-Incidence Small-Angle X-ray Scattering (GISAXS) is a surface-sensitive scattering technique used to probe the nanostructure of thin films; essentially a reflection-mode version of SAXS. It is a versatile and powerful technique, which enables studies of nanoscale objects deposited on surfaces (e.g. nanoparticles), thin and ultra-thin layers of nanomaterials (e.g. block-copolymers) or nanostructured surfaces (e.g. lithographic patterns).

A typical GISAXS experiment involves directing a focused and collimated X-ray beam towards the surface of a thin film supported on a flat substrate. The grazing-incidence angle is carefully controlled using a sample-tilt stage and is typically on the order of 0.05° to 0.50°. At these shallow angles, the X-ray beam is efficiently reflected off the sample or substrate surfaces (**Fig. 5.12A**). The scattering from the sample is then recorded with a two-dimensional (2D) X-ray detector. The beam interacts with the sample structure, giving rise to scattering features (peaks, rings, diffuse scattering, etc.), which encode the nanoscale order in the sample (**Fig. 5.12B**). Careful analysis of the 2D scattering pattern enables quantification of many structural parameters of scientific interest, as described during the different chapters of this thesis.

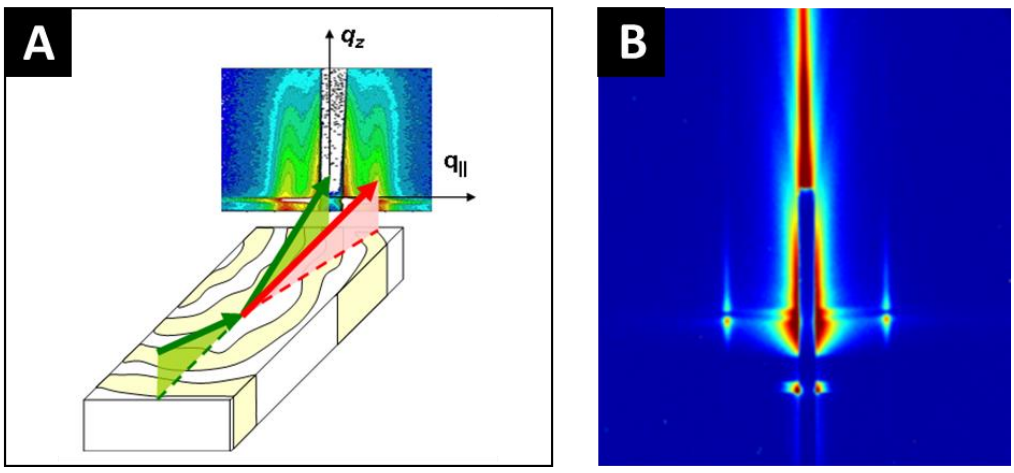

Figure 5.12: *(A) Geometry of a GISAXS experiment. The incident beam strikes the sample under a small angle close to the critical angle of total external X-ray reflection. The intense reflected beam as well as the intense scattering in the incident plane are attenuated by a rod-shaped beam stop. The diffuse scattering from the sample (red arrow) is recorded with an area detector. (B) Example of GISAXS pattern for a BCP thin film.*

In our case, GISAXS experiments were performed on the Dutch Belgian Beamline at the European Synchrotron Radiation Facility (ESRF) station BM26B in Grenoble (12 keV) (**Chapter 2**) and on SIRIUS (Soft Interfaces and Resonant Investigation on Undulator Source) station at the SOLEIL synchrotron (Gif-sur-Yvette) (8 keV) (**Chapter 3** and **4**).

In both cases, the incidence angle was set in the range of 0.12 – 0.19, which is between the critical angle of the PS-*b*-P2VP film and the silicon substrate. The beam illuminates the samples with a typical footprint of 150 mm^2. 2D scattering patterns were collected with a PILATUS 1M Dectris detector and the sample-to-detector distance was set to 3060 mm (ESRF) and 4459 mm (SOLEIL). The beam center position and the angular range were calibrated using a silver behenate standard sample.

In the case of the experiments performed at ESRF, GISAXS patterns were reduced using a home-made Matlab-based code. Intensity cuts along the horizontal q_y and vertical q_z were extracted from the GISAXS patterns after normalization for the incident photons and the exposure time by averaging the intensity of 5 adjacent pixel arrays, where $q_y = 2\pi/\lambda\left[\sin(2\theta_f)\cos(\alpha_f)\right]$ and $q_z = 2\pi/\lambda\left[\sin(\alpha_f) + \sin(\alpha_i)\right]$ are the modulus of the scattering vectors in the direction parallel and perpendicular to the substrate plane and α_i, $2\theta_f$ and α_f are the incident and scattering angles in the horizontal and vertical directions, respectively. For the GISAXS patterns obtained in SOLEIL the structural characterization was done using FitGISAXS software[14].

4.6. Spectral reflectometry

Reflectometry is especially suitable for thickness measurements. Light is reflected from the different surfaces (wafer and top of the film), and interferences are incurred upon collection. The light going through the longer path acquires an additional phase. This phase difference leads to an oscillatory behavior of the reflected intensity, with a frequency directly related to thickness (**Fig. 5.13A**). For this work a FILMETRICS F20-UV reflectometer with a thickness range from 1 nm to 40 µm was used (**Fig. 5.13B**). The results were fitted with the software provided by FILMETRIC.

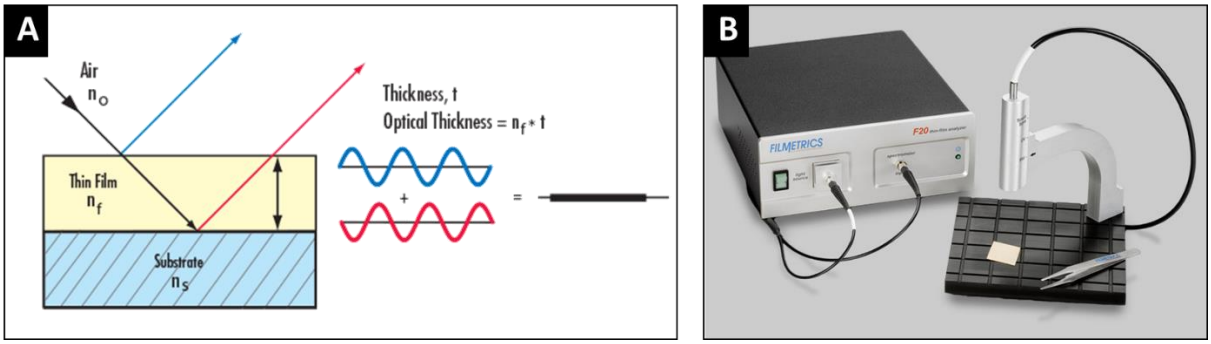

Figure 5.13: *(A) Schematic of principle of the spectroscopic reflectometry and its correlation with the film thickness and (B) system used during this study.*

4.7. Variable angle spectroscopic ellipsometry

Spectroscopic ellipsometry (SE) is an optical technique used for thin films and measures the change of polarization of the reflected (or transmitted) light as a function of the wavelength[15,16]. The two fundamental values in the measurements are Ψ and Δ, which represent the module ratio and phase difference between reflected light waves known as p- and s-polarized light waves, respectively (see **Fig. 5.14**). These are defined with respect to the plane of incidence, which contains by definition the incident beam and the normal to the sample surface. The p-polarized light is a wave polarized parallel to the plane of incidence and s-polarized light is a wave polarized perpendicular to the plane of incidence.

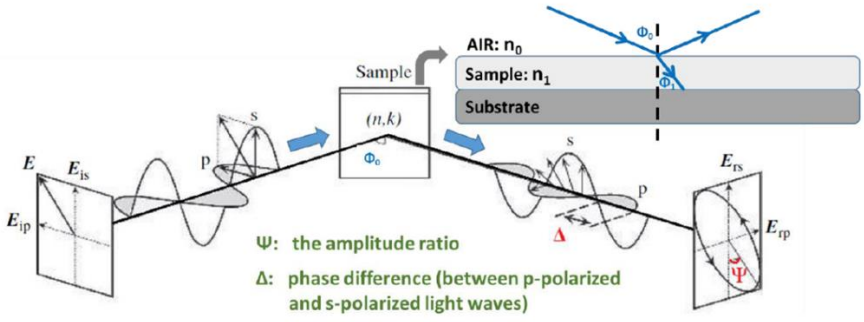

Figure 5.14 *Schematic of the principle of ellipsometry*

The measured parameters Ψ and Δ are the ellipsometric angles and are related to the ratio of the complex reflection coefficients r_s and r_p (s-polarized light and p-polarized light, respectively), defined as

$$r_s = \frac{I_s^{ref}}{I_s^{inc}} = |r_s|e^{i\delta_s} \quad (5.2)$$

$$r_p = \frac{I_p^{ref}}{I_p^{inc}} = |r_p|e^{i\delta_p} \quad (5.3)$$

Where $|r_s|$ and $|r_p|$ are the modules and δ_s and δ_p are the phases of the reflection coefficients.

The relation between the ellipsometric angles Ψ and Δ and the reflection coefficients for parallel and perpendicular polarizations is given by the following expression, that constitute the basic equation in ellipsometry

$$\rho = \frac{|r_p|}{|r_s|}e^{i(\delta_p - \delta_s)} = \tan(\Psi)e^{i\Delta} \quad (5.4)$$

In our case, the optical study of the films deposited on silicon-wafers was performed using variable angle spectroscopic ellipsometry (VASE) in reflection with a phase modulated spectroscopic ellipsometer (UVISEL, from Horiba Scientific) on the spectral range [0.6–4.8 eV or 258–2000 nm]. We used the UVISEL II (*A* = 45°; *M* = 0°) configuration, where *A* and *M* denote the azimuthal orientations of the input polarizer and the photoelastic modulator, respectively, with respect to the plane of incidence. Three values of the incidence angle θ_0 = 50°, 60° and 70° were used, unless said otherwise, and analysed simultaneously. The spot size was 1 mm and the measured data were checked to be similar at three different locations on the samples.

We acquired the ellipsometric quantities $I_s = \sin2(\psi)\sin(\Delta)$ and $I_c = \sin2(\psi)\cos(\Delta)$. The values of I_s and I_c vs. wavelength were then analysed using the DeltaPsi2 software from Horiba Scientific. The silicon wafers that we use as substrate have a native silica layer of few nm on top (**Fig. 5.15A**). In order to quantify it, spectroscopic ellipsometry data measured on the bare silicon substrate were analysed using the Si and SiO_2 tabulated dielectric functions and yielded a thickness value (2.0 nm) for the native silica layer on the surface, which was fixed in the further analyse. Ellipsometry data are usually analysed by representing the sample as a stack of flat and homogeneous layers (**Fig. 5.15B**). Our gold decorated surfaces are not flat and not homogeneous (**Fig. 5.15C**). Thereby, in order to analyse them, a homogeneous flat layer with a certain volume fraction of each component (gold and air) was established (**Fig. 5.15D**)

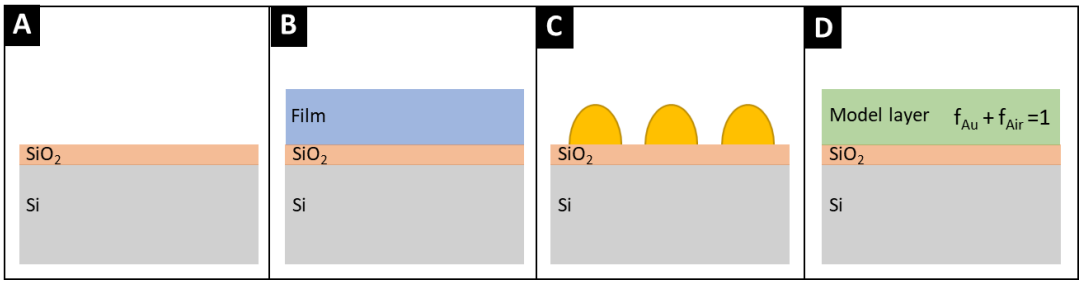

Figure 5.15: *Schematics of (A) silicon substrate used during the experiment with the native SiO_2 layer, (B) sample analysed by ellipsometry formed by stacked flat layers (C) our decorated gold surfaces and (D) model used during the analysis with DeltaPsi2 software.*

The extraction of the unknown parameters, which are *d* the thickness of the layer, *f* the gold volume fraction and the optical indices (n(λ), k(λ)) or alternatively the permittivity (ε'(λ)+ iε"(λ)) of the layer, is done by a fitting procedure. In order to model the thin film decorated with gold nanoparticles, we use an effective medium model. The Maxwell-Garnett effective medium approximation (EMA)[17], was chosen to describe our samples, and it is defined as

$$\frac{\varepsilon_{eff}-\varepsilon_m}{\varepsilon_{eff}+2\varepsilon_m} = f\frac{\varepsilon_{Au}-\varepsilon_m}{\varepsilon_{Au}+2\varepsilon_m} \tag{5.5}$$

Where ε_{eff} is the effective permittivity of the gold NP-matrix composite, ε_m is the matrix permittivity, ε_{Au} is the NP gold permittivity, and *f* is the gold volume fraction in the film.

The original derivation of the Maxwell-Garnett EMA assumed that material B consisted of spherical inclusions within the host matrix composed of material A. The Maxwell-Garnett EMA is considered a valid approximation in the limit of small spherical inclusions well separated from each other. In practice, volume fractions of less than 30%, and diameters of less than one fifth of the wavelength, are normally acceptable. An extension of the model for ellipsoidal objects can be used[18] by introducing a new parameter, the depolarization factor (*L*). *L* is related to the aspect ratio, *b*/*a*, of the ellipsoids, and values for *L* with $0 \le L \le 1/3$ (prolate ellipsoids), $L = 1/3$ (sphere) and $1/3 \le L \le 1$ (oblate ellipsoids) are possible.

The goodness of the fits was assessed by the value of the parameter χ^2 with *N* the number of measured points (typically several hundreds).

$$\chi^2 = \sum_{i=1}^{N}\left[\left(I_{s,fit}-I_{s,exp}\right)_i^2 + \left(I_{c,fit}-I_{c,exp}\right)_i^2\right] \tag{5.6}$$

1. Schulz, M. F. *et al.* Phase Behavior of Polystyrene−Poly(2-vinylpyridine) Diblock Copolymers. *Macromolecules* **29,** 2857–2867 (1996).

2. Uhrig, D. & Mays, J. W. Experimental techniques in high-vacuum anionic polymerization. *J. Polym. Sci. Part A Polym. Chem.* **43,** 6179–6222 (2005).

3. Hadjichristidis, N. & Hirao, A. *Anionic polymerization : principles, practice, strength, consequences and applications*.

4. Wadley, M. L., Hsieh, I.-F., Cavicchi, K. A. & Cheng, S. Z. D. Solvent Dependence of the Morphology of Spin-Coated Thin Films of Polydimethylsiloxane-Rich Polystyrene-*block* -Polydimethylsiloxane Copolymers. *Macromolecules* **45,** 5538–5545 (2012).

5. Lee, D. H., Park, S., Gu, W. & Russell, T. P. Highly Ordered Nanoporous Template from Triblock Copolymer. *ACS Nano* **5,** 1207–1214 (2011).

6. Park, S., Wang, J.-Y., Kim, B., Chen, W. & Russell, T. P. Solvent-Induced Transition from Micelles in Solution to Cylindrical Microdomains in Diblock Copolymer Thin Films. *Macromolecules* **40,** 9059–9063 (2007).

7. Ting, Y.-H. *et al.* Plasma etch removal of poly(methyl methacrylate) in block copolymer lithography. *J. Vac. Sci. Technol. B Microelectron. Nanom. Struct.* **26,** 1684 (2008).

8. Borah, D. *et al.* Plasma etch technologies for the development of ultra-small feature size transistor devices. *J. Phys. D. Appl. Phys.* **44,** 174012 (2011).

9. Sirard, S. *et al.* Plasma etch of block copolymers for lithography. *SPIE Newsroom* (2016). doi:10.1117/2.1201603.006351

10. Zou, J. J., Zhang, Y. P. & Liu, C. J. Reduction of supported noble-metal ions using glow discharge plasma. *Langmuir* **22,** 11388–11394 (2006).

11. Horcas, I. *et al.* WSXM : A software for scanning probe microscopy and a tool for nanotechnology. *Rev. Sci. Instrum.* **78,** 013705 (2007).

12. Venables, J. A. & Harland, C. J. Electron back-scattering patterns—A new technique for obtaining crystallographic information in the scanning electron microscope. *Philos. Mag.* **27,** 1193–1200 (1973).

13. Melitz, W., Shen, J., Kummel, A. C. & Lee, S. Kelvin probe force microscopy and its application. *Surf. Sci. Rep.* **66,** 1–27 (2011).

14. Babonneau, D. FitGISAXS: Software package for modelling and analysis of GISAXS data using IGOR Pro. *J. Appl. Crystallogr.* **43,** 929–936 (2010).

15. Azzam, R. M. A. & Bashara, N. M. *Ellipsometry and polarized light*. (North-Holland, 1987).

16. Schubert, M. *Infrared ellipsometry on semiconductor layer structures : phonons, plasmons, and polaritons*. (Springer, 2004).

17. Garnett, J. C. M. Colours in Metal Glasses and in Metallic Films. *Philos. Trans. R. Soc. A Math. Phys. Eng. Sci.* **203,** 385–420 (1904).

18. Heilmann, A. in 149–197 (Springer, 2003). doi:10.1007/978-3-662-05233-4_6